Kent Academic Repository

Njogu, Peter (2023) ***Additive Manufactured Antennas and Novel Frequency Selective Sensors.*** **Doctor of Philosophy (PhD) thesis, University of Kent,.**

Downloaded from
https://kar.kent.ac.uk/101078/ The University of Kent's Academic Repository KAR

The version of record is available from
https://doi.org/10.22024/UniKent/01.02.101078

This document version
UNSPECIFIED

DOI for this version

Licence for this version
CC BY-NC-ND (Attribution-NonCommercial-NoDerivatives)

Additional information

Versions of research works

Versions of Record
If this version is the version of record, it is the same as the published version available on the publisher's web site. Cite as the published version.

Author Accepted Manuscripts
If this document is identified as the Author Accepted Manuscript it is the version after peer review but before type setting, copy editing or publisher branding. Cite as Surname, Initial. (Year) 'Title of article'. To be published in ***Title of Journal*** , Volume and issue numbers [peer-reviewed accepted version]. Available at: DOI or URL (Accessed: date).

Enquiries
If you have questions about this document contact ResearchSupport@kent.ac.uk. Please include the URL of the record in KAR. If you believe that your, or a third party's rights have been compromised through this document please see our Take Down policy (available from https://www.kent.ac.uk/guides/kar-the-kent-academic-repository#policies).

Additive Manufactured Antennas and Novel Frequency Selective Sensors

A Thesis Submitted to The University of Kent

for the Degree of Doctor of Philosophy

in Electronic Engineering

July 2022

By

Peter Muthondio Njogu

Abstract

The research work carried out and reported in this thesis focuses on the application of additive manufacturing (AM) for the development antennas and novel frequency selective surfaces structures. Various AM techniques such as direct writing (DW), material extrusion, nanoparticle conductive inks are investigated for the fabrication of antennas and FSS based sensors.

This research has two parts. The first involves the development of antennas at the microwave and millimetre wave bands using AM techniques. Inkjet printing of nanoparticle silver inks on paper substrate is employed in the fabrication of antennas for an origami robotic bird. This provides an exploration on the practicability of developing foldable antennas which can be integrated on expendable robots using low-cost household inkjet printers. This is followed using Aerosol jet printing in the fabrication of fingernail wearable antennas. The antennas are developed to operate at microwave and millimetre wave bands for potential use in 5G Internet of Things (IoT) or body-centric networks.

The second part of the research work involves the development of frequency selective sensors. Trenches have been incorporated on an FSS structure to produce a new concept of liquid sensor. The sensor is fabricated using standard etching techniques and then using FDM method in conjunction with nanoparticle conductive ink. Finally, a new concept displacement sensor using an FSS coupled with a retracting substrate complement is introduced. The displacement sensor is a 3D structure which is conveniently fabricated using AM techniques.

Peter M. Njogu

Acknowledgements

Firstly, I would like to thank and acknowledge the support of my supervisor Dr. Benito Sanz-Izquierdo for his support and guidance during the nearly four years of this work. He has been supportive of my work offering advice and guidance as and when needed with an always open office door policy. I am also grateful for the freedom given to me during my research.

I would also like to thank Professor Emeritus Edward Parker for sharing his immense expertise in frequency selective surfaces and the associated topics and his suggestions and feedback during insightful discussions.

I would also like to give my special thanks to all the staff of the School of Engineering and Digital Arts at University of Kent for providing me with all the necessary help whenever needed. Special thanks to Antonio Mendoza for assistance with antenna fabrication and measurement, Andrew Brookman for facilitating the fabrication of the milled sensor at Printech Circuit Laboratories, Keith Greenhouse for the 3D printing of the models, Julien Soosaipillai and Mr. Colin Cresser for assistance in cutting of the foam spacers.

I would also like to thank my former research colleague and now Dr. Anshuman Shastri, and all the fellow researchers who kept me focused and motivated throughout the journey.

Lastly, I would like to thank my beloved wife, Happy, whose boundless patience, support, and encouragement made the journey much more bearable.

Table of Contents

List of Figures

List of Tables

List of Acronyms

ABS	Acrylonitrile butadiene styrene
AM	Additive manufacturing
c	Speed of light
C	Capacitance
C_i	Intrinsic capacitance
CPI	Centre for Process Innovation
cP	centipoise
L_i	Intrinsic inductance
CAD	Computer-aided design
DOD	Drop-on-demand
DW	Direct write
CSRR	Complementary split ring resonator
CPW	Coplanar waveguide
f	Frequency
FFF	Fused filament fabrication
FDM	Fused deposition modelling
FSS	Frequency Selective Surfaces
EBG	Electromagnetic bandgap
EBM	Electron Beam Melting
GHz	Gigahertz
IoT	Internet of Things
L	Inductance
LUT	Liquid under test
ε	Permittivity

ε_{eff}	Effective permittivity
ε_r	Relative permittivity
λ	Wavelength
ρ	Resistivity
σ	Conductivity
Ω	Ohms
Ω/sq	Ohm per square
WLAN	Wireless local area network
Wi-Fi	Wireless Fidelity
MIMO	Multi in multiple out
RFID	Radio frequency Identification
RF	Radio frequency
PET	Polyethylene terephthalate
PLA	Polylactic acid
PVD	physical vapour deposition
THz	Terahertz
VSWR	Voltage standing wave ratio
3D	Three dimensions
5G	Fifth generation
CAD	Computer-aided design
SLM	Selective laser melting
SMA	Sub-Miniature Version A
UHF	Ultra high frequency
UV	Ultraviolet
SLS	Selective laser sintering
SLA	Stereolithography

mPa·s	milliPascals seconds
g/ml	gram/millimeter
TM	Transverse Magnet mode
TE	Transverse Electric mode
μm	micrometre
EC	Equivalent circuit
nH	nano Henrys
mN/m	milliNewton per meter
μΩcm	micro-ohms centimeter
S/m	Siemens per meter
VNA	Vector network analysis
wt%	weight percent

CHAPTER 1: INTRODUCTION

1.1 Overview

Additive manufacturing (AM) which is also known as 3D printing technology was developed in the 1980s and is a process that involves making objects by joining materials from 3D model masks layer by layer in contrast to subtractive manufacturing (SM) techniques [1] in which objects are made by removing material from a big piece. This enables the production of parts with complex geometry and rapid prototyping of scaled-down or complete structures and devices before the final product is made [2] [3]. This feature allows the fabrication of complex geometries and enables designers to verify the best product design fit within a short period of the CAD design completion [4]. This has led to AM attracting significant interest from both the research community as well as the manufacturing industry [5]-[9].

Several AM methodologies exists which includes selective laser sintering (SLS) [10], electron beam melting (EBM) [11], stereolithography (SLA) [12], fused deposition modelling (FDM) [13], inkjet printing [14], Aerosol Jet printing [15][16] among others. Some of AM methodologies outlined were employed in the development of electromagnetic applications presented in this thesis i.e., antennas and frequency selective surfaces (FSS). The radiating part of the electromagnetic propagation devices developed is metallic conductors printed on dielectric substrates which provide conductivity across the 3D printed area.

The role that AM is likely to play in the future of manufacturing is demonstrated in Figure 1, [17]. It forecast the global 3D printing market size to continuously grow between the period 2022 and 2030. This will mainly be driven by the increased research and development in 3D printing and a growing demand for prototyping from industries such healthcare [18]-[20]; automotive [21][22], aerospace [23][24], construction [25]-[27] and defence [28]-[30].

As wireless communication and sensing become ubiquitous [31], demand for better and cheaper electromagnetic sign propagation devices like antennas, waveguides, filters, etc. will increase. Investigations have been on-going on 3D printing for the realization of advanced wireless communication antennas [32]-[36]. Besides focusing on the fabrication of conventional wireless antennas and circuits, the creation of innovative, difficult-to-implement 3D designs has also been reported [37].

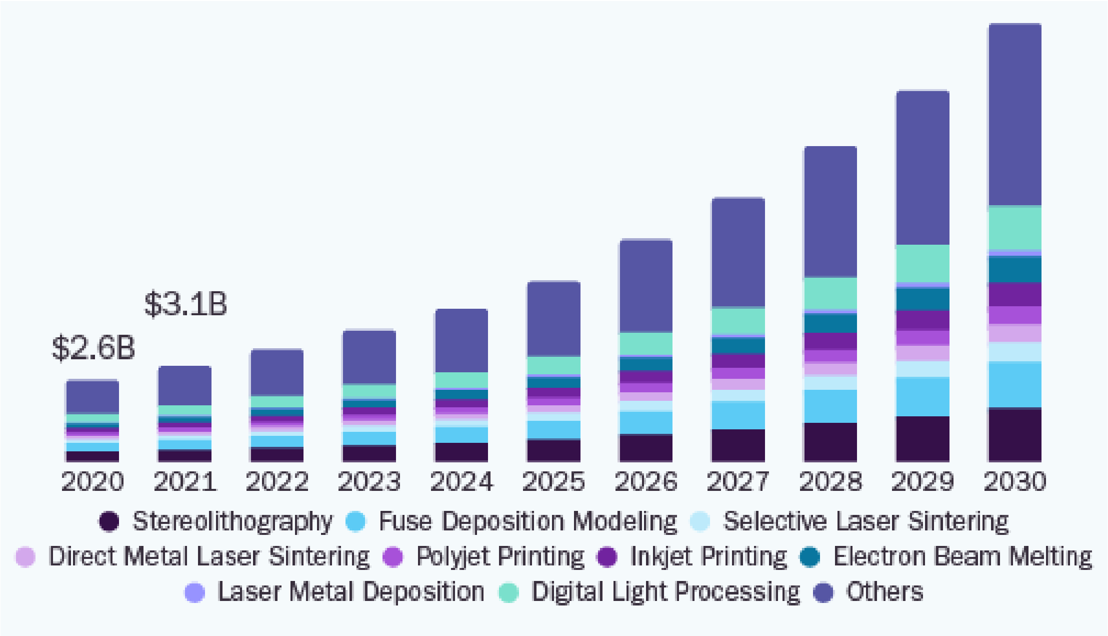

Figure 1.1 North America 3D printing Market Size, by technology, 2020-2030 [17]

1.2 Research motivation and contribution to knowledge

Electromagnetic propagation devices such as antennas are vital components for wireless communication. Advances in wireless networks have led to advances in complex antenna designs for high precision applications. The fabrication of these types of devices is challenging using the conventional fabrication method and thus the need for alternative methods. As outlined in section 1.1, AM technology can be a solution for fabricating modern antennas and other electromagnetic devices.

The aim of this work is to investigate the use of AM processes in the development of novel electromagnetic devices. The focus is on the fabrication of antennas and frequency selective surfaces for microwave and millimetre wave applications.

This thesis presents modern antennas and frequency selective sensors developed using AM techniques. Antennas of different shapes, as well as frequency selective surface sensors for various applications, are presented. The main fabrication processes employed are inkjet printing, aerosol jet printing, Fused filament fabrication (FFF), and direct write (DW) of solver conductive pastes. The fabrication techniques are analysed in terms of surface characteristics of the printed layers, and the radio frequency (RF) devices are studied using their S-parameter and far field responses.

The main contributions that have come out of this work are listed below. These contributions are supported by the list of publications presented in section 1.3.

The primary contributions are:

(1) The development of antennas that can be integrated with low-cost inkjet printing electronics on disposable photo paper robotic origami robotic bird. This is demonstrated to be an inexpensive and quick method of antenna manufacture. The print was found to have good electrical conduction across the printed area implying that it is a good for the proposed application. The fabricated antennas have acceptable performance for efficient communication between the origami robot and a remote controller which is shown in simulation and experimental results.

(2) Manual hand printing of silver ink using a brush, a form of direct write, and Aerosol Jet printing can be employed in the development of wearable antenna applications. Such wearable application can be employed in sensing, tracking, wireless communication, medical application etc. This is demonstrated in the development of microwave and millimetre wave antennas for customized fingernail antennas. The manual hand deposition of the silver nanoparticle ink demonstrates is an inexpensive antenna development technique while the use of the Aerosol Jet machine printing facilitates the flexibility needed for smooth and precise application of the silver nanoparticle ink on the curvature of the fingernail.

(3) The use of trenched FSS structures for microwave liquid sensing applications. The Frequency Selective Surface (FSS) based sensor is suitable for sensing liquids falling onto a surface. In the sensor concept, the sensing function is achieved by altering the capacitance between adjacent FSS elements when chemical liquids of different electrical characteristics are inserted in grooves around the loop conductors. The change in capacitance produces a change in the frequency resonance based on the liquid's electrical characteristics, which is detected as the transmission response of the FSS.

(4) A new concept of application of microwave and 3D printing in displacement sensing using three dimensional structures. The FSS displacement sensor is based on changing the effective permittivity as a complement substrate is withdrawn from the FSS. The wireless sensor works by modifying the transmission response when the substrate complement is gradually withdrawn. This sensor is ideal for instances requiring real-time monitoring of a structural change e.g., sinking, or lateral displacement.

The antennas and frequency selective sensors presented in this work have been simulated using CST Microwave Studio^{TM} software. This is discussed in detail in chapter 2, section 2.8.

1.3 List of publications arising from this work

Journal papers

[1] **Peter M. Njogu**, Benito Sanz-Izquierdo; Sung Yun Jun; Gabriel Kalman; Steven Gao; Asish Malas and Gregory J. Gibbons, "Evaluation of Planar Inkjet-Printed Antennas on a Low-Cost Origami Flapping Robot", IEEE Access, vol. 8, pp. 164103-164113, 2020. **DOI:** 10.1109/ACCESS.2020.3020824

[2] **Peter M. Njogu**, Benito Sanz-Izquierdo, Ahmed Elibiary, Sung Yun Jun, Zhijiao Chen and David Bird, "3D Printed Fingernail Antennas for 5G Applications", *IEEE Access*, vol. 8, pp. 228711 - 228719, 2020. **DOI:** 10.1109/ACCESS.2020.3043045

[3] **Peter M. Njogu**, Benito Sanz-Izquierdo and E.A. Parker, "A Liquid Sensor based on Frequency Selective Surfaces" IEEE Transactions on Antennas and Propagation, vol. 71, no. 1, pp. 631 - 638, 2023. **DOI:** 10.1109/TAP.2022.3219540

[4] **Peter M. Njogu**, Benito Sanz-Izquierdo and E.A. Parker," 3D FSS Based Displacement Sensor" to be submitted to IEEE Sensors Journal (**Under revision**)

Conference papers

[1] **Peter Njogu** and Benito Sanz-Izquierdo," Removable Finger Nail Antenna" 14th European Conference on Antennas and Propagation (EuCAP), 2020, Copenhagen, Denmark **DOI:** 10.23919/EuCAP48036.2020.9135744

[2] **Peter Njogu**, Paul Jablonski, Anshuman Shastri and Benito Sanz-Izquierdo," Origami Boat Sensing Antenna" 15th European Conference on Antennas and Propagation (EuCAP), 2021 Dusseldorf, Germany **DOI:** 10.23919/EuCAP51087.2021.9411024

[3] A. Shastri, **P. Njogu**, B. Sanz-Izquierdo, S. Gao and Z. Chen," Low-cost Inkjet Printed Paper Poster FSS for 5G Applications" 15th European Conference on Antennas and Propagation (EuCAP) 2021 Dusseldorf, Germany **DOI:** 10.23919/EuCAP51087.2021.9411448

[4] **Peter Njogu**, Benito Izquierdo and Stephen Gao," Disposable 3D printed Liquid sensor" 16th European Conference on Antennas and Propagation (EuCAP), 2022 Madrid, Spain (KAR id:96093)

[5] **Peter Njogu**, Sung Jun and Benito Sanz-Izquierdo, Zhijiao Chen, Steven Gao "3D Printed Millimeter wave Antenna Integrated into a Ring for 5G Applications" MMS2022: Mediterranean Microwave Symposium 2022, Pizzo Calabro, Italy **DOI:** 10.1109/MMS55062.2022.9825614

[6] **Peter Njogu**, Anshuman Shastri, Adam Smith, Steven Gao and Benito Sanz-Izquierdo, "Screen-Printed FSS Plasterboard for Wireless Indoor Applications" MMS2022: Mediterranean Microwave Symposium 2022, Pizzo Calabro, Italy **DOI:** 10.1109/MMS55062.2022.9825506

1.4 The organization of the thesis

The rest of this thesis is organized as follows:

Chapter 2 gives an overview of additive manufacturing (AM) processes and their application to antenna and microwave components as well as FSS structures. It also provides some basic theories of antennas and frequency selective surfaces.

Chapter 3 presents an antenna integrated with an expendable paper origami flipping robot using inkjet printing technology. The antenna elements are directly printed onto a photo paper substrate using silver nanoparticle conductive ink. The substrate is then folded into the origami robotic bird. An ordinary low-cost home desktop inkjet printer is used in the deposition of conductive metallic parts of the antenna. Three antenna solutions are provided. The antennas operate at the frequency bands allocated for drone control.

Chapter 4 presents the manual application of antenna radiator as well as that of Aerosol Jet technology in the printing of a 3D wearable fingernail antenna. A manually painted as well as Aerosol Jet printed antennas were developed, at microwave and at the millimetre wave bands. The designs have been printed directly onto an acrylonitrile butadiene styrene (ABS) fake fingernail substrate. The wearable antennas are proposed, and their performance are discussed.

Chapter 5 describes a new concept for microwave liquid sensors based on Frequency Selective Surfaces structure. The sensor uses trenches between FSS elements to modify the transmission response when liquids with different permittivity are inserted. Though the initial design is milled, simple and inexpensive fused filament fabrication (FFF) is employed to fabricate a disposable AM version of the FSS structure. Hand painting is used to make the metallic parts of the FSS. The independent resonant nature due to individual chemicals allows the device to be reused for different liquids thus reducing cost.

In Chapter 6, an FSS based displacement sensor using a retractable dielectric substrate is described. The sensor uses a retractable substrate that is a complement of the FSS. The retractable substrate is gradually withdrawable from the FSS. As the complement substrate is withdrawn from the FSS, the effective permittivity of the FSS structures varies which changes the transmission response. The optimised solution is a 3D FSS structure and complement which a fabricated using AM techniques. This sensor is intended for structural displacement applications.

Chapter 7 summarises the conclusion of each chapter as well as suggests potential future advancement of each piece of work.

References

[1] F. Calignano, D. Manfredi, E. P. Ambrosio, S. Biamino, M. Lombardi, E. Atzeni, A. Salmi and P. Fino, "Overview on Additive Manufacturing Technologies," *Proceedings of the IEEE,* vol. 105, no. 4, pp. 593 - 612, 2017.

[2] E. Macdonald, R. Salas, D. Espalin, M. Perez, E. Aguilera, D. Muse and R. B. Wicker, "3D Printing for the Rapid Prototyping of Structural Electronics," *IEEE Access,* vol. 2, pp. 234 - 242, 2014.

[3] I. Gibson, D. Rosen and B. Stucker, Additive Manufacturing Technologies: 3D Printing, Rapid Prototyping, and Direct Digital Manufacturing, New York: Springer New York, 2015.

[4] D. Pham and R. S. Gault, "A comparison of rapid prototyping technologies," *International Journal of Machine Tools and Manufacture,* vol. 38, no. 10-11, pp. 1257-1287, 1998.

[5] A. Bandyopadhyay, S. Vahabzadeh, A. Shivaram and S. Bose, "Three-dimensional printing of biomaterials and soft materials," *Materials Research Societ,* vol. 40, pp. 1162-1168, 2015.

[6] V. Sanchez-Romaguera, M. A. Ziai, D. Oyeka, S. Barbosa, J. S. R. Wheeler, J. C. Batchelor, E. A. Parker and S. G. Yeates, "Towards inkjet-printed low cost passive UHF RFID skin mounted tattoo paper tags based on silver nanoparticle inks," *Journal of Materials Chemistry C,* vol. 1, p. 6395–6402, 2013.

[7] J. M. E. Matthew R. Skorskia, Z. Ahmed, A. E. Miller and M. R. Hartings, "The chemical, mechanical, and physical properties of 3D printed materialscomposed of TiO2-ABS nanocomposites," *Science and Technology of Advanced Materials,* vol. 17, no. 1, p. 89–97, 2016.

[8] S. C. Ligon, R. Liska, J. Stampfl, M. Gurr and R. Mülhaupt, "Polymers for 3D Printing and Customized Additive Manufacturing," *Chemical Reviews,* vol. 117, p. 10212−10290, 2017.

[9] H. Xin and M. Liang, "3-D-Printed Microwave and THz Devices Using Polymer Jetting Techniques," *Proceedings of the IEEE,* vol. 105, no. 4, pp. 737-755, 2017.

[10] B. Zhang, Z. Zhan, Y. Cao, H. Gulan, P. Linnér, J. Sun, T. Zwick and H. Zirath, "Metallic 3-D Printed Antennas for Millimeter- and Submillimeter Wave Applications," *IEEE Transactions on Terahertz Science and Technology,* vol. 6, no. 4, pp. 592 - 600, 2016.

[11] H. Galarraga, D. A.Lados, R. R. Dehoff, M. M.Kirka and P. Nandwana, "Effects of the microstructure and porosity on properties of Ti-6Al-4V ELI alloy fabricated by electron beam melting (EBM)," *Additive Manufacturing,* vol. 10, pp. 47-57, 2016.

[12] B. Khatri, M. Frey, A. Raouf-Fahmy, M.-V. Scharla and T. Hanemann, "Development of a Multi-Material Stereolithography 3D Printing Device," *Micromachines,* vol. 11, no. 5, pp. 1-17, 2020.

[13] Melnikova, A. Ehrmann and K. Finsterbusch, "3D printing of textile-based structures by Fused Deposition Modelling (FDM) with different polymer materials," *IOP Conference Series: Materials Science and Engineering,* vol. 62, pp. 1-7, 2018.

[14] B. S. Cook and A. Shamim, "Inkjet Printing of Novel Wideband and High Gain Antennas on Low-Cost Paper Substrate," *IEEE Transactions on Antennas and Propagation,* vol. 60, no. 9, pp. 4148 - 4156, 2012.

[15] J. A. Paulsen, M. Renn, K. Christenson and R. Plourde, "Printing conformal electronics on 3D structures with Aerosol Jet technology," in *2012 Future of Instrumentation International Workshop (FIIW) Proceedings*, Gatlinburg, TN, USA, 2012.

[16] A. Shastri, B. Sanz-Izquierdo, E. A. Parker, S. Gao, P. Reynaert, Z. Chen and L. Winchester, "3D Printing of Millimetre Wave and Low-Terahertz Frequency Selective Surfaces Using Aerosol Jet Technology," *IEEE Access,* vol. 8, pp. 177341 - 177350, 2020.

[17] Grand View Research, "3D Printing Market Size, Share & Trends Analysis Report By Component (Hardware, Software, Services), By Printer Type, By Technology, By Software, By Application, By Vertical, By Region, And Segment Forecasts, 2022 - 2030," Grand View Research, 04 05 2022. [Online]. Available:

https://www.grandviewresearch.com/industry-analysis/3d-printing-industry-analysis. [Accessed 04 05 2022].

[18] M. N. Nadagouda, V. Rastogi and MeganGinn, "A review on 3D printing techniques for medical applications," *Current Opinion in Chemical Engineering,* vol. 28, pp. 152-157, 2020.

[19] R. J. Morrison, K. N. Kashlan, C. L. Flanangan, J. K. W. B. G. E. Green, S. J. Hollister and K. J. Weatherwax, " Regulatory Considerations in the Design and Manufacturing of Implantable 3D-Printed Medical Devices," *Clinical and Translational Science,* vol. 8, no. 5, pp. 594-600, 2015.

[20] M. D. Prima, J. Coburn, D. Hwang, J. Kelly, A. Khairuzzaman and L. Ricles, "Additively manufactured medical products – the FDA perspective," *3D Printing in Medicine,* vol. 2, no. 1, pp. 1-6, 2016.

[21] Center for Automotive Research," Assessing the Potential of Additive Manufacturing for Lower-Cost Tools in the Automotive Industry: Moving from Rapid Prototyping to Production Applications" white paper, Stratasys, [online] Available: WP_FDM_AutomotiveResearch_A4_0816a.indd (sys-uk.com)

[22] SMARTECH, "Additive Automotive: Advancing 3D Printing Adoption In the Automotive Industry," SmarTech Markets Publishing, Charlottesville, 2015.

[23] A. Gisario, M. Kazarian, F. Martina and M. Mehrpouya, "Metal additive manufacturing in the commercial aviation industry: A review," *Journal of Manufacturing Systems,* vol. 53, pp. 124-149, 2019.

[24] M. Kalender, S. E. Kılıç, S. Ersoy, Y. Bozkurt and S. Salman, "Additive Manufacturing and 3D Printer Technology in Aerospace Industry," in *9th International Conference on Recent Advances in Space Technologies (RAST)*, Istanbul, Turkey, 2019 .

[25] P. Wua, J. Wang and X. Wang, "A critical review of the use of 3-D printing in the construction industry," *Automation in Construction,* vol. 68, pp. 21-31, 2016.

[26] B. Furet, P. Poullain and S. Garnier, "3D printing for construction based on a complex wall of polymer-foam and concrete," *Additive Manufacturing,* vol. 28, pp. 58-64, 2019.

[27] C. Buchanan and L. Gardner, "Metal 3D printing in construction: A review of methods, research, applications, opportunities and challenges," *Engineering Structures,* vol. 180, pp. 332-348, 2019.

[28] M. J. Louis, T. Seymour and J. Joyce, "3D opportunity in the Department of Defense: Additive manufacturing fires up," Deloitte University Press , 2014.

[29] A. Busachi, D. Kuepper, J. Brunelli, W. Heising, C. Moeller, D. Fisher, C. Watts and R. Drake, "Modelling Applications of Additive Manufacturing in Defence Support Services: Introducing the AM - Decision Support System," NATO Science & Technology Organization, Bristol, 2017.

[30] M. Fey, "3D Printing and International Security: Risks and Challenges of an Emerging Technology," Peace Research Institute Frankfurt (PRIF) , Frankfurt, 2017.

[31] A. Schmidt, "Ubiquitous Computing: Are We There Yet?," *Computer,* vol. 43, no. 2, pp. 95 - 97, 2010.

[32] D. Helena, A. Ramos, T. Varum and J. N. Matos, "Antenna Design Using Modern Additive Manufacturing Technology: A Review," *IEEE Access,* vol. 8, pp. 177064 - 177083, 2020.

[33] P. Nayeri, M. Liang, R. A. Sabory-Garcı´a, M. Tuo, F. Yang, M. Gehm, H. Xin and A. Z. Elsherbeni, "3D Printed Dielectric Reflectarrays: Low-Cost High-Gain Antennas at Sub-Millimeter Waves," *IEEE Transactions on Antennas and Propagation ,* vol. 62, no. 4, pp. 2000 - 2008, 2014.

[34] V. T. Bharambe, J. Ma, M. D. Dickey and J. J. Adams, "Planar, Multifunctional 3D Printed Antennas Using Liquid Metal Parasitics," *IEEE Access,* vol. 8, pp. 134245 - 134255, 2019.

[35] K. Johnson, M. Zemba, B. P. Conner, J. Walker, E. Burden, K. Rogers, K. R. Cwiok, E. Macdonald and P. Cortes, "Digital Manufacturing of Pathologically-Complex 3D Printed Antennas," *IEEE Access,* vol. 7, pp. 39378 - 39389, 2019.

[36] J. Kimionis, M. Isakov, B. S. Koh, A. Georgiadis and M. M. Tentzeris, "3D-Printed Origami Packaging With Inkjet-Printed Antennas for RF Harvesting Sensors," *IEEE Transactions on Microwave Theory and Techniques,* vol. 63, no. 12, pp. 4521 - 4532, 2015.

[37] M. Liang and H. Xin, "Three-Dimensionally Printed/Additive Manufactured Antennas," in *Handbook of Antenna Technologies*, Singapore, Springer Nature, 2016, pp. 661-697.

CHAPTER 2: LITERATURE REVIEW AND THEORETICAL BACKGROUND

2.1 Introduction

This chapter offers a review of the existing work on additive manufacturing (AM), which is also known as 3D printing (3DP) technology [1], and its application in antenna and electromagnetic devices development. The literature background focuses on the various additive manufacturing methods (AM), their application in the fabrication of antennas, and frequency selective surfaces (FSS). Various electromagnetic devices that have been fabricated using AM and their applications are also reviewed.

Traditional subtractive manufacturing (SM) like milling [2] [3] and turning [4] [5] have been used in the manufacture of high precision parts in various industries. SM processes involve the subtraction of material from a larger piece such as metals, plastics, or composites to develop an object or device. This is wasteful because the removed parts are likely to be unusable because of size, shape, state, etc. This makes SM costly for high value parts manufacturing. The machines on which SM processes are implemented have a linear and rotational axis that moves the cutting tool to a given orientation and position on the piece under manufacture [6]. Computer aided manufacturing, processes, and planning has been incorporated into modern SM to adapt to automation and integration of design and manufacturing demands. However, it does not address the question of SM method's wastefulness and high cost.

Additive manufacturing (AM), however, has shown to have minimal material wastefulness, better cost and lead-time efficiency and enablement of rapid casting [7][8]. It also enables multiple-pieces part to be manufactured as one single unit [9] which enhances strength and durability of the part.

Antennas and frequency selective surfaces (FSS) are generally made up of metallic layer and a dielectric substrate. AM methods can variously be employed in the development of either their substrate or metallic layer or both. The radiating part of electromagnetic devices (antennas and FSS) are usually the metallic layer which need to be highly conductive. On the other hand, the electrical properties of the dielectric substrate are relative permittivity, loss tangent and the substrate thickness. The electrical properties of these layers influence the behaviour of the application under design.

2.2 A Brief Summary of Antenna Theory

Antennas are devices that radiates or receive electromagnetic radio waves [10] [11]. They are transitional or transducers that interfaces energy from electronics circuit to free space i.e., converts electrical current in EM waves at the transmitter as shown in Figure 2.1 and vice versa receiver. Figure 2.1(a) illustrates a signal travelling through the electronics circuit conductor connected to an antenna. Figure 2.1(b) illustrates the free space waves formed at the point where the circuit conductor end. At the antenna point, energy is radiated into free space. The radiated energy is symbolised by the antenna radiation patterns. Radiation patterns represents the way the radiated energy is distributed into space in relation to its direction as soon in Figure 2.2.

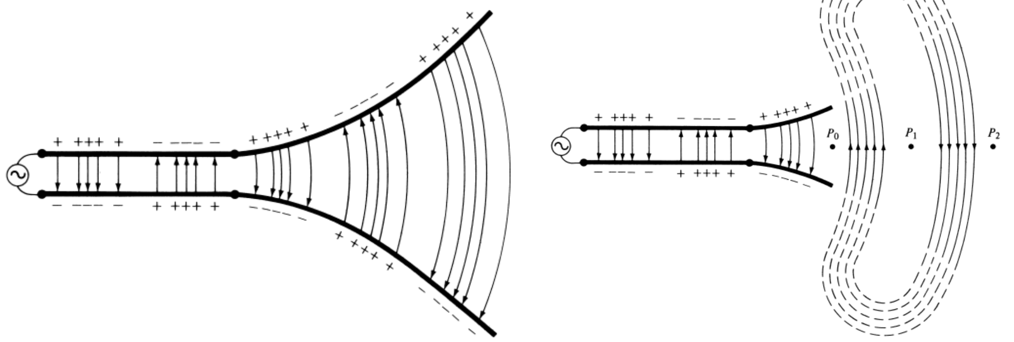

Figure 2.1 Illustrative (a) antenna and electric field lines (b) antenna and free space waves [11]

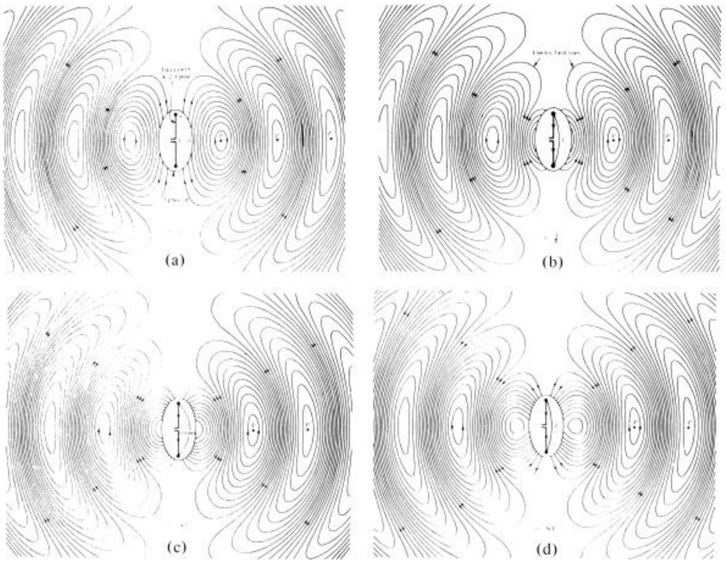

Figure 2.2 Electric field lines of free space wave for a dipole antenna at various time after the signal is radiated [11].

There are different types of antennas. They include wire, aperture, microstrips, array, reflector, and lens antennas. A brief discussion on microstrip antennas is given as part of this work involved development of microstrip based antennas.

Microstrips antennas can be patch, dipole, or slot and are usually designed for specific applications. They are planar [12] in nature and come in various shapes and sizes on a dielectric material. They offer the unique characteristics of low profile, lightweight, low cost, versatility, and integrability with other circuits as well as conformability to the surfaces of the substrate [13]. This coupled with their inherently small sizes, flat structure, conformal modelling, and ease of manufacture make them ideal for biomedical devices, sensing, missiles, space, satellite applications, that require small sized antennas [14]. Their planar nature make them geometrically adaptable for AM printing techniques. A range of parameters is measured for all types of antennas to evaluate their performance. These are scattering (S) parameters, impedance bandwidth, radiation patterns, directivity, efficiency, and gain. Microstrip planar antenna applications are presented in Chapter 3 and Chapter 4.

2.3 A general overview of Additive Manufacturing Methodologies

As was mentioned in chapter 1, AM employs layer by layer material deposition fabrication techniques to create structure directly from computer-aided design (CAD) files [15] - [18]. The 3D CAD models are initially converted to a standard tessellation language (.STL) file format. In a virtual environment, the .STL file is sliced to form two-dimensional (2D) sections stacked along the height dimension. A 3D printer then derives information from the slice-file which it uses to build the 2D layer. The building starts from the base and each layer is built on top of the previous one. This continues until the product under construction is realized, thus translating 3D CAD models into a physical object. The CAD digital slicing and subsequent scanning of the 3D data for use by AM processes to build a continuous objects layer by layer without moulding or machining enables decentralized fabrication of customized objects. This renders AM processes flexible, autonomous, resulting in rapid product development cycle.

Additive Manufacturing Technology is classified into various additive manufacturing processes. These are material extrusion, material jetting, binder jetting, sheet lamination and vat photopolymerization, powder bed fusion, and directed energy deposition [19]. They all follow a generalised process shown in Figure 2.3.

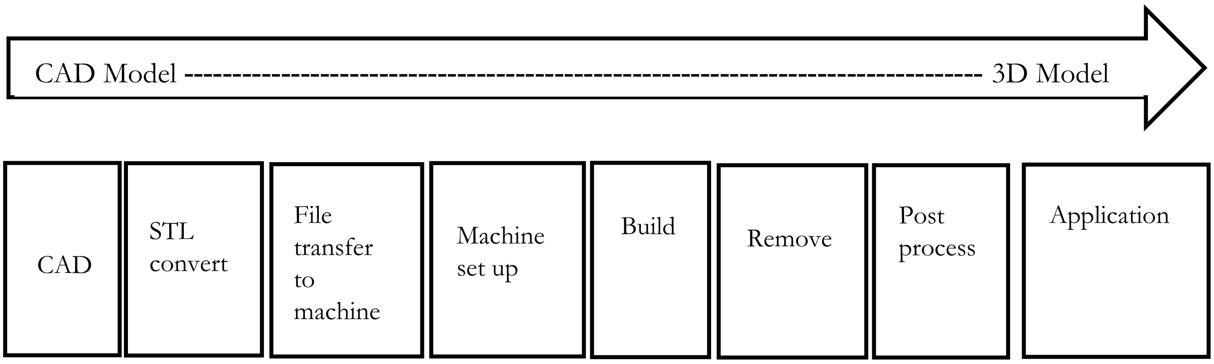

Figure 2.3 Generalized Additive Manufacturing Process [20]

As a modern manufacturing model, AM has attracted interest in the development of electronics [21] [22]. This is especially due to some of its process' ability to combine multiple materials in a single build. This has enabled the production of volumetric designs such as 3D structural electronics [23]-[28] where both the substrate, the conductive elements, and the components can be simultaneously built. Further, due to its flexibility and the ability of manufacturers to optimize the design with minimal waste during production, AM processes are environmentally friendly [7]. This is as opposed to the traditional manufacturing processes that impose constraints on the product design, requiring subprocesses. These subprocesses translate to more energy consumption. AM is thus the technology of the future for the development of systems like the next generation microwave and millimetre wave systems [29].

2.4 Additive Manufacturing for Antennas and Electromagnetic devices

Antennas are electromagnetic devices used in applications such as wireless communication, biomedical imaging, and military radar [30] whose design using modern AM technology has been reported [31]. Various types of antennas developed development using AM processes include patch antennas [32] [33], meander line antennas [34], horn antennas [35], Lens Antenna [36] reflect array antennas [37], and gradient index (GRIN) lens antennas [38]. Multi-material fabrication using AM methods has been employed to develop metallic antenna elements [39], On-Chip THz 3D Antennas [40], dielectric antenna [41], and dielectric-metal combined antenna [33][37]. With the emergence of wireless body-centric networks [42], the need for wearable antennas has arisen [43] [44]. Wearable AM manufactured antennas have been reported in the literature space [45]-[52].

The conductive part of the antenna is metallic. There are two ways in which they can be manufactured using AM methods. One way is print the unit wholly metallic using direct metal printing AM methods. The other is to print a polymer mould and then using electroplating [53] process to metalise it.

Powder Bed Fusion is a direct metal printing AM method used to print metallic structures while material jetting is a polymer printing AM technique. Direct metal printing the need for subsequent metal plating of the fabricated RF and electromagnetic propagation device and is thus less complicated. A brief description of the two methods is given next.

2.4.1 Powder Bed Fusion

The most applicable AM processes for direct metal printing of RF and microwave devices are powder bed fusion processes. Powder Bed Fusion processes include Direct Metal Laser Sintering (DMLS), Electron Beam Melting (EBM), Selective Laser Melting (SLM) and Selective

Laser Sintering (SLS) [54]. Figure 2.4 shows a schematic diagram of generic equipment for powder bed fusion manufacturing technology.

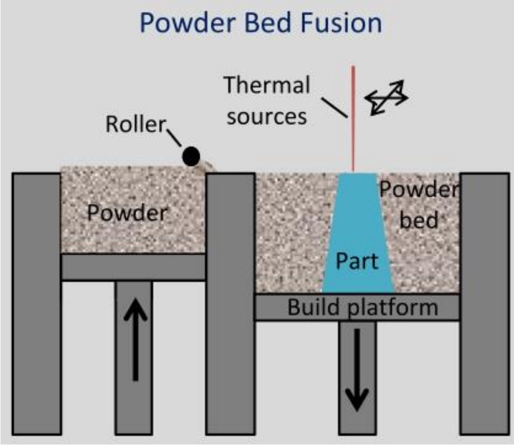

Figure 2.4 Diagram of a typical powder bed fusion equipment [29]

The powder bed fused process involves the build platform moving down by a predefined layer thickness measure. More powder is then added and spread to form the next layer to create a homogenous powder layer. The powder is then exposed to an energy source, usually a laser or electron beam for melting and subsequent solidification. Using the predefined laser parameters in the powder bed fusion file, the energy source scans the outer and inner part contour on the powder layer in the build file [55] to obtain information of the object under print. Application of direct metal printing is illustrated in Figure 2.5. Figure 2.5(a) is a selective laser melting 3D printed conical horn antennas for Millimetre and Submillimetre Wave Applications [56]. Figure 2.5(b) and Figure 2.5(c) shows the oblique and the top views respectively, of a Sierpinski fractal antenna [57] printed using metal powder binder [58] method.

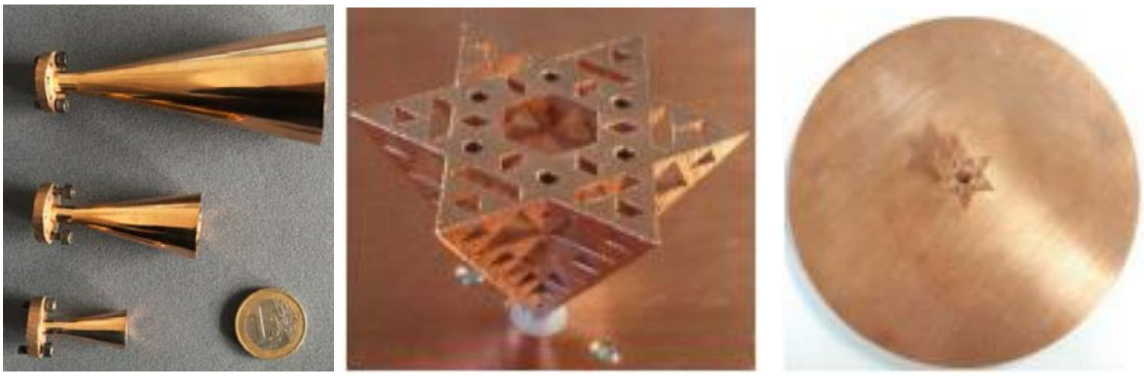

(a) (b) (c)

Figure 2.5 (a)SLM printed Cu-15Sn conical horn antennas [56] and Sierpinski fractal antenna's (b) oblique, (c) top view [57]

2.4.2 3D polymer printing and metallization

There are several polymer printing techniques. Among them, Polyjet has the uniqueness of enabling production of high resolution parts with a wide range of properties [59]. It employs inkjet techniques but instead of ink, it dispenses polymers. Ultra violet (UV) light is used to cure the dispensed material. After a layer has printed and cured, another is deposted and cured on top of it and the process continues until the 3D objected under manufacture is completed [60]. Figure 2.6 is schematic diagram of the Polyjet process. The developed part can then be metalised to make it conductive.

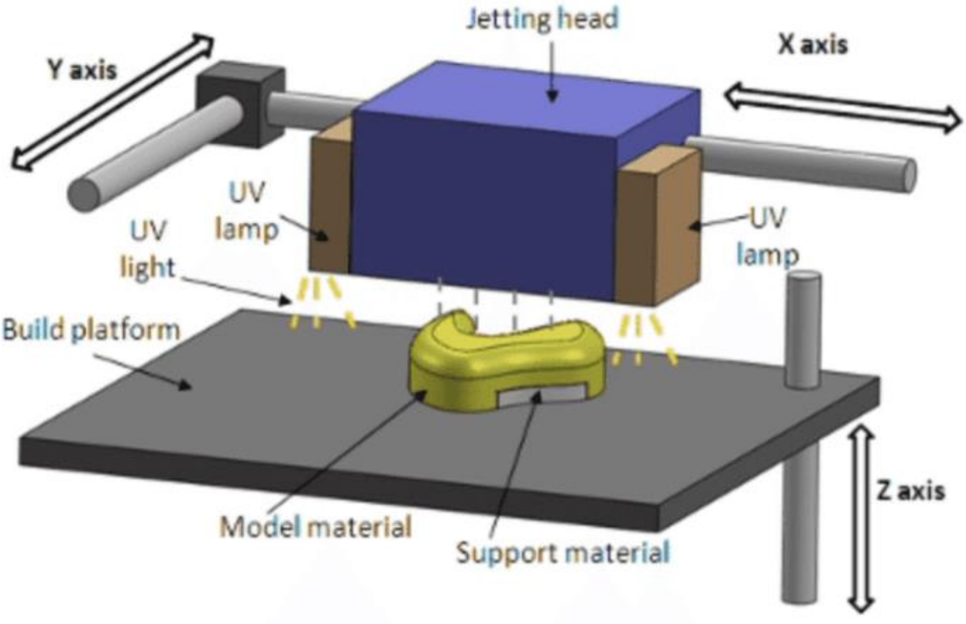

Figure 2.6 Schematic diagram of a PolyJet 3D printer [61]

The technique of 3D printing Polymer antenna structures followed by metallization is described in [62] and [63] in the manufacture of rectangular horn antenna and parabolic mirror and high-gain Vivaldi antennas respectively shown in Figure 2.7. Figure 2.7(a) shows a polyjet horn antenna and a parabolic mirror. Figure 2.7(b) shows the rectangular horn antenna and parabolic mirror (Figure 2.7(a)) after metallic plating. In Figure 2.7(c), the ABS UWB High-Gain Vivaldi antennas before and after are depicted.

There are several metallization methods that can be used to metalize polymers. These includes electroless metallization [64] [65], electrodeposition [66], chemical metallization of plastics [67] and sputtering physical vapour deposition (PVD) [68], which has been employed in [69] - [71]. In PVD, a process that includes vacuum metallization, a metal vapour is produced through spraying of solid targets with gaseous Argon ions. The produced vapour is then deposited on the printed polymeric antenna to form a thin metallic film. Application of the conductive part of an AM developed RF device can also be achieved by directed manual application of the conductive material on a polymer material. This was employed in this work. Silver nanoparticle ink was manually painted on FFF printed FSS substrate structures developed as described in Chapters 5 and Chapter 6, using an ordinary artist's brush. This method of application of conductive material is both inexpensive and environmentally friendly as no expensive equipment is needed nor is any energy required.

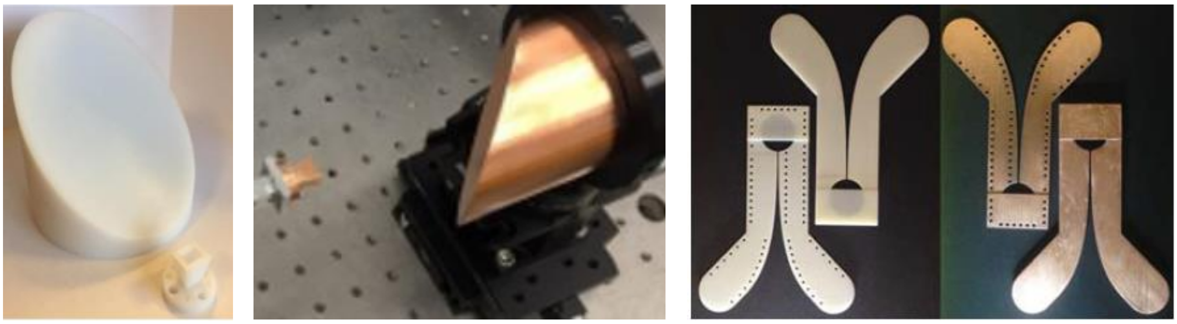

(a) (b) (c)

Figure 2.7 (a) Polyjet printed rectangular horn antenna and parabolic mirror prior to metal plating (b) after plating [62] (c) Metalized- ABS Vivaldi Antennas before and after metallization [63]

2.4.3 Direct write (DW) AM approaches

Direct writing is an AM process that uses different methods to transfer material for the creation of linear or complex structures on a substrate. DW processes employ various techniques or energy form to dispense material, usually ink, for the creation of features ranging from nanometres (nm) to millimetres (mm). These techniques include inkjet, laser, mechanical pressure, and tips [72]. DW can be categorised into droplet, energy beam, flow and tip based on the material transfer mechanism. Material jetting (MJ), a process that cures liquid polymer in a selective manner to build an object [73] falls under direct write. It uses multi-nozzle print head for quick deposition or for simultaneous deposition of different materials [29]. The different simultaneously deposited materials can be the conductor and the substrate [74] as demonstrated in Figure 2.8 [75]. In the development of the Yagi-Uda antenna; the conductive radiating elements, the director, and reflector conductors has been patterned using drop-by-drop deposition of nanoparticle inks. This was achieved using a Dimatrix DMP-2831, a piezoelectric drop-on-demand inkjet printing system, capable of patterning both metallic and dielectric inks pattern which was then cured and sintered to enable effective bonding of the silver ink and the substrate. Employing a combination of nanoparticle-based metallic and polymer-based dielectric inks, the fully printed with selectively patterned thin dielectric substrate was fabricated.


Figure 2.8 Inkjet-printed multilayer 5-director Yagi–Uda antennas with the printed dielectric substrate for the microstrip-to-slotline feeding transition [75]

Inkjet printing [76] and aerosol jet printing [72] [77] belong to the droplet-based category of DW. They work by depositing liquid material (ink) droplets selectively and then leaving them to cool and solidify [78]. They have been employed in the development of various RF and microwave devices. Aerosol jet printing was employed in the development of a frequency selective surface (FSS) [79] using Optomec Aerosol Jet printing technology [80]. A combination of fused filament fabrication (FFF) and aerosol jet printing to develop a wearable application is proposed in [51]. Inkjet printing has previously also been employed in the development of [81] and RFID Tags [82] on paper substrate. The use of Inkjet printing in the development of an antenna in this work is described in Chapter 3 while that of aerosol jet printing is described in Chapter 4. The principles of operation of these two AM technologies are briefly discussed in Subsections 2.4.4 and 2.4.5 respectively.

2.4.4 Inkjet printing technology

Studies have been conducted on printable conductive inks in fabrication of electronics. This is driven by demand for miniaturization, reduction of the geometrical footprint as well as the demand for flexible electronics devices [83]. Printed electronics promises to transform the rigid components of electronic devices into flexible thin layers thus offering unique customer level features of inexpensive and disposable electronics gadgets [84]. The advent of printable conductive inks, attention growing interest in flexible electronics [85] and electronics disposability fit well with the developing inkjet printing technology and the future of electronics components/devices developments. The material (ink) used should have the desired electrical properties for the conductive element under development [86].

The printing occurs when an electronically controlled ink drops ejection occurs through a nozzle. It falls onto a predetermined surface (substrate) [87] - [89] in a patterned manner. An advantage of the inkjet printing technology is its material (ink) conservation nature [76]. The material consumption reduction is achieved by shortening the processing time by performing the patterning operation as a single step. It works by ejection of a pre-set amount of ink from a compartment through an outlet by a sudden contraction of the compartment volume due to piezoelectric action. An electrically controlled piezoelectric actuator creates a pressure pulse. This causes the ink filled compartment to contract in response. The sudden contraction sends a shockwave through the liquid causing an ink droplet to eject through the nozzle [76]. The ejected ink drops impinge on the surface of the substrate. The ink comprises a dissolved solute in a solvent. The droplet flows along the substrate surface aided by momentum and its surface tension and then dries as the solvent evaporates [90]. Figure 2.9 demonstrates the principle of the inkjet printing technique. Synchronization of the electronics and the ejection system can be set such that complex layouts can be patterned on a planar surface.

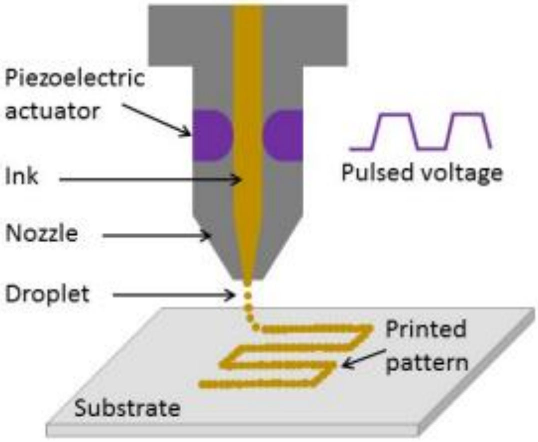

Figure 2.9 Schematic of typical inkjet printing systems [89] [91]

Figure 2.10 shows common printers that employs inkjet technology. Figure 2.10(a) is a Fujifilm Dimatix 2800 printer while Figure 2.10(b) is a brother inkjet printer. Fitted with nanoparticle ink cartridges they have been employed in development of electromagnetic devices and other electronics components/devices as illustrated in Figure 2.11.

Figure 2.10(a) Dimatix DMP 2800 inkjet printer [92] [93] and (b) Brother inkjet printer with a printed antenna [94]

The printer cartridges are filled with the conductive ink and the printing of the electronics circuits or devices is performed as normal printing would be done on a substrate. Several types of nanoparticle inks that can be used in inkjet printing are copper ink [95], Graphene Nanoflakes [96], and silver nanoparticle-based inks [97]. The silver nanoparticle is the most nanotechnology derived product and most widely studied [84] [98] [99]. A brief discussion of Inkjet printed electromagnetic, and microwave fabricated devices is given in Subsection 2.4.4.1.

2.4.4.1 Inkjet printed antennas and microwave devices

Antennas and other microwave devices have been fabricated using inkjet printing with nanoparticle ink on various dielectric materials. Popular dielectric materials for silver nanoparticle ink printing are polyamide [100], PET (Polyethylene terephthalate) [101] [102], paper [103], "skin-like" conformal silicone and polyvinyl alcohol (PVA) substrates [104] and PEL Nano-P60 paper [105]. There has been research on paper-based electronics [106] - [111] due to its availability, affordability, flexibility, biodegradability and lightweight. It makes for a promising substrate for flexible electronics, electronics components, and electromagnetic devices such as antennas. The use of inkjet printing on various substrates is illustrated in Figure 2.11. Figure 2.11(a) shows an inkjet printed electrode on paper, Figure 2.11(b) is a monopole antenna printed on PET substrate, Figure 2.11(c) shows a monopole.

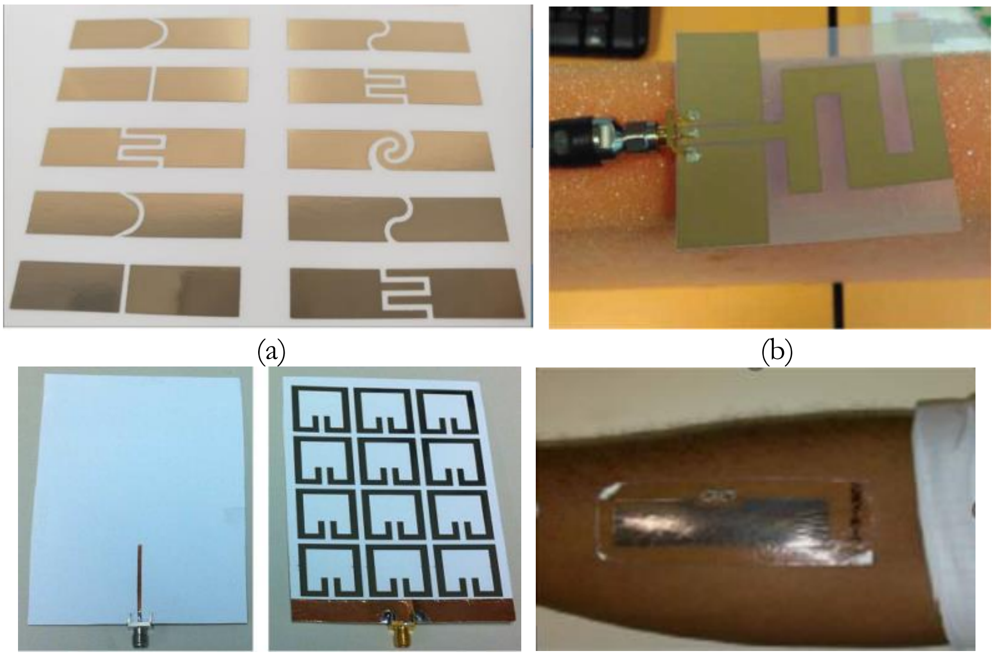

(a) (b)

(c) (d)

Figure 2.11 Inkjet printed flexible (a) electrodes on paper [86], (b) conformal monopole antenna on PET [100], (c) monopole antenna with inkjet printed EBG array on paper [103] (d) Inkjet printed UHF RFID on transfer tattoo paper [104] antenna with inkjet printed EBG array on paper while Figure 2.11(d) is a UHF RFID transfer tattoo paper [104] conformal silicone and polyvinyl alcohol (PVA) substrates. These demonstrate the use of nanoparticle inks to construct conductive track using the inkjet printing methods employing readily available desktop printers. This offers good prospects for future inexpensive development of electronics and antenna designs.

2.4.5 Aerosol jet direct writing

The other type of DW technique is Aerosol Jet Printing (AJP). It employs a focused aerosol beam as opposed to individual ink droplets as in inkjet technology [77] [112]. It is non-contact and line-of-sight with complementary advantages over the traditional methods such as screen printing, photolithography, and micro-dispensing for which it is emerging as a replacement and is seen as superior to inkjet printing [113] - [115]. Its operating principle is illustrated in Figure 2.12. The process aerodynamically focuses the conductive ink for high resolution deposition and patterning onto a substrate which may be planar or 3D. The ink is first atomized in the pneumatic atomizer chamber to generate aerosol. The generated aerosols is then dynamically focused at the printer head into a concentrated beam. This beam is then projected onto the substrate material. Post fabrication curing follows. The curing could be sintering in an oven, light, or may involve ultraviolet curing [116] depending on the material and its properties. The curing process also enhances material properties such as electrical conductivity.

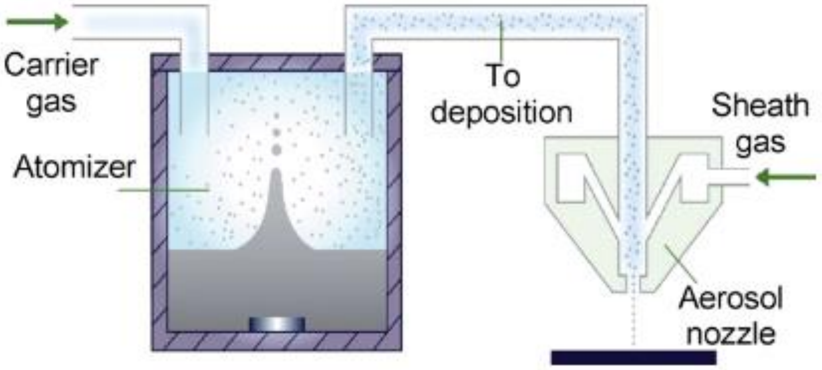

Figure 2.12 Principle of the Aerosol Jet system [72]

One of the advantages of Aerosol Jet technology is that it can reliably achieve ultra-fine feature circuitry that inkjet processes cannot. This feature enables the production of smaller, high-performance components with complex geometries demanded of size-sensitive applications used in wireless and mobile wireless stations [117]. These would include passive as well as active components like lump components, filters, micro antennas, etc. Aerosol Jet technology has been used to fabricate electromagnetic devices such as FSS [79], wearable antenna [51] as well as other electrical devices such as solar cells metallization [118], electronic circuit [116] [119], and [120], Micro-scale graphene interconnects [121]. Figure 2.13 shows an Optomec aerosol printer while Figure 2.14 depicts the printing process as well a printed quasi-Yagi-Uda antenna [122].

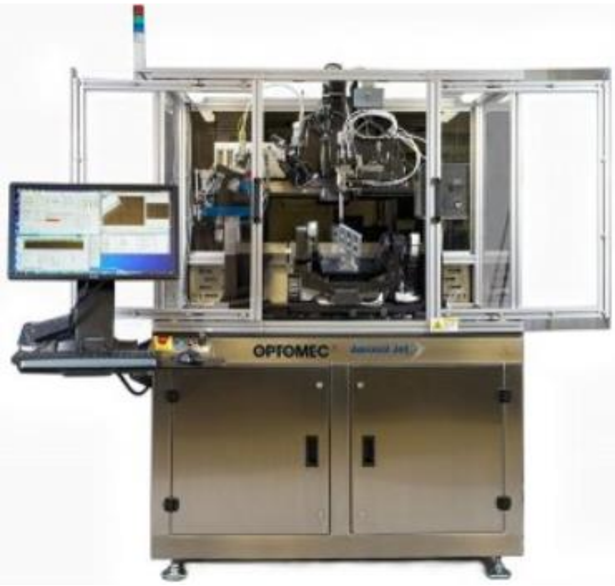

Figure 2.13 An aerosol jet printing system [123]

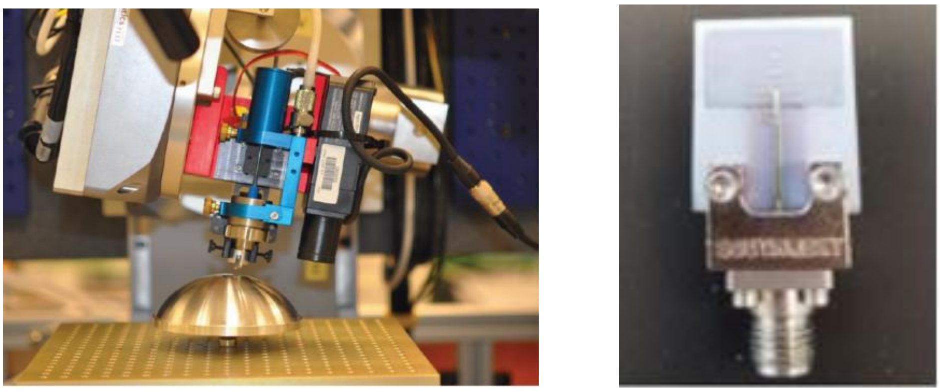

(a) (b)

Figure 2.14 Aerosol Jet (a) printing process [1] (b) quasi-Yagi-Uda antenna [122]

Further discussion on the aerosol jet fabrication process in the fabrication of electromagnetic devices is given in Chapter 4, Subsection 4.2.2.

2.4.6 Material Extrusion: Fused Filament Fabrication (FFF)

Fused filament fabrication (FFF), also known as material extrusion or fused deposition modelling (FDM) process, involves heating a material which is then dispensed through a nozzle layer by layer. A continuous filament of thermoplastic material is used as the base material for the printing of objects. The melted material is extruded through a nozzle and deposited onto a platform that may be heated for additional bonding. The extruder and the platform then recede from each other after a layer has been printed to allow the subsequent layer to be deposited to form a continuous profile [124] - [126] of the object under print. Figure 2.15 illustrates the FFF printing principle.

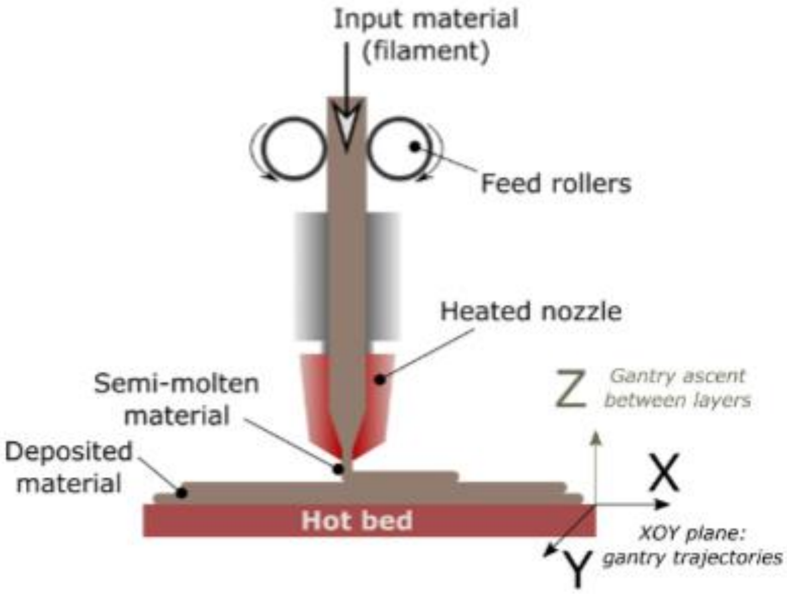

Figure 2.15 Schematic representation of a fused deposition modelling system [124]

FFF as a 3D printing methodology has been employed in the cost-effective, versatile fabrication of thermoelectric materials. It is the most used method in the manufacturing of 3D polymer parts. It is low cost and offers high resolution with a wide range of materials e.g., polylactic acid (PLA), applicable in its use.

2.5 Frequency Selective Surfaces

Frequency Selective Surfaces (FSS) are periodic structures of identical elements arranged in one- or two-dimensional infinite array [127] developed on a dielectric material or substrate. As resonant structures, they function as the fields across their surface become resonant, perfectly superimposing in certain directions at specific frequencies [128] and thus reflecting or transmitting all energy at that frequency. The type and shape of the element, its periodicity, inter element spacing as well as its supporting structure i.e., substrate determines its surface characteristics such as its frequency response, polarisation, and bandwidth [127]. This implies that changes in these parameters affect the electromagnetic responses of the FSS structures. This feature is factored in the FSS design and allows for the FSS optimisation for specific applications [129]. FSS structures have been widely studied in the past [130] - [133] and have evolved from simple geometries to complex ones driven by performance requirements and modern applications. They act as electromagnetic wave filters [134]. Their reflective and transmissive properties allow them to control the electromagnetic responses of the structure

[135]. Thus, FSS resonant structure can be designed to give either a reflective response or transmissive response at prescribed frequency or frequencies.

As FSS are usually constructed on a substrate, their resonance frequency $\mathrm{f_c}$ is affected by the presence of the substrate due to the substrate's dielectric loss. From Maxwell's equation, it has been inferred that surrounding the periodic structure with a substrate of dielectric constant ε_r causes its resonance frequency to reduce by a factor $\sqrt{\varepsilon_r}$. On the other hand, if the substrate material is on only one side of the periodic structure, the resonance frequency shifts downwards by a factor $\sqrt{(\varepsilon_r + 1)/2}$ [127]. This is a phenomenon that can be applied in determining FSS structure parameters for specified operating frequencies. This can be realised by employing substrate materials of differing electrical characteristics i.e., ε_r and loss tangent. Altering the dielectric substrate thickness can be tailored to produce a predetermined operating frequency when the FSS is embedded in the dielectric substrate. It is also possible to employ symmetrical embedding of FSS within the dielectric to tune out losses' due dielectric losses [136] by manipulating the substrate thickness.

Typical FSS elements, categorised into four groups are shown in Figure 2.16, composed of arbitrary shapes, slots, and dipole arrays. Group 1 elements are referred to as centrally connected or N-poles e.g., dipole, tripole, crosses, group 2 are loops (circular, square, hexagonal loops), group 3 are solids such as patches of various shapes while group 4 are combinations of the other three.

FSS designers make use of arrays of elements from any of the groups or a combination depending on the application envisioned. As already, mentioned, FSS acts as electromagnetic wave filters. Depending on the geometry, FSS arrays can be categorised under the four types of filters. These are bandstop and bandpass [127] and lowpass (capacitive) and high pass (inductive) [133] [137] as shown in Figure 2.17. Figure 2.17(a) shows the bandstop type of filters which comprises the square loops elements of conductor width t, inter-element separation g, and period P. Figure 2.17(b) is its slot complement equivalent bandpass filters. Figure 2.17(c) and Figure 2.17(d) show the low pass and high pass types of filters which comprises solid patch elements and the slot patches complements respectively.

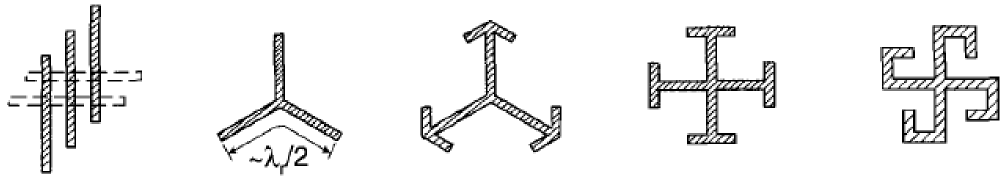

Group 1: "Center Connected" or "N-Poles"

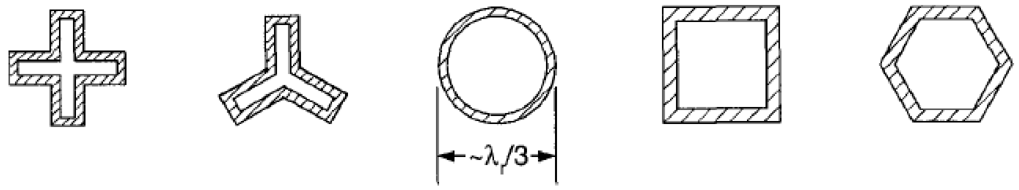

Group 2: "Loop Types"

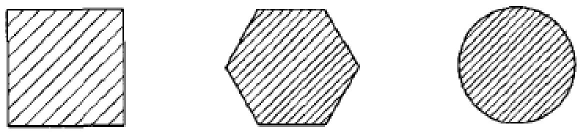

Group 3: "Solid Interior" or "Plate Type"

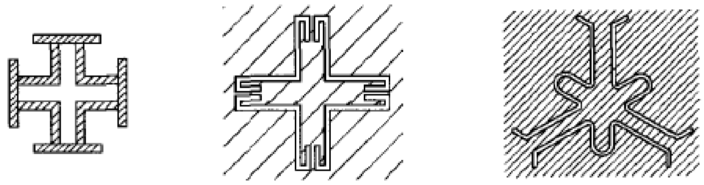

Group 4: "Combinations"

Figure 2.16 Typical element types arranged in groups [127]

A stable resonance response with varying angles of incidence is expected of a good element [130]. As FSS are usually illuminated by a wave normally incident to it, their angle of incidence of the electric field affects its resonant frequency. This is because the capacitance and inductance of an FSS are dependent on the angle of incidence, angle of polarization as well as whether polarization is TE or TM. Thus, as the values of both the capacitive and inductive reactance varies with the angle of incidence (θ) as well as whether polarization is TE or TM [138], variation in the resonant frequency of the FSS occurs. The effect of the angle of incidence on the capacitive and inductive reactance of the FSS is demonstrated in the derivation of the lumped elements equivalents in Section 2.5.3.

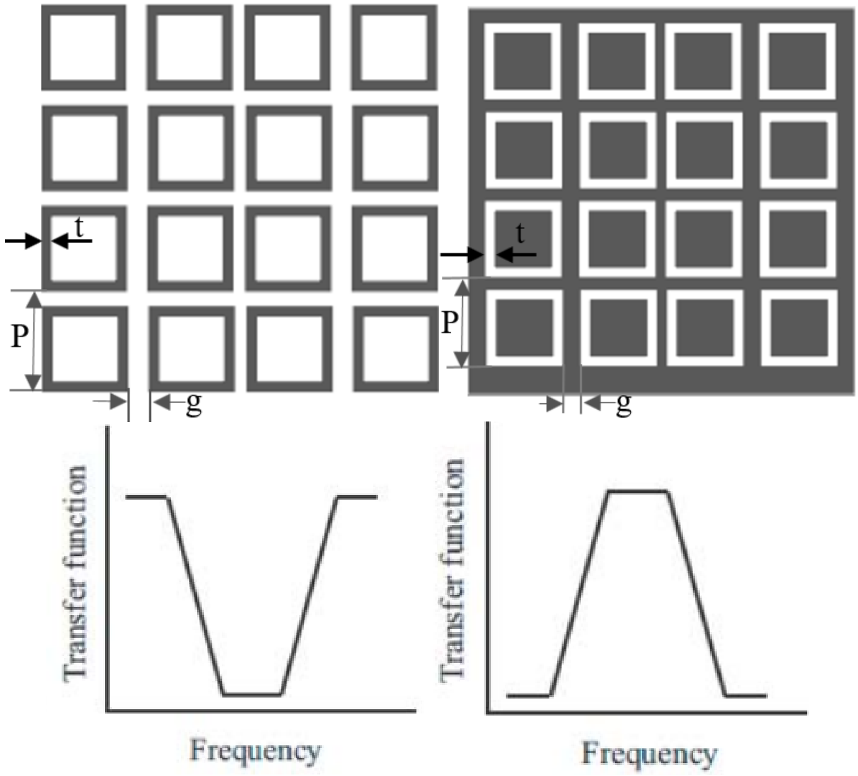

(a) Square loops array bandstop filter (b) Square slot patch array Bandpass

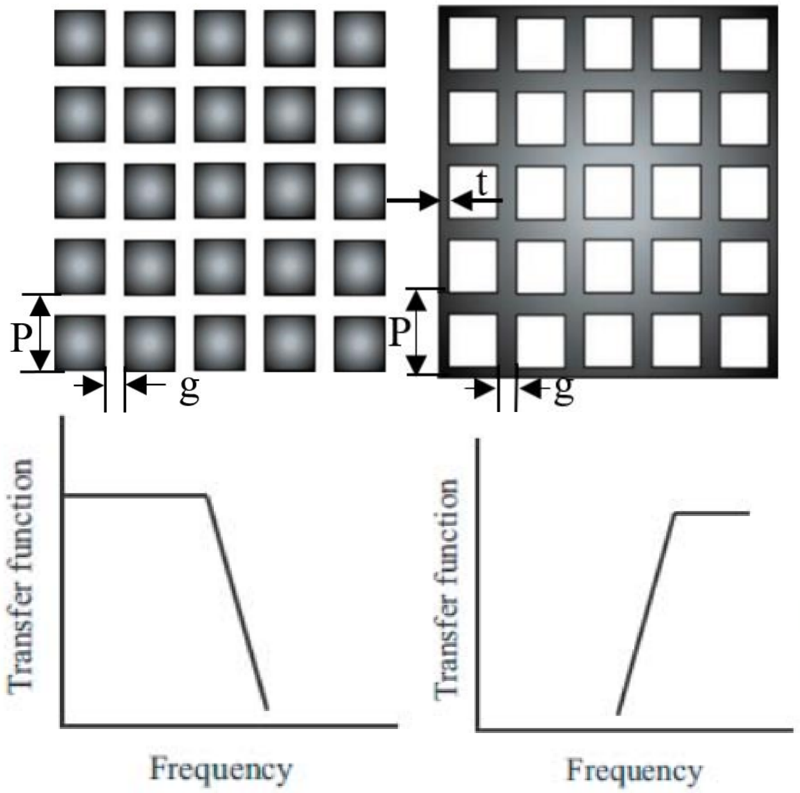

(c) patch array lowpass filter (d) Slot patch array highpass filter

Figure 2.17 Types of FSS filter and their responses, (a) band stop loop array (b) band pass slot loop array (c) low pass solid patch array (d) high pass *slot* array [137] [139]

2.5.1 3D FSS for Electromagnetic Devices

Due to their transmissive and reflective behaviour, FSS have been employed in various application. These includes radar absorption material [135] [140] [141], remote sensing [142], RF shielding [143], gyro multiplier [144], offset reflector [145], beam steering [146], beam switching [147] [148], Terahertz sensor [149]. Conventional planar FSS are designed for uniform illumination by a plane wave. However, depending on the requirements of an application as well as the need of modern RF systems to use structurally integrated components for electromagnetic and structural robustness, or to meet structural constraint or aerodynamism, the propagation element may take a predetermined shape. The agility that comes with 3D printing enables fabrication of such predetermined FSS shapes regardless of their complexity. Figure 2.18 shows a 3D printed conformally bent FSS with an incorporated support structure. The structure is made of PLA plastic that is printed using FFF to create the conformal structure. The structure has then been metalized using copper electroplating to make it conductive.

Figure 2.18 A self-supporting 3D printed conformal FSS with the settings after metallization of the optimized print [150].

The flexibility afforded by 3D printing also enables size miniaturization which may be ideal in some FSS applications. One way in which size miniaturization is achieved in FSS designs is by the introduction of convolution in the FSS designs. Convolution allows the electrical dimensions of an FSS application to be reduced without affecting its angular stability as demonstrated in [151] where convoluted square loop FSS structure are shown to have better stability compared to simple square loops. Further, [152] has demonstrated convoluting approach for unit element unit size reduction helps tighten curved structures and isolate the grating lobes effect from the fundamental frequency resonance. The minimization of FSS cell size through convolution enables the realization of convoluted structures such as shown in Figure 2.19. These structures can be incorporated into the building process to establish the electromagnetic architecture of a building as suggested in [153]. They can find application in office screening for better wireless reception [154].

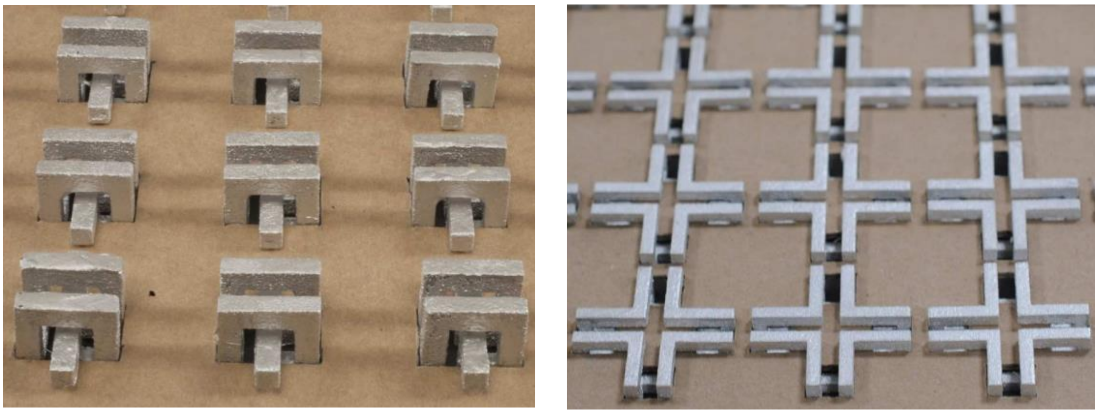

Figure 2.19 (a) 3D folded dipole element (b) 3D folded loop FSS [2]

2.5.2 FSS Frequency Reconfigurability in Electromagnetic Applications

An important feature of FSS structures is frequency reconfigurability. This can be achieved either by mechanical manipulation of passive flexible FSS or by using active FSS. This feature of FSS frequency reconfigurability feature can be harnessed for use for applications such as sensing described in Chapters 5 and Chapter 6. Mechanically reconfigurable passive FSS in the Subsection 2.5.2.1 while Active FSS are discussed in Subsection 2.5.2.2.

2.5.2.1 Mechanical reconfigurability

Mechanically reconfigurable FSS structures have been 3D printed in the past as demonstrated in [155]-[158]. As demonstrated in [158], the reconfigurability feature of origami-based shape shifting structures allows for their employment in reconfigurable FSS structures when the employed resonators have the necessary flexibility and changes their shape along with the underlying origami structure. Folding of an origami structure can cause reduction in the electrical length of the resonators on the FSS structures. Thus, without altering the dipoles' physical length, the folding permits another degree of continuous-state reconfigurability through an increase in effective capacitance to the bandstop Miura-FSS structure, resulting in a resonant frequency shift to higher frequencies. This is demonstrated in the multilayer Miura FSS structure on which dipole resonators are printed. The Miura-FSS which consists of Muira-Ori patterns with inkjet-printed dipole elements on each unit cell demonstrates a mechanically frequency reconfigurable FSS structure. Two configurations of two layers Miura-FSS are shown in Figure 2.20. Figure 2.20 (a) is a mirrored stack. It consists of two Miura-FSS layers linked along the valleys in a mirror fashion. Figure 2.20(b) is an inline-stacked configuration linked along the valley fold. The stacking of both is such that they are flat-foldable and allows in-plane foldability of the structures in accordance with Miura-Ori pattern geometry and angles of fold.

The inkjet-printed dipole run over the mountain fold of the structures in such a way that they are centred along the mountain fold length while simultaneously allowing high flexibility of the conductive trace. The conductive trace flexibility is key in the origami inspired tuneable FSS structures over a continuous array of states. Dipoles as a fundamental electromagnetic structure enable understanding of the Miura-FSS frequency reconfigurable behaviour with the folding.

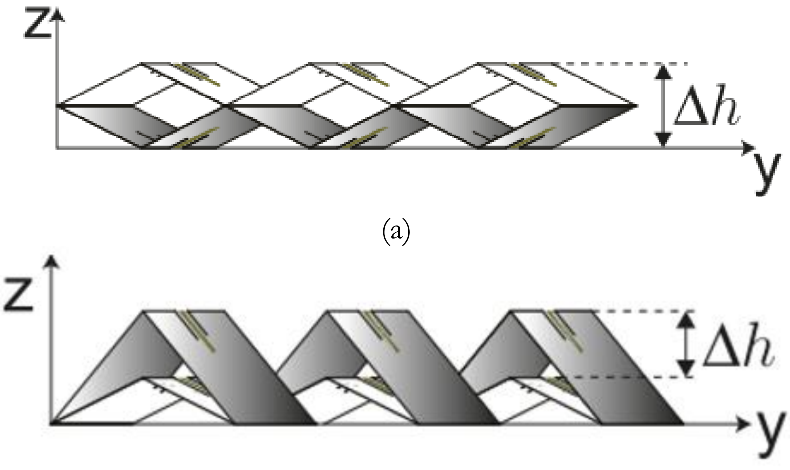

(a)

(b)

Figure 2.20 (a) Mirror-stacked Miura-FSS, and (b) inline-stacked Miura-FSS [158].

As the folding angle decreases, the resonating frequency of the configuration's increases. This is because of the reduction of the effective dipole elements length when they change from flat configuration to a V-shaped structure as the Miura-FSS structure is folded. The Miura-FSS structure resonance frequency is shown to be mechanically reconfigurable by varying its folding angles.

2.5.2.2 Active FSS reconfigurability

Active FSS is achieved by incorporating active components in the FSS array. This can make the surface reactance, reflectivity, transparency, or signal absorption, a variable characteristic allowing the structure user the ability to vary it as and when required. The active device can be located inter-array elements, intra-element, or between the layer and ground plane. The adjustment of the state of the active device and therefore the state of the FSS structure can be achieved by applying a DC or current bias, intensity of optical illumination, or localised temperature changes [159].

Reconfiguration by means of applied bias is demonstrated in [160], Figure 2.21, where a reconfigurable active AM printed FSS that can be employed for indoor spectrum control is presented. A biasing voltage is used to reconfigure the FSS resonance frequency. The FSS is inkjet printed on paper and uses a PIN diode to block a signal band in the OFF and transmit in the ON condition respectively. The concept of active FSS has been harnessed in the development of other applications such as Intelligent Omni-Surfaces for Full-Dimensional Wireless Communications [161] and Beamforming for Reconfigurable Intelligent Surface based

Multi-User Communications [162]. 3D printed 5G FSS security application harnessing the filtering property of FSS have also been developed in [163] [164].

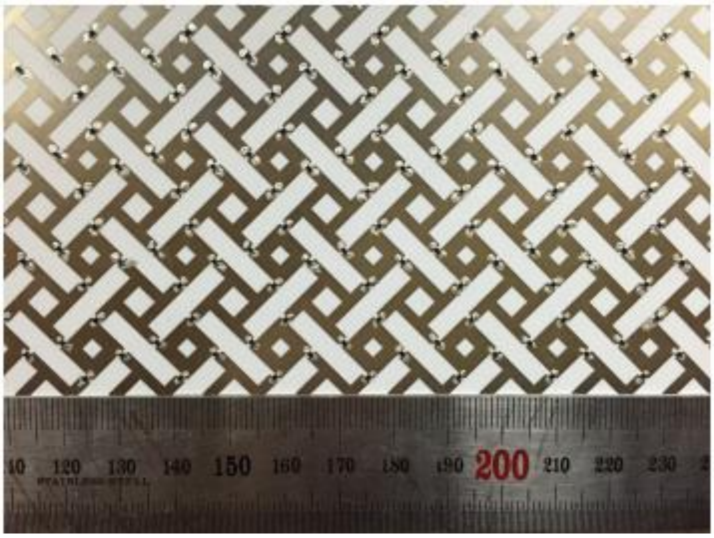

Figure 2.21 Inkjet printed reconfigurable FSS [160]

2.5.2 FSS based sensors

The reconfigurability of FSS by alteration of one of its parameters enables its use in applications such as sensing. FSS based sensor has been developed which exploits the dependence of FSS structure resonance frequency on its length as per microwave theory. Thus $f_{resonance} \approx 1/\ell$ or the equivalent lumped $f_{resonance} \approx 1/2\pi\sqrt{LC}$ of the FSS elements [165]. When a signal impinges on the FSS, the signal is re-radiated response is either reflective or t transmissive at a particular resonance frequency. This signal response is dependent on the shape and dimensions of the FSS elements and properties of the substrate material on which the FSS sits [166]. The dependence of reflective and/or transmissive signal response properties can be employed as a measurement parameter whereby a change in any of the FSS states causes a change in the reflective/transmissive responses [167]. This implies that FSS structures can be used as sensor devices whose signature responses (reflective or transmissive) are used as measurement parameters. Changes to these parameters can thus be monitored to determine changes in a measurement stimulus. FSS based sensors have been developed for measurement stimuli such as concurrent temperature and strain [166], strain [167] [168] [169], and structure health monitoring [170]. Further discussion on the employment of the FSS structures as sensing applications are discussed in Chapters 5 and Chapter 6 where liquid and displacement sensors respectively are presented.

2.5.3 Square loop FSS structures

Square loops FSS element are employed in the applications developed in Chapters 5 and Chapter 6. A brief introduction of the derivation of the equivalent lumped circuit elements circuit for the squire loops FSS is presented in this section. Figure 2.22(a) is an illustration of a square FSS while Figure 2.22(b) is the lumped element circuit equivalent.

An array of square loops in their patch form acts as a bandstop filter whose frequency response is dependent on the FSS structure dimensions. They resonate when the circumference is approximately one wavelength and thus each side of the loop is approximately a quarter of a wavelength $(\lambda/4)$ [171]. Transmission through a periodic array of conducting strips depends on the frequency as well as the orientation of the incident electric field relative to the strips [134]. Transmission of a square loop FSS structure can be described in terms of the equivalent impedance of a section of a transmission line representing propagation in free space [128].

For the transmission of a plane wave normally incident upon a grid of thin, parallel conducting metal strips of period *P*, when the *P* is far greater than the wavelength λ of pane wave, the equivalent impedance is a shunt inductance or a capacitance depending on whether the electric component of the incident wave is parallel to or perpendicular to the edges of the strips. Thus, the analogy with a transmission line of the characteristic impedance of free space can be employed to model it. The strip has intrinsic capacitance C_i and intrinsic inductance L_i that creates capacitive and inductive reactance respectively.

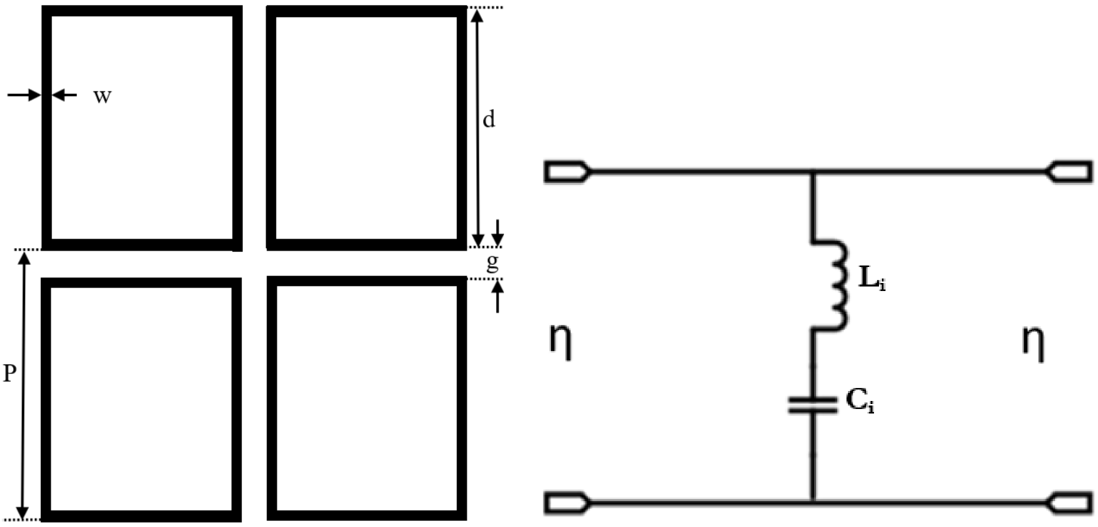

Figure 2.22 (a) Square loop FSS design (b) Lumped elements equivalent circuit

The model can be represented as a single circuit L_iC_i shunted across the transmission line of impedance η, the characteristic impedance of free space. The values of intrinsic L_i and C_i can be derived as follows. The strip's reactance is inductive when the incident electric field is parallel to the strip and thus highly reflective and with low transmission at low frequencies. The low transmission is a result of decreasing inductance as the periodicity *P* decreases or the width w of the strip increases. The value of the reactance depends on *P*, *w*, the angle of incidence (*θ*) as well as whether the incidence is TE or TM. The approximate value of inductance [172] is

$$L_i = \frac{\eta P cos\theta}{2\pi c}\left\{In\ cosec\left(\frac{\pi w}{2P}\right)\right\} \tag{2.1}$$

Where *c* is the speed of electromagnetic wave in space and *θ* is the angle of incidence of the wave.

Similarly, when the electric field component of the electromagnetic plain wave is perpendicular to the strip conductor, the capacitance of the array is approximated as

$$C_i = \frac{2P cos\theta}{\pi c \eta}\left\{In\ cosec\left(\frac{\pi g}{2P}\right)\right\} \tag{2.2}$$

Where *g* is the gap between two adjacent loops. A more detailed derivation of the lumped circuit equivalent of an FSS of liquid sensor is given in Chapter 5, Section 5.2.2.

2.5.4 CST Microwave Studio Suite Modeler

All the designs and simulations proposed in this thesis were done using CST MWS^{TM} electromagnetic (EM) modeler. It is a 3D EM analysis modeler for the design, analysis, as well as optimization of EM components and systems that combine all the EM field solvers from the EM spectrum [173]. It is based on the finite integration technique (FIT) that discretizes Maxwell's equations before they are executed by the modeler. This technique describes Maxwell's equations on a grid space which can be represented in both the time domain and frequency domain [174]. The advantage of the CST MWS time domain solver is that its resource requirement scales linearly with the mesh nodes amount. This means that it can handle large radiating structures including arrays comprising radiating elements in their hundreds. Extraction of high-resolution data of a broadband antenna is made possible by the time domain solver's ability in a single simulation run, to specify and compute a huge number of far-field monitors [174]. This is a significant advantage as it avoids the simulation of a large number of discrete frequencies as is in the case in non-Time Domain methods, to extract broadband data. The frequency domain solver is also available on the modeler. It is based on Hexa-and tetrahedral meshing and focuses on problems in narrowband antenna, electrically small devices, and or phased array unit cells.

In time domain methods, the hexahedral mesh is used. In this mesh, the computational volume i.e., simulation space containing the model is discretized. This discretization takes the form of variable rectangular cuboids, referred to as a mesh cells [175]. The mesh cells in the discretized form represent a volume in space in which computation of electric and magnetic fields are done. Deep discretization means more accuracy. However, this impacts the simulation time.

An FSS design starts with the definition of a unit cell. The periodic structure is constructed using a Floquet window after which the simulation is run in the frequency domain. CST modeler applies two waves, a horizontally polarised wave (1) and a corresponding vertically polarised wave (2). The scattering (S) parameters of the simulated model are represented by its amplitude and phase output as files with different filenames such as Z(max) (1) Z(min)(1) and Z(max)Z(max) (1). These represent a simulated structure with unit cell boundary conditions, in the frequency domain and in the z-axis (direction of propagation) with Z(max) and Z(min) ports. These represent port-1 and port-2. S21 is represented by Z(max) (1) Z(min)(1) with same modes and S11 by Z(max)Z(max) (1). The numeral (1) represents wave (1) and a numeral (2) in the file name represents wave (2)

CST responses filenames can be generally classified as follows:

a) SZmax(1), Zmax(1) represents the vertically polarised wave (wave(1)) S11
b) SZmax(2), Zmax(1) represents the horizontally polarised wave (wave(2)) S11
c) SZmin(1), Zmax(1) represents the vertically polarised wave (wave(1)) S21
d) SZmin(2), Zmax(1) represents the cross polarisation between wave(1 and wave(2) S21
e) SZmax(1), Zmax(2) represents the Cross Polarisation between wave(1) and wave(2) S11
f) SZmax(2), Zmax(2) represents the horizontally polarised wave (wave(2)) S11
g) SZmin(1), Zmax(2) represents the cross polarisation between wave(1 and wave(2) S21
h) SZmin(2), Zmax(2) represents the horizontally polarised wave (wave(2))S21

2.6 Summary

In this chapter, a review of additive manufacturing methodologies and their applications in the manufacture and development of RF and microwave antenna applications has been presented. The operation, application, and development of FSS using AM techniques has also been discussed. The filtering behaviour of the FSS depending on the geometry has been discussed as well as the equivalent circuit model of an array of square loops which has been used in development of some of the applications presented in this thesis. A brief discussion on the modeler used in the design, simulation and assessment of the applications proposed in this thesis is also given.

References

[1] D. Snelling, Q. Li, N. Meisel, C. B. Williams, R. C. Batra and A. P. Druschitz, "Lightweight Metal Cellular Structures Fabricated via 3D Printing of Sand Cast Molds," *Advanced Engineering Materials,* vol. 17, no. 7, pp. 923-932, 2015.

[2] J. Fleischer, M. Deuchert, C. K. C. Ruhs, G. Halvadjiysky and C. Schmidt, "Design and manufacturing of micro milling tools," *Microsystem Technologies,* vol. 14, p. 1771–1775, 2008.

[3] T. Mohanraj, S. Shankar, R. Rajasekar, N. R. Sakthivel and A. Pramanik, "Tool condition monitoring techniques in milling process — a review," *J Mater Res Technol ,* vol. 9, no. 1, pp. 1032-1042, 2020.

[4] A. E. Diniz and R. Micaroni, "Cutting conditions for finish turning process aiming: the use of dry cutting," *International Journal of Machine Tools & Manufacture ,* vol. 42, p. 899–904, 2002.

[5] L. Zhu, Z. Jiang, J. Shi and C. Jin, "An overview of turn-milling technology," *Int J Adv Manuf Technol,* vol. 81, p. 493–505, 2015.

[6] R. Lynn, M. Dinar, N. Huang, J. Collins, J. Yu, C. Greer, T. Tucker and T. Kurfess, "Direct Digital Subtractive Manufacturing of a Functional Assembly Using Voxel-Based Models," *Journal of Manufacturing Science and Engineering,* vol. 170, pp. 1-14, 2018.

[7] S. H. Huang, P. Liu, A. Mokasdar and L. Hou, "Additive manufacturing and its societal impact: a literature review," *Int J Adv Manuf Technol ,* vol. 67, p. 1191–1203, 2013.

[8] E. Bassoli, A. Gatto, L. Iuliano and M. G. Violante, "3D printing technique applied to rapid casting," *Rapid Prototyping Journal,* vol. 13, no. 3, pp. 148-155, 2007.

[9] M. I. M. Ghazali, K. Y. Park, J. A. Byford, J. Papapolymerou and P. Chahal, "3D printed metalized-polymer UWB high-gain Vivaldi antennas," in *2016 IEEE MTT-S International Microwave Symposium (IMS)*, San Francisco, CA, USA, 2016.

[10] "IEEE standard definitions of terms for antennas," *IEEE Transactions on Antennas and Propagation,* vol. 17, no. 3, pp. 262 - 269, 1969.

[11] C. A. Balanis, Antenna Theory Analysis and Design, Hoboken, New Jersey: John Wiley & Sons, Inc., 3rd Edition, 2005.

[12] Z. N. Chen, M. J. Ammann, X. Qing, X. H. Wu, T. S. See and A. Cai, “Planar antennas,” *IEEE Microwave Magazine,* vol. 7, no. 6, pp. 63 - 73, 2006.

[13] Z. N. Chen and M. Y. W. Chia, Broadband Planar Antennas Design and Applications, Chichester, West Sussex, England: John Wiley & Sons, Ltd, 2006.

[14] M. B. Bicer and E. A. Aydin, “A novel 3D printed curved monopole microstrip antenna design for biomedical applications,” *Physical and Engineering Sciences in Medicine ,* vol. 44, p. 1175–1186, 2021.

[15] E. Sachs, M. Cima, P. Williams, D. Brancazio and J. Cornie, “Three Dimensional Printing: Rapid Tooling and'Prototypes Directly from a CAD Model,” *Transactions of the ASME,* vol. 114, pp. 481-488, 1992.

[16] A. Bandyopadhyay, S. Vahabzadeh, A. Shivaram and S. Bose, “Three-dimensional printing of biomaterials and soft materials,” *Materials Research Societ,* vol. 40, pp. 1162-1168, 2015.

[17] M. R. Skorski, J. M. Esenther, Z. Ahmed, A. E. Miller and M. R. Hartings, “The chemical, mechanical, and physical properties of 3D printed materials composed of TiO2-ABS nanocomposites,” *Science and Technology of Advanced Materials ,* vol. 17, no. 1, p. 89–97, 2016.

[18] O. Ivanova, C. Williams and T. Campbell, “Additive manufacturing (AM) and nanotechnology: promises and challenges,” *Rapid Prototyping Journal,* vol. 19, pp. 353–364, 2013.

[19] S. C. Ligon, R. Liska, J. Stampfl, M. Gurr and R. Mulhaupt, “Polymers for 3D Printing and Customized Additive Manufacturing,” *Chemical Reviews,* vol. 117, pp. 10212−10290, 2017.

[20] I. Gibson, D. Rosen and B. Stucker, Additive Manufacturing Technologies: 3D Printing, Rapid Prototyping, and Direct Digital Manufacturing, New York: Springer, 2015.

[21] P. Sarobol, A. Cook, P. G. Clem, D. Keicher, D. Hirschfeld, A. C. Hall and N. S. Bell, “Additive Manufacturing of Hybrid Circuits,” *Annual Review of Materials Research,* vol. 46, pp. 41-62, 2016.

[22] H. W. Tan, T. Tran and C. K. Chua, "A review of printed passive electronic components through fully additive manufacturing methods," *Virtual and Physical Prototyping,* vol. 11, no. 4, pp. 271-288, 2016 .

[23] A. H. E. Jr., J. R. C. Dizon, Q. Chen and R. C. Advincula, "3D-printing and advanced manufacturing for electronics," *Progress in Additive Manufacturing,* vol. 4, pp. 245–267, 2019.

[24] B.-H. Lu, H.-B. Lan and H.-Z. Liu, "Additive manufacturing frontier: 3D printing electronics," *Opto-Electronic Advances,* vol. 1, no. 1, pp. 1-10, 2018.

[25] E. Macdonald, R. Salas, D. Espalin, M. Perez, E. Aguilera, D. Muse and R. B. Wicker, "3D Printing for the Rapid Prototyping of Structural Electronics," *IEEE Access,* vol. 2, pp. 234 - 242, 2014.

[26] M. Liang and H. Xin, "Three-Dimensionally Printed/Additive Manufactured Antennas," in *Handbook of Antenna Technologies*, Singapore, Springer Nature, 2016, pp. 661-697.

[27] N. Arnal, T. Ketterl, Y. Vega, J. Stratton, C. Perkowski, P. Deffenbaugh, K. Church and T. Weller, "3D multi-layer additive manufacturing of a 2.45 GHz RF front end," in *2015 IEEE MTT-S International Microwave Symposium*, Phoenix, AZ, USA, 2015.

[28] N. GUO and M. C. LEU, "Additive manufacturing: technology, applications and research needs," *Front. Mech. Eng. ,* vol. 8, no. 3, p. 215–243, 2013, 8(3): 215–243.

[29] R. Sorrentino and O. A. Peverini, "Additive Manufacturing: A Key Enabling Technology for Next-Generation Microwave and Millimeter-Wave Systems," *Proceedings of the IEEE,* vol. 104, no. 7, pp. 1362 - 1366, 2016.

[30] L. Carin, N. Geng, M. McClure, J. Sichina and L. Nguyen, "Ultra-wide-band synthetic-aperture radar for mine-field detection," *IEEE Antennas and Propagation Magazine,* vol. 41, no. 1, pp. 18 - 33, 1999.

[31] D. Helena, A. Ramos, T. Varum and J. N. Matos, "Antenna Design Using Modern Additive Manufacturing Technology: A Review," *IEEE Access,* vol. 8, pp. 177064 - 177083, 2020.

[32] M. F. Farooqui and A. Kishk, "3D-Printed Tunable Circularly Polarized Microstrip Patch Antenna," *IEEE Antennas and Wireless Propagation Letters,* vol. 18, no. 7, pp. 1429 - 1432, 2019.

[33] M. Liang, C. Shemelya, E. MacDonald, R. Wicker and H. Xin, "3-D Printed Microwave Patch Antenna via Fused Deposition Method and Ultrasonic Wire Mesh Embedding Technique," *IEEE Antennas and Wireless Propagation Letters ,* vol. 14, pp. 1346 - 1349, 2015.

[34] J. J. Adams, E. B. Duoss, T. F. Malkowski, M. J. Motala, B. Y. Ahn, R. G. Nuzzo, J. T. Bernhard and J. A. Lewis, "Conformal Printing of Electrically Small Antennas on Three-Dimensional Surfaces," *Advanced Material,* vol. 23, p. 1335–1340, 2011.

[35] Y. Huang, X. Gong, S. Hajela and W. Chappell, "Layer-by-layer stereolithography of three-dimensional antennas," in *IEEE Antennas and Propagation Society International Symposium*, Washington, DC, USA, 2005 .

[36] J. M. Monkevich and G. P. L. Sage, "Design and Fabrication of a Custom-Dielectric Fresnel Multi-Zone Plate Lens Antenna Using Additive Manufacturing Techniques," *IEEE Access,* vol. 7, pp. 61452 - 61460, 2019.

[37] P. Nayeri, M. Liang, R. A. Sabory-Garcı´a, M. Tuo, F. Yang, M. Gehm, H. Xin and A. Z. Elsherbeni, "3D Printed Dielectric Reflectarrays: Low-Cost High-Gain Antennas at Sub-Millimeter Waves," *IEEE Transactions on Antennas and Propagation ,* vol. 62, no. 4, pp. 2000 - 2008, 2014.

[38] M. Liang, W.-R. Ng, K. Chang, K. Gbele, M. E. Gehm and H. Xin, "A 3-D Luneburg Lens Antenna Fabricated by Polymer Jetting Rapid Prototyping," *IEEE Transactions on Antennas and Propagation,* vol. 62, no. 4, pp. 1799 - 1807, 2014.

[39] C. Garcia, R. Rumpf, H. Tsang and J. Barton, "Effects of extreme surface roughness on 3D printed horn antenna," *Electronics Letters,* vol. 49, no. 12, pp. 1-2, 2013.

[40] P. Nenzi, F. Tripaldi, V. Varlamava, F. Palma and M. Balucani, "On-chip THz 3D antennas," in *IEEE 62nd Electronic Components and Technology Conference*, San Diego, CA, USA, 2012.

[41] Z. Wu, M. Liang, W.-R. Ng, M. Gehm and H. Xin, "Terahertz Horn Antenna Based on Hollow-Core Electromagnetic Crystal (EMXT) Structure," *IEEE Transactions on Antennas and Propagation ,* vol. 60 , no. 12, pp. 5557 - 5563, 2012.

[42] A. Pellegrini, A. Brizzi, L. Zhang, K. Ali, Y. Hao, X. Wu, C. C. Constantinou, Y. Nechayev, P. S. Hall, N. Chahat, M. Zhadobov and R. Sauleau, “Antennas and Propagation for Body-Centric Wireless Communications at Millimeter-Wave Frequencies: A Review [Wireless Corner],” *IEEE Antennas and Propagation Magazine,* vol. 55, no. 4, pp. 262 - 287, 2013.

[43] K. N. Paracha, S. K. A. Rahim, H. T. Chattha, S. S. Aljaafreh, S. u. Rehman and Y. C. Lo, “Low-Cost Printed Flexible Antenna by Using an Office Printer for Conformal Applications,” *Hindawi International Journal of Antennas and Propagation,* pp. 1-8, 2018.

[44] N. H. M. Rais, P. J. Soh, F. Malek, S. Ahmad, N. Hashim and P. Hall, “A review of wearable antenna,” in *2009 Loughborough Antennas & Propagation Conference*, Loughborough, UK, 2009 .

[45] W. G. Whittow, A. Chauraya, J. C. Vardaxoglou, Y. Li, R. Torah, K. Yang, S. Beeby and J. Tudor, “Inkjet-Printed Microstrip Patch Antennas Realized on Textile for Wearable Applications,” *IEEE Antennas and Wireless Propagation Letters,* vol. 13, pp. 71 - 74, 2014.

[46] A. Chauraya, W. G. Whittow, J. C. Vardaxoglou, Y. Li, R. Torah, K. Yang, S. Beeby and J. Tudor, “Inkjet printed dipole antennas on textiles for wearablecommunications,” *IET Microw. Antennas Propag.,* vol. 7, no. 9, p. 760–767, 2013.

[47] A. Paraskevopoulos, D. d. S. Fonseca, R. D. Seager, W. G. Whittow, J. C. Vardaxoglou and A. A. Alexandridis, “Higher-mode textile patch antenna with embroidered vias for on-body communication,” *IET Microwaves, Antennas & Propagation,* vol. 10, no. 7, p. 802 – 807, 2016.

[48] P. Njogu, B. Sanz-Izquierdo, A. Elibiary, S. Y. Jun, Z. Chen and D. Bird, “3D Printed Fingernail Antennas for 5G Applications,” *IEEE Access,* vol. 8, pp. 228711 - 228719, 2020.

[49] P. Njogu and B. Sanz-Izquierdo, “Removable Finger Nail Antenna,” in *14th European Conference on Antennas and Propagation (EuCAP)*, Copenhagen, Denmark, 2020.

[50] P. Njogu, S. Jun, B. Sanz-Izquierdo, Z. Chen and S. Gao, “3D Printed Millimeter wave Antenna Integrated into a Ring for 5G Applications,” in *Mediterranean Microwave Symposium* , Pizzo Calabro, Italy, 2022.

[51] S. Y. Jun, A. Elibiary, B. Sanz-Izquierdo, L. Winchester, D. Bird and A. McCleland, "3-D Printing of Conformal Antennas for Diversity Wrist Worn Applications," *IEEE Transactions on Components, Packaging and Manufacturing Technology ,* vol. 8, no. 12, pp. 2227 - 2235, 2018.

[52] M. Rizwan, M. W. A. Khan, L. Sydänheimo, J. Virkki and L. Ukkonen, "Flexible and Stretchable Brush-Painted Wearable Antenna on a Three-Dimensional (3-D) Printed Substrate," *IEEE Antennas and Wireless Propagation Letters ,* vol. 16, pp. 3108 - 3112, 2017.

[53] N. A. Hamza, A. S. Majeed and S. M. Jawd, "Review on Types and Methods of Electroplating on Metals Power Electronics and Devices," *Journal of Power Electronics and Devices,* vol. 7, no. 1, pp. 44-51, 2021.

[54] G.-L. Huang, Z.-P. Zhong and T. Yuan, "3-D metal printing in microwave components and antennas applications," in *2018 International Workshop on Antenna Technology (iWAT)*, Nanjing, China, 2018.

[55] G. Jacob, A. Donmez, J. Slotwinski and S. Moylan, "Measurement of powder bed density in powder bed fusion additive manufacturing processes," *Meas. Sci. Technol. ,* vol. 27 , pp. 1-13, 2016.

[56] B. Zhang, Z. Zhan, Y. Cao, H. Gulan, P. Linn´er, J. Sun, T. Zwick and H. Zirath, "Metallic 3-D Printed Antennas for Millimeter- and Submillimeter Wave Applications," *IEEE Transactions On Terahertz Science and Technology,* vol. 6 , no. 4, pp. 592-600, 2016.

[57] S. Y. Jun, B. Sanz-Izquierdo, E. A. Parker, D. Bird and A. McClelland, "Manufacturing Considerations in the 3-D Printing of Fractal Antennas," *IEEE Transactions on Components, Packaging and Manufacturing Technology,* vol. 7, no. 11, pp. 1891 - 1898, 2017.

[58] I. Gibson, D. Rosen and B. Stucker, Additive Manufacturing Technologies: 3D Printing, Rapid Prototyping, and Direct Digital Manufacturing, New York: Springer New York, 2015.

[59] Y. L. Tee, C. Peng, P. Pille, M. Leary and P. Tran, "PolyJet 3D Printing of Composite Materials: Experimental and Modelling Approach," *The Minerals, Metals & Materials Society,* vol. 72, p. 1105–1117, 2020.

[60] A. Bandyopadhyay and B. Heer, "Additive manufacturing of multi-material structures," *Materials Science & Engineering R,* vol. 129, pp. 1-16, 2018.

[61] "Polyjet 3D Printing: Technology Overview," Xometry, 02 07 2022. [Online]. Available: https://xometry.eu/en/polyjet-3d-printing-technology-overview/. [Accessed 22 07 2022].

[62] S. Lucyszyn, X. Shang, W. J. Otter, C. W. Myant, R. Cheng and N. M. Ridler, "Polymer-based 3D Printed Millimeter-wave Components for Spacecraft Payloads," in *2018 IEEE MTT-S International Microwave Workshop Series on Advanced Materials and Processes for RF and THz Applications (IMWS-AMP)*, Ann Arbor, MI, USA, 2018.

[63] M. I. M. Ghazali, K. Y. Park, J. A. Byford, J. Papapolymerou and P. Chahal, "3D printed metalized-polymer UWB high-gain Vivaldi antennas," in *2016 IEEE MTT-S International Microwave Symposium (IMS)*, San Francisco, CA, USA, 2016.

[64] R. Bernasconi, C. Credi, M. Tironi, M. Levi and L. Magagnin, "Electroless Metallization of Stereolithographic Photocurable Resins for 3D Printing of Functional Microdevices," *Journal of The Electrochemical Society,* vol. 164, no. 5, pp. 3059-3066, 2017.

[65] P. Cheng, C. Chen, T. Ichibayashi, T. M. Chang, M. Sone and S. Nishimura, "Metallization of 3D-printed polymer structures via supercritical carbon dioxide-assisted electroless plating," *Materials Research Society Communications,* vol. 11, pp. 278–282 , 2021.

[66] X. Su, X. Li, C. Y. A. Ong, T. S. Herng, Y. Wang, E. Peng and J. Ding, "Metallization of 3D Printed Polymers and Their Application as a Fully Functional Water-Splitting System," *Advanced Science ,* vol. 6, pp. 1-8, 2019.

[67] V. Kyovtorov, I. Georgiev, S. Margenov, D. Stoychev, F. Oliveri and D. Tarchi, "New antenna design approach – 3D polymer printing and metallization experimental test at 14–18 GHz," *International Journal of Electronics and Communications (AEÜ),* vol. 73, pp. 119–128, 2017.

[68] A. Baptista, F. Silva, J. Porteiro, J. M. and G. Pinto, "Sputtering Physical Vapour Deposition (PVD) Coatings:A Critical Review on Process Improvement and Market Trend Demands," *MPDI: Coatings,* vol. 8, pp. 1-22, 2018.

[69] A. Romani, A. Mantelli, P. Tralli, S. Turri, M. Levi and R. Suriano, "Metallization of Thermoplastic Polymers and Composites 3D Printed by Fused Filament Fabrication," *MDPI: Technologies,* vol. 9, no. 3, pp. 1-14, 2021.

[70] E. Decrossas, T. Reck, C. Lee, C. Jung-Kubiak, I. Mehdi and G. Chattopadhyay, "Evaluation of 3D printing technology for corrugated horn antenna manufacturing," in *IEEE International Symposium on Electromagnetic Compatibility (EMC)*, Ottawa, ON, Canada, 2016 .

[71] C. Gu, S. Gao, V. Fusco, G. Gibbons, B. Sanz-Izquierdo, A. Standaert, P. Reynaert, W. Bösch, M. Gadringer, R. Xu and X. Yang, "A D-Band 3D-Printed Antenna," *IEEE Transactions on Terahertz Science and Technology,* vol. 10, no. 5, pp. 433 - 442, 2020.

[72] K. K. B. Hon, L. Li and I. M. Hutchings, "Direct writing technology—Advances and developments," *CIRP Annals,* vol. 57, no. 2, pp. 601-620, 2008.

[73] O. Gülcan, K. Günaydın and A. Tamer, "The State of the Art of Material Jetting—A Critical Review," *MPDI: Polymers,* vol. 13, pp. 1-19, 2021.

[74] F. Zhang, E. Saleh, J. Vaithilingam, Y. Li, C. J. Tuck, R. J. M. Hague, R. D. Wildman and Y. He, "Reactive material jetting of polyimide insulators for complex circuit board design," *Additive Manufacturing,* vol. 25, pp. 477-484, 2019.

[75] B. K. Tehrani, B. S. Cook and M. M. Tentzeris, "Inkjet Printing of Multilayer Millimeter-Wave Yagi-Uda Antennas on Flexible Substrates," *IEEE Antennas and Wireless Propagation Letters,* vol. 15, pp. 143 - 146, 2015.

[76] M. Singh, H. M. Haverinen, P. Dhagat and G. E. Jabbour, "Inkjet Printing—Process and Its Applications," *Advanced Materials,* vol. 22, no. 6, pp. 673-685, 2010.

[77] E. B. Secor, "Principles of aerosol jet printing," *Flexible and Printed Electronics,* vol. 3, pp. 1-12, 2018.

[78] M. Vaezi, P. Drescher and H. Seitz, "Beamless Metal Additive Manufacturing," *MDPI: Materials,* vol. 13, pp. 1-36, y 2020.

[79] A. Shastri, B. Sanz-Izquierdo, E. A. Parker, S. Gao, P. Reynaert, Z. Chen and L. Winchester, "3D Printing of Millimetre Wave and Low-Terahertz Frequency Selective Surfaces Using Aerosol Jet Technology," *IEEE Access ,* vol. 8, pp. 177341 - 177350, 2020.

[80] "Optomec Aerosol Jet printing technology effectively produces 3D printed electronics.," Optomec, 07 03 2022. [Online]. Available: https://optomec.com/printed-electronics/aerosol-jet-technology/. [Accessed 07 03 2022].

[81] B. S. Cook and A. Shamim, “Inkjet Printing of Novel Wideband and High Gain Antennas on Low-Cost Paper Substrate,” *IEEE Transactions on Antennas And Propagation,* vol. 60, no. 9, pp. 4148-4156, 2012.

[82] M. Moras, C. Martínez-Domingo, R. Escudé, C. Herrojo, F. Paredes, L. Terés, F. Martín and E. Ramon, “Programmable Organic Chipless RFID Tags Inkjet Printed on Paper Substrates,” *Applied Sciences ,* vol. 11, no. 17, pp. 1-12, 2021.

[83] E. Dimitriou and N. Michailidis, “Printable conductive inks used for the fabrication of electronics: an overview,” *Nanotechnology ,* vol. 32 , pp. 1-24, 2021.

[84] K. Rajan, I. Roppolo, A. Chiappone, S. Bocchini, D. Perrone and A. Chiolerio, “Silver nanoparticle ink technology: state of the art,” *Nanotechnology, Science and Applications,* vol. 9, pp. 1–13, 2016 .

[85] B.-H. Lee, D.-I. Lee, H. Bae, H. Seong, S.-B. Jeon, M.-L. Seol, J.-W. Han, M. Meyyappan, S.-G. Im and Y.-K. Choi, “Foldable and Disposable Memory on Paper,” *scientific reports,* vol. 6, pp. 1-8, 2016.

[86] I. J. Fernandes, A. F.Aroche, A. Schuck, P. Lamberty, C. R. Peter, W. Hasenkamp and T. L. C. Rocha, “Silver nanoparticle conductive inks: synthesis, characterization, and fabrication of inkjet-printed fexible electrodes,” *Scientific Reports,* vol. 10, pp. 1-10, 2020.

[87] J. Li, F. Rossignol and J. Macdonald, “Inkjet printing for biosensor fabrication: combining chemistry and technology for advanced manufacturing,” *Lab Chip ,* vol. 15, pp. 2538–2558, 2015 .

[88] custompartnet,"Inkjet printing” custompartnet, 14 02 2022. [Online]. Available: https://www.custompartnet.com/wu/ink-jet-printing. [Accessed 14 02 2022].

[89] T. Kawase, S. Moriya, C. J. Newsome and T. Shimoda, “Inkjet Printing of Polymeric Field-Effect Transistors and Its Applications,” *Japanese Journal of Applied Physics,* vol. 44, no. 6A, pp. 3649–3658, 2005.

[90] J. A. Lim, W. H. Lee, H. S. Lee, J. H. Lee, Y. D. Park and K. Cho, “Self-Organization of Ink-jet-Printed Triisopropylsilylethynyl Pentacene via Evaporation-Induced Flows in a Drying Droplet,” *Adv. Funct. Mater.,* vol. 18, pp. 229–234, 2008.

[91] E. Jabari, F. Ahmed, F. Liravi, E. B. Secor, L. Lin and E. Toyserkani, "2D printing of graphene: a review," *2D Mater. ,* vol. 6 , pp. 1-24, 2019.

[92] Dimatix, "Dimatix Materials Printer DMP-2800 Series User Manual", Santa Clara, CA: FUJIFILM Dimatix, Inc. , 2006 [online]. Available at: PM000040 Rev. 05, DMP-2800 Series (ilabsolutions.com)

[93] Y. Al-Naiemy, T. A. Elwi, H. R. Khaleel and H. Al-Rizzo, "A Systematic Approach for the Design, Fabrication, and Testing of Microstrip Antennas Using Inkjet Printing Technology," *International Scholarly Research Network ISRN Communications and Networking,* pp. 1-11, 2012.

[94] A. M. Mansour, N. Shehata, B. M. Hamza and M. R. M. Rizk, "Efficient Design of Flexible and Low Cost Paper-Based Inkjet-Printed Antenna," *International Journal of Antennas and Propagation,* vol. 2015, pp. 1-6, 2015.

[95] J. S. Kang, H. S. Kim, J. Ryu, H. T. Hahn, S. Jang and J. W. Joung, "Inkjet printed electronics using copper nanoparticle ink," *J Mater Sci: Mater Electron,* vol. 21, pp. 1213–1220, 2010.

[96] T. Leng, X. Huang, K. Chang, J. Chen, M. A. Abdalla and Z. Hu, "Graphene Nanoflakes Printed Flexible Meandered-Line Dipole Antenna on Paper Substrate for Low-Cost RFID and Sensing Applications," *IEEE Antennas and Wireless Propagation Letters,* vol. 15, pp. 1565 - 1568, 2016.

[97] L. Mo, Z. Guo, Z. Wang, L. Yang, Y. Fang, Z. Xin, X. Li, Y. Chen, M. Cao, Q. Zhang and L. Li, "Nano-Silver Ink of High Conductivity and Low Sintering Temperature for Paper Electronics," *Nanoscale Research Letters,* vol. 14, no. 197, pp. 1-11, 2019.

[98] K. Rajan, I. Roppolo, A. Chiappone., S. Bocchini, D. Perrone and A. Chiolerio, "Silver nanoparticle ink technology: state of the art," *Nanotechnology, Science and Applications,* vol. 9, pp. 1–13, 2016.

[99] E. Tekin, P. J. Smith and U. S. Schubert, "Inkjet printing as a deposition and patterning tool for polymers and inorganic particles," *Soft Matter,* vol. 4, pp. 703–713, 2008.

[100] S. Ananda, D. S. Kumar, R. J. Wu and M. Chavali, "Graphene nanoribbon based terahertz antenna on polyimide substrate," *Optik,* vol. 125, pp. 5546–5549, 2014.

[101] S. F. Jilani and A. Alomainy, "Planar millimeter-wave antenna on low-cost flexible PET substrate for 5G applications," in *2016 10th European Conference on Antennas and Propagation (EuCAP)*, Davos, Switzerland, 2016 .

[102] K. N. Paracha, S. K. A. Rahim, P. J. Soh and M. Khalily, "Wearable Antennas: A Review of Materials, Structures, and Innovative Features for Autonomous Communication and Sensing," *IEEE Access,* vol. 7, pp. 56694 - 56712, 2019.

[103] S. Kim, Y.-J. Ren, H. Lee, A. Rida, S. Nikolaou and M. M. Tentzeris, "Monopole Antenna With Inkjet-Printed EBG Array on Paper Substrate for Wearable Applications," *IEEE Antennas and Wireless Propagation Letters,* vol. 11, pp. 663 - 666, 2012.

[104] V. Sanchez-Romaguera, M. A. Ziai, D. Oyeka, S. Barbosa, J. S. R. Wheeler, J. C. Batchelor, E. A. Parker and S. G. Yeates, "Towards inkjet-printed low cost passive UHF RFID skin mounted tattoo paper tags based on silver nanoparticle inks," *Journal of Materials Chemistry C,* vol. 1, pp. 6395–6402, 2013.

[105] V. Sanchez-Romaguera, S. W¨unscher, B. M. Turki, R. Abbel, S. Barbosa, D. J. Tate, D. Oyeka, J. C. Batchelor, E. A. Parker, U. S. Schubert and S. G. Yeates, "Inkjet printed paper based frequency selective surfaces and skin mounted RFID tags: the interrelation between silver nanoparticle ink, paper substrate and low temperature sintering technique," *Journal of Materials Chemistry C,* vol. 3, pp. 2132–2140, 2015.

[106] D. Tobjörk and R. Österbacka, "Paper Electronics," *Adv. Mater.,* Vol. 23, pp. 1935–1961, 2011 .

[107] A. C. Siegel, S. T. Phillips, M. D. Dickey, N. Lu, Z. Suo and G. M. Whitesides, "Foldable Printed Circuit Boards on Paper Substrates," *Adv. Funct. Mater.,* vol. 20, pp. 28–35, 2010.

[108] S. Liu, X. S. Junpeng Li, E. Gao, Z. Xu, H. Tang, K. Tong, Q. Pei, J. Liang and Y. Chen, "Rollerball-Pen-Drawing Technology for Extremely Foldable Paper-Based Electronics," *Adv. Electron. Mater. ,* vol. 3, no. 7, pp. 1-12, 2017.

[109] A. Russo, B. Y. Ahn, J. J. Adams, E. B. Duoss, J. T. Bernhard and J. A. Lewis, "Pen-on-Paper Flexible Electronics," *Adv.Mater.,* vol. 23, no. 30, pp. 3426-3430, 2011.

[110] S. M. Khan, J. M. Nassar and M. M. Hussain, "Paper as a Substrate and an Active Material in Paper Electronics," *ACS Appl. Electron. Mater. ,* vol. 3, no. 1, pp. 30−52, 2021.

[111] Y. Zhang, L. Zhang, K. Cui, S. Ge, X. Cheng, M. Yan, J. Yu and H. Liu, “Flexible Electronics Based on Micro/Nanostructured Paper,” *Adv. Mater.,* vol. 30, no. 51, pp. 1-39, 2018.

[112] N. J. Wilkinson, M. A. A. Smith, R. W. Kay and R. A. Harris, “A review of aerosol jet printing—a non-traditional hybrid,” *The International Journal of Advanced Manufacturing Technology,* vol. 105, pp. 4599–4619, 2019.

[113] A. Mahajan, C. D. Frisbie and L. F. Francis, “Optimization of Aerosol Jet Printing for High-Resolution, High-Aspect Ratio Silver Lines,” *ACS Applied Materials & Interfaces,* vol. 5, no. 11, pp. 4856−4864, 2013.

[114] S. Binder, M. Glatthaar and E. Rädlein, “Analytical Investigation of Aerosol Jet Printing,” *Aerosol Science and Technology,* vol. 48, pp. 924–929, 2014.

[115] Optomec, “Aerosol Jet® Printed Electronics Overview,” Optomec, whitepaper [online] Available:https://www.optomec.com/wp-content/uploads/2014/04/AJ_Printed_Electronics_Overview_whitepaper.pdf

[116] C. Goth, S. Putzo and J. Franke, “Aerosol Jet printing on rapid prototyping materials for fine pitch electronic applications,” in *2011 IEEE 61st Electronic Components and Technology Conference (ECTC)*, Lake Buena Vista, FL, USA, 2011.

[117] C. Cooper and B. Hughes, “Aerosol Jet Printing of Electronics: An enabling technology for wearable devices,” in *Proceedings of the SMTA Pan Pacific Microelectronics Symposium*, HI, USA, 2020.

[118] A. Mette, P. L. Richter, M. H.¨rteis and S. W. Glunz, “Metal Aerosol Jet Printingfor Solar Cell Metallization,” *Progress in photovoltaics: Research and Applications,* vol. 15, pp. 621–627, 2007.

[119] C. Goth, S. Putzo and J. Franke, “Aerosol Jet printing on rapid prototyping materials for fine pitch electronic applications,” in *IEEE 61st Electronic Components and Technology Conference (ECTC)*, Lake Buena Vista, FL, USA, 2011 .

[120] J. A. Paulsen, M. Renn, K. Christenson and R. Plourde, “Printing conformal electronics on 3D structures with Aerosol Jet technology,” in *2012 Future of Instrumentation International Workshop (FIIW) Proceedings*, Gatlinburg, TN, USA, 2012.

[121] E. Jabari and E. Toyserkani, "Micro-scale aerosol-jet printing of graphene interconnects," *Carbon,* vol. 91, pp. 321-329, 2015.

[122] Y. He, C. Oakley, P. Chahal, J. Albrecht and J. Papapolymerou, "Aerosol Jet printed 24 GHz end-fire quasi-Yagi-Uda antenna on a 3D printed cavity substrate," in *2017 International Workshop on Antenna Technology: Small Antennas, Innovative Structures, and Applications (iWAT)*, Athens, Greece, 2017.

[123] "Aerosol Jet Technology," Optomec, 04 06 2022. [Online]. Available: https://optomec.com/printed-electronics/aerosol-jet-technology/. [Accessed 04 06 2022].

[124] G. Gomez-Gras, R. Jerez-Mesa, J. A. Travieso-Rodriguez and J. Lluma-Fuentes, "Fatigue performance of fused filament fabrication PLA specimens," *Materials and Design,* vol. 140, pp. 278–285, 2018.

[125] C. Oztan, S. Ballikaya, U. Ozgun, R. Karkkainen and E. Celik, "Additive manufacturing of thermoelectric materials via fused filament fabrication," *Applied Materials Today,* vol. 15, pp. 77-82, 2019.

[126] C. Huber, G. Mitteramskogler, M. Goertler, I. Teliban, M. Groenefeld and D. Suess, "Additive Manufactured Polymer-Bonded Isotropic NdFeB Magnets by Stereolithography and Their Comparison to Fused Filament Fabricated and Selective Laser Sintered Magnets," *Materials ,* vol. 13, no. 8, pp. 1-8, 2020.

[127] B. A. Munk, Frequency Selective Surfaces: Theory and Design, Chichester: John Wiley & Sons, Inc., 2000.

[128] I. Anderson, "On the Theory of Self-Resonant Grids," *The Bell System Technical Journal,* vol. 54, no. 10, pp. 1725 - 1731, 1975.

[129] P. E. C. Kinzel, C.-P. K. M. Donnell and C.-P. K. Chandrashekhara, "Structural Health Monitoring and Remote Sensing of Transportation Infrastructure Using Embedded Frequency Selective Surfaces," Center for Transportation Infrastructure and Safety/NUTC program Missouri University of Science and Technology, Rolla, 2014.

[130] R. S. Anwar, L. Mao and H. Ning, "Frequency Selective Surfaces: A Review," *MPDI Applied Sciences,* vol. 8, no. 9, pp. 1-47, 2018.

[131] D. S. Wang, S.-W. Qu and C. H. Chan, “Frequency Selective Surfaces,” in *Handbook of Antenna Technologies*, Singapore, Springer Nature, 2016, pp. 471-525.

[132] W. Mohyuddin, D. H. Kim, H. C. Choi and K. W. Kim, “Comparative Study of Square and Circular Loop Frequency Selective Surfaces for Millimeter-Wave Imaging Diagnostics Systems,” *MPDI Sensors (Basel),* vol. 18, no. 9, pp. 1-13, 2018.

[133] T. K. Wu, Frequency Selective Surface and Grid Array, New York: John Wiley & Sons Inc., 1995.

[134] E. Parker, “The Gentleman’s Guide To Frequency Selective Surfaces,” in *17th Q.M.W. Antenna Symposium*, London, 1991.

[135] R. Shavit, Radome Electromagnetic: Theory and Design, Hoboken: JohnWiley & Sons Ltd, 2018.

[136] P. Callaghan, E. A. Parker and R. J. Langley, “Influence of supporting dielectric layers on the transmission properties of frequency selective surfaces,” *IEE PROCEEDINGS-H,* vol. 138, no. 5, pp. 448 – 454, 1991.

[137] F. Costa, A. Monorchio and G. Manara, “An Overview of Equivalent Circuit Modeling Techniques of Frequency Selective Surfaces and Metasurfaces,” *The Applied Computational Electromagnetics Society Journal (ACES),* vol. 29, no. 12, pp. 960-976, 2014.

[138] O. Luukkonen, C. Simovski, G. Granet, G. Goussetis, D. Lioubtchenko, A. V. Raisanen and S. A. Tretyakov, “Simple and Accurate Analytical Model of Planar Grids and High-Impedance Surfaces Comprising Metal Strips or Patches,” *IEEE Transactions on Antennas and Propagation,* vol. 56, no. 6, pp. 1624 - 1632, 2008.

[139] J. T. Murugan, T. R. S. Kumar, P. Salil and C. Venkatesh, “Dual frequency selective transparent front doors for microwave oven with different opening areas,” *Progress In Electromagnetics Research Letters,* vol. 52, pp. 11–16, 2015.

[140] F. Sakran, Y. Neve-Oz, A. Ron, M. Golosovsky, D. Davidov and A. Frenkel, “Absorbing frequency-selective-surface for the mm-wave range,” *IEEE Transactions on Antennas and Propagation,* vol. 56, no. 8, pp. 2649-2655, 2008.

[141] S. Chakravarty, R. Mittra and N. Williams, “On the application of the microgenetic algorithm to the design of broad-band microwave absorbers comprising frequency-

selective surfaces embedded in multilayered dielectric media," *IEEE Transactions on Microwave Theory and Techniques,* vol. 49, no. 6, pp. 1050 - 1059, 2001.

[142] B. G. Xia, D. H. Zhang, J. Meng, J. Huang, C. F. Yao and J. S. Zhang, "Terahertz FSS for space borne passiveremote sensing application," *Electronics Letters,* vol. 49, no. 22, pp. 1398-1399, 2013.

[143] A. A. Dewani, S. G. O'Keefe, D. V. Thiel and A. Galehdar, "Window RF Shielding Film Using Printed FSS," *IEEE Transactions on Antennas and Propagation,* vol. 66, no. 2, pp. 790 - 796, 2018.

[144] M. Euler, V. Fusco, R. Dickie, R. Cahill and J. Verheggen, "Sub-mm Wet Etched Linear to Circular Polarization FSS Based Polarization Converters," *IEEE Transactions on Antennas and Propagation,* vol. 59, no. 8, pp. 3103 - 3106, 2011.

[145] L. E. Comtesse, R. J. Langley and E. A. P. a. J. C. Vardaxoglou, "Frequency Selective Surfaces in dual and Triple Band Offset Reflector Antennas," in *1987 17th European Microwave Conference*, Rome, Italy, 1987.

[146] L. Zhang, Q. Wu and T. A. Denidni, "Electronically Radiation Pattern Steerable Antennas Using Active Frequency Selective Surfaces," *IEEE Transactions on Antennas and Propagation,* vol. 61, no. 12, pp. 6000 - 6007, 2013.

[147] B. Liang, B. Sanz-Izquierdo, E. A. Parker and J. C. Batchelor, "Cylindrical Slot FSS Configuration for Beam-Switching Applications," *IEEE Transactions on Antennas and Propagation,* vol. 63, no. 1, pp. 166 - 173, 2015.

[148] C. Gu, B. S. Izquierdo, S. Gao, J. C. Batchelor, E. A. Parker, F. Qin, G. Wei, J. Li and J. Xu, "Dual-Band Electronically Beam-Switched Antenna Using Slot Active Frequency Selective Surface," *IEEE Transactions on Antennas and Propagation,* vol. 65, no. 3, pp. 1393 - 1398, 2017.

[149] C. Debus and P. H. Bolivar, "Frequency Selective Surfaces for High-Sensitivity Terahertz Sensors," *Applied Physics Letters,* vol. 91, no. 18, pp. 1-3, 2007.

[150] H. F. Álvarez, D. A. Cadman, A. Goulas, M. E. d. C. Gómez, D. S. Engstrøm, J. C. Vardaxoglou and S. Zhang, "3D conformal bandpass millimeter-wave frequency selective surface with improved felds of view," *Scientifc Reports,* vol. 11, pp. 1-12, 2021.

[151] M. Nauman, R. Saleem, A. K. Rashid and M. F. Shafique, "A Miniaturized Flexible Frequency Selective Surface for X-Band Applications," *IEEE Transactions on Electromagnetic Compatibility ,* vol. 58 , no. 2, pp. 419 - 428, 2016.

[152] E. A. Parker and A. N. A. E. Sheikh, "Convoluted array elements and reduced size unit cells for frequency-selective surfaces," *1EE Proceedings-H,* vol. 138, no. 1, pp. 19-22, 1991.

[153] B. Sanz-Izquierdo and E. A. Parker, "3-D Printing of Elements in Frequency Selective Arrays," *IEEE Transactions On Antennas and Propagation,* vol. 62, no. 12, pp. 6060-6066, 2014.

[154] E. Parker, J. Batchelor, R. Chiang, A. Williamson, B. Sanz-Izquierdo, M. Neve and K. Sowerby, "Frequency selectively screened office incorporating convoluted FSS window," *Electronics Letters ,* vol. 46, no. 5, p. 317 – 318, 2010.

[155] S. Abirami, E. F. Sundarsingh and V. S. Ramalingam, "Mechanically Reconfigurable Frequency Selective Surface for RF Shielding in Indoor Wireless Environment," *IEEE Transactions on Electromagnetic Compatibility,* vol. 62, no. 6, pp. 2643 - 2646, 2020.

[156] Y. Cui, S. A. Nauroze and M. M. Tentzeris, "Novel 3D-Printed Reconfigurable Origami Frequency Selective Surfaces With Flexible Inkjet-Printed Conductor Traces," in *IEEE MTT-S International Microwave Symposium (IMS)*, Boston, MA, USA, 2019 .

[157] S. N. Azemi, K. Ghorbani and W. S. T. Rowe, "A Reconfigurable FSS Using a Spring Resonator Element," *IEEE Antennas and Wireless Propagation Letters,* vol. 12, pp. 781 - 784, 2013.

[158] S. A. Nauroze, L. S. Novelino, M. M. Tentzeris and G. H. Paulino, "Continuous-range tunable multilayer frequency-selective surfaces using origami and inkjet printing," Proceedings of the National Academy of Sciences *(PNAS),* vol. 115 , no. 52, pp. 13210–13215, 2018 .

[159] E. A. Parker and S. Massey, "Application of FSS Structures to Selectively Control the Propagation of signals into and out of buildings Annex 5: Survey of Active FSS," Ofcom, Surrey UK, 2004.

[160] S.-S. Cho and I.-P. Hong, "Design of a paper-based reconfigurable frequency selective surface structure," *IEICE Electronics Express,* vol. 13, no. 16, pp. 1-7, 2016.

[161] H. Zhang, S. Zeng, B. Di, Y. Tan, M. D. Renzo, M. Debbah, Z. Han, H. V. Poor and L. Song, “Intelligent Omni-Surfaces for Full-Dimensional Wireless Communications: Principles, Technology, and Implementation,” *IEEE Communications Magazine,* vol. 60, no. 2, pp. 39 - 45, 2022.

[162] B. Di, H. Zhang, L. Song, Y. Li, Z. Han and H. V. Poor, “Hybrid Beamforming for Reconfigurable Intelligent Surface based Multi-User Communications: Achievable Rates With Limited Discrete Phase Shifts,” *IEEE Journal on selected areas in communications,* vol. 38, no. 8 , pp. 1809-1822, 2020.

[163] P. Njogu, A. Shastri, S. Gao and Sanz-Izquierdo, “Screen-Printed FSS Plasterboard for Wireless Indoor Applications,” in *Mediterranean Microwave Symposium*, Pizzo Calabro, Italy, 2022.

[164] A. Shastri, P. Njogu, B. Sanz-Izquierdo, S. Gao and Z. Chen, “Low-cost Inkjet Printed Paper Poster FSS for 5G,” in *15th European Conference on Antennas and Propagation (EuCAP)*, Düsseldorf, Germany, 2021.

[165] S.-D. Jang, B.-W. Kang and J. Kim, “Frequency selective surface based passive wireless sensor for structural health monitoring,” *Smart Materials and Structures,* vol. 22, no. 2, pp. 1-8, 2013.

[166] M. Mahmoodi and K. M. Donnell, “Novel FSS-Based Sensor for Concurrent Temperature and Strain Sensing,” in *2017 IEEE International Symposium on Antennas and Propagation & USNC/URSI National Radio Science Meeting*, San Diego, CA, USA, 2017.

[167] E. Kinzel, “Design of a Frequency-Selective Surface strain sensor,” in *IEEE Antennas and Propagation Society International Symposium (APSURSI)*, Memphis, TN, USA, 2014.

[168] M. Mahmoodi and K. M. Donnell, “Active frequency selective surface for strain sensing,” in *IEEE International Symposium on Antennas and Propagation & USNC/URSI National Radio Science Meeting*, San Diego, CA, USA, 2017.

[169] S. Soltani, P. S. Taylor, E. A. Parker and J. C. Batchelor, “Popup Tunable Frequency Selective Surfaces for Strain Sensing,” *IEEE Sensors Letters,* vol. 4, no. 4, 2020.

[170] S. Deshmukh and H. Huang, “Wireless interrogation of passive antenna sensors,” *Meas. Sci. Technol.,* vol. 21, no. 3, pp. 1-9, 2010.

[171] R. J. Langley and E. A. Parker, “Equivalent circuit model for arrays of square loops,” *Electronics Letters,* vol. 18, no. 7, pp. 294-296, 1982 .

[172] N. Marcuvitz, Waveguide Handbook, Exeter: Short Run Press, 1986.

[173] “Dassault Systèmes,” Dassault Systèmes, 19 07 2022. [Online]. Available: https://www.3ds.com/. [Accessed 19 07 2022].

[174] F. Hirtenfelder, “,Effective Antenna Simulations using CST Microwave Studio®,” *2nd International ITG Conference on Antennas*, Municc, Germany, 2007.

[175] Computer Simulation Technology, “Understanding Time Domain Meshing in CST MICROWAVE STUDIO®,” white paper, Computer Simulation Technology, 2010.

CHAPTER 3: EVALUATION OF ANTENNAS INTEGRATED ON EXPENDABLE ROBOTS

3.1 Overview

This chapter details the development of antenna solutions for expendable origami robotic structures presented in [1] and [2]. In [1], inkjet printed monopole antennas resonating at the two commonly used drone control frequency bands, 2.4 GHz, and 5.2 GHz, were designed on the limited space available on the folded origami robotic bird structure. Two dual-band monopole antennas were developed. The first antenna is located on the robot's spine and the second on its tail. A space diversity configuration was also studied. The antennas were printed directly onto a photo paper substrate using an ordinary desktop inkjet printer fitted with silver nanoparticle conductive ink cartridges. The antenna bearing photopaper was then folded into an origami robotic crane's body structure in such a way that the antenna was aligned with the robot's geometrical structure. A good agreement between the measured and simulated reflection coefficient results was achieved with a reasonable bandwidth realized in all three cases studied. This multidisciplinary work initially combines antenna design and inkjet technologies for application in development of origami robot's antenna application on inexpensive and readily available paper substrate. The study was extended to investigate the antenna on an origami robotic boat for surface detection [2]. This second antenna design was etched on a non-porous A4 sized mylar sheet that was then folded into an origami boat because it was to be tested on water which could soak up the photo paper. It is proposed as surface detector by exploiting the influence on the reflection, penetration, transmission, and resonation of a signal due to the dielectric properties of the material of the surface.

The rest of this chapter is organized as follows: Section 3.2 is the introduction. Section 3.3 describes the design and analyses of the antenna located on the spine, section 3.4 discusses the antenna located on the tail, section 3.5 describes diversity antenna system solution while Section 3.6 discusses the application of an origami robotic boat as a surface sensor. Section 3.7 is the discussion and conclusion of the chapter.

3.2 Introduction

Small robots have attracted interest from both the academic and industrial world in recent years. This seems to be driven by the increasing miniaturization of mechanical, electrical, and electronic components [3][4]. Progress in the development of small machines has inspired research in robotics, with the area of robotics miniaturization experiencing rapid growth [5]. Different types of small robots have been developed including remotely controlled vehicles [6] and flying robots [7][8]. Origami foldable robots have also stirred researchers' interests and have been studied from various perspectives [9] driven by the unique ways of fabricating and assembling of various types of origami-inspired structures [10]. Among origami inspired applications are electronic components [11], robots [12], Origami-inspired antenna solutions [13] [14] and sensing application [2].

Flying robots have found use in the military, security, civil as well as in commercial applications in areas such as correction and relaying of real-time data of ongoing occurrences. They facilitate effective and timely responses in areas like disaster zones, farming, reconnaissance, environmental observation and monitoring, meteorological observation and research, mineral exploitation, etc. [15]-[17].

For swift and flexible mobility controllability and operation of the flying robots, wireless communication for which antennas are an essential element is key. A firm, compact, low-profile aerodynamic enhancing antenna mounted on a robot facilitates reliable drone-controller communication. In most cases, this antenna should provide an omnidirectional radiation pattern and vertical polarisation for efficient communication with the controller [18].

3D inkjet printing with nanoparticle silver ink is a rapidly advancing manufacturing method. It is a layer-by-layer fabrication process where a design is printed directly from a digital model as described in chapter 2. It enables rapid prototyping as well as reduces product manufacturing process cycles. This is in such areas as electronics, microwave, and radio frequency (RF) [19].

Inkjet printing is a liquid material deposition technique whose operational process is as described in chapter 2, subsection 2.4.4. The liquid material (ink) is a solution involving a solute dissolved in solvent [20]. It is an AM technique that has been employed in the development of antennas on various substrates. These substrates include 3D printed polylactic acid (PLA) [21] [22], thermoplastic acrylonitrile butadiene styrene polycarbonate (ABS-PC) [23], polyethylene terephthalate (PET) [24], flexible thermoplastic polyurethane (NinjaFlex) [25], textile [26], Rogers RO 3203 [27] etc. Further, developments in inkjet printing technology have enabled printing of antennas on paper-based substrates. Examples of these are the monopole antennas and designs suitable for RFID applications in [28], ultra-wideband antennas [29]-[31], and fractal geometries based on a triangular Sierpinski concept [32]. Miniaturized MIMO antennas have also been proposed printed on Kodak film paper and then folded into a cylindrical shape [33].

In this section, investigation has been conducted on the integration of an inkjet-printed antenna on an origami robot produced using traditional origami folding techniques [34]. These types of flying robots are gaining popularity in the research and development community [35][36]. This work seeks to contribute in this research space by investigating the integration of inkjet printed antennas on a flying robot made using traditional origami techniques, with emphasis on the antennas' placement on its geometry. The work combines antenna designing, manufacturing and fabrication techniques and origami structures for future origami-based paper robots.

Inkjet printing, a direct write AM method is employed to print monopole antennas on paper substrate. Each antenna was printed to fit on a particular part of the geometry of the origami robotic bird folded from an A4 paper sheet. A compact dual-band antenna consisting of a triangular shape with a horizontal slot on top of a semi-elliptic monopole printed using low-cost inkjet printing on photo paper substrate is proposed. Three locations were identified as suitable for the antenna: the triangular neck, the spine, and the tail. Consequently, two versions of the same antenna designs were produced. One that fits on the robot's spine and another that fits on the tail or/and the neck. A diversity configuration was also investigated.

A further monopole antenna for controlling an origami boat, with a built-in surface sensing functionality is proposed and discussed in Section 3.6. This investigates the same antenna design with some adjustments, as a surface sensor for potential amphibious origami robotic boats with integrated surface sensing functionality. Two arms extending from each of the antenna's ground planes provide a 1.5 GHz resonance for the surface detection functionality.

3.3 The origami robotic bird spine antenna design and analysis

This section discusses the design, geometry, fabrication, measurements as well as the conductive surface analysis of the proposed spine antenna.

3.3.1 The antenna design analysis and geometry

A traditional origami robotic bird with potential electromechanical and antenna component locations is illustrated in Figure 3.1.

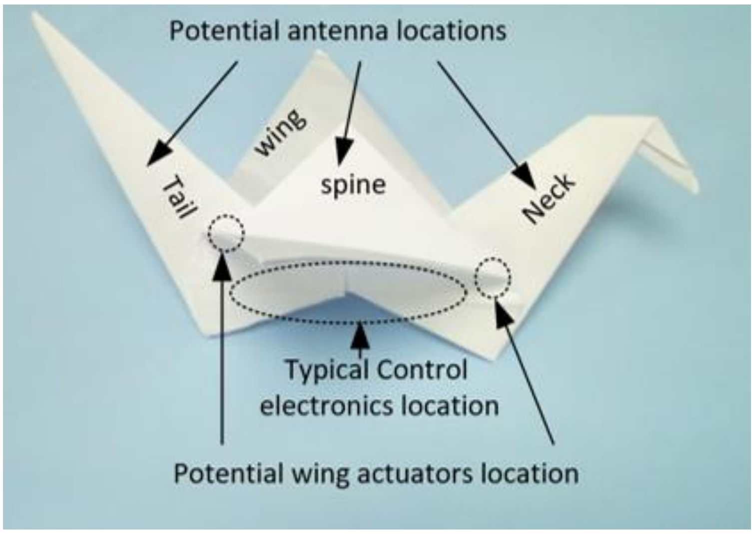

Figure 3.1 The origami robotic bird and potential antenna locations

The proposed planar monopole antenna, Figure 3.2 (a), is based on [39] [40] and its geometry is modelled around [41]. The origami structure is made by origami folding as demonstrated in Figure 3.2(b) which shows the fold lines along which the origami bird is folded from a 210 mm square (about A4 size) sheet. It also shows the potential location of the spine antenna. The frequency bands targeted for the flying robot application are 2.4 GHz and 5.2 GHz WLAN/WiFi communication bands [37][38]. It is a leave shaped monopole with a semi-elliptical bottom and a triangular top into which a horizontal slot has been cut. Its dimensions are given in Table 3.1. R_1 and R_2 are the major and minor radii of the elliptical part of the antenna structure. The lower semi-elliptical section fit in the lower wider section of the triangular spine while the triangular upper part fits in its apex as shown in Figure 3.2 (c) which shows various

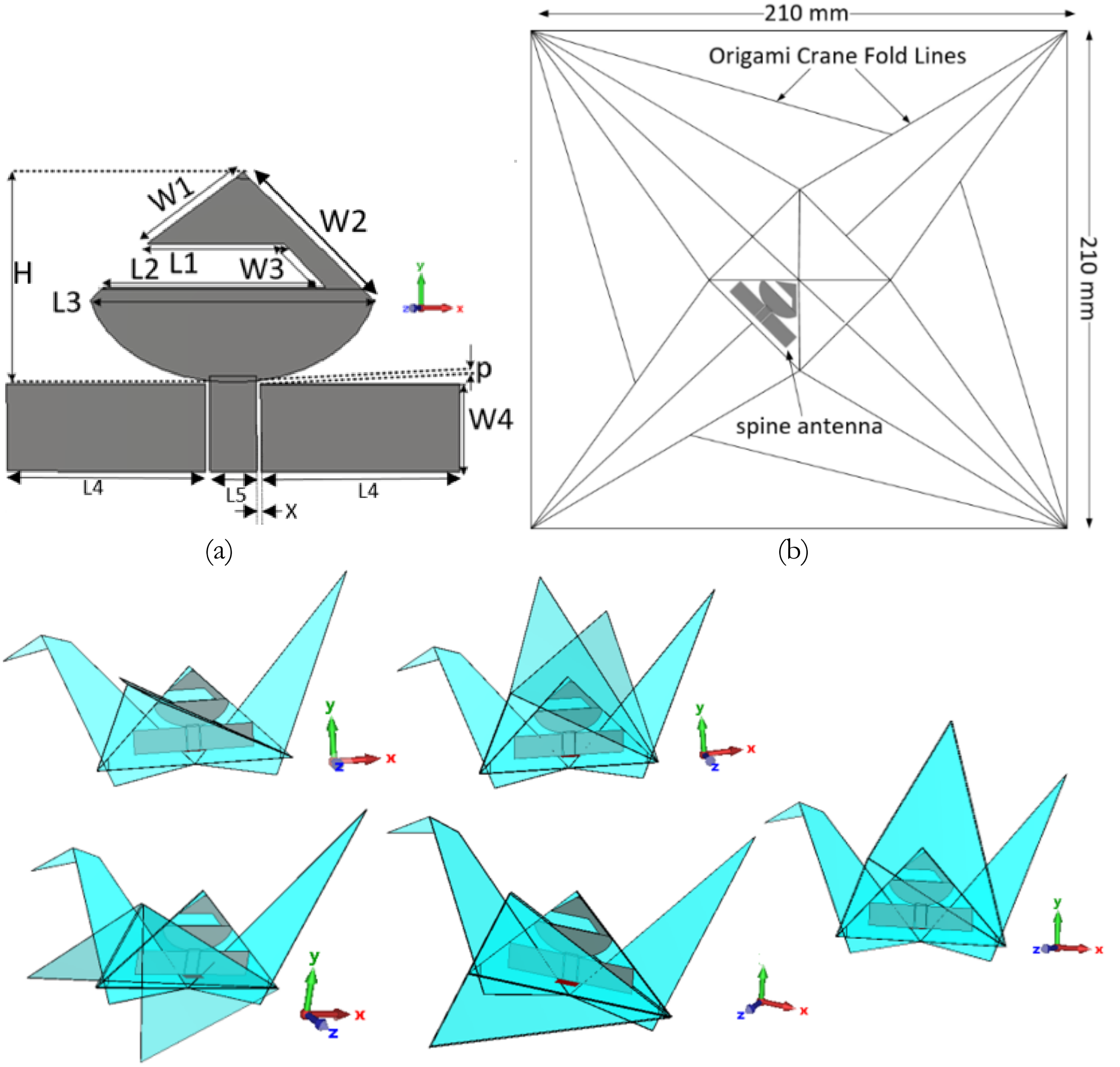

(a)

(b)

(c)

Figure 3.2 (a)The proposed spine antenna (b) illustrative location in the unfolded layout (c) location of the antenna on the geometry of the robot with its wings in various angles of flap.

Table 3.1 Antenna optimum dimensions in millimetres (mm)

Dimensions	L_1	L_2	L_3	L_4	L_5	W_1	W_2
Value (mm)	15.4	25.1	32.2	22.5	5.3	13.6	19
Dimensions	W_3	W_4	H	R_1	R_2	p	x
Value (mm)	2.2	10.1	24.24	16.4	11.75	0.4	0.5

orientations showing location of the antenna on the robot's geometry. The antenna orientation is as that of the spine i.e., upright. A 50Ω CPW line feeds the antenna. Two rectangular ground planes are on either side of the CPW feed line.

3.3.2 Derivation Planar Monopole Antenna Dimensions

The antenna is partly ellipsoidal, and the dimensions of the underlying ellipse were derived as follows. According to [40], the lower frequency (f_L) of a planar elliptical disc monopole corresponding to $VSWR = 2$ is approximated by equating its area to the area of an equivalent cylindrical monopole of the same height L and equivalent radius r. Hence

$$2\pi rL = \pi R_1 R_2 \tag{3.1}$$

where R_1 and R_2 are the longer and shorter half lengths of ellipse's radii respectively. Equation (3.1) thus gives:

$$r = (R_1\ R_2)/2L \tag{3.2}$$

A quarter wavelength monopole antenna has an input impedance equivalent to half of that of a half wavelength dipole antenna. The input impedance of an infinitesimally thin monopole antenna is thus $36.5 + j21.25\Omega$, an inductive impedance. The real impedance is obtained by using a slightly smaller length, L, of the monopole given by [42] as:

$$L = 0.24\lambda F \tag{3.3}$$

where λ is the free space wavelength and F is the length-to-radius parameter for the stub monopole given by

$$F = (L/r)/(1 + L/r) = L/(L + r) \tag{3.4}$$

From equations (3.3) and (3.4), the wavelength λ is obtained as:

$$\lambda = (L + r)/0.24 \tag{3.5}$$

Thus, the lower frequency f_L is:

$$f_L = c/\lambda = (30 \times 0.24)/(L + r) = 7.2/(L + r) \tag{3.6}$$

After accounting for the effect of probe length, *p*, which increases the antenna length and thus reduces the frequency, (3.6) can accordingly be modified to

$$f_L = 7.2/(L + r + p) \tag{3.7}$$

where f_L is in GHz and *L*, *r* and *p* are in cm. (3.3) to (3.7) are empirical equations for the approximation of the length and the first order of the resonance of the cylindrical monopole [40] and [42]. For the half lengths axes R_1 and R_2 of the ellipse, the ellipticity ratio, R_1/R_2, chosen was 1.3 to restrict the bandwidth to the range of interest. The antenna was fed along the minor axis of the semi ellipse. For elliptical monopole fed along the minor axis, $L = 2R_2$ and $r = R_1/4$. For a f_L equal to 2.4 GHz, the radii R_1 and R_2 of the semi-ellipse after optimization were obtained.

A planar triangular monopole of height H (height from feed point to apex) and base length W was superimposed on the semi elliptical monopole. H is the height of the equivalent cylindrical monopole of radius r. H and r are calculated from (3.6), (3.8) and (3.9):

$$H = \sqrt{3}W/2 \tag{3.8}$$

$$r = W/4\pi \tag{3.9}$$

The actual height H is less than the calculated height due to the dielectric substrate and fringing currents effect. It should be noted that the superimposed rounded triangular monopole base is the semi-elliptical disc.

3.3.3 The design simulations

The model was designed and simulated on a 0.177 mm thick paper substrate of relative permittivity, ε_r, of 3 and tan δ of 0.05 [28] using CST Microwave Studio™. AGIC-AN01 silver nanoparticle ink was used to print the antenna. Its conductivity was calculated in the simulation of the antenna. According to AGIC-AN01 silver nanoparticle ink manufacturer's datasheet [43], (appendix 3.1), its sheet resistivity is 0.2 [Ω/sq]. Its conductivity was thus calculated as follows: The thickness, *t*, of the print was estimated to be about 1µm. This was confirmed after the optical microscopic image measurement of the printed antenna were done. From

$$\rho s = \frac{\rho}{t}[\Omega/sq] \tag{3.10}$$

where ρs is the sheet resistance, ρ is the resistivity and *t* are the print's thickness, the resistivity of the silver nanoparticle ink was obtained from which conductivity, σ, was calculated as:

$$\sigma = \frac{1}{0.2 \times 1.0\mu m} = 5 \times 10^6\ S/m \tag{3.11}$$

The antenna radiator conductor was thus simulated using the AGIC-AN01 silver nanoparticle ink of the calculated conductivity, equation (3.11).

The model was simulated reflection coefficient, S_{11} response were obtained for various components of the radiator and is shown in Figure 3.3. The results show that the semi-elliptical radiator provides resonance at the upper band i.e., 5.2 GHz. The semi-elliptical radiator with superimposed triangular monopole exhibits wideband characteristics. The lower frequency is higher than the targeted 2.4 GHz. This could be due to the rounded (semi-ellipse) base of the triangular monopole which reduces the size of the-radiator thus raising f_L. By inserting and optimizing the dimension of a horizontal slot across the triangle, the lower resonance point was shifted to 2.4 GHz while maintaining the upper band as well as rejecting frequencies between the two bands of interest. The final antenna has two distinct resonant modes corresponding to the triangular radiating section and the semi ellipse. The gap '*p*' between the ground plane and radiating element acts as a matching network and improves impedance bandwidth. The optimum impedance bandwidth is achieved when the capacitance due to the gap '*p*' between the radiating element and ground plane edges balances with the antenna inductance. The size of the ground plane is also critical in the design of compact antennas [44] and [45].

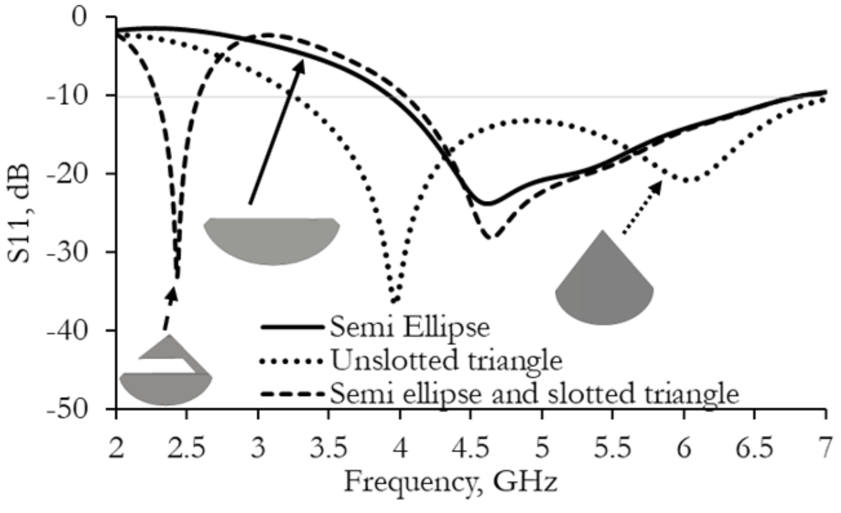

Figure 3.3 . Radiating element configuration for respective resonance

Further simulation was done to see the behaviour of the prototype when the resonator is made of copper. Simulation was also done for AGIC-AN01 silver ink the lossless paper substrate and the results were then compared. The simulated reflection coefficient results, S_{11}, for AGIC-AN01 silver ink, with lossless paper and for copper radiator are shown in Figure 3.4. The radiation patterns of the same are depicted in Subsection 3.3.5. As copper and silver are good conductors, their S_{11} results are more or else the same. When a lossless photo paper is used, a slightly shallower depth of the S_{11} at the higher frequency is observed.

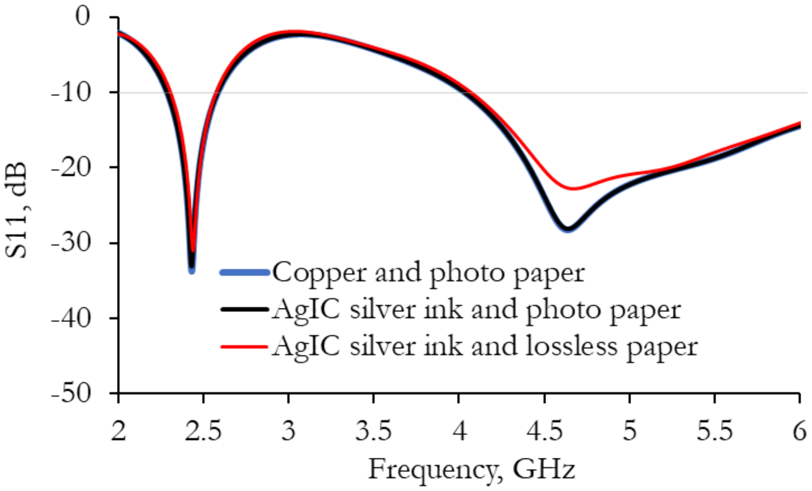

Figure 3.4 Simulated S_{11} for the various materials

The surface current distribution on the antenna is shown in Figure 3.5. As expected, at 2.4 GHz, Figure 3.5(a), most of the currents are concentrated in the triangular section.

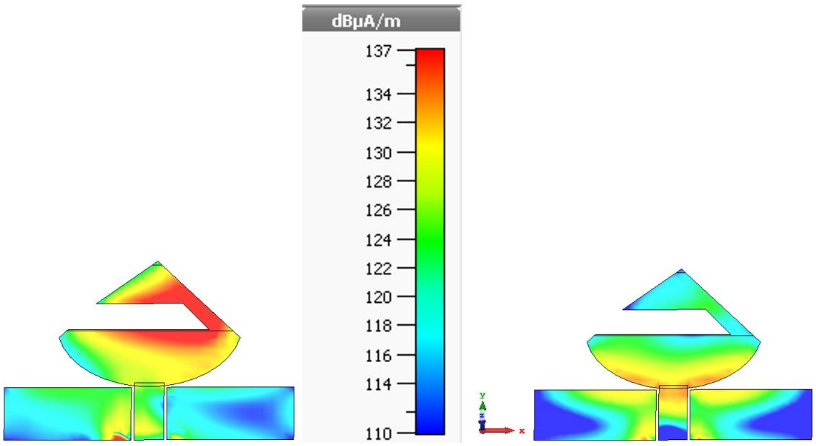

(a) (b)

Figure 3.5 Surface current distribution for spine antenna (a) 2.4 GHz and (b) 5.2 GHz

At 5.2 GHz, Figure 3.5(b), most of the currents are in the lower section of the semi-ellipse. As with all compact antennas on small ground planes, some currents are also present on the antenna's ground elements. These currents are strongest at the upper edges of the rectangular ground planes at 5.2 GHz than at 2.4 GHz. Taking this into consideration, it can be inferred that the surface current distribution could change with the size and the shape of the ground plane and/or with introduction of cable and/or RF connector to the antenna. This is likely to introduce differences in the measurements in relation to simulations.

3.3.4 Investigation of Effect Wings Movement

The effect on the antenna performance as the robot's wings flap during flight was investigated. Figure 3.6 depicts the flap angle α of the wings in relation to vertical core of the bird structure. Figure 3.7 shows the simulation reflection coefficients (S_{11}) for various values of α: 0°, 45°, 90°, 135° and 180°. The horizontal position of the wings was defined as the 90° position. The wings extreme upward flap was designated as 0° and the extreme downward as 180°. In the horizontal position, -10 dB impedance bandwidth of the antenna is from 2.3 GHz to about 2.6 GHz at the lower band and from 4 GHz to 6 GHz at the higher band. There is no significant change in S_{11} from 1° to 180°. Only angles of less than 1° produced an S_{11} higher than -10 dB at the target 2.4 GHz to 2.5 GHz band. In the worst scenario, at 0°, the S_{11} was less than -8 dB across the 2.4 GHz band.

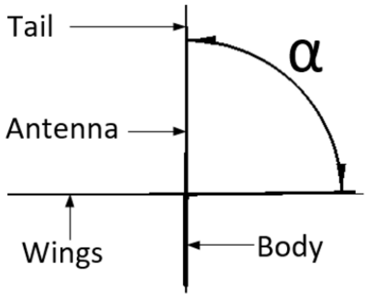

Figure 3.6 Wing angle α relative to the wings horizontal position

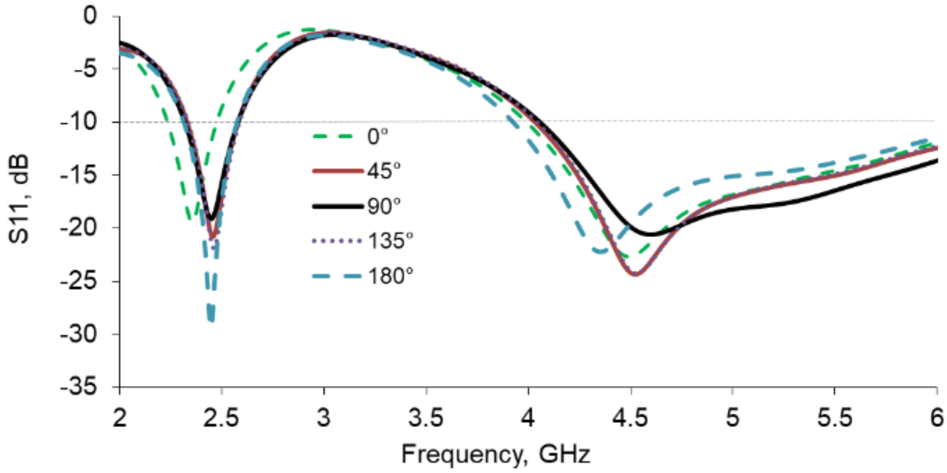

Figure 3.7 Effect of change of angle α on the reflection coefficient

3.3.5 Spine Antenna Fabrication and Measurements

The CST model was exported to Gerber (single layer) and then converted to a PDF file using ViewMate. The PDF was then printed using silver nanoparticle ink that is based on chemical sintering. Chemical sintering technology was used to avoid the prolonged heat sintering and the damage it can cause when the substrate used is a paper-based material [46]. In chemical-based sintering, a polymer latex and halide emulsion solvent dissolve silver nanoparticles of less than 0.1μm in diameter. Conductivity appears moments after the solution has dried. This makes the ink based on chemical sintering ideal for inkjet printing of the proposed antennas. A 1200×6000 dpi resolution and piezo with 210x3 colour print head home desktop Brother MFC-J5910DW printer, Figure 3.8, was used to print the antenna.

Figure 3.8 A Brother MFC-J5910DW printer used to print the antenna

Physical properties such as density, viscosity and surface tension are important when choosing the conductive ink. They determine the ink jettability, the ink droplet's size, shape as well as the wetting of the substrate and the location of the jetted drops. For inkjet printing, viscosity of 1-25 mPa.s is generally acceptable. This is considered low enough to allow fast refilling of the ink reservoir if/when required as well as ejection of the droplet through the nozzle when a transient pressure pulse is applied. A surface tension between 25 and 50 mNm^{-1} is considered high enough to prevents the dripping of the ink from the nozzle and low enough to allow the expelled droplet to detach away from the nozzle [47]. Silver nanoparticle conductive ink used in this work exhibits good chemical stability, electrical conductivity, and low chemical reactivity and is cheaper compared to other conductive inks such as gold and graphene [48]. Additionally, silver oxide also conducts electricity in the event the silver oxidises. AgIC-AN01 Silver Nano Ink was loaded in the 3 colour cartridges to produce a thick print layer that could achieve sufficient conductivity. Its composition is as follows: silver (15%), water Ethylene glycerol and Ethanol according to the manufacturer, AgIC Inc. It has a conductivity of 0.2Ω/sq, viscosity of 2-3 mPa.s, and surface tension of 30-35 mN/m [43]. It was used to print the antenna on an AgIC-CP01A4 photo paper of thickness 0.177 mm. Tests on the printed tracks were carried out using the equation for the resistivity, ρ:

$$\rho = R\frac{A}{l} \tag{3.12}$$

where *R* is the measured resistance, *A* is the cross-sectional area and *l* is the length of the track. The values of resistivity obtained were between $2\text{x}10^{-7}$ ohm-meter which is about the same value to the one provided by the manufacturers for a layer thickness of about 1µm.

The fabricated antenna is shown in Figure 3.9. Figure 3.9(a) is the printed antenna on an A4 size photo paper while Figure 3.9(b) shows the printout folded into the robotic bird. The antenna was concealed inside the structure to protect the printed metallic layers from environmental damage as the figure shows. Thermal and mechanical stability of the printed layers were provided by AgIc. Heat resistance can be allowed for up to 30 minutes at 100°C. In cross-cut tests (ISO 2409), the mechanical stability is between 0 to 1 (0 is highest and 5 is lowest).

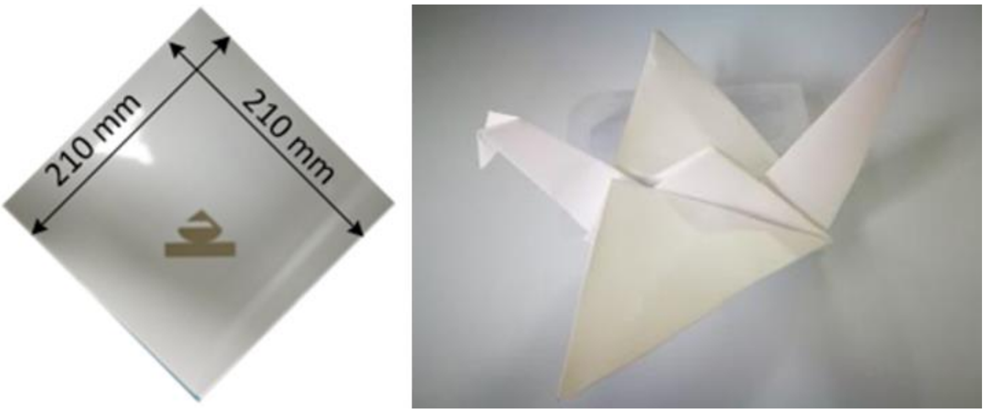

(a) (b)

Figure 3.9 (a) Photo paper printed antenna (not to scale) and (b) folded into a robotic bird

Surface profiles of the printed antenna's silver ink were obtained using white light interferometry (profilometer) and results are shown in Figure 3.10. The images at 50x magnification are depicted in Figure 3.10(a). An average surface roughness of approximately Sa 200nm was obtained. The image indicated a non-uniform 3D print as the substrate can be seen through the silver ink in some places (the blue sections of Figure 3.10(a)). The droplets are visible, and the measured roughness is for both paper substrate and silver droplets. Figure 3.10(b) is an optical image of top view of the printed antenna of 1µm silver ink height taken with x10 magnification. It also shows uneven surface. Black regions are seen within the sample which could be deeper unevenness of ink surface. Figure 3.10(c) shows the narrow gap between CPW, and the ground plane taken with x20 magnification for the 1µm silver ink height. Some isolated silver ink particles can be seen inside the gap, but their isolation prevents short circuit across the two parts. The presence of ink particles in the gap does not have any significant effect on the performance of the antennas as the foregoing tests shows. This could be because the particle sizes are much smaller compared to the wavelength of the frequencies involved.

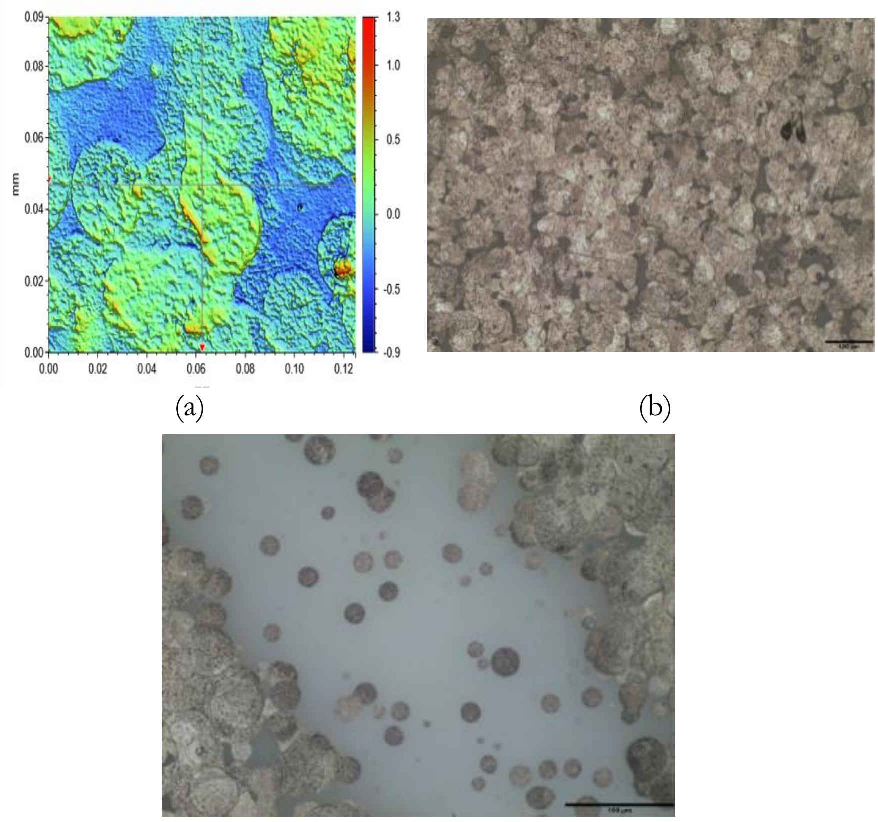

(a) (b)

(c)

Figure 3.10 (a) Silver paint optical interferometry image (b) Silver ink top view optical microscopic image (c) image of the gap between CPW and the ground plane

To test for the antenna performance, a 3.5 mm female SMA connector end launcher of 50 Ω impedance with an operating frequency range of 0 to 18 GHz from RS components [49] was attached to the antenna. The SMA end launcher was positioned such that the signal pin rested on the CPW feedline while two ground pins rested on the monopole antenna ground planes on either side of the CPW feedline. The SMA end launcher, Figure 3.11, has four ground pins. To ensure that the required electrical contact was made between the end launcher connector and the antenna, the ground pins on one side of the connector were glued onto the paper substrate side using araldite rapid epoxy adhesive as shown in Figure 3.12(a). Precautions was taken when bonding SMA end launcher and the paper substrate to ensure that the signal pin was rightly positioned on the antenna CPW feedline. This was done in such way that as one set of ground pins were firmly glued onto the paper substrates for robustness, the other two ground pins rested on the ground planes on either side of the signal pin making proper electrical contact. The signal pin itself rested on the CPW feedline also making good electrical contact.

Figure 3.11 The SMA connector end launcher [49]

With the ground and signal pins in place, RS pro silver vial epoxy conductive adhesive [50] was applied to hold them in place, Figure 3.12(b), and then left for 36 hours in room temperature to cure. Figure 3.12(c) shows the antenna in place after the connector has been attached and the glue cured while Figure 3.12(d) shows the location of the antenna on the robotic bird and its launcher connector fixed in place.

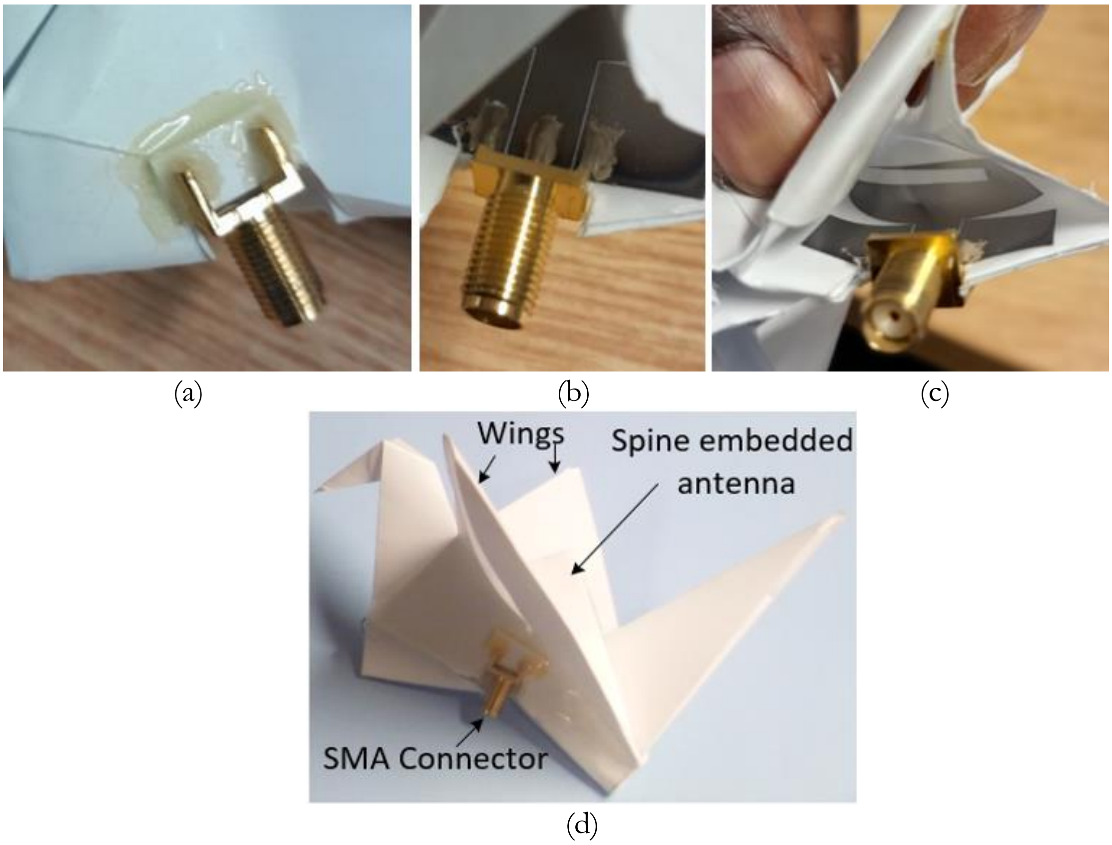
(a) (b) (c)

(d)

Figure 3.12 The antenna-SMA launch connector (a) the connector glued on to the paper substrate (b) the attached connector (c) the antenna in place after connector fixation, and (d) the robotic bird with the antenna position with the connector fixed

The antenna was concealed inside the structure to protect the printed metallic layers from environmental damage. A Rohde & Schwarz ZVL vector network analyser was then used to measure the S_{11}. Figure 3.13 shows the simulated and measured S_{11} when the wings are horizontal. The measured lower band has -10 dB impedance bandwidth from 2.2 GHz to 2.7 GHz while the upper band has a bandwidth from 3.9 GHz to 5.5 GHz thus covering both target bands. The slight discrepancy between the simulated and the measured S_{11} can be attributed to fabrication, folding and measurements errors. These include non-uniformly deposited silver conductive ink and resistive losses of the printed tracks, the bending of the substrate, as well as the SMA connector.

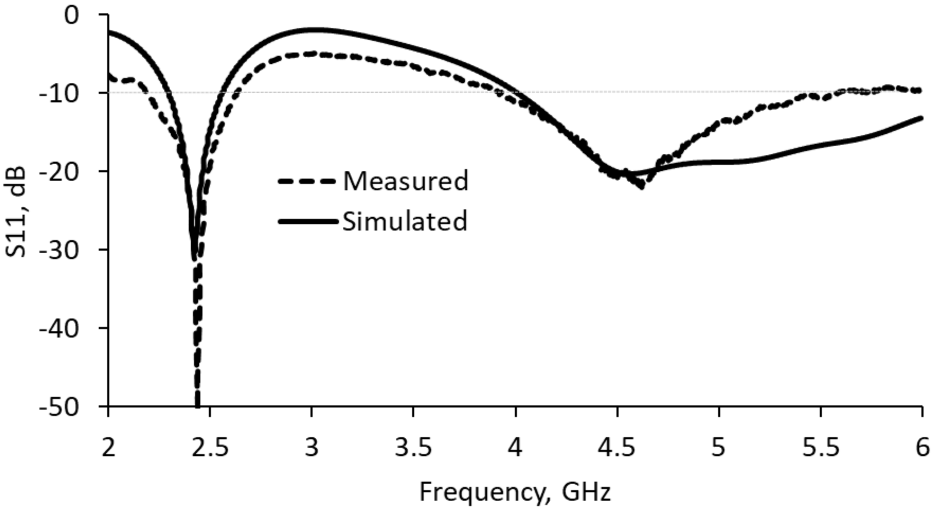

Figure 3.13 Comparison of the measured and simulated S_{11} results of the spine antenna

Radiation pattern measurements of the antenna were conducted in the anechoic chamber and the results are shown in Figure 3.14. The figure also shows the simulated radiation pattern for the silver ink on photo paper, copper conductor, silver ink on a lossless photo paper, whose simulations are described in Subsection 3.3.3, as well as the measured at (a) 2.4 GHz and (b) 5.2 GHz for the robot's horizontal wing position i.e., α is equal to 90°. The simulated results for the silver ink, potential copper nano ink, silver nano ink on a lossless photopaper do not show many discrepancies. This could be due to the silver and copper both being highly conductive and the loss tangent of the photo paper being low. The simulated results show that as expected for this type of antenna, the planes xy and yz have nulls in the y axis while plane xz displays an omnidirectional pattern. Tests showed no significant effect on the radiation pattern when the position of the wings varied from 0° to 180° relative to the robot's core. The measured antenna radiation patterns are consistent with the simulations. As with planar monopoles [51], it exhibits high cross polarization. The high cross polarization component could be a result of excitation order modes and radiation due to Jx current at the top edges of the ground plane near the radiating element. Also, discontinuity at the substrate and metallic radiator results in surface waves which can add to cross polarization [52].

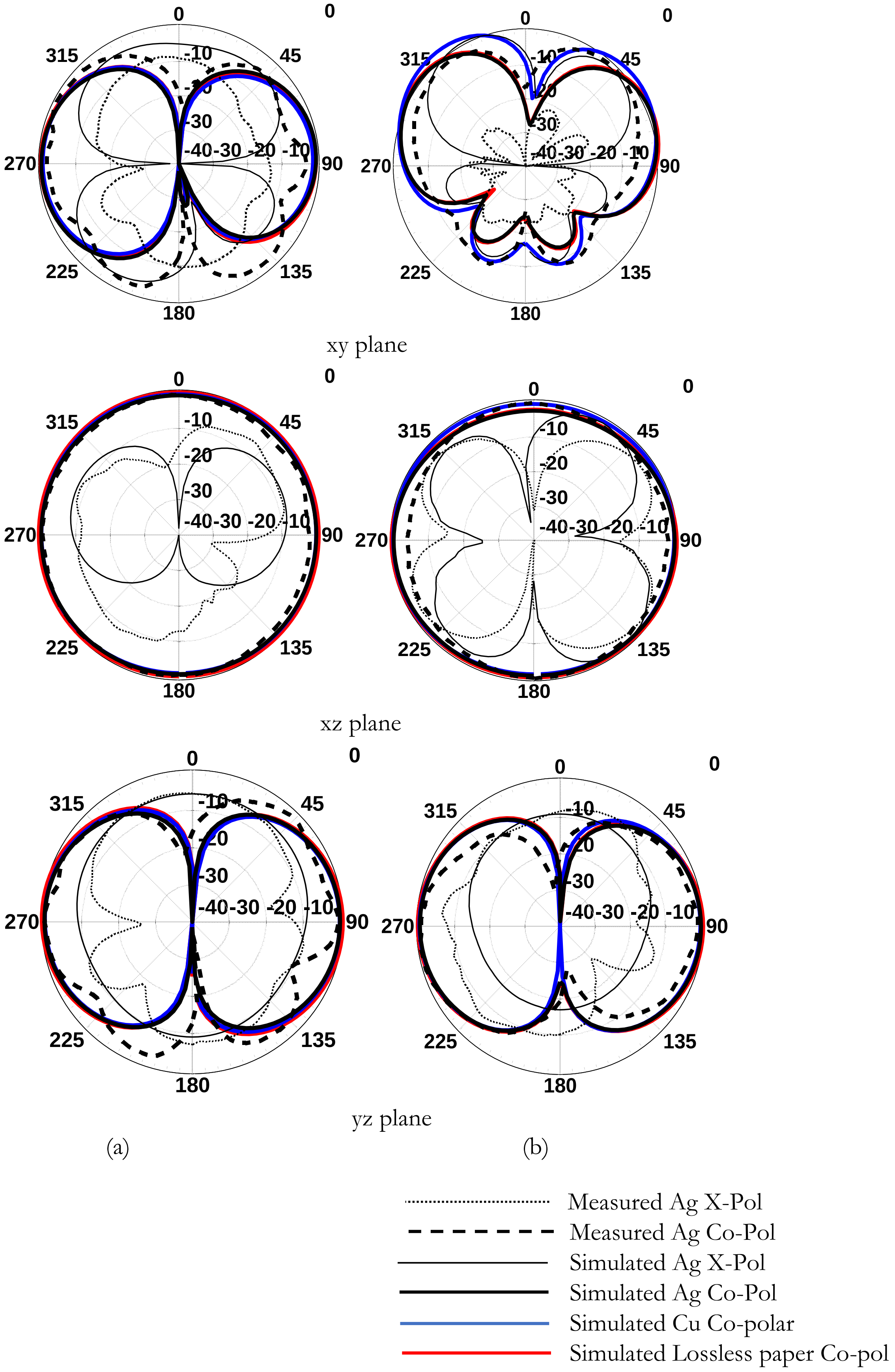
xy plane

xz plane

yz plane

(a) (b)

Figure 3.14 Simulated and measured normalised radiation pattern for planes xy, xz and yz at (a) 2.4 GHz and (b) 5.2 GHz

Figure 3.15 shows the simulated and measured gain vs frequency response for the selected frequency bands. The simulated gain is shown for the antenna radiator made of copper; silver ink (AGIC-AN01) printed on a photopaper substrate as a well as silver printed on a lossless paper substrate. The results shows that the measured antenna gains were 1.4 dBi and 2.7 dBi at 2.4 GHz and 5.2 GHz respectively, about 0.1 dB and 0.5 dB lower than the simulated ones for the silver ink antenna. The differences between the simulated and measured gain could also be due to fabrication and folding errors, cables, and connectors. The gain results also show the results for copper and silver ink are nearly identical. This could be because the two have high conductivity. The gain result for the silver antenna on a lossless paper is higher due to the losslessness of the paper substrate.

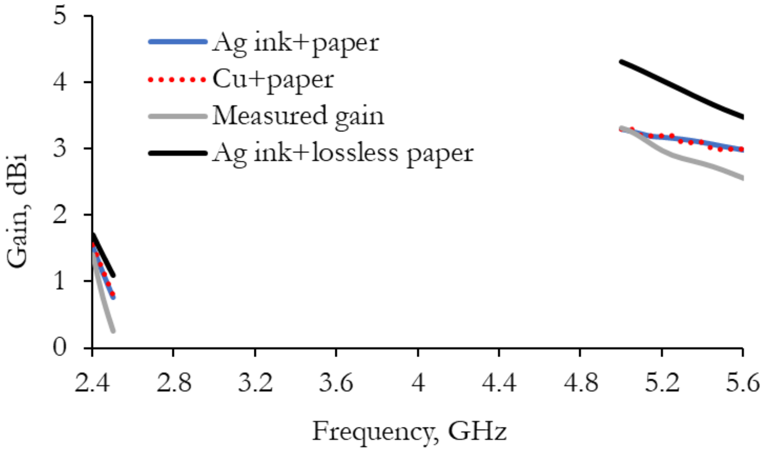

Figure 3.15 Spine antenna gain-frequency response at 2.4 and 5.2 GHz of the folded origami

3.4 A Single CPW-Fed Tail Antenna

This section details the design, simulations, wings flapping effect, fabrication, and measurements results of the proposed tail/neck antenna.

3.4.1 Tail Antenna Design

An alternative antenna location for the antenna was the tail of the origami crane. This is demonstrated in Figure 3.16. Figure 3.16(a) illustrates the location of a tail antenna as well as the potential symmetrical location of an identical neck antenna, on a 210 by 210 mm unfolded photo paper substrate. Figure 3.16(b) show the antenna's structure and dimensions while Figure 3.16(c) shows its location on the robot's tail, rotated to fit on the tail's orientation. Like the spine antenna, the tail antenna is also concealed inside structure to protect the printed metallic layers from environmental damage. The antenna is similar in shape and construction to that described in Section 3.2 but with slight dimensional adjustments to fit in the narrower tail area as well as achieve the bandwidths of interest. Table 3.2 show its final dimensions. The same dielectric material, a photo paper, with same substrate thickness was used.

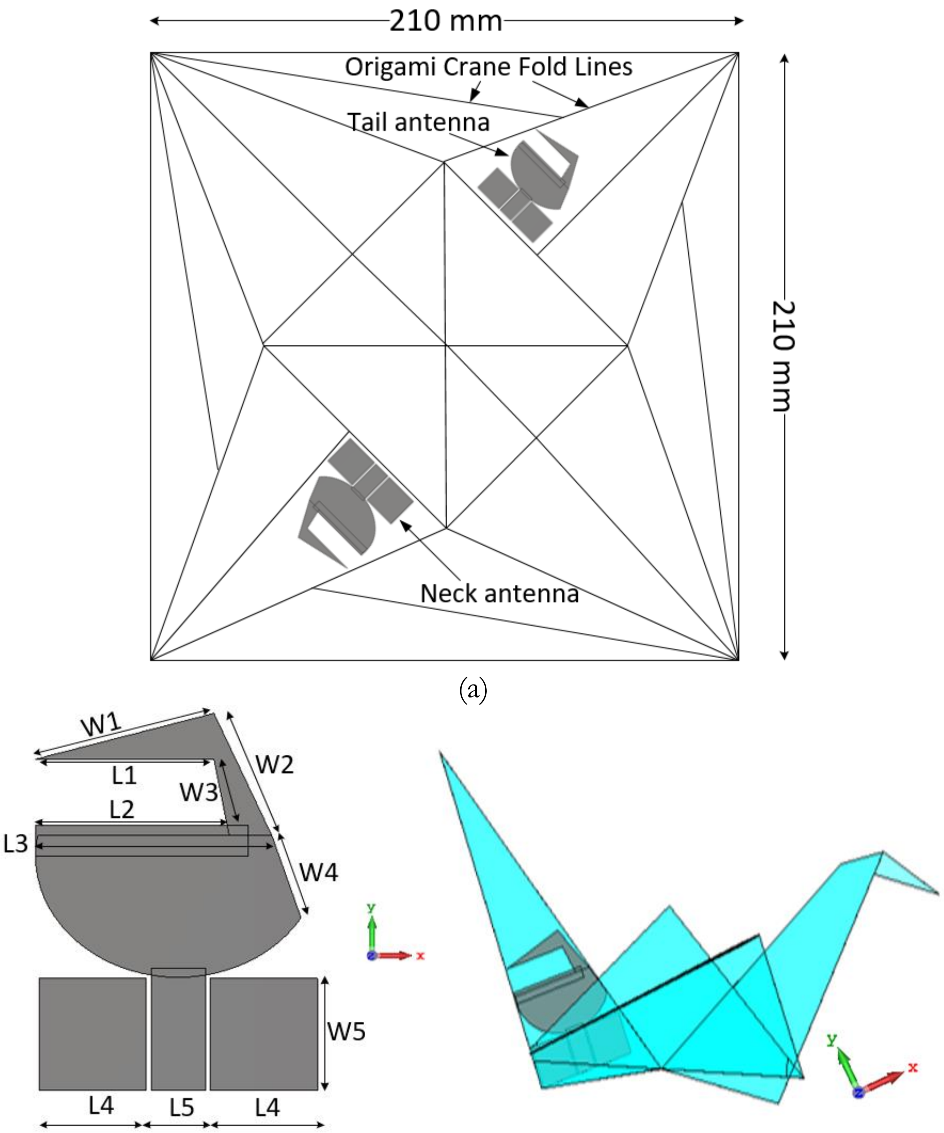

(a)

(b) (c)

Figure 3.16 Antenna integrated onto the tail of the origami crane: (a) illustrative tail and neck antenna's location in the unfolded layout, (b) tail antenna and (c) location on the robot.

Table 3.2 Final dimensions of the optimized tail antenna (mm)

L_1	L_2	L_3	L_4	L_5	W_1	W_2	W_3	W_4	W_5
17.5	19	23	10.5	5.8	18	13.28	7.65	8.55	11

The simulated S_{11} results, Figure 3.17, indicates a narrower -10 dB bandwidth at the 2.4 GHz band but a wider -10 dB bandwidth at the 5.2 GHz bands for the angle α of the wing flapping. The antenna covers the desired frequency bands for the range of the flap angles. These results also show a near negligible effect on S_{11} by the flapping of the wings compared to the spine antenna. This could be due to the antenna on the tail being removed from the wings bearing section of the origami bird structure which makes the antenna less obstructed as the wings flap compared to the antenna on the spine (Figure 3.9(b)). The current distribution on the tail antenna is shown in Figure 3.18. The higher red tone indicates the strongest surface current.

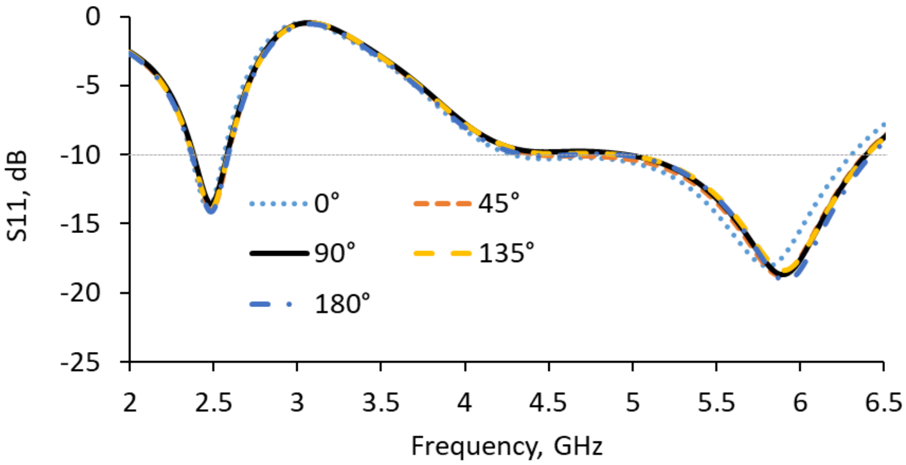

Figure 3.17 Tail antenna simulated S11 for angle α

Figure 3.18(a) and Figure 3.18(b) depicts the surface current distribution at 2.4 GHz and 5.2 GHz respectively. The figure indicates a high level of surface current at the triangular and rounded sections of the antenna at 2.4 GHz and 5.2 GHz resonance points respectively. A high surface current level is also observed on the ground plane at the two bands due to its small size which makes it a sensitive part of the radiating structure [44].

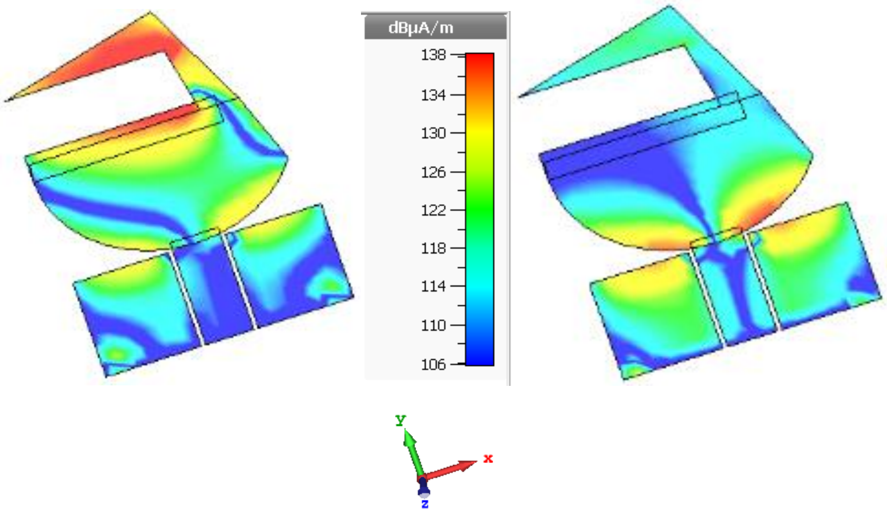

(a) (b)

Figure 3.18 Surface current distribution at (a) 2.4 GHz and (b) 5.2 GHz

3.4.2 Fabrication and Measurements

The fabrication procedure used in Section 3.3.3 was followed for the tail antenna. Figure 3. 19(a) shows the printed tail antenna on a photo paper and Figure 3.19(b), the origami crane after the paper was folded up. SMA connector end launcher was connected to the tail antenna as described in Subsection 3.3.5. S_{11} of less than -10 dB at both 2.4 GHz and 5.2 GHz bands compares well to that of the simulation as shown in Figure 3.20 for flap angle α of 90°.

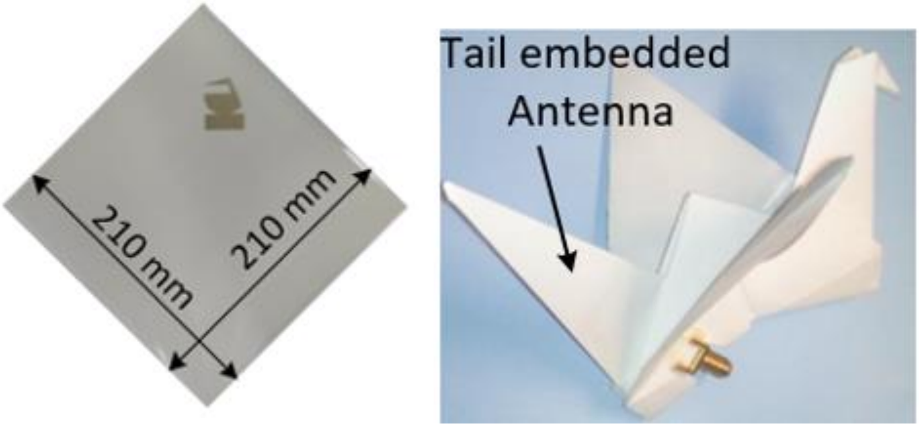

(a) (b)

Figure 3.19 Tail antenna printed on a photo paper and (b) folded into a robotic bird

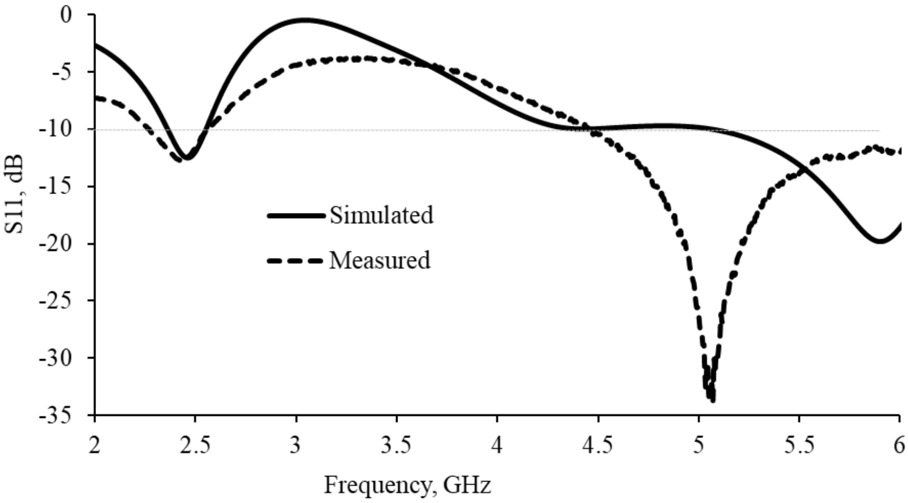

Figure 3.20 Measured vs simulated tail antenna S_{11}

Figure 3. 21 shows simulated and measured antenna radiation patterns at (a) 2.4 GHz and (b) 5.2 GHz bands. Both planes xy and yz have nulls on the y-axis while plane xz indicates omnidirectional radiation. Differences between the measured and the simulated radiation pattern could be due to the small ground plane and the introduction of an RF connector/cable to the antenna which affects the current distribution in the ground plane. This changes the impedance and radiation performance with the results being that the measured results differ slightly from the simulated results and potentially can make the design validation difficult.

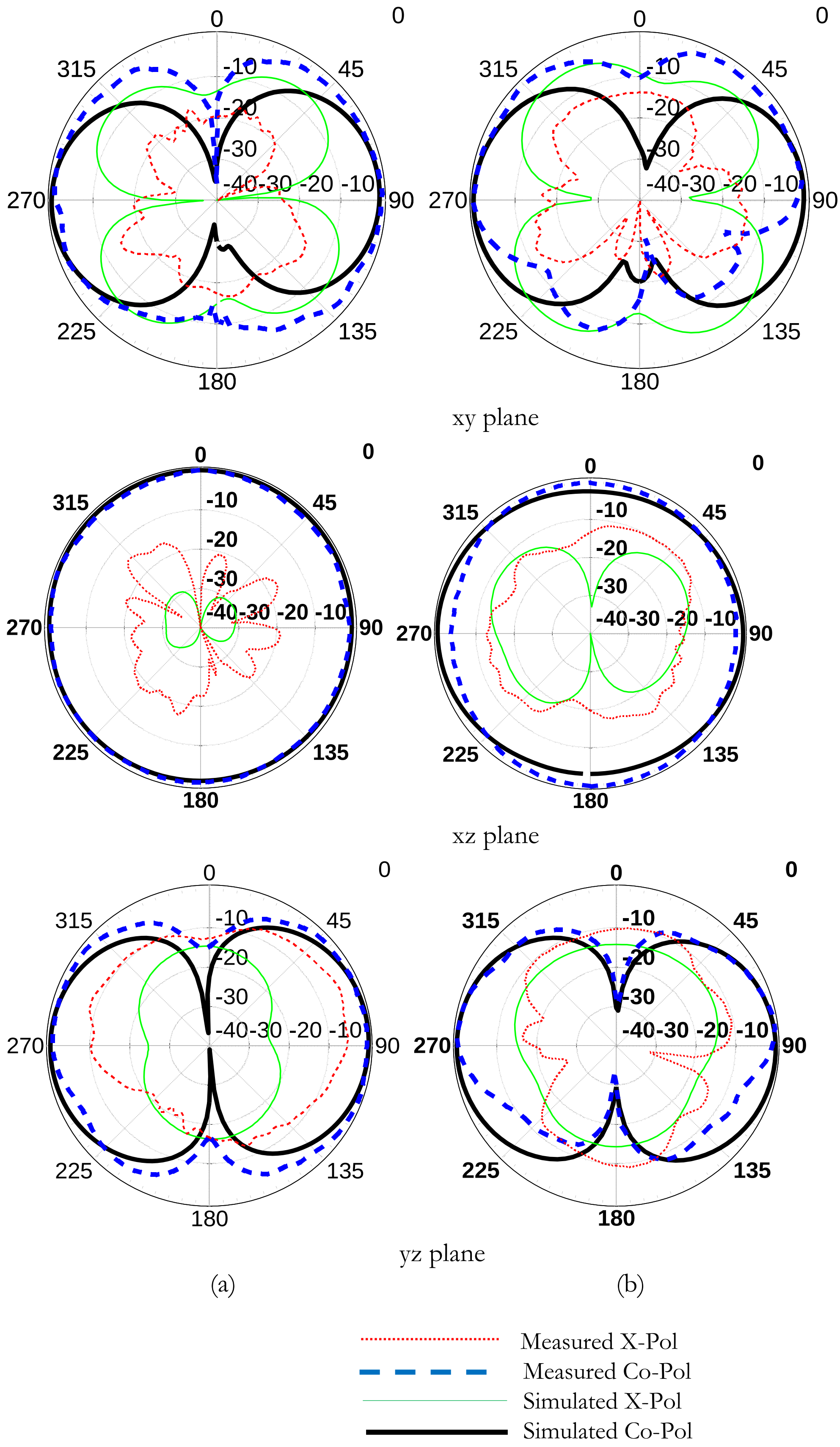

Figure 3.21 Simulated and measured normalised radiation patterns for xy, xz, and yz planes at (a) 2.4 GHz and (b) 5.2 GHz

The gain of the fabricated tail antenna was measured. Figure 3.22 shows the measured and simulated gain versus frequency response at the two frequency bands of interest (2.4-2.5 GHz and 5.0-5.6 GHz). The measured gains are in general lower than simulation ones possibly due to fabrication inaccuracies. The measured gains were about 1.5 dBi at 2.4 GHz and about 2.5 dBi at 5.2 GHz, which is in congruence with the simulated gain at the two frequencies bands.

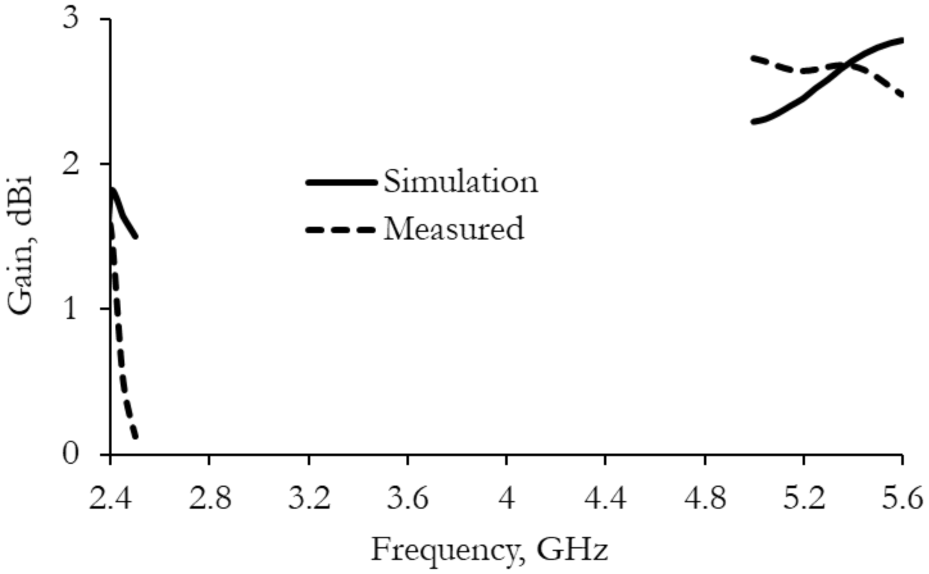

Figure 3.22 Tail antenna gain-frequency response at 2.4 and 5.2 GHz

3.5 Diversity Antenna System Solution

3.5.1 Diversity Antenna System Design

Antenna diversity enables the improvement of radio communication and enhances the probability of a signal from a transmitter reaching a receiver in a dynamic environment [53] by reducing signal fading and thus increasing the coverage of the communication system, etc.

A diversity antenna was created on the neck of the robot, Figure 3.23, and rotated to fit the neck orientation. Each antenna requires an independent RF circuitry and electronics connection and the ability to communicate with the control station. The S-parameters i.e., S_{11}, S_{12}, S_{21}, and S_{22} of the simulated model were obtained and are shown in Figure 3.24. The S_{11} curve is slightly different from the S_{22} curve. This is due to the robot's wings extending over the front antenna and acting as an extra layer of substrate. S_{11} of -10 dB impedance bandwidths from 2.36 GHz to 2.55 GHz at the lower band and 5.07 GHz to 6 GHz at the higher band respectively were realized. S_{22} of -10 dB impedance bandwidths from 2.27 GHz to 2.50 GHz and 5.11 GHz to 6 GHz at lower and upper bands respectively were realized. S_{12} and S_{21} of less than -10 dB at the resonance frequencies indicate a good antenna isolation between the two antennas. Simulated diversity antenna co-polarization radiation patterns are shown in Figure 3.25(a) at 2.4 GHz and (b) at 5.2 GHz bands for planes xy, xz and yz for the tail and neck antenna.

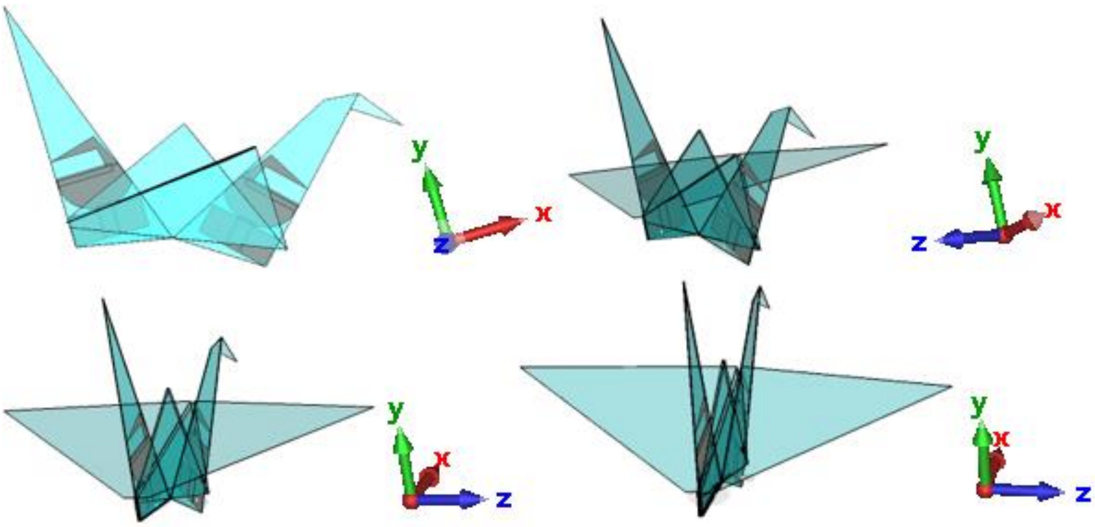

Figure 3.23 Simulated orientations of the robot with embedded neck diversity antennas.

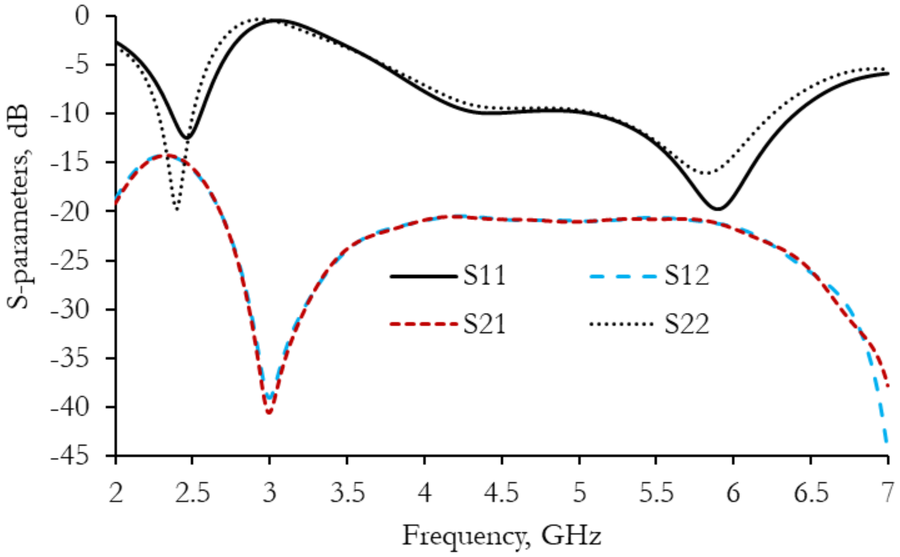

Figure 3.24 Simulated diversity (neck and tail) antennas S-parameters

The radiation pattern indicates nulls about the y-axis for xy and yz planes and an omnidirectional radiation pattern for the xz plane for both the tail and neck antennas at both bands. There is an improvement in coverage in all planes compared to just one antenna on the tail. The radiation patterns of the two antennas are generally in the same direction which could be due to the two antennas being similarly orientated.

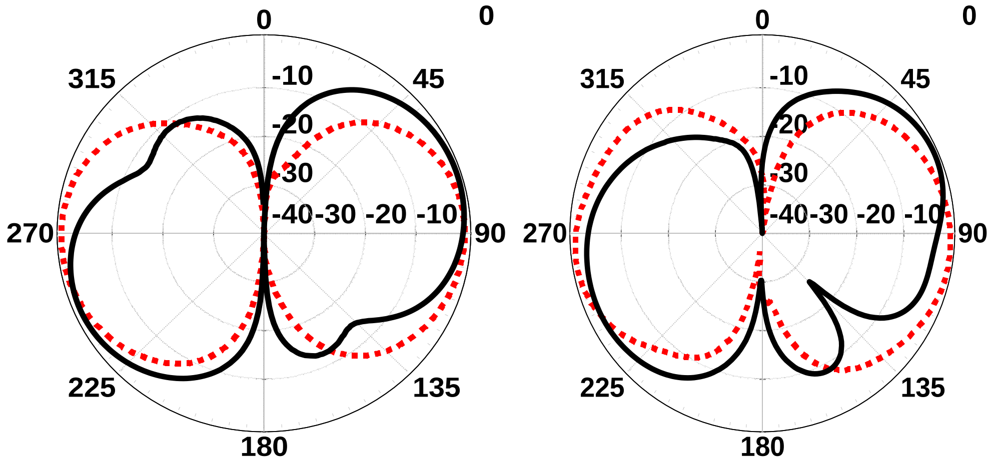

xy plane

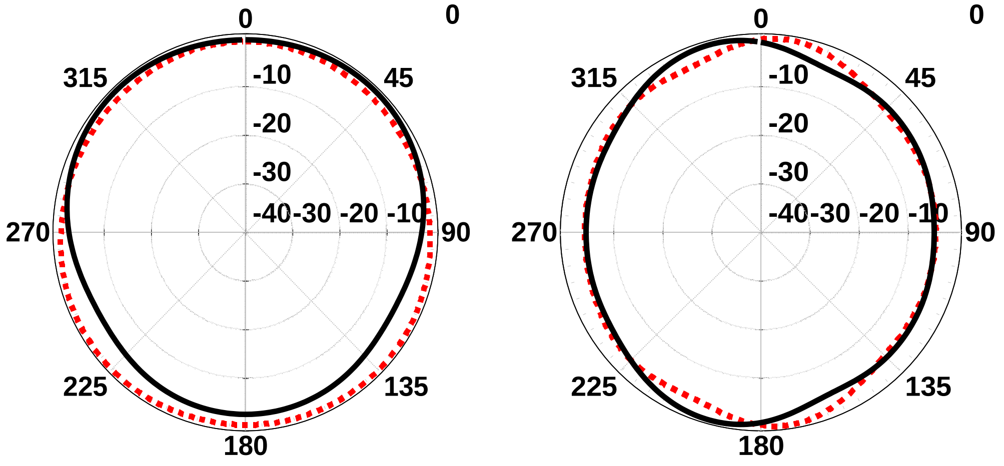

xz plane

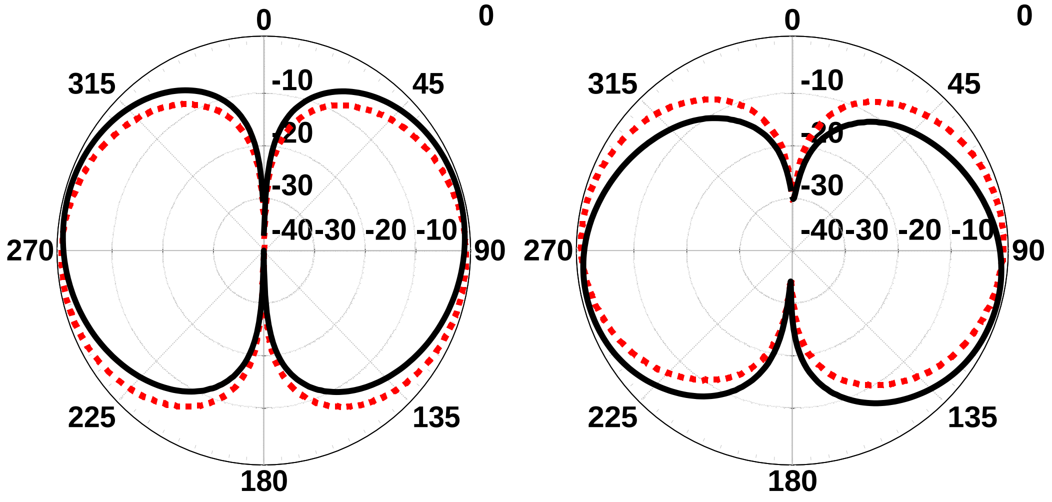

yz plane

(a) (b)

- - - Tail Antenna

— Neck Antenna

Figure 3.25 Simulated diversity antennas radiation pattern for planes xy, xz, and yz at (a) 2.4 GHz and (b) 5.2 GHz

Figure 3.26 shows the surface current distribution for the diversity antennas at both the 2.4 GHz and 5.2 GHz bands. Figure 3.26(a) and Figure 3.26(b) shows the surface current distribution for the neck and tail antennas respectively at 2.4 GHz while Figure 3.23(c) and Figure 3.26(d) shows for the same at 5.2 GHz. As is the case with the spine and tail antennas (Figure 3.5(a) and (b) and Figure 3.18 (a) and (b)), the radiation is primarily caused by the current distribution on the triangular section of the antenna for the 2.4 GHz band for both the neck and tail antennas. It is the same case for the 5.2 GHz band. The radiation is primarily due to the elliptical section of the antenna (Figure 3.5(a) and (b) and Figure 3.18(a) and (b)).

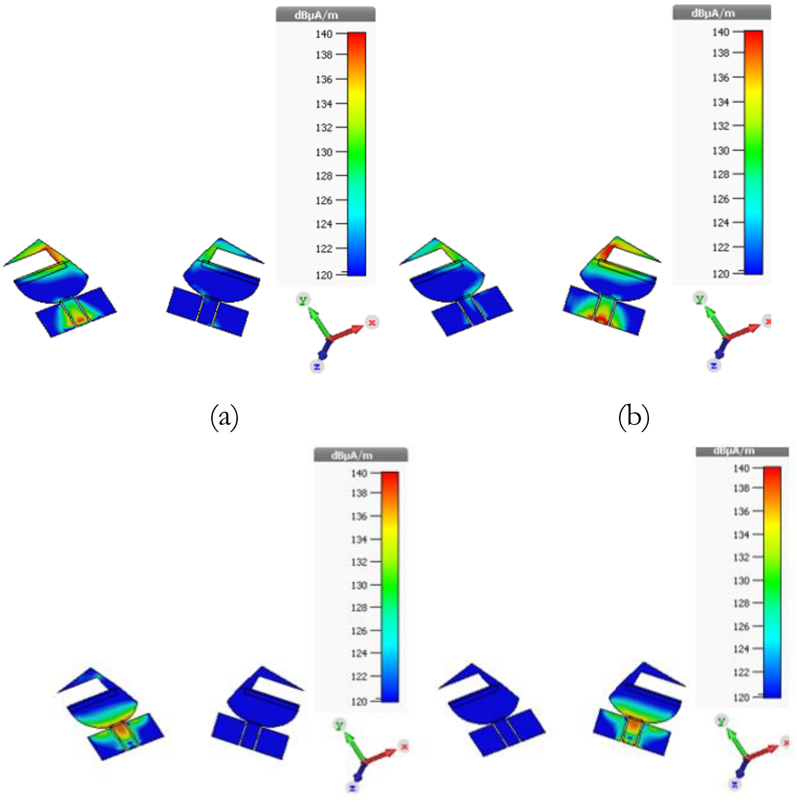

(a) (b)

(c) (d)

Figure 3.26 Surface current distributions at 2.4 GHz for the (a) neck, (b) tail; and at 5.2 GHz for on the (c) neck, and (d) tail antennas

3.5.2 Fabrication and Measurement

The diversity antennas were fabricated as per the procedure described in Subsection 3.3.3. The fabricated diversity antennas on an origami robot are shown in Figure 3.27. SMA connectors end launcher were connected to the two antennas as described in Subsection 3.3.5. As in the spine and tail antennas, the diversity antennas were embedded inside the robot's structure to protect them from environmental damage.

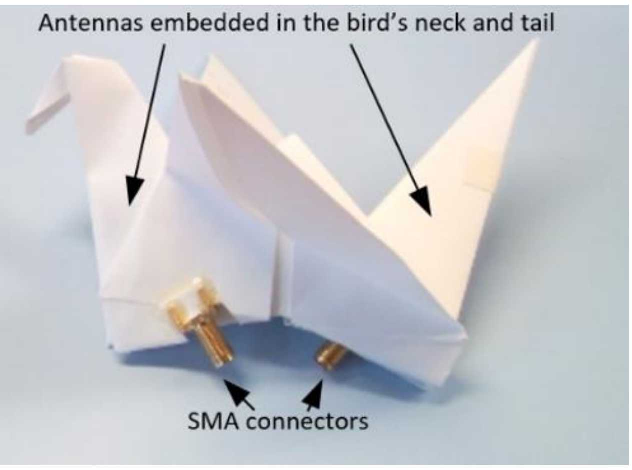

Figure 3.27 Fabricated diversity antennas

After the fabrication of the antennas, a VNA was used to measure the antennas' S-parameters. The measured results are shown in Figure 3.28. An S_{11} -10dB impedance bandwidth from 2.3 GHz to 2.55 GHz at the lower band and 4.5 GHz to 6 GHz at the upper band respectively was achieved for a flap angle α of 90°. An S_{22} -10 dB bandwidth from 2.2 GHz to 2.65 GHz at the lower band and 4.3 GHz to 6 GHz the upper band respectively was also realized. S_{12} and S_{21} of less than -23 dB at both 2.4 GHz and 5.2 GHz bands indicates good isolation between the two antennas.

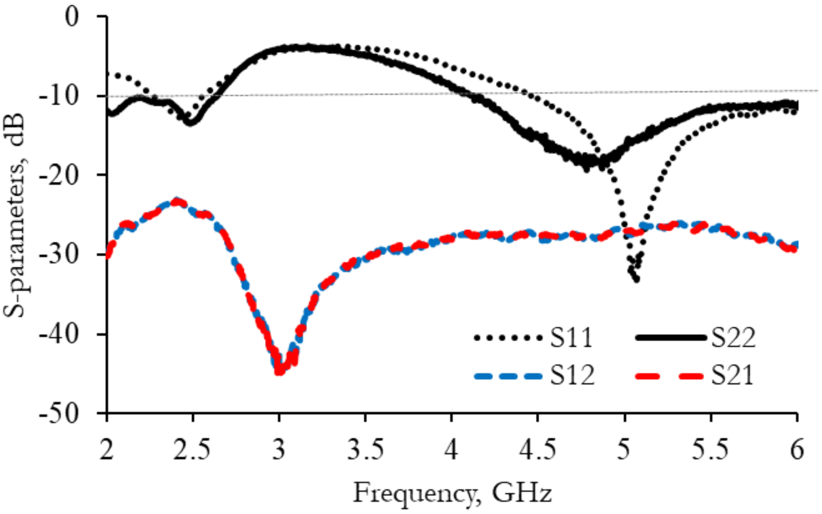

Figure 3.28 Measured diversity antenna S-parameters

The orientation of the axis for the measurement of the radiation pattern of the neck antenna is symmetrical to that of the tail antenna. The two form the diversity antenna system. The radiation pattern of the antennas was measured, and the results are shown in Figure 3.29. It depicts the measured radiation patterns of planes xy, xz and yz respectively at (a) 2.4 GHz and (b) 5.2 GHz for the two antennas.

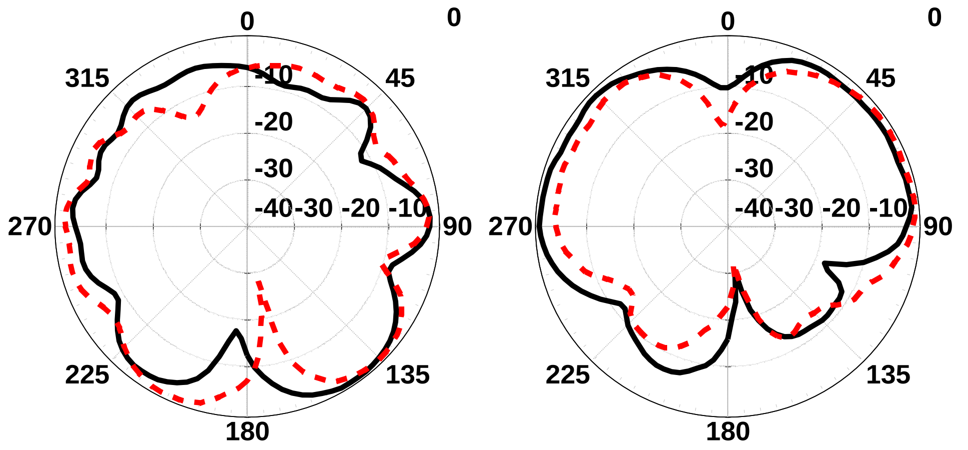

xy plane

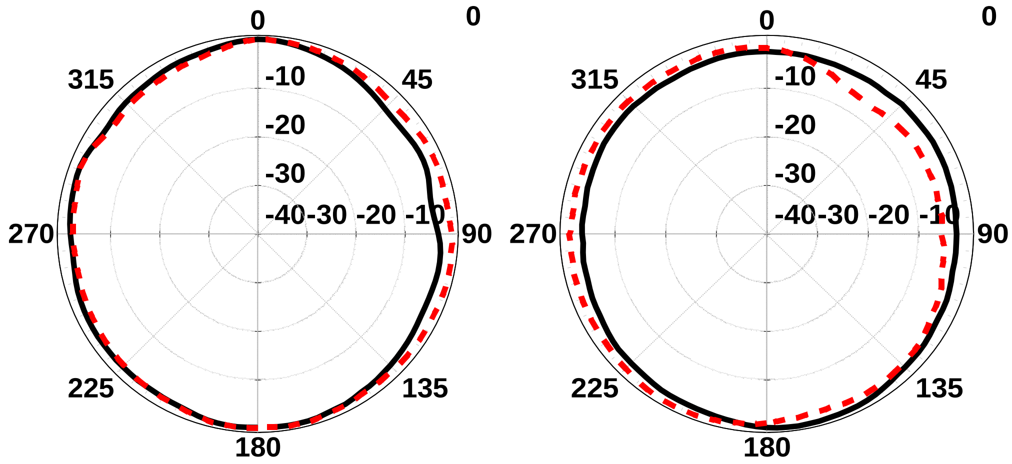

xz plane

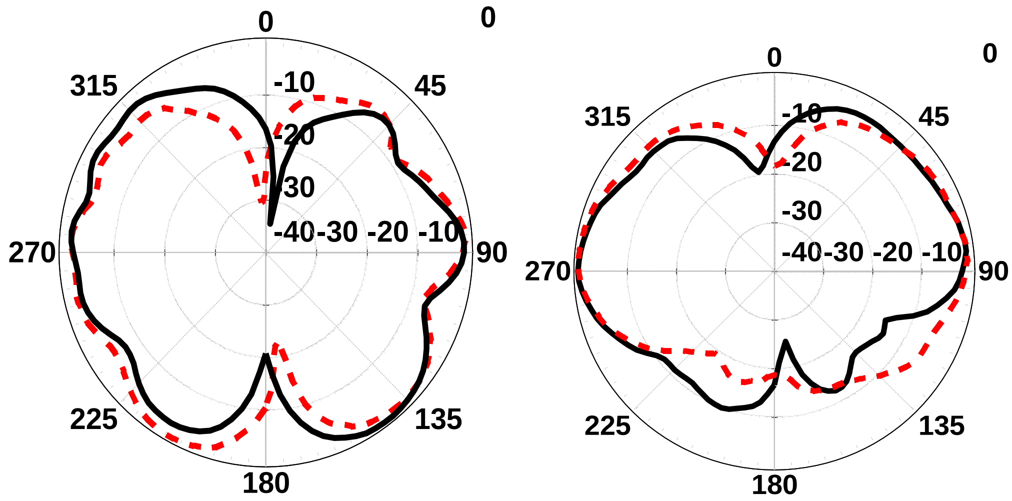

yz plane

(a)

(b)

- - - Tail Antenna

— Neck Antenna

Figure 3.29 Measured diversity antenna radiation patterns for planes xy, xz and yz at (a) 2.4 GHz and (b) 5.2 GHz

It indicates nulls in the xy and yz planes and omnidirection in the xz plane for the two frequency bands which is commensurate with simulation results. As expected, the radiation patterns for the two antennas are similar. Improvement in coverage was observed for the diversity antenna system.

Table 3.3 is a comparison of the dual bands WLAN inkjet printed antennas previously developed with the one proposed in this work. It shows that with comparable gain and bandwidth, the proposed antenna is relatively small and is the only one specifically designed to fit the space available on the origami flapping robot.

Table 3.3 Comparison of the proposed antenna and previous WLAN inkjet printed antennas

Reference	Substrate	Size (mm^3)	Frequency (GHz)	Bandwidth (GHz)	Gain (dBi)
[54]	PET	45×40×0.14	2.45	0.77	1.81
			5.8	2.91	3.92
[25]	NinjaFlex	65×54×1.2	2.4	1.12	-7.2
[55]	Paper	54×57×0.18	2.4	0.9	3.74
			5.8	2.9	4.96
This work	Paper	51×34×0.18	2.4	0.45	1.40
			5.2	1.60	2.7

3.6 The antenna integrated into a disposable origami boat for surface sensing

Keeping with the theme of antenna on an origami structure as well as the proposed antenna design, investigations were done on the application of the antenna as a surface detector/sensor when integrated into an origami boat.

Traditionally, sensors are used for purposes such as safety improvement, environmental monitoring control, and data acquisition applications. Response due to changes in relative permittivity (ε_r) of an antenna dielectric material due to an external influence can and has been harnessed for sensing purposes. Low-cost wireless sensors applications have been employed in detection and monitoring of structural health [56], temperature [57], soil moisture [58], pressure [59], and in health applications [60]. The proposed antenna sensor solution is a proof of concept envisioned for potential remotely controlled robotic origami boat for use in inaccessible environments like disaster zones. It is envisioned to be capable of detecting the surface underneath it, be it water, dry land, wet land etc., either for mission environment survivability or mission purpose or both.

To develop the sensor/detector antenna solution, the origami bird antenna design was altered by adding two arms extending from each of the two ground planes of the monopole antenna. The two extended arms provide the surface detection function. The radiator was also slightly adjusted to optimise it for the new use. The new version of the antenna both wirelessly control the origami boat as well as sense/detect the type of surface it is on. The intended use of the proposed origami boat integrated antenna is surface sensing/detector including watery surfaces. It was thus not inkjet printed on a paper to prevent it from soaking, and thus destroy both the robotic boat and the antenna. It was etched on an impervious Mylar polyester film and then folded into an origami boat such that the antenna fit on its mast. The origami boat is wirelessly controllable through the dual band monopole antenna operating at the unlicensed drone control frequency bands of 2.4 GHz and 5.2 GHz. A lower 1.5 GHz resonance frequency provides the sensing function. The performance of the prototype was tested on various surfaces.

3.6.1 The tri band CPW-fed origami boat antenna design

The proposed antenna design is shown in Figure 3.30 and its dimensions are in Table 3.4. It was simulated on a 261 mm x 185 mm Mylar sheet of 0.16 mm thickness and a dielectric constant, ε_r, of 3. The location of the antenna on the Mylar sheet is presented in Figure 3.31(a) and is such that it fits on the sail of the origami boat into whose structure the sheet was folded, Figure 3.31(b). The antenna consists of a semi-circular section, a triangular section, CPW line, two rectangular ground planes on either side of the CPW and two arms extending from the ground plates. The semi-circular sections provide resonance at the 5.2 GHz band. The triangular section provides resonance at the 2.4 GHz band while the two arms extending from the ground plates provides the lower 1.5 GHz sensing frequency. The initial simulation was done for the model in free space (Figure 3.31(b)).

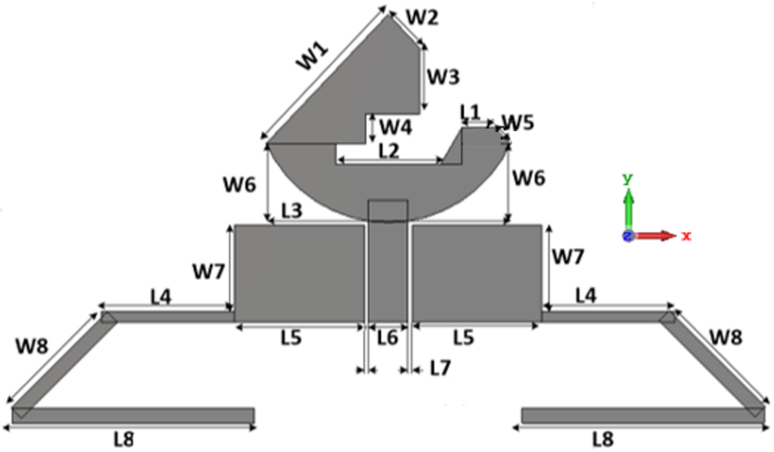

Figure 3.30 The simulated antenna geometry

Table 3.4 The dimensions of the sensor antenna design

Parameter	W_1	W_2	W_3	W_4	W_5	W_6	W_7	W_8	L_1	L_2	L_3	L_4	L_5	L_6	L_7	L_8
Value (mm)	2.4	6.2	8.9	4	3.1	11	13	17.7	4.3	14	33	18	17.5	5.3	0.5	32.5

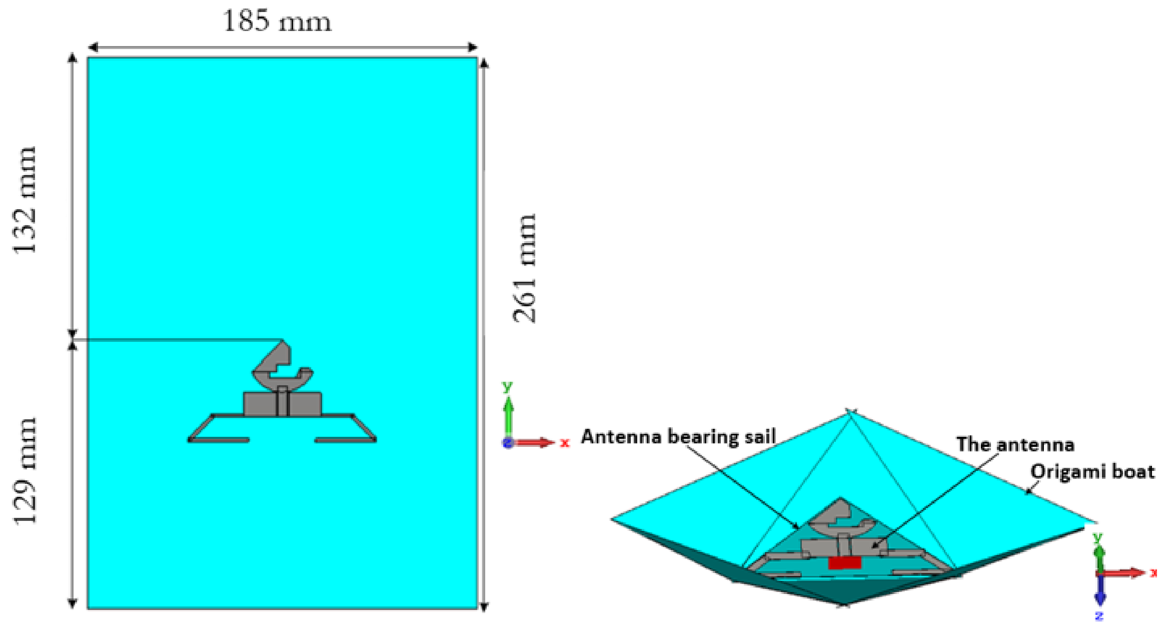

(a) (b)

Figure 3.31 Antenna on (a) Mylar sheet folded into (b) an origami USV

3.6.2 Simulation for Different Environmental Conditions

To investigates the proposed solution behaviour on different surfaces, simulations were done with the origami boat floating on water and on a concrete block. Figure 3.32(a) shows the USV floating in water in a container of depth 100 mm, width 150 mm and length 200 mm, while Figure 3.32(b) shows it on a cuboid concrete block of dimensions 440 mm x 225 mm x 100 mm with a typical ε_r between 2.1 and 2.3 [61].

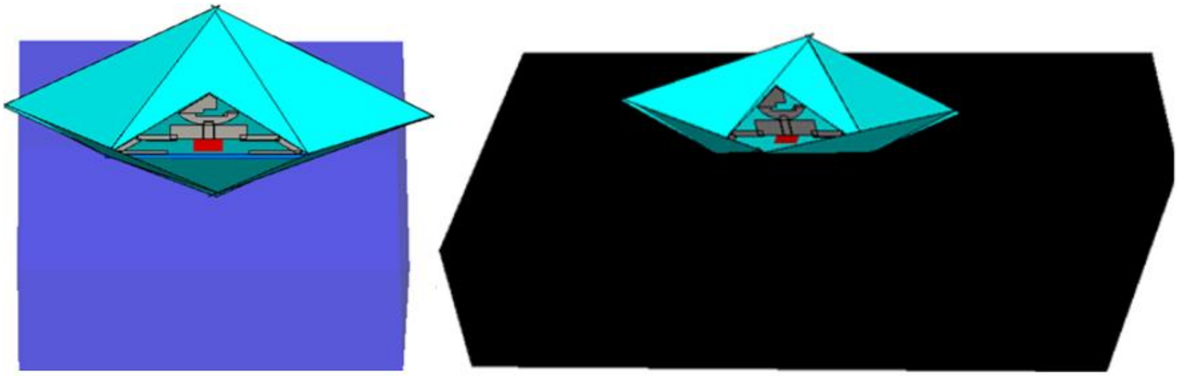

(a) (b)

Figure 3.32 Simulation of the USV on (a) water and (b) a concrete block

Figure 3.33 depicts the reflection coefficient, S_{11} results for the scenarios. The reflection coefficient, S11, results of the simulations were obtained at the 1.5 GHz, 2.4 GHz and 5.2 GHz bands for the free space, on-water, and on-concrete block scenarios. The resonance points of the 1.5 GHz progressively shift to the left with each surface. It is 1.51 GHz in free space, 1.45

GHz on concrete block and 1.25 GHz on water. This frequency shift can be employed to determine the surface the robot is on.

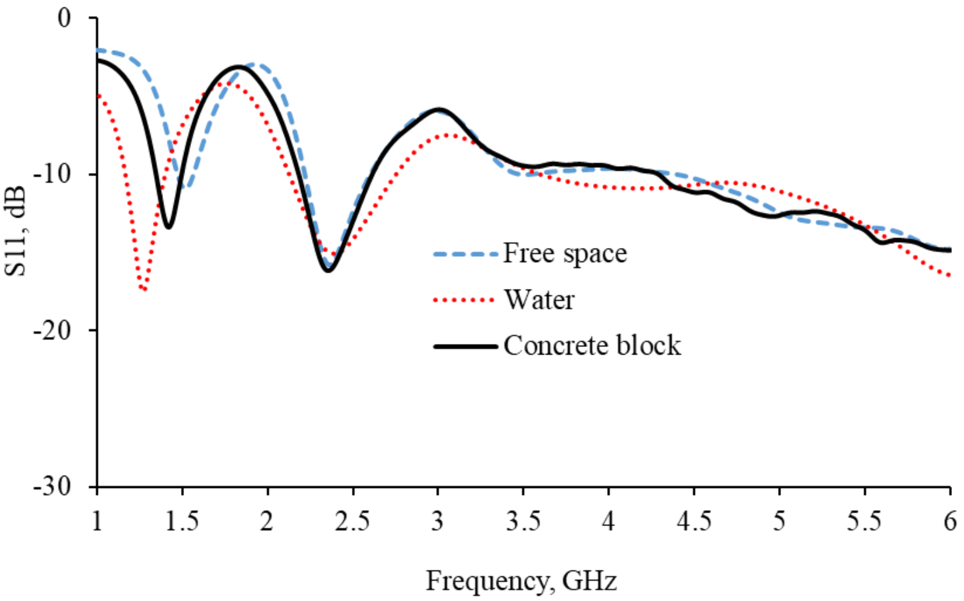

Figure 3.33 Simulated S_{11} results for the boat on different surfaces

The target control frequencies bands for wireless unlicensed drone control of 2.4 GHz and 5.2 GHz bands were realised in the three simulations. Figure 3.34 depicts the surface current distribution of the proposed antenna at the three resonance frequencies. At the 1.5 GHz, Figure 3.34(a), frequency, the current intensity is mostly in arms extending from the ground planes of the antenna structure. At 2.4 GHz, Figure 3.34(b), the surface current intensity is highest and evenly distributed over the feedline, the semi-circular section, and the upper triangular section. At 5.2 GHz, Figure 3.34(c), the surface current is mostly around the semi-circular edges of the radiator.

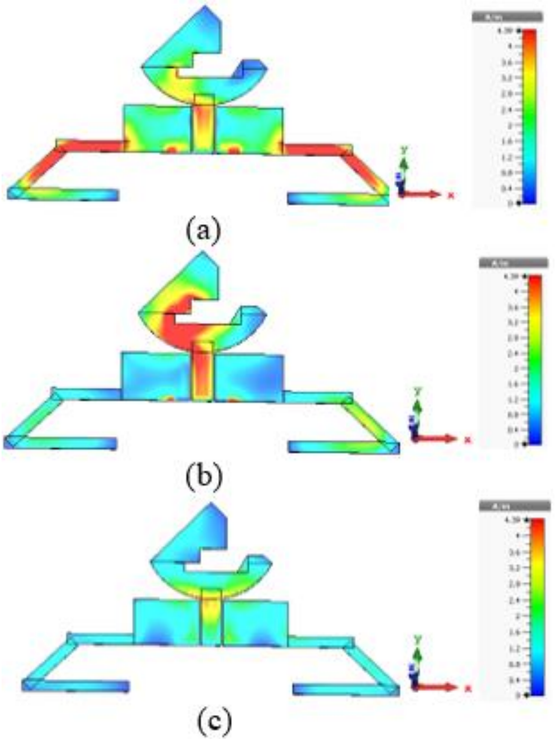

Figure 3.34 Surface current distribution for the proposed antenna design at (a) 1.5 GHz (b) 2.4 GHz and (c) 5.2 GHz

3.6.3 The Antenna Fabrication, Measurements and Results

The USV was etched on a 261 mm x 185 mm x 0.16 mm Mylar polyester film. Figure 3.35(a) shows the etched antenna on the Mylar sheet while Figure 3.35(b) shows the sheet folded into the model origami boat structure. Figure 3.35(c) is the antenna. Reflection coefficient, S_{11}, and radiation patterns measurements were measured to determine the fabricated antenna performance. The S_{11} measurements were conducted on the antenna for the free space, on water and on concrete block situations using Rohde & Schwarz ZVL vector network analyser. The origami boat was floated in a 200 mm x 150 mm x 100 mm water container to measure the S_{11} as shown in Figure 3.36(a). On concrete block S_{11} measurements were conducted on a concrete block of size 440 mm x 210 mm x 95 mm as shown in Figure 3.36(b).

Figure 3.37 shows the S_{11} results for the antenna sensor in free space, on water and on a concrete block. It shows that the 1.5 GHz band resonance frequency shifts follows the same pattern as the simulations. The resonance frequencies are 1.45 GHz for in free space, 1.32 GHz for on concrete block and 1.20 GHz for on water. The sensing functionality triggers when the antenna is energised. The measured S_{11} results indicates that the 2.4 GHz and 5.2 GHz bands drone control frequency bands were achieved in all the three scenarios.

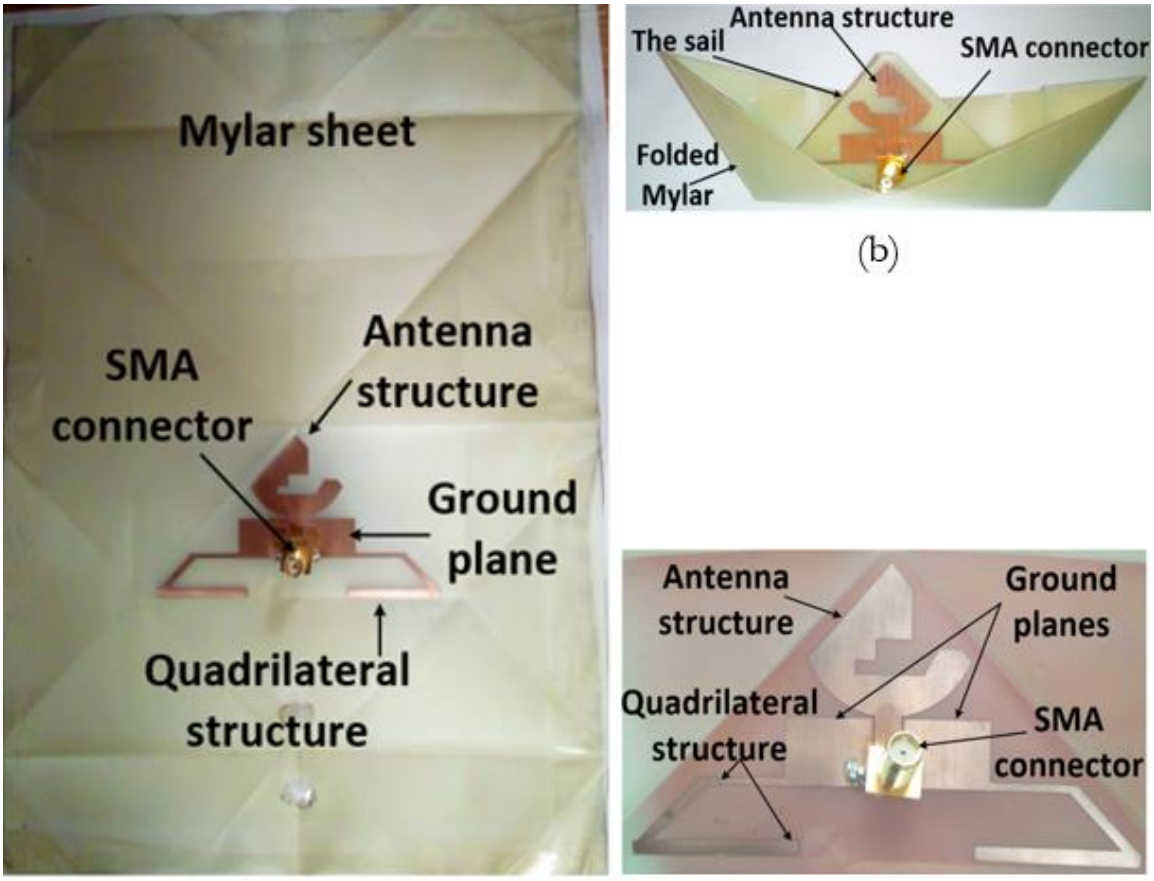

(a) (b) (c)

Figure 3.35 The fabricated (etched) antenna sensor solution the Mylar sheet (a) unfolded (b) folded into an origami boat (c) the antenna

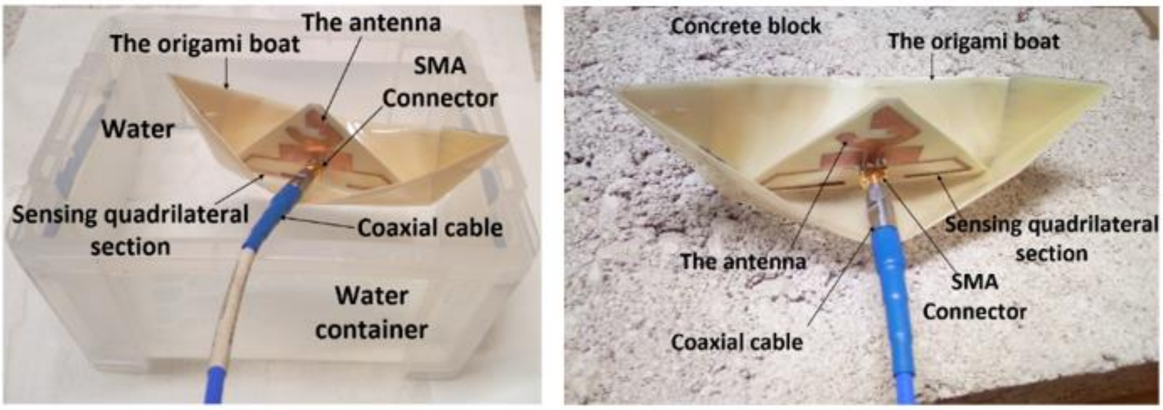

(a) (b)

Figure 3.36 The fabricated antenna sensor solution floating on (a) water (b) concrete block

The measured resonance points are all slightly shifted to the left away from the simulated resonance points. This could be due to the fabrications and measurement inaccuracies.

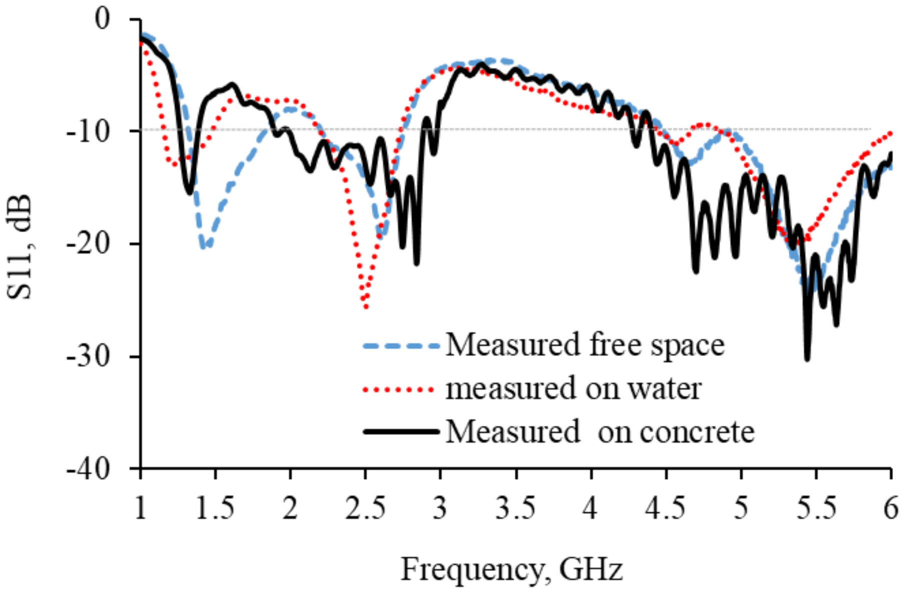

Figure 3.37 Measured S11 results of the boat on different surfaces

The shifting behaviour of the resonance of the sensing frequency band can be explained as due to the influence on the reflection, penetration, transmission, and resonation of the 1.5 GHz signal due to the dielectric properties of the material of the surface [62]. The lower frequency of 1.5 GHz was used for the sensing purpose because it much more likely to go through the surfaces whereas the higher frequencies are much more likely to be absorbed, scattered, or reflected. Complex permittivity of the medium through with which the electromagnetic signal interacts determines the signals behaviour in terms of reflection, transmission, and resonance. Complex permittivity, $\varepsilon_{r,}$ comprises of ε_r' and ε_r'', the dielectric constant and dielectric loss factor respectively. By observing/measuring the reflection and the resonance modes of the electromagnetic signal the dielectric properties of the surface material can be determined to reveal its parameters and thus the type of the surface.

The radiation patterns of the antenna were also measured in the anechoic chamber for the yz, xy and xz planes. Figure 3.38 depicts the comparison between the simulated and measured radiation pattern which indicates a consistency between the two. A null exists in the y-axis of planes yz and xy for both measured and simulated radiation patterns. Radiation pattern in the xz plane exhibits omnidirectionality.

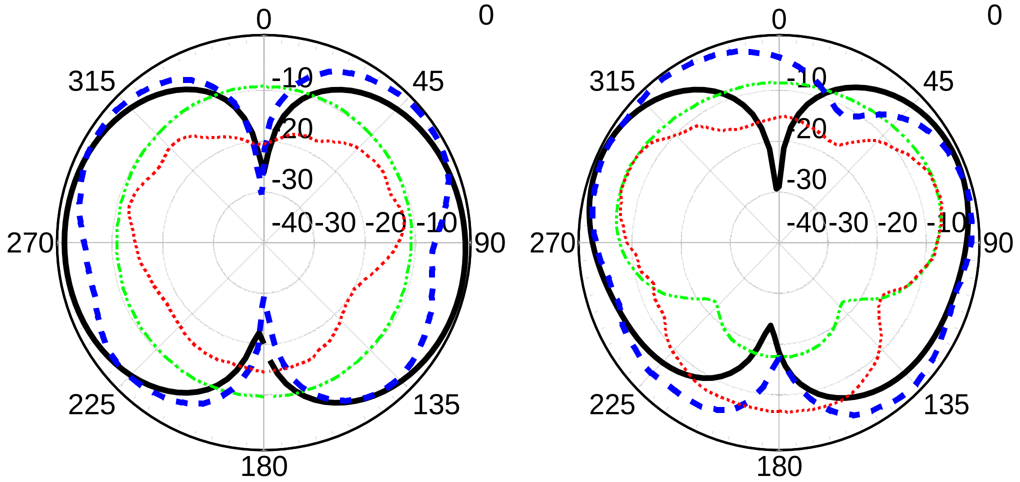

yz planes

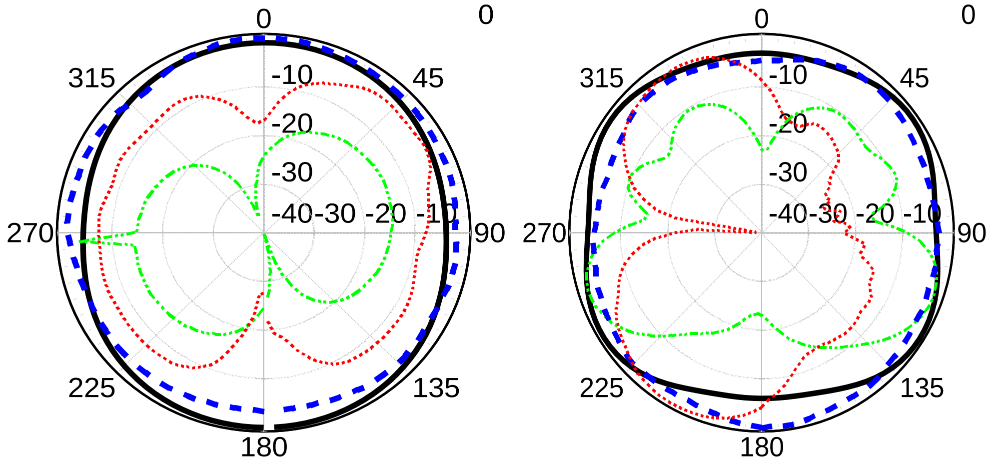

xz planes

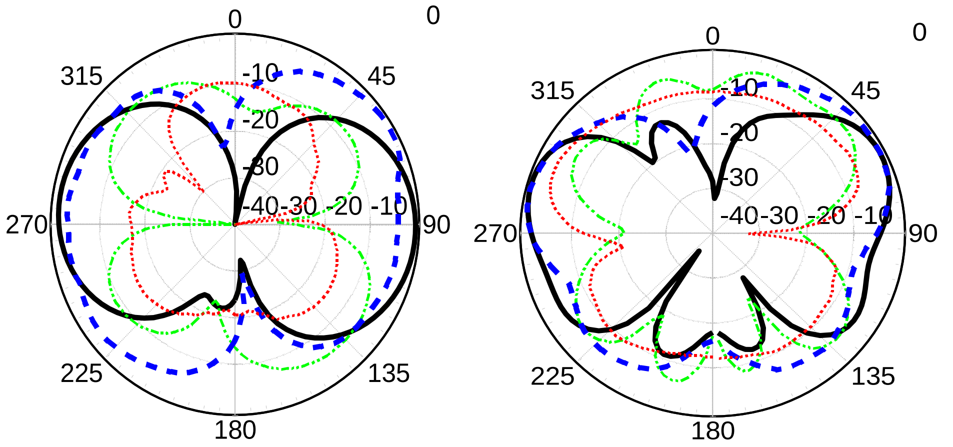

xy planes

(a) (b)

Measured X-polar
Measured Co-polar
Simulated X-polar
Simulated Co-polar

Figure 3.38 Measured and simulated radiation patterns for (a) 2.4 GHz and (b)5.2 GHz bands

3.7 Discussion and Conclusion

The integration of inkjet printed planar monopole antennas on an origami robotic bird has been demonstrated. A wideband monopole antenna consisting of a semi-elliptical shape with a triangular part and a horizontal slot has been developed and tested. The dimensions of the triangular section determine resonance at 2.4 GHz while the dimensions of the semi-elliptical section determine resonance at the 5.2 GHz band, the unlicensed frequency bands for drones' control.

The antenna fits on the available space on the traditional origami structure and operates at the required bands. Two optimal solutions were achieved: one on the spine and the other on tail and/or neck.

A diversity system involving the tail and neck antennas was also realized. This increases coverage in a communication system. All the antennas exhibited nearly omnidirectional radiation pattern in the xz planes at both frequency bands making them suitable for the purpose. The monopole antennas have been fabricated on a standard photo paper substrate. A chemical sintering-based silver nanoparticle conductive ink cartridge was used to print the antennas using an inexpensive and ordinary home inkjet printer and photo paper. This made fabrication of the antenna cheap and fast. The successful outcome promises the potential of integration of antennas with flexible electronic systems using inkjet printing technology.

This holds out prospects of appropriation of instant printing technology for fast integration of antenna to other flexible electronic systems on paper substrate [62] for future wireless controlled aerial robots. This promises potential realization of other electronics components on a paper substrate as well as potential realization of fully integrated expendable robot.

A tri-band monopole antenna with surface detection functionality for origami sensing robotic boat solution has also been demonstrated. The antenna operates at three frequencies bands. The unlicensed 2.4 GHz and 5.2 GHz frequency bands are utilised for the USV remote control while the 1.5 GHz band provides the surface detection function. The fabricated solution has shown satisfactory performance results in three likely sensing scenarios in free space, on water and on a concrete block as a surface sensor. The simulated and measured results demonstrated good agreement.

Acknowledgement

In this work and the resulting output journal paper [1], Peter Njogu did the research, laboratory experimentation, and writing; Peter Njogu and Gabriel Kalman printed the model; Asish Malas and Gregory J. Gibbons of University of Warwick performed the print surface characterisation;

B. Sanz-Izquierdo, S. Y. Jun and S. Gao gave guidance. In the work that resulted in [2], Peter Njogu did the research, experimentation, and writing. P. Jablonski participated in the simulation of the model. The rest gave guidance.

References

[1] P. M. Njogu, B. Sanz-Izquierdo, S. Y. Jun, G. Kalman, S. Gao, A. Malas and G. J. Gibbons, "Evaluation of Planar Inkjet-Printed Antennas on a Low-Cost Origami Flapping Robot," *IEEE Access,* vol. 8, pp. 164103 - 164113, 2020.

[2] P. Njogu, P. Jablonski, A. Shastri and B. Sanz-Izquierdo, "Origami Boat Sensing Antenna," in 2021 15th European Conference on Antennas and Propagation (EuCAP), Dusseldorf, Germany, 2021.

[3] M. Siegel, "Smart Sensors and Small Robots," in *IEEE Instrumentation and Measurement Technology* , Budapest, Hungary, 2001.

[4] J. Huddleston, "The use of small robots for laboratory manipulations," *Journal of Physics E: Scientific ,* vol. 18, no. 11, pp. 891–896, 1985.

[5] V. K. Bandari and O. G. Schmidt, "System-Engineered Miniaturized Robots: From Structure to Intelligence," *Advanced Intelligent Systems,* vol. 3, no. 10, pp. 1-22, 2021.

[6] J. W. Simatupang and M. Yosua, "A Remote Controlled Car Using Wireless," *Journal of Electrical and Electronics Engineering,* vol. 1, no. 2, pp. 56 -61, 2016.

[7] H. Kim, D. Shim and S. Sastry, """Flying robots: modeling, control and decision making," in *Proceedings 2002 IEEE International Conference on Robotics and Automation*, Washington, DC, USA, 2002.

[8] M. Bualat, J. Barlow, T. Fong, C. Provencher and A. Z. T. Smith, "Astrobee: Developing a Free-flying Robot for the International Space Station," in *AIAA SPACE 2015 Conference and Exposition*, Moffett Field, CA, USA, 2015.

[9] H. Shigemune, S. Maeda, Y. Hara, N. Hosoya and S. S. Hashimoto, "Origami Robot: A Self Folding Paper Robot with an Electrothermal Actuator Created by Printing," *IEEE/ASME Transactions on Mechatronics ,* vol. 21, no. 6, pp. 2747-2754, 2016.

[10] E. Hernandez, D. Hart and D. Lagoudas, “Design and simulation of origami structures with smooth folds,” *Proc.R. Soc. A,* vol. 473, no. 2200, pp. 1-27, 2017.

[11] Z. Song, T. Ma, R. Tang, Q. Cheng, X. Wang, D. Krishnaraju, R. Panat, C. K. Chan, H. Yu and H. Jiang, “Origami lithium-ion batteries,” N*ature Communications ,* vol. 5, pp. 1-6, 2014.

[12] S. Miyashita, S. Guitron, M. Ludersdorfer, C. R. Sung and D. Rus, “An untethered miniature origami robot that self-folds, walks, swims, and degrades,” in *2015 IEEE International Conference on Robotics and Automation (ICRA)*, Seattle, WA, USA, 2015.

[13] G. J. Hayes, Y. Liu, J. Genzer, G. Lazzi and M. D. Dickey, “Self-Folding Origami Microstrip Antennas,” *IEEE Transactions on Antennas and Propagation,* vol. 62, no. 10, pp. 5416 - 5419, 2014.

[14] S. I. H. Shah and S. Lim, “Review on recent origami inspired antennas from microwave to terahertz regime,” *Materials and Design,* vol. 198, pp. 1-15, 2021.

[15] Y. A. Nijsure, G. Kaddoum, N. K. Mallat, G. Gagnon and F. Gagnon, “Cognitive Chaotic UWB-MIMO Detect-Avoid Radar for Autonomous UAV Navigation,” *IEEE Transactions on Intelligent Transportation Systems,* vol. 17, no. 11, pp. 3121 - 3131, 2016.

[16] C. Liu, G. Wang, Y. Yan, C. Bao, Y. Sun and D. Fan, “Pint-sized military UAV engine's tele-adjusting arm based on force feedback,” in *2010 2nd International Asia Conference on Informatics in Control, Automation and Robotics (CAR 2010)*, Wuhan, 2010.

[17] P. J. Singh and R. d. Silva, “Design and implementation of an experimental UAV network,” in *2018 International Conference on Information and Communications Technology (ICOIACT)*, Yogyakarta, Indonesia, 2018.

[18] D.-G. Kang and J. Choi, “Compact segmented loop antenna for UAV applications,” in *2017 International Symposium on Antennas and Propagation (ISAP)*, Phuket, Thailand, 2017.

[19] V. Camarchia, A. Chiolerio, M. Cotto, J. Fang, G. Ghione, P. Pandolfi, M. Pirola, R. Quaglia and C. Ramella, “Assessment of silver nanoparticle inkjet-printed microstrip lines for RF and microwave applications,” in *2013 IEEE International Wireless Symposium (IWS)*, Beijing, China, 2013.

[20] M. Singh, H. M. Haverinen, P. Dhagat and G. E. Jabbour, “Inkjet Printing—Process and Its Applications,” *Advanced Materials,* vol. 22, no. 6, pp. 673-685, 2010.

[21] J. Heirons, S. Jun, A. Shastri, B. Sanz-Izquierdo, D. Bird, L. Winchester, L. Evans and A. McClelland, “Inkjet printed GPS antenna on a 3D printed substrate using low-cost machines,” in *2016 Loughborough Antennas & Propagation Conference (LAPC)*, Loughborough, UK, 2016.

[22] S. Jun, B. Sanz-Izquierdo and M. Summerfield, “UWB antenna on 3D printed flexible substrate and foot phantom,” in *2015 Loughborough Antennas & Propagation Conference (LAPC)*, Loughborough, UK, 2015 .

[23] D. Unnikrishnan, D. Kaddour, S. Tedjini, E. Bihar and M. Saadaoui, “CPW-Fed Inkjet Printed UWB Antenna on ABS-PC for Integration in Molded Interconnect Devices Technology,” *IEEE Antennas and Wireless Propagation Letters ,* vol. 14, pp. 1125 - 1128, 2015.

[24] S. F. Jilani and A. Alomainy, “An inkjet-printed MMW frequency-reconfigurable antenna on a flexible PET substrate for 5G wireless systems,” in *Loughborough Antennas & Propagation Conference (LAPC 2017)*, Loughborough, 2018.

[25] M. Rizwan, M. W. A. Khan, L. Sydänheimo, J. Virkki and L. Ukkonen, “Flexible and Stretchable Brush-Painted Wearable Antenna on a Three-Dimensional (3-D) Printed Substrate,” *IEEE Antennas and Wireless Propagation Letters ,* vol. 16, pp. 3108 - 3112, 2017.

[26] W. G. Whittow, A. Chauraya, J. C. Vardaxoglou, Y. Li, R. Torah, K. Yang, S. Beeby and J. Tudor, “Inkjet-Printed Microstrip Patch Antennas Realized on Textile for Wearable Applications,” *IEEE Antennas and Wireless Propagation Letters,* vol. 13, pp. 71 - 74, 2014.

[27] Y. Al-Naiemy, T. A. Elwi, H. R. Khaleel and H. Al-Rizzo, “A Systematic Approach for the Design, Fabrication, and Testing of Microstrip Antennas Using Inkjet Printing Technology,” *ISRN Communications and Networking,* pp. 1-11, 2021.

[28] D. E. Anagnostou, “Organic Paper-Based Antennas,” *” WIT Transactions on State of the Art in Science and Engineering,* vol. 82, 2014.

[29] A. M. Mansour, N. Shehata, B. M. Hamza and M. R. M. Rizk, “Efficient Design of Flexible and Low Cost Paper-Based Inkjet-Printed Antenna,” *International Journal of Antennas and Propagation,* vol. 2015, pp. 1-6, 2015.

[30] G. Shaker, S. Safavi-Naeini, N. Sangary and M. M. Tentzeris, "Inkjet Printing of Ultrawideband (UWB) Antennas on Paper-Based Substrates," *IEEE Antennas and Wireless Propagation Letters ,* vol. 10, pp. 111 - 114, 2011.

[31] B. S. Cook and A. Shamim, "Inkjet Printing of Novel Wideband and High Gain Antennas on Low-Cost Paper Substrate," *IEEE Transactions on Antennas and Propagation,* vol. 60, no. 9, pp. 4148 - 4156, 2012.

[32] H. A. Elmobarak, S. K. A. Rahim, M. Himdi, X. Castel and T. A. Rahman, "Low cost instantly printed silver nano ink flexible dual-band antenna onto paper substrate," in *2017 11th European Conference on Antennas and Propagation (EUCAP)*, Paris, France, 2017.

[33] T. A. Elwi, "Applications, A Miniaturized Folded Antenna Array for MIMO," *Wireless Personal Communications ,* vol. 98, p. 1871–1883, 2018.

[34] R. J. Lang, The Complete Book of Origami, New York: Dover Publications, Inc., 1988.

[35] BBC, "“Origami bird gets BBC reporter in a flap," BBC, 5 3 2019. [Online]. Available: https://www.bbc.co.uk/news/av/technology-37568222. [Accessed 5 3 2019].

[36] A. Bolton, "Japanese electronics maker creates Origami-style drone," 2019 03 05. [Online]. Available: https://www.cnet.com/tech/tech-industry/helping-an-origami-crane-fly-with-a-little-help-from-some-modern-technology/. [Accessed 2019 03 05].

[37] J. Romeu, A. Aguasca, J. Alonso, S. Blanch and R. R. Martins, "Small UAV radiocommunication channel characterization," in *Proceedings of the Fourth European Conference on Antennas and Propagation*, Barcelona, Spain, 2010.

[38] J. Chen, K.-F. Tong and J. Wang, "A triple band arc-shaped slot patch antenna for UAV GPS/Wi-Fi applications," in *2013 Proceedings of the International Symposium on Antennas & Propagation*, Nanjing, China, 2013.

[39] N. Agrawall, G. Kumar and K. Ray, "Wide-band planar monopole antennas," *IEEE Transactions on Antennas and Propagation,* vol. 46, no. 2, pp. 294 - 295, 1998.

[40] G. Kumar and K. P. Ray, Broadband Microstrip Antennas, Norwood, MA: Artech house, 2003.

[41] C.-H. Hsu, "Planar multilateral disc monopole antenna for UWB application," Microwave And Optical Technology Letter*,* vol. 49, no. 5, pp. 1101-1103, 2007.

[42] C. A. Balanis, Antenna Theory Analysis and Design, Hoboken, New Jersey: JOHN WILEY & SONS, INC., 3rd Edition, 2005.

[43] AGICAN01 Silver Nano Ink, “AGICCP01A4 Special Coated Paper, AgIC datasheet,” Tokyo, Japan, 2014.

[44] Z. N. Chen, T. S. P. See and X. Qing, “Small Printed Ultrawideband Antenna With Reduced Ground Plane Effect,” *IEEE Transactions on Antennas and Propagation,* vol. 55, no. 2, pp. 383 - 388, 2007.

[45] M. d. Cos and F. Las-Heras, “Polypropylene-Based Dual-Band CPW-Fed Monopole Antenna [Antenna Applications Corner],” *IEEE Antennas and Propagation Magazine,* vol. 55, no. 3, pp. 264 - 273, 2013.

[46] Y. Kawahara, S. Hodges, C. Zhang and G. D. Abowd, “Instant inkjet circuits: lab-based inkjet printing to support rapid prototyping of UbiComp devices,” in *UbiComp’13*, Zurich, Switzerland, 2013.

[47] G. Cummins and M. P. Desmulliez, "Inkjet printing of conductive materials: a review," Circuit World, vol. 38, no. 4, p. 193–213, 2012.

[48] I. J. Fernandes, A. F.Aroche, A. Schuck, P. Lamberty, C. R. Peter, W. Hasenkamp and T. L. C. Rocha, "Silver nanoparticle conductive inks: synthesis, characterization, and fabrication of inkjet-printed fexible electrodes," Scientific Reports, vol. 10, pp. 1-11, 2020.

[49] RS Components, “RS Pro Straight Panel Mount Bulkhead Fitting SMA End Launcher Connector, jack, Solder Termination” 526-5779 datasheet [online] https://docs.rs-online.com/3623/0900766b81585daf.pdf

[50] RS Components,” RS PRO Silver Conductive Adhesive Epoxy, 10g Vial” RS Stock No.: 186-3616 datasheet [online] https://docs.rs-online.com/5bcb/A700000008879607.pdf

[51] Z. N. Chen, M. J. Ammann, X. Qing, X. H. Wu, T. S. See and A. Cai, “Planar antennas,” *IEEE Microwave Magazine,* vol. 7, no. 6, pp. 63 - 73, 2006.

[52] K. S. Ryu and A. A. Kishk, “UWB Dielectric Resonator Antenna Having Consistent Omnidirectional Pattern and Low Cross-Polarization Characteristics,” *IEEE Transactions on Antennas and Propagation,* vol. 59, no. 4, pp. 1403 - 1408, 2011.

[53] S. Johnsrud and S. Hellan, “Application Report: Antenna Diversity,” Texas Instruments Incorporated, Texas, 2014.

[54] M. M. Bait-Suwailam and A. Alomainy, “Flexible Analytical Curve-Based Dual-Band Antenna for Wireless Body Area Networks,” *Progress In Electromagnetics Research M,* vol. 84, pp. 73-84, 2019.

[55] S. Jun, J. Heirons and B. Sanz-Izquierdo, “Inkjet printed dual band antenna for paper UAVs,” in *2017 11th European Conference on Antennas and Propagation (EUCAP)*, Paris, France, 2017.

[56] R. Matsuzaki and M. a. A. T. Melnykowycz, "Antenna/sensor multifunctional composites for the wireless detection of damage," Composites Science and Technology, vol. 69, p. 2507–2513, 2009.

[57] J. W. Sanders, J. Yao and H. Huang, "Microstrip Patch Antenna Temperature Sensor," IEEE Sensors Journal, vol. 15, no. 9, pp. 5312-5319, 2015.

[58] P. Soontornpipit, C. M. Furse, Y. C. Chung and B. M. Lin, "Optimization of a Buried Microstrip Antenna for Simultaneous Communication and Sensing of Soil Moisture," IEEE Transactions on Antennas And Propagation, vol. 54, no. 3, pp. 797-800, 2006.

[59] H. Cheng, G. Shao, S. Ebadi, X. Ren, Kyle Harris, J. Liu, C. Xu, L. An, and X. Gong, "Evanescent-mode-resonator-based and antenna integrated wireless passive pressure sensors for harsh-environment applications," Sensors and Actuators A: Physical, vol. 220, p. 22–33, 2014

[60] A. Alomainy, Y. Hao and F. Pasveer, "Numerical and Experimental Evaluation of a Compact Sensor Antenna for Healthcare Devices," IEEE Transactions on Biomedical Circuits and Systems, vol. 1, no. 4, pp. 242-249, 2007

[61] "microwaves101," 9 9 2019. [Online]. Available: https://www.microwaves101.com/encyclopedias/miscellaneous-dielectric-constants. [Accessed 9 9 2019].

[62] Z. Meng, Z. Wu and J. Gray, "Microwave sensor technologies for food evaluation and analysis: Methods, challenges and solutions," Transactions of the Institute of Measurement and Control, vol. 40, no. 12 , p. 3433–3448, 2018.

[63] G. Grau, E. J. Frazier and V. Subramanian, "Printed unmanned aerial vehicles using paper-based electroactive polymer actuators and organic ion gel transistors," *Microsystems & Nanoengineering*, vol. 2, pp. 1-8, 2016.

CHAPTER 4: 3D PRINTED NAIL ANTENNAS FOR 5G APPLICATIONS

4.1 Overview

This chapter details the development of a 3D printed patch antennas on Acrylonitrile butadiene styrene (ABS) material removable fingernail for on-body communications. Manual brush painting that mimics nail polish application as in manicure procedures, and Aerosol Jet printing AM techniques were employed in the development of the proposed designs. Silver nanoparticle conductive ink was used to create the radiators. Manual brush painting of the antenna radiator [1] is inexpensive, requires no expensive equipment and is environmentally friendly as no energy is required . The work was extended in [2] where Aerosol Jet technology, a material deposition technique, was employed to counter the challenge of silver ink spreading encountered during the fabrication of the manually painted antenna. This is discussed in Subsection 4.3.3. Optomec machine was used to print the Aerosol jet printed microwave and millimeter wave antennas. A copper layer was further overlaid on the millimeter wave antenna via an electroplating process. The simulated and the measured reflection coefficients (S_{11}) and radiation patterns performance parameters were in good agreement. The proposed on-body antennas can find applications in the Internet of Things (IoT) ecosystem where large amount of sensing data can be shared at the microwave and millimeter wave spectrum of future 5G communications. The removable fingernails could be on electronic devices such as on-body sensors, computational, storage and communication systems. The rest of the chapter is organized as follows. Section 4.2 is the introduction, section 4.3 describes the design and fabrication of the manually hand painted antenna, 4.4 describes the Aerosol jet printed design and fabrication microwave nail antenna and section 4.5 the millimeter wave antenna. Section 4.6 is the discussion and conclusion.

4.2 Introduction

Internet of Things (IoT) brings together sensing, computation, data collection and communication functions into one information platform. This allows electronics devices of different capabilities to participate in data exchange [3]. This data exchange from multiple sources and destinations creates an increasing need for large storage, exchange, and exploitation of information for control/sensing. This in turn calls for the support of ubiquitous connectivity of large data volume by the next generation of wireless communication to cater for the progressively increasing demand for high data rates and mobility [4]. An ever-increasing demand also exists for higher capacity, increased connectivity and reliability, higher versatility as well as application specific topologies [5]. 5G technology aims to provide reliable and robust global connectivity for communication between entities that can communicate creating massive Internet of Things (IoT) [6]. Its frequency spectrum is expected to span the microwave and millimeter wave frequencies spectrums [7]. Massive IoT are envisioned to enable smart devices to independently and mutually interact and share data [8]. This network ecosystem may include Body Area Network (BAN). Advances in microelectronics miniaturization alongside new communciation technologies has facilitated wireless BANs, igniting interest in human body mountable antenna for wearable applications such as in sports, military, health etc., [9] [10].

On-body antennas can be mounted on or integrated on wearables for communication of uninterruptedly monitored parameters e.g. body temperature, heartbeat etc or the wearer's location to other devices. They are generally light, flexible with small surface coverage to ensure an unobstrusive integration with body environment [11]. Various on-body antennas suitable for 5G technologies have been developed. Textiles have been used as a substrate [12] [13] in some of these developments. In [14], button antenna is proposed at millimeter wave inspired by an earlier work at microwaves in [15]. Smart watches [16], armbands [17] and glasses [18] [19] are other types of wearable's antennas that has been developed. Antennas have also been attached directly to the skin [20] and on bandage [21].

As outlined in chapter 2, additive manufacturing (AM) or 3D printing is a cluster of emerging technologies that enables creation of objects bottom-up through layer by layer addition of materials. AM processes use computer-aided design (CAD) virtual 3D models that are then translated into physical objects. 3D printing fabrication processes reduce waste, tooling and material costs; leads to fast production and enables realization of complex designs unfeasible with conventional fabrication processes [22] [23]. AM have been employed for development of antennas for various applications including antennas for 5G systems. AM has also been used to print metallic structures [24], dielectric layers [25] or both layers [26] of an antenna. Dielectric lenses [27] and dielectric resonator antennas [28] are example of dielectric only printed antennas. Full 3D printing with metals has been realized using techniques such as Selective laser melting (SLM) [29] and metal binder jetting [30]. It has also been used for the development of complex microwave antennas [31] and millimeter wave and Terahertz (THz) antennas [32] [33]. However, these techniques lack the design flexibility that other direct write (DW) techniques like inkjet and aerosol jet offer. Inkjet printing technique precisely deposits digitally controlled ink drops onto substrate surface as in [34] while Aerosol jetting aerodynamically focusing atomized nanoparticle inks droplets as collimated beam to print high precision designs as in [35].

The advantages inherent in AM manufacturing processes have been harnessed in the development of wearable antennas operating at UHF and microwave band [36], [37]. These include dipole antennas on 3D printed wrist bands using a variety of techniques for depositing the metallic layers [38], a wearable RFID application manufactured using 3D direct-write dispensing on a fabric [39] and antennas printed on textiles [40], 3D printed flexible substrates for wearable tile array antenna [41] and a brush painted stretchable silver conductive paste patch antenna [42]. More recently, a 5G millimeter wave antenna has been embedded into a medallion using a 3D printing technique which combines fused deposition modelling (FDM) for the substrate and syringe dispensing for the metallic layers [43].

In this chapter, design, and fabrication of 3D printed antennas on a removable fingernail for on-body communications are proposed. Antennas for on body communication have already been developed at both microwave and millimeter waves on various wearables or as part of wearables [11]-[21]. From the literature space, there does not seem to exist an antenna printed on a fingernail and more so for 5G frequency bands [44] for good bandwidth. Thus, an AM fabricated on-fingernail applications are proposed. Removable fingernail provides conformality to the body, lightweight, unobstructedness, low profile, and robustness, features that are desirable to wearable antennas. Further, a fake fingernail is a beauty accessory. An antenna printed on it in a similar manner as used in manicure procedures can seamlessly blend in as part of the aesthetic design enhancement. AM methods were used to realize simple patch on one. Such antenna can be used in on-body sensing and communications through potential future manicure-based electronics as illustrated in Figure 4.1.

Figure 4.1 Illustrative on-fingernail antenna communication environment

The initial procedure in the development of the antenna is akin to most common manicure procedures. By using manicure methods, an antenna can be inexpensively seamlessly fabricated. As an initial proof of concept, a coaxial-fed antenna was designed to operate at 10 GHz. Nanoparticle silver ink was manually hand painted on the removable fingernail with a brush. Spreading of silver ink as it was manually applied posed a challenge during the fabrication process necessitating exploration of an alternative way to apply the silver ink. Thus, Aerosol Jet Technology was employed to produce small features antennas operating at 15 GHz and 28 GHz as well as counter the ink spreading challenge. The 15 GHz band antenna was tested directly after the Aerosol printing and curing while an additional copper plating process was applied to the 28 GHz band antenna. The antennas' removability offers the prospects of portability of the electronic equipment it serves from one individual to another or the antenna from one device to another facilitating reusability.

4.3 The Manually Painted Microwave Nail Antenna

This section describes the processes employed for the manually painted antennas.

4.3.1 The antenna design

A patch antenna was designed and simulated using CST Microwave Studio™ and is shown in Figure 4.2(a). The silver ink that was used to make the radiator has a resistivity of 0.001Ω-cm according to the manufacturer's datasheet [45]. Thus, the conductivity of the ink was computed to be 10^5 S/m and used in the simulations. For simulation purposes, the conductor thickness was set at 0.035 mm. The antenna dimensions, Table 4.1, were optimized so that the antenna resonates at around 10 GHz. The thickness of the substrate used was 1 mm with a relative permittivity (ε_r) of 2.7 and tan δ of 0.009 [45]. The conductive material used for the patch was nanoparticle silver paint while the ground plane was made of copper. The antenna was fed via a coaxial probe. The designed antenna was curved along its length into a smooth 46° arc to mimic the curvature of the fake nail as shown in Figure 4.2(b) and Figure 4.2(c). Reflection coefficient (S_{11}), radiation pattern and the surface current distribution performance parameters were used to determine the antenna functional effectiveness. Reflection coefficient, S_{11}, obtained for the antenna before and after it was curve are shown in Figure 4.3. The curved antenna S_{11} results indicate a slight-shift to the left of those of the flat antenna. The -10 dB impedance bandwidth covers the targeted 10 GHz to 10.125 GHz in both cases, about 9.9 GHz to 10.25 GHz for the flat and 9.9 GHz to10.2 GHz for the curved antenna. Figure 4.4 is the surface current distribution indicating a symmetrical pattern of surface current.

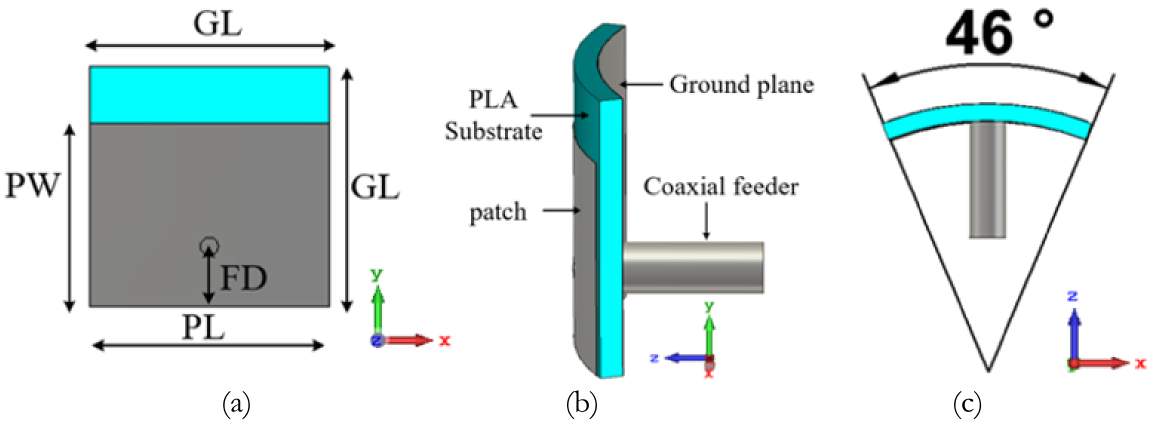

(a) (b) (c)

Figure 4.2 The (a) designed patch (b) after curving, and (c) curvature angle

Table 4.1 The patch antenna dimensions

Length PL	Width PW	Ground Length GL	Feeder distance FD	Substrate Thickness
12 mm	9 mm	12 mm	3 mm	1 mm

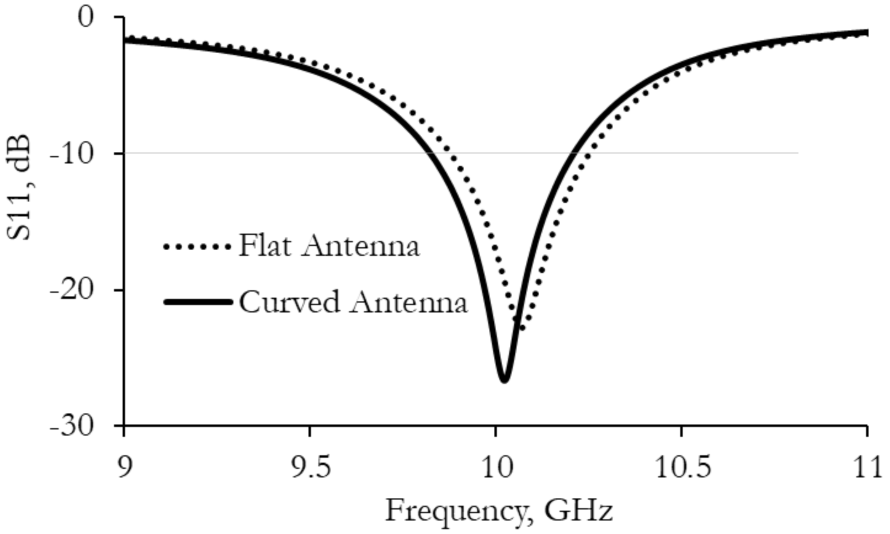

Figure 4.3 Simulated unbent and bent antenna S_{11}

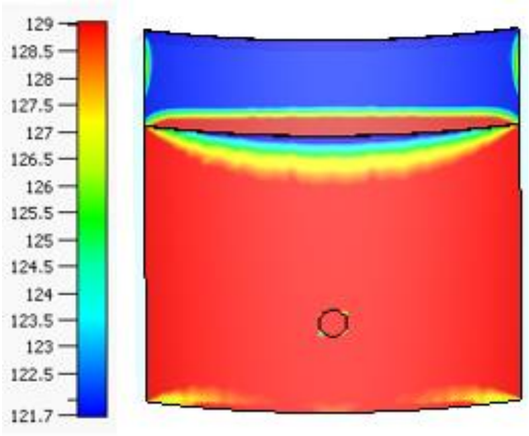

Figure 4.4 Surface current distribution on the patch radiator

4.3.2 Fabrication, Measurements and Results

The silver ink brush painted antenna was then fabricated. To fabricate the patch, a masking tape was used to delineate the space on the removable fingernail, the substrate, where the patch was painted using a brush as shown in Figure 4.5(a). RS 186-3600 silver conductive paint [46] from RS components Ltd was hand painted onto the substrate to create the patch on the fingernail. The antenna was coaxial cable fed. The inner conductor was inserted through the nail to connect to the patch while its outer conductor was connected to the ground plane.

Figure 4.5(b) shows the fabricated patch antenna while Figure 4.5(c) shows its ground plane. Figure 4.5(d) depicts the placement of antenna on the finger. The structure was left to cure in room temperature. According to the manufacturer, the ink has a cure time of 30 minutes.

Though great care was taken to ensure a clear outline of the patch due to the spreading of the silver ink, some managed to spread underneath the edges of the masking tape that was used delineate the space on which the antenna printed. The patch edges thus had to be trimmed with a sharp-edged scalpel to ensure correct dimensions and thus resonance frequency.

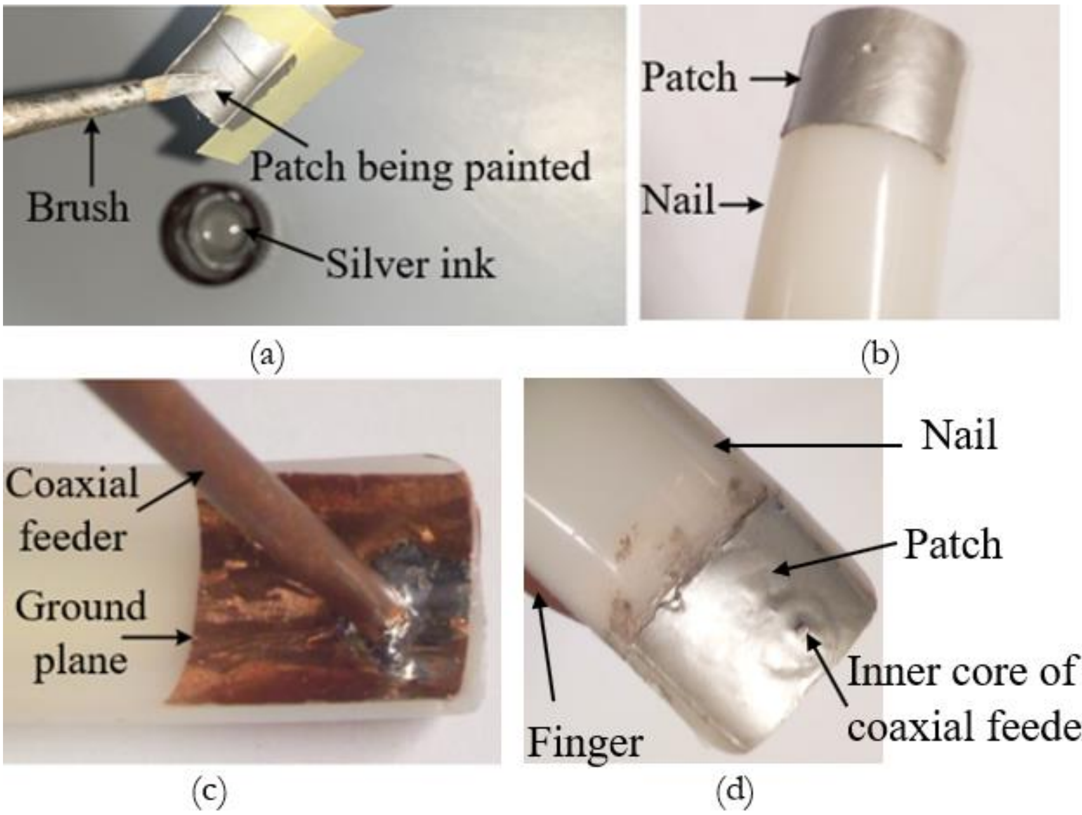

Figure 4.5 The silver patch (a) fabrication process (b) the fabricated patch (c) its ground plane (d) antenna worn on the finger

A multi-meter was used to test the electrical continuity across the painted surface. Using a Rohde & Schwarz ZVL vector network analyser, S_{11} tests of the fabricated model were conducted. Figure 4.6 shows both the simulated and measured S_{11} results of the prototype. The measured and simulated antenna have almost similar reflection coefficient indicating that the fabricated brush painted silver ink antenna is viable. The measured S_{11} is slightly shifted to the right of the simulated S_{11}. This could be due to inaccuracies caused by the manual application of the conductive radiator. The measured -10 dB impedance bandwidth of the proposed antenna is 400 MHz (from 9.9 GHz to 10.3 GHz). This is wider than the target bandwidth (10 GHz to10.125 GHz) and thus better than the simulated results. The measured and simulated antenna S_{11} results are consistent indicating that the fabricated brush painted silver ink antenna works well. Figure 4.7 shows the xy, xz and yz planes of the measured and simulated radiation pattern of the antenna which shows a good agreement for all planes. They all show hemispherical directivity with the expected tilt in the yz plane.

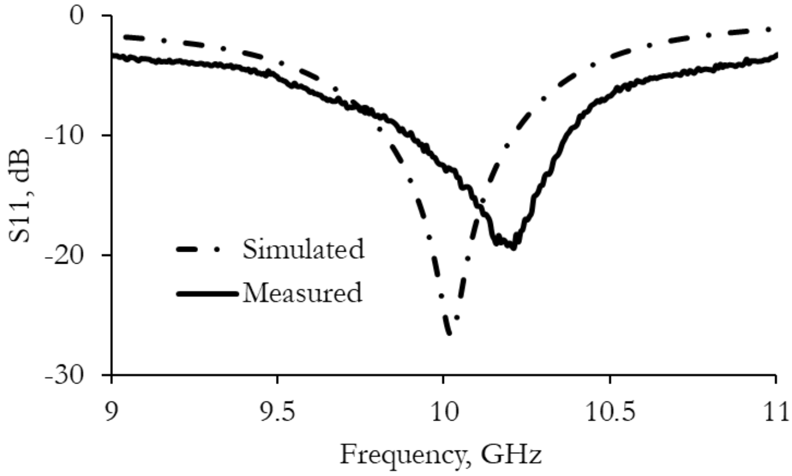

Figure 4.6 Measured and simulated antenna reflection coefficient (S_{11}) of the silver ink antenna

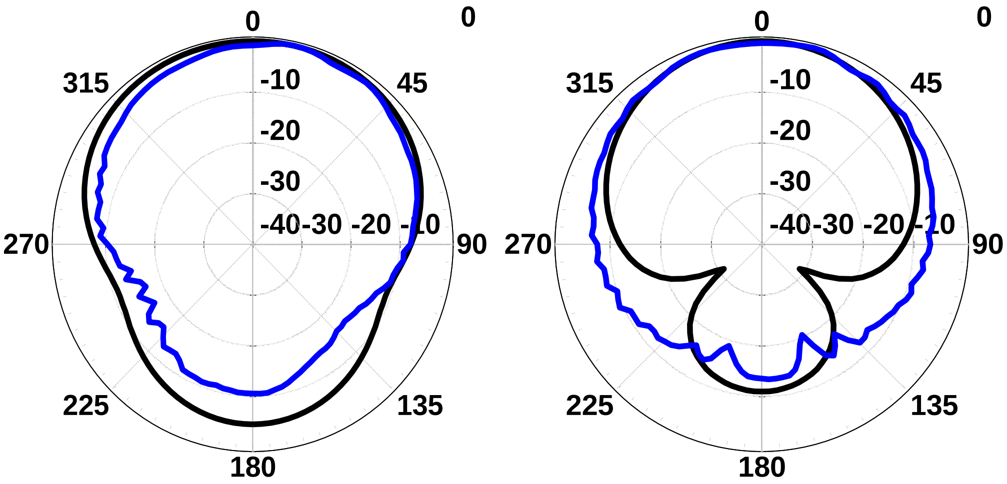

xy plane

xz plane

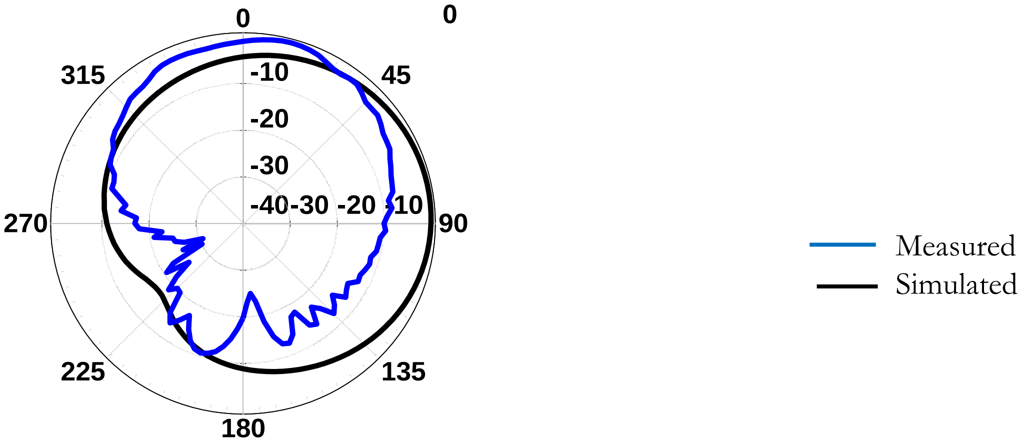

yz plane

Figure 4.7 Measured and CST simulated radiation pattern of the patch antenna.

A second copper prototype was developed. In keeping with the additive manufacturing (AM) theme, the copper prototype was fabricated using an adhesive copper tape for both the patch and the ground plane. An adhesive copper tape piece was cut according to the dimensions of the patch given in Table 4.1 and then fixed onto the fake fingernail which also serves as the substrate. The copper patch antenna, like the silver-paste-made one was coaxial cable fed as shown Figure 4.8. Figure 4.8(a) shows the patch while Figure 4.8(b) shows the ground plane and the coaxial cable feeder. The copper tape patch could be soldered to the inner conductor of the coaxial feeder. S_{11}, performance of the copper made antenna was compared with that of the silver paste brush painted antenna. The results are shown in Figure 4.9 and are comparable.

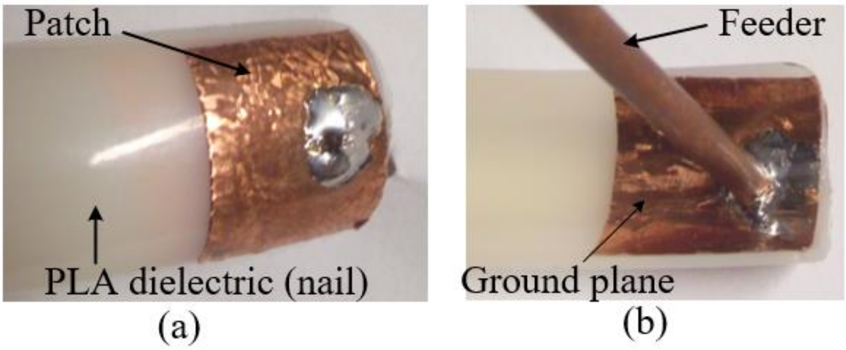

Figure 4.8 (a) The copper nail antenna (b) its ground plane and coaxial feeder

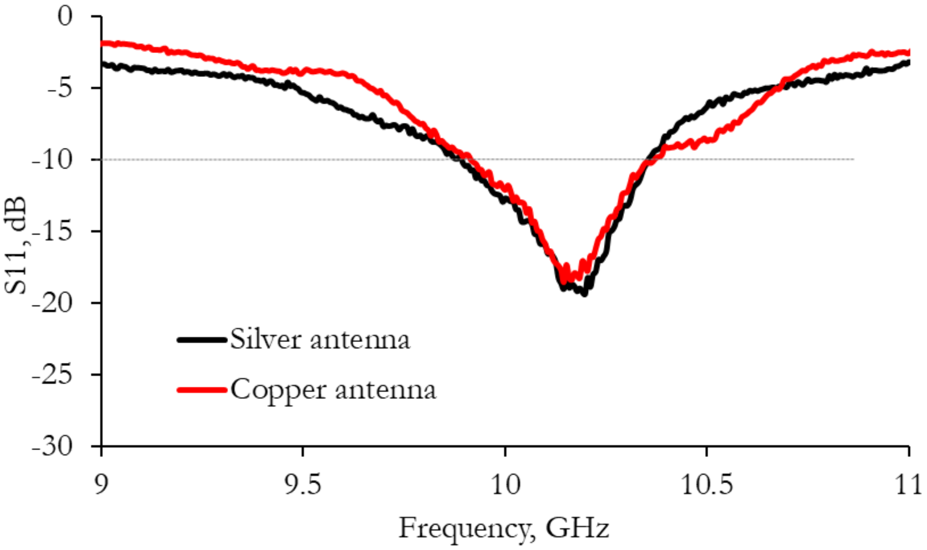

Figure 4.9 The silver and copper patch antennas reflection coefficient (S_{11})

4.3.3 The challenges of the spreading ink and the alternative solution

The silver-paste-hand-painted coaxial-fed antenna was found to be viable. However, the coaxial feeding was found to be a problem because it was at the front of the fingernail which made its wearability cumbersome. The patch-feeder contact point is also a potential weak point as it could become loose with movement depriving the silver painted antenna robustness. This could be resolved by using glue to hold the feeder firmly in place. However, the weight of the coaxial piece could still pose a problem in as far as ensuring robustness of the patch/feeder joint is concerned. An alternative feeding method was thus required. Coplanar waveguide (CPW) feeding of the antenna is a better alternative solution. However, hand painting with a brush of the usually thin CPW is difficult. This is because the viscous silver paste/ink spreads, when applied on a surface. This spreading makes the painting of the usually thin CPW feedline which requires precise breadth difficult. The problem of spreading of the silver ink can be seen in Figure 4.5(d) where, because of the spreading, the patch had to be trimmed, causing untidiness. To deal with this challenge, Aerosol Jet printing, discussed in detail in Subsection 4.4.2, was employed as an alternative in the development of the fingernail antenna. Its fine features, material deposition characteristics means that the patch radiator and its CPW feedline could be printed to their specification. Development of antenna on fingernail using Aerosol jet technique was therefore investigated and is described in Section 4.4 and Section 4.5.

4.4 3D Aerosol Jet Printed Microwave Nail Antenna

This section describes the design, simulation, and fabrication of the microwave antenna.

4.4.1 Antenna Design

A 15 GHz antenna was designed and simulated using CST Microwave Studio™. The fake fingernail substrate was made of Acrylonitrile butadiene styrene (ABS). Measurement using a caliper showed it thickness to be about 0.5 mm. It has a relative permittivity (ε_r) of about 2.7 and loss tangent of 0.009 [45]. The designed antenna comprises of a rectangular radiating patch with a CPW microstrip transmission line and a rectangular ground on the backplane.

A sprayable (aerosol ultrasonic atomization) silver inks nanoparticle ink qualified for Optomec Aerosol Jet printing is water-based Metalon® JS-A221AE, a highly conductive silver nanoparticle ink by Novacentrix inc. According to the manufacturer's datasheet [47], it has good adhesion and is ideal for plastic, glass, and metal substrates. It was used to print the radiator and the CPW feedline conductive material. According to the datasheet, its resistivity ranges from $9.1 \times 10^{-6}\ \Omega$-cm to $4.2 \times 10^{-4}\ \Omega$-cm, silver content of 50 wt%, viscosity of 10-20 cP, average dispersed particle size and specific gravity of 1.8. The ink conductivity thus ranges from $2.4 \times 10^{5}\ \mathrm{S/m}$ to $1 \times 10^{7}\ \mathrm{S/m}$. The antenna simulation was done using the lower conductivity of the silver ink. The designed antenna is illustrated in Figure 4.10. Figure 4.10(a) and Table 4.2 represent its dimensions. Figure 4.10(b) shows the antenna curved to the shape of a nail while Figure 4.10(c) depicts the angle, 55.26°, of the curvature. Simulation of the antenna with the radiator and CPW made of copper was also done for comparison with silver ink one.

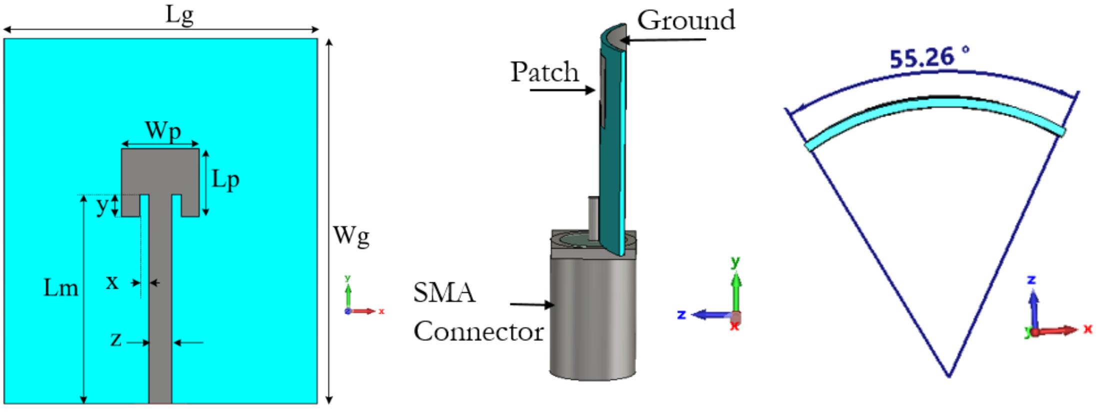

(a) (b) (c)

Figure 4.10 The designed (a) patch antenna (b) curved into an arc and (c) degree of curvature

Table 4.2 Dimensions of the patch of the 15 GHz antenna (mm)

W_g	L_g	W_p	L_p	L_m	**x**	**y**	**z**
15	19	7.8	6.5	13	1.5	1.75	1.0

The simulated reflection coefficient, S_{11}, results for the sliver ink flat and curved antenna as well as copper made models are shown in Figure 4.11. The results show a slightly wider bandwidth for the curved than the flat antenna. The results indicate a -10 dB impedance bandwidth from 14.8 GHz to 15.3 GHz (2.9%) and 14.88 GHz to 15.37 GHz (3.2%) for the flat and curved antennas respectively.

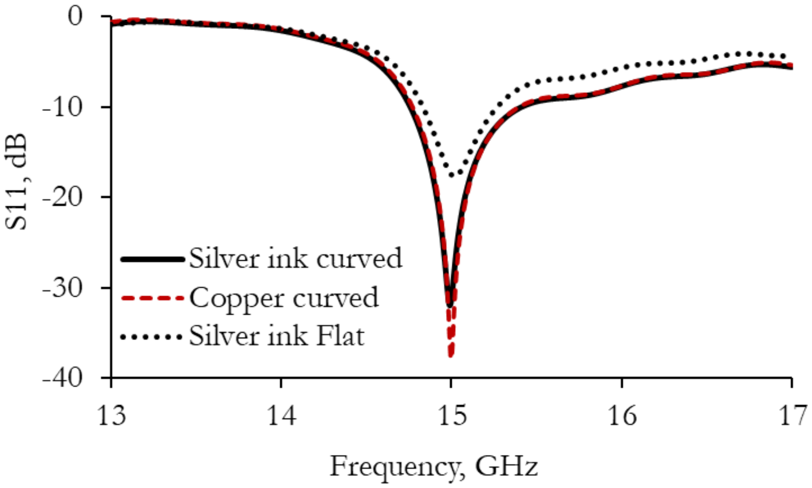

Figure 4.11 Simulated S11 results of flat and curved simulated antennas at 15 GHz

4.4.2 Optomec's Aerosol Jet Fabrication

The microstrip patch nail antennas were fabricated by depositing conductive ink using Optomec's aerosol jet technology. Aerosol Jet Printing manufacturing technology is emerging as a substitute for the traditional thick-film processes such as screen-print, photolithography and micro-dispensing and has been described as superior to inkjet printing [48]. Figure 4.12 depicts the working priciple of the Aerosol Jet Technology. The Aerosol Jet process uses aerodynamics to deposit functional material aerosolized droplets onto a substrate. The functional liquid is aerosolized into globules and then focused as collimated beams of a diameter of around 10 microns after it has been passed through a deposition head. The deposition head sends out the aerosol beam which impinges the droplet on the substrate [49]. To print the features, the deposition head is translated in the XYZ and Theta directions with respect to the substrate. The CAD design file generated tool path guides the deposition head translation. This allows the deposition head to print in any orientation. Thus, it can print on 3D surfaces and not just on a smooth and flat surface. To fabricate the antennas, the digital model was exported from CST Microwave Studio^{TM} to an STL file. The metallic layers that constitute the radiator and the microstrip transmission line were uniformly deposited onto the fake nail using Optomec's aerosol jetting process that sprays silver conductive ink. The antennas were left to dry for about 24 hours before being transferred to a NovaCentrix PulseForge [50] machine to cure. The fabrication was done at the Centre for Process Innovation (CPI) [51].

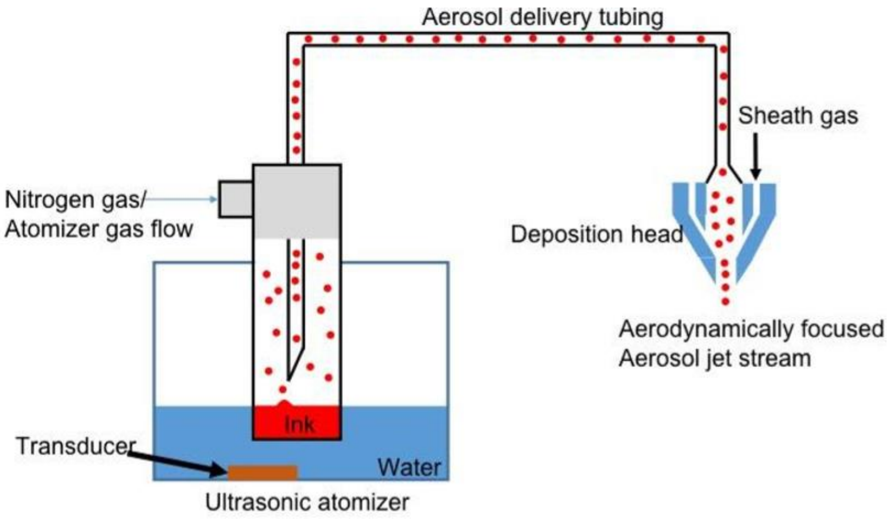

Figure 4.12 Schematic of Aerosol jet printing process [52]

Figure 4.13 shows the development process of the antenna. Figure 4.6(a) shows the fake nail on which the antennas were printed, Figure 4.6(b), the fabrication process, and Figure 4.6(c), the fabricated antenna. An SMA end launcher connector jack of operating frequency 0 to 18 GHz [53] was attached to the feedline of the antenna (Figure 4.13 (c)).

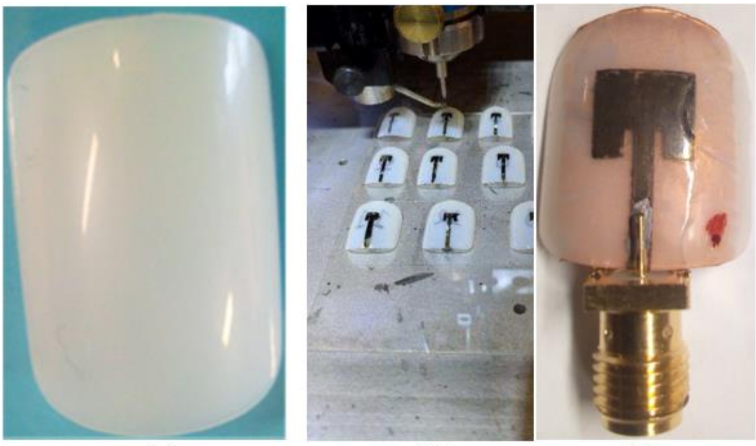

(a) (b) (c)

Figure 4.13 (a) The removable nail (b) printing of the antennas (c) the fabricated antenna

The surface profile of the antenna was conducted on the fabricated antenna. Figure 4.14 shows the surface profile of the silver ink layer of the patch element of antenna.

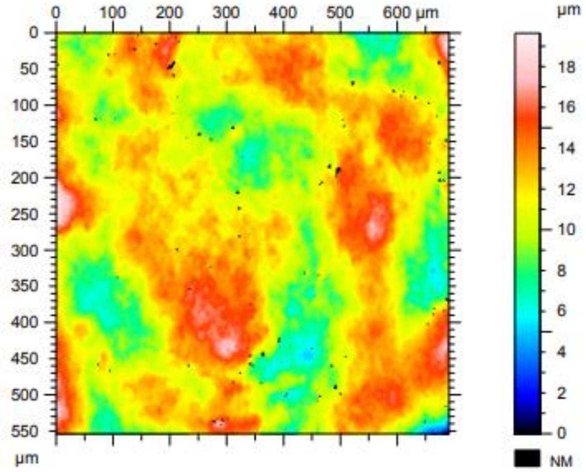

Figure 4.14 Surface profile of the antenna patch

The analysis was done using Talysurf CCI interferometer at CPI and showed a roughness of about 1μm. The ground plane of the antenna was created using adhesive copper tape which was fixed to the back of the ABS fingernail.

4.4.3 RF Measurements

The S_{11} and radiation patterns of the fabricated antenna were measured to determine its performance. The S_{11} measurements were obtained using an Anritsu 37397C vector network analyzer (VNA) for the nail antenna. A graph of the measured and simulated S_{11} results is shown in Figure 4.15. The measured S_{11} results shows a better matching and wider $-10\ \mathrm{dB}$ impedance bandwidth relative to the simulated results. This could be due to further resistive losses in the materials not accounted for in simulation, connectors, and errors in the fabrication. The measured resonant points shifted slightly to the right of the simulated one. Measured -10 dB impedance bandwidths from 14.6 to 16.0 GHz (9.8%) was observed for the antenna. A slight shift of the resonance point to the left is observed for the on-finger antenna.

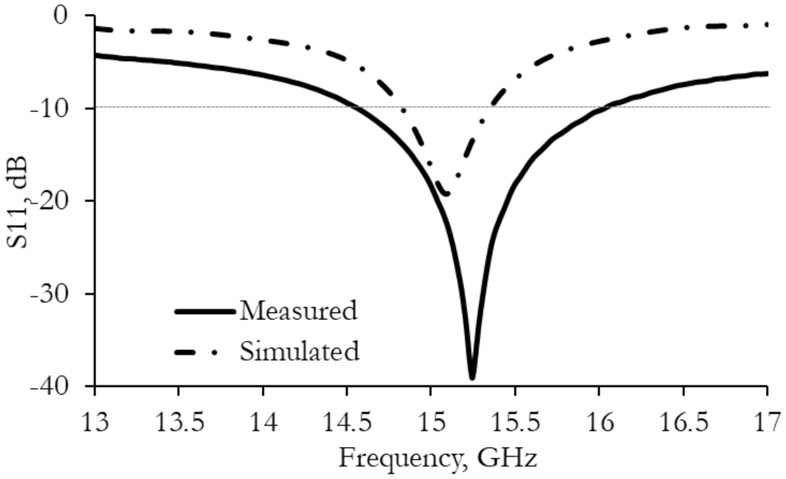

Figure 4.15 Comparison of measured and simulated S_{11} of the optimized 15 GHz antenna

Far field radiation pattern was performed in an anechoic chamber. On-body radiation patterns were also measured for both off- and on-body. Figure 4.16 shows the antenna on-body radiation pattern measurement process. After health and safety assessment, a platform was built and fixed to the base of chamber pole. The antenna wearer stood on the platform during the measurement process. The white plastic pole observed in the figure was fixed to the platform. The cable connecting the antenna was attached to the pole using plastic straps. The antenna remained fixed during for the xy, yz and xz planes radiation patterns' measurement cycles. The wearer stood on the platform and kept the finger fixed to the antenna for the on-body radiation pattern measurement. Figure 4.17 shows the radiation patterns for both simulated and fabricated

Figure 4.16 Measurement of the on-body radiation pattern in the anechoic chamber

antennas. Patterns are as expected for a patch antenna on a small, curved ground plane with the main lobe out of the fingernail and lower radiation towards the finger and body. The radiation pattern for both simulated and fabricated antennas shows consistency in xy, xz and yz planes.

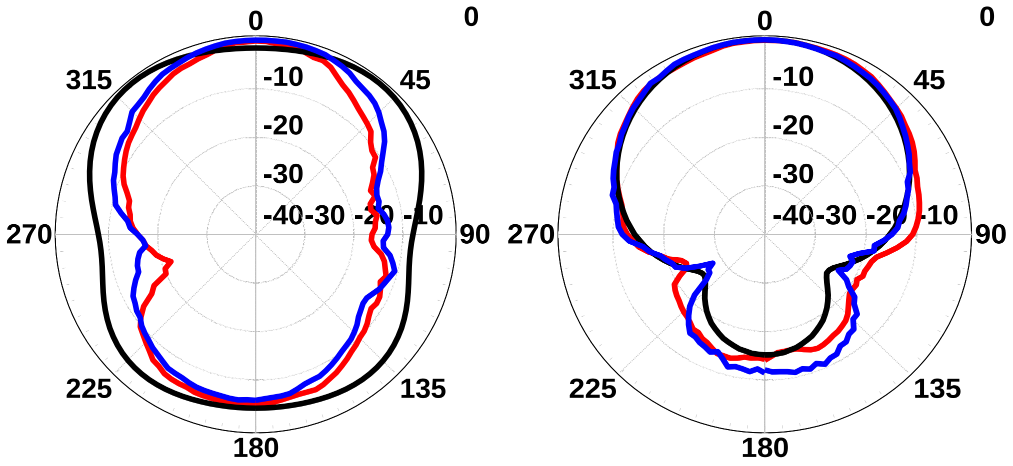

xz plane

yz plane

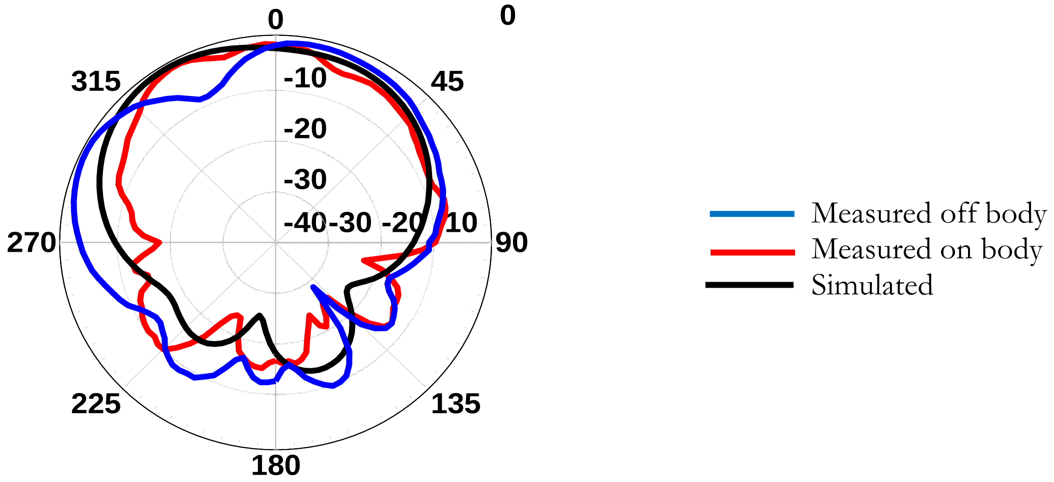

xy plane

Figure 4.17 Radiation pattern for the xy, xz and yz planes at 15 GHz

The slight variations are attributable to fabrication and measurement errors as well as the antenna connector. The simulated gain and efficiency on the body were about 6.9 dBi and 80% respectively at 15 GHz while off-body was about 0.3 dB higher. The measured gain was almost the same for on and off-body. It was about 6.4 dBi, and the antenna efficiency was 70%. The measured gains and corresponding efficiency include any potential impedance mismatch.

4.5 Millimeter Wave Nail Antenna

This section describes the design and   fabrication, and analysis of the millimeter wave antenna.

4.5.1 Antenna Design

Higher frequencies can typically increase the communication bandwidth and thus the amount of data that can be transferred. For the higher frequency, a higher conductivity antenna surface material is preferable. To improve conductivity, a layer of copper can be added to the metallic tracks using an electroplating process. A millimeter wave frequency antenna with dimensions shown in Table 4.3 was designed and simulated Reflection coefficient and radiation pattern performance parameters were used to gauge the performance of the antennas. Figure 4.18 shows the simulated S_{11} of the flat, and curved antennas. The antenna resonance at 28 GHz have only a minor frequency shifts between the two cases. The results indicate a -10 dB impedance bandwidth of 27.5 GHz to 28.6 GHz (3.9%) and 27.5 GHz to 28.5 GHz (3.6%) for the flat and curved microstrip patch antenna respectively.

Table 4.3 Dimensions of the 28 GHz patch antenna (mm)

W_g	L_g	W_p	L_p	L_m	x	y	z
14.96	17.45	3.72	3.25	10.0	0.44	1.06	1.10

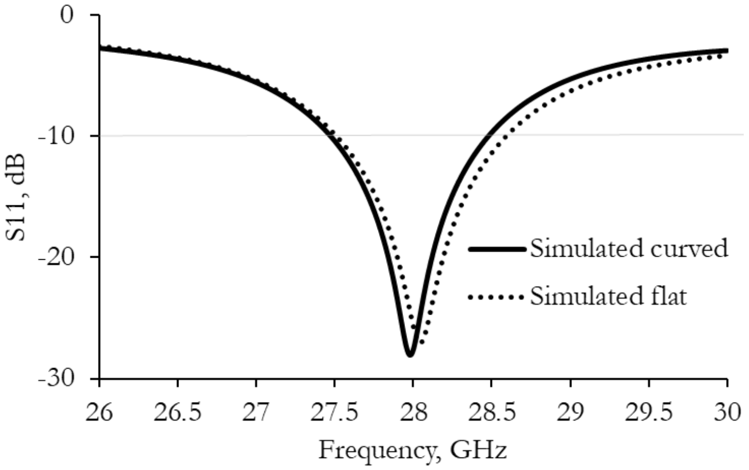

Figure 4.18 Simulated S_{11} of the flat and curved antennas at 28 GHz

4.5.2 Millimeter Wave Antenna Fabrication, Surface Analysis and Measurements

The 28 GHz antenna was fabricated using the same fabrication process as the 15 GHz antenna. After the radiator and microstrip transmission line were printed and cured, a copper layer was added through an electroplating process.

A digital microscope from Keyence (UK) Limited was used to observe the antenna surface, measure its roughness and photograph the surface. Figure 4.19 shows the surface of the copper plated radiator and its feedline at x50 magnification.

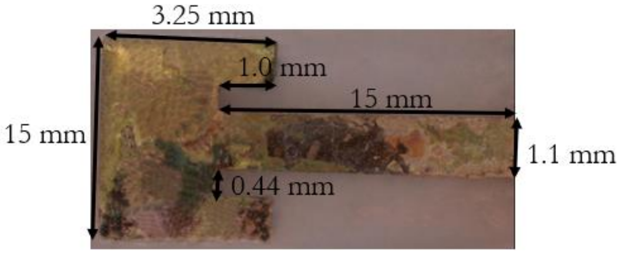

Figure 4.19 Photo of the patch antenna and feedline

Surface roughness measurements of the radiator are shown in Figure 4.20. Figure 4.20(a) shows the two points marked 1 and 2, on either side of the feedline inset at which the measurements were taken.

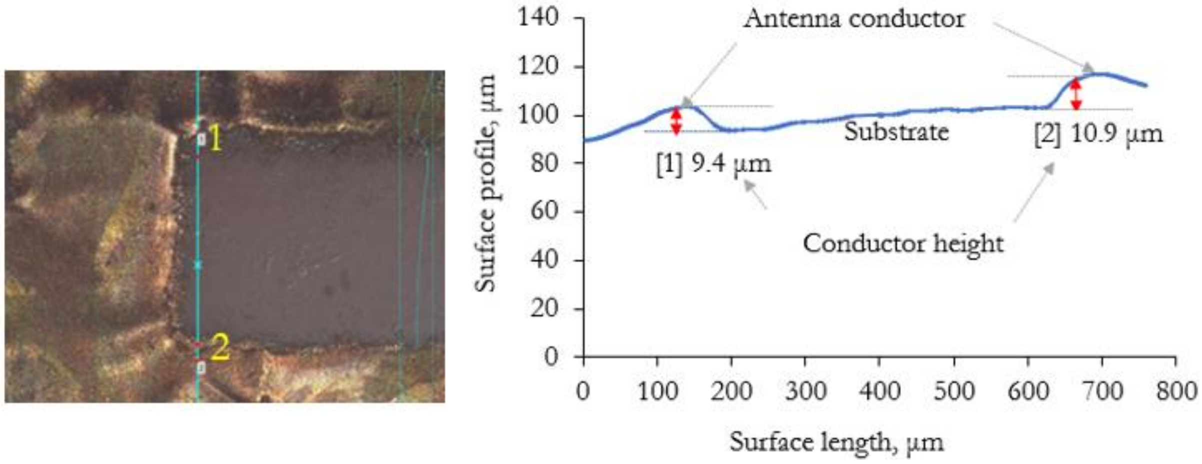

(a) (b)

Figure 4.20 Conductor profile (a) measurement points (b) graphical height representation at the two inset points

The image and conductive print height were obtained using a digital microscope VHX 7000 from Keyence® UK. Figure 4.20(b) is the graphical representation of the conductor height showing actual height of 9.4 μm and 10.9 μm at points 1 and point 2 respectively.

The conductor height was also measured at the inset/patch point longitudinal to the feedline at the point marked 1, Figure 4.21. Figure 4.21(a) shows the measuring point while Figure 4.21(b) shows the graphical representation of the print at the inset. The conductor height is about 13.5 μm implying that though the antenna is viable, the fabrication process produced uneven surface.

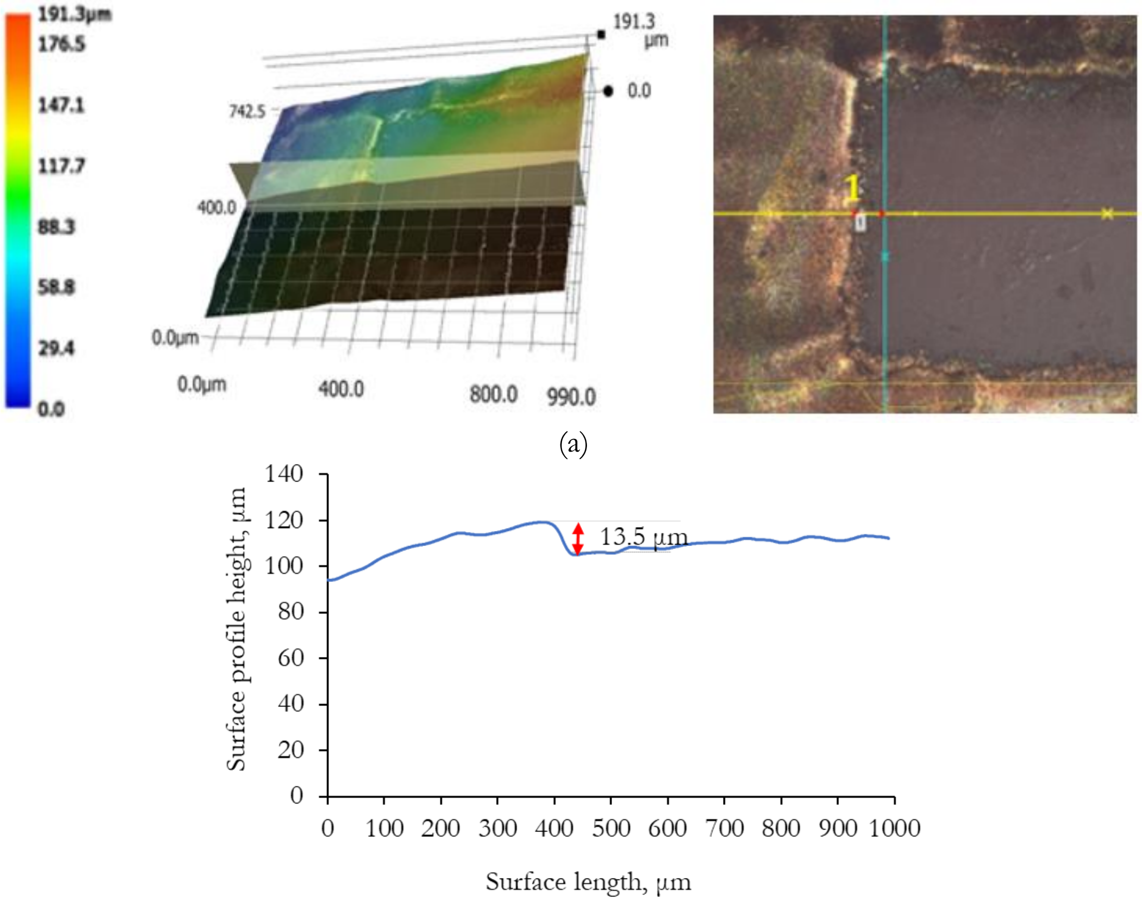

(a)

(b)

Figure 4.21 (a) The conductor height measured at the inset/patch point longitudinal to the feedline (b) graphical representation of the height at the measuring point

The center line average surface roughness (Ra) was measured at the feedline section of the antenna and is shown in Figure 4.22. Figure 4.22(a) shows the roughness which was found to be 0.8 µm in the profile depiction shown in Figure 4.22(b).

The patch antenna microstrip feedline was connected a low profile 2.92 mm SMA Jack (female) end launch connector with a range of up to 67 GHz [54] from Southwest Microwave, Inc., Figure 4.23. Figure 4.23(a) shows the fabricated antennas after the electroplating process and the 2.92 mm SMA Jack (female) end launch connector attached while Figure 4.23(b) shows the antenna worn on a finger.

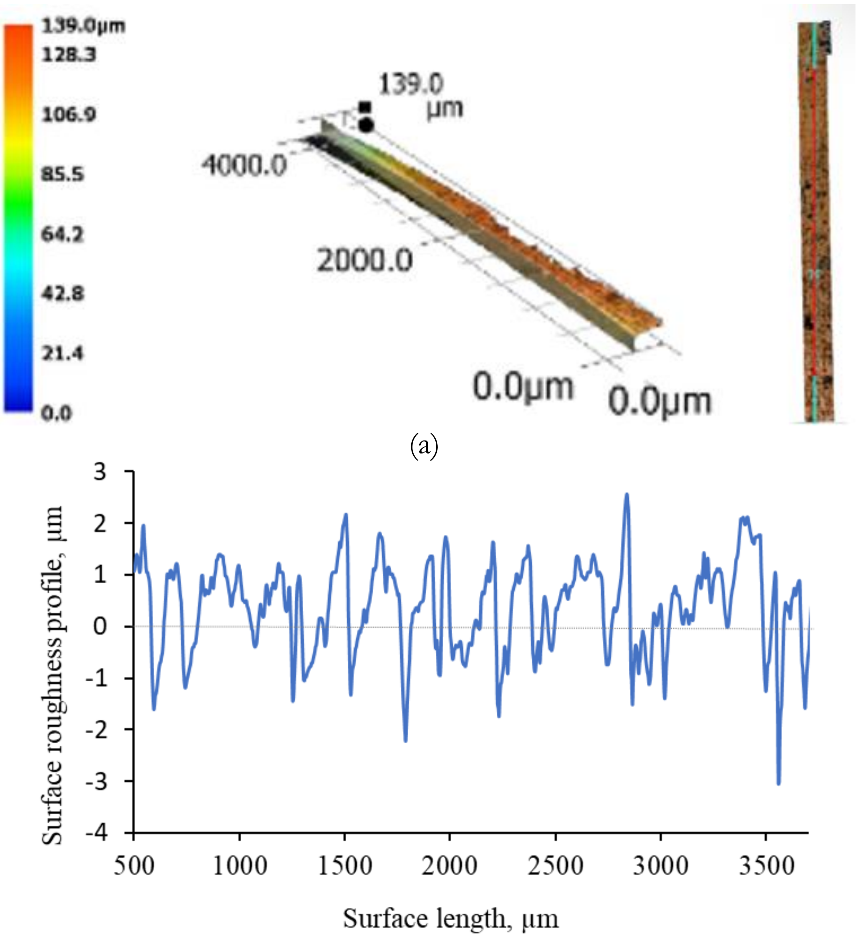

(a)

(b)

Figure 4.22 Microstrip feed line surface profile (a) the feedline (b) its roughness profile

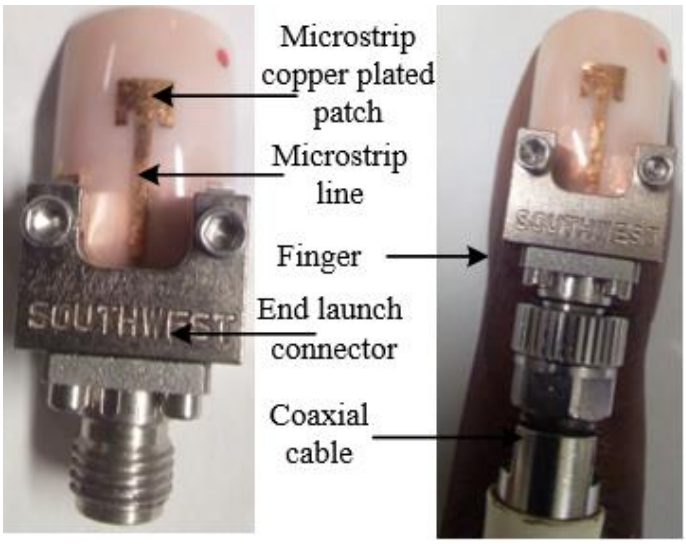

(a) (b)

Figure 4.23 The (a) fabricated antenna (b) antenna worn on a finger

The reflection coefficient (S_{11}) of the antenna was measured. Figure 4.24 shows the measured S_{11} results of the fabricated antenna compared with the simulated results.

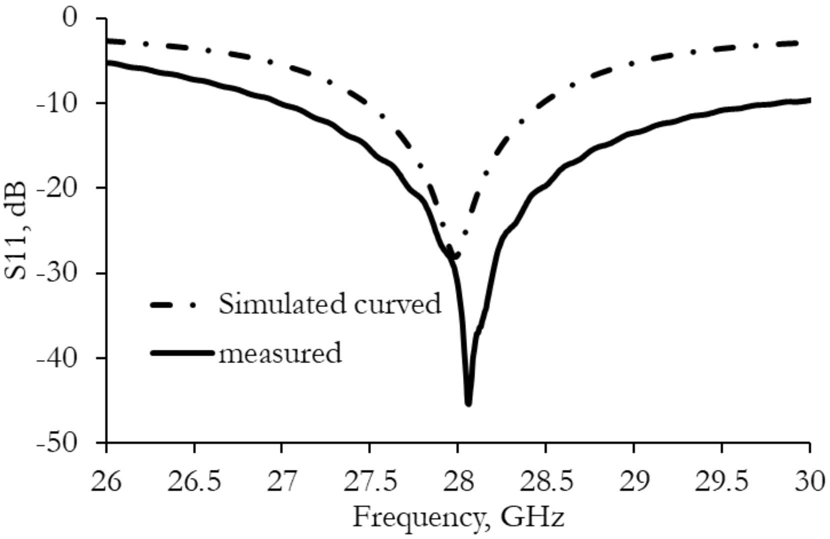

Figure 4.24 Measured and simulated S_{11} of the optimized antenna

The measured bandwidth was 27.0 GHz to 29.8 GHz (10%) antennas and compared well with simulated ones in terms of resonant frequency. The fabricated antenna has better matching and wider $-10\ dB$ impedance bandwidth compared to the simulated one. This could be due to electrical losses not accounted for in simulations, connectors, and errors in the fabrication. The metal ground plane was made using copper tape with an adhesive layer and was attached by hand. This may leave some air gaps which could potentially increase matching and bandwidth.

Far field pattern results are shown in Figure 4.25 for planes xy, xz, and yz. The results show the expected patch antenna's hemispherical radiation pattern with moderate directivity. The main lobe points out of the fingernail while low back radiation is realised. Back radiation is also lower than for the antenna at 15 GHz (Figure 4.9) due to the smaller size of the patch at 28 GHz in relation to the metallic ground plane.

The simulated and measured patterns were in reasonable agreement. The main differences between simulations and measurements, particularly in the yz plane, could be due to the metallic parts of the end-launch connector (Figure 4.13(c)). The simulated gain and efficiency were about 7.5 dBi and 81% respectively while the measured gain and efficiency were about 7.4 dBi and 80% respectively.

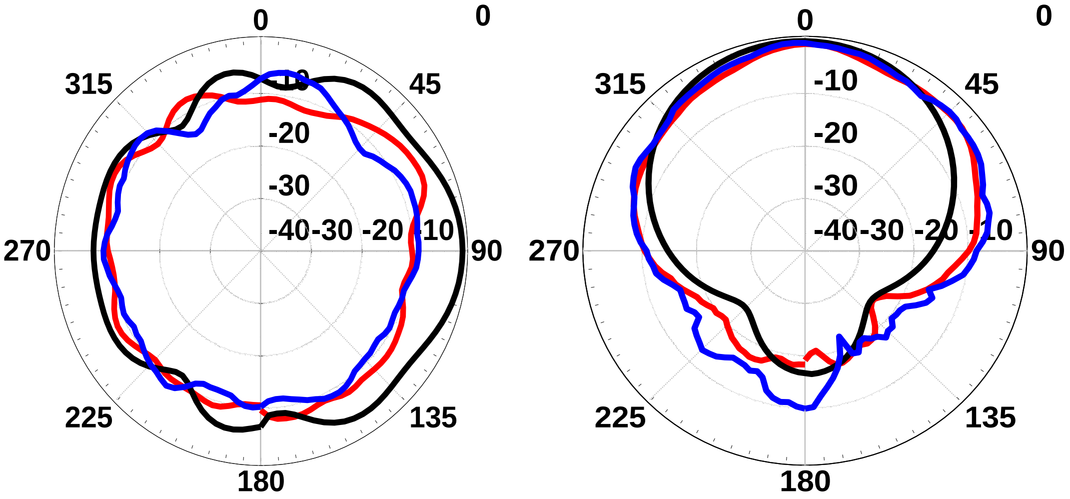

xy plane xz plane

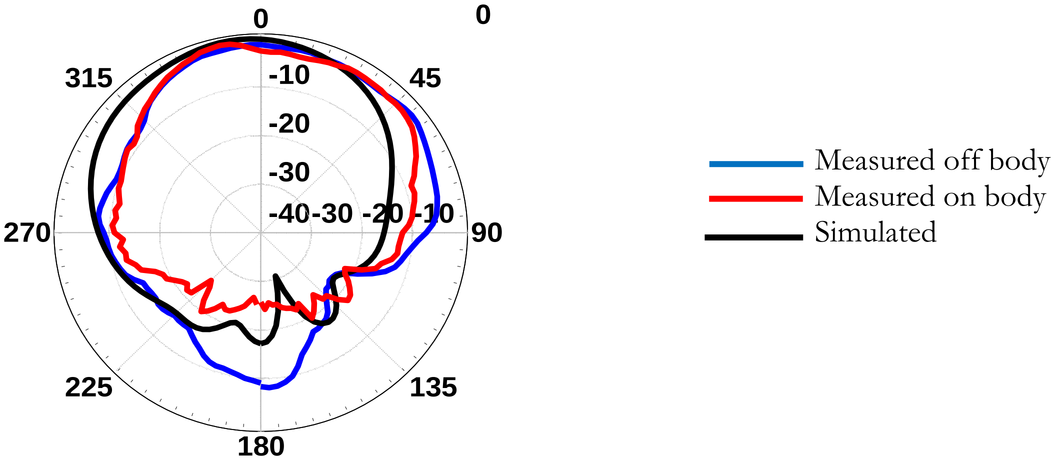

yz plane

Figure 4.25 Radiation patterns at xy, xz and yz planes at 28 GHz

Table 4.5 compares the proposed antenna with previous wearable antennas. The benefit of this patch antenna is that it offers a good gain and is not affected by the body movement.

Table 4.4 Comparison of the proposed antenna and other wearable antennas at 28 GHz

Reference	Frequency (GHz)	Bandwidth (GHz)	Gain (dB)	Substrate
[42]	28	1	**7**	PLA Medallion
[55]	28	15	3.5	Jeans
[56]	28	2.68	2.1	Rogers 5880
[57]	26/28	10	7	woven polyester
This work	28	2.87	7.5	ABS fingernail

4.6 Discussion and Conclusion

Antennas on removable fingernails have been demonstrated. Manually painted 10 GHz patch antenna on ABS fingernail have been developed and tested. Manual hand brush painting as an

AM technique has been demonstrated to be an inexpensive solution for the fabrication of antenna integrated on a wearable device. The proposed fabrication technique requires just a simple paintbrush and no expensive equipment.

The concept was extended to antennas operating at 15 GHz and 28 GHz using Aerosol Jet printing. Aerosol Jet printing and flush curing were successfully employed to deposit layers of silver ink on the curved nails. The technique produced the high resolution required for the printed antennas as well as smooth and thin metallic layers. An additional copper layer was added to the 28 GHz through a copper plating process. The fabricated antennas provided good performance in terms of impedance match and bandwidth. Radiation patterns were as expected for a patch antenna with the main lobe out of the fingernail and low radiation towards the finger and body. The 28 GHz antenna provides lower back radiation and higher gain than the 15 GHz mainly due to the smaller size of the patch in relation to the ground plane. The antenna designs presented in this work can potentially be deployed in IoT solutions for 5G technology. The proposed nail antenna design is light, cheap, easy to install, part of a beauty accessory, which occupies a small surface area and is easy to wear. The requirement of different equipment at different stages presents a case for a production chain process. This could enable scaling up to a mass production industrial process. Further, multiple fingers on a human hand can make antenna arrays and diversity systems feasible for signal reception improvement.

Acknowledgement

In this work and the subsequent conference paper [1], Peter Njogu did the research, simulation, fabrication, lab measurement and writing. In the work that resulted in [2], Peter Njogu did the research, design, simulation, experimentation, and writing; David Bird facilitated the fabrication at CPI by Ahmed Elibiary, Benito Sanz-Izqueirdo and Sung Yun Jun gave guidance while Zhijiao Chen did a pre-submission review of the journal paper.

References

[1] P. Njogu and B. Sanz-Izquierdo, "Removable Finger Nail Antenna," *in 14th European Conference on Antennas and Propagation (EuCAP)*, Copenhagen, Denmark, 2020.

[2] P. Njogu, B. Sanz-Izquierdo, A. Elibiary, S. Y. Jun, Z. Chen and D. Bird, "3D Printed Fingernail Antennas for 5G Applications," *IEEE Access,* vol. 8, pp. 228711 - 228719, 2020.

[3] M. Masoud, Y. Jaradat, A. Manasrah and I. Jannoud, "Sensors of Smart Devices in the Internet of Everything (IoE) Era: Big Opportunities and Massive Doubts," *Hindawi Journal of Sensors,* vol. 2019, pp. 1-26, 2019.

[4] M. Agiwal, A. Roy and N. Saxena, "Next Generation 5G Wireless Networks: A Comprehensive Survey," *IEEE Communications Surveys & Tutorials,* vol. 18, no. 3, pp. 1617-1655, 2016.

[5] A. Shahraki, M. Abbasi, J. Piran and A. Taherkordi, "A Comprehensive Survey on 6G Networks: Applications, Core Services, Enabling Technologies, and Future Challenges," *IEEE Transactions on Network and Service Management,* vol. x, no. x, pp. 1-21, 2021 https://arxiv.org/pdf/2101.12475.pdf.

[6] H. Rahimi, A. Zibaeenejad and A. A. Safavi, "A Novel IoT Architecture based on 5G-IoT and Next Generation Technologies," in *2018 IEEE 9th Annual Information Technology, Electronics and Mobile Communication Conference (IEMCON)* , Vancouver, BC, Canada , 2018

[7] M. Shafi, J. Zhang, H. Tataria, A. F. Molisch, S. Sun, T. S. Rappaport, F. Tufvesson, S. Wu and K. Kitao, "Microwave vs. Millimeter-Wave Propagation Channels: Key Differences and Impact on 5G Cellular Systems," *IEEE Communications Magazine,* pp. 14 - 20 , 7 December 2018.

[8] S. Li, L. D. Xu and S. Zhaof, "5G Internet of Things: A survey," *Journal of Industrial Information Integration,* vol. 10, pp. 1-10, 2018.

[9] B. Sanz-Izquierdo, E. Parker, J. Batchelor and J. Miller, "Body armour with integral high impedance surface," in *Proceedings of the 5th European Conference on Antennas and Propagation (EUCAP)* , Rome, 2011 .

[10] A. Sabban, Novel Wearable Antennas for Communication and Medical Systems, New York: CRC Press , 2019 .

[11] M. L. Scarpello, I. Kazani, C. Hertleer, H. Rogier and D. V. Ginste, "Stability and Efficiency of Screen-Printed Wearable and Washable Antennas," *IEEE Antennas and Wireless Propagation Letters ,* vol. 11, pp. 838 - 841 , 2012.

[12] N. Chahat, M. Zhadobov, L. L. Coq and R. Sauleau, "Wearable Endfire Textile Antenna for On-Body Communications at 60 GHz," *IEEE Antennas and Wireless Propagation Letters ,* vol. 11, pp. 799 - 802 , 2012.

[13] M. Joler and M. Boljkovac, "A Sleeve-Badge Circularly Polarized Textile Antenna," *IEEE Transactions on Antennas and Propagation,* vol. 66, no. 3, pp. 1576-1579, 2018.

[14] G. S. Karthikeya, K. K. Devaiah, R. S. G. Sharma, M. H. B. Patel, N. R. Mandi and T. Thyagaraj, "Wearable button antenna array for V band application," in *5th Asia-Pacific Conference on Antennas and Propagation (APCAP)* , Kaohsiung, 2016.

[15] B. Sanz-Izquierdo, J. Miller, J. C. Batchelor and M. Sobhy, "Dual-band wearable metallic button antennas and transmission in body area networks," *IET microwaves, antennas & propagation,* vol. 4, no. 2, pp. 182-190, 10.

[16] A. Shafqat, F. A. Tahir and H. M. Cheema, "A Compact Uniplanar Tri-band Antenna for Wearable Smart Watches," in *18th International Symposium on Antenna Technology and Applied Electromagnetics (ANTEM)* , Waterloo, ON, Canada, 2018.

[17] S. M. Abbas, K. P. Esselle and Y. Ranga, "An armband-wearable printed antenna with a full ground plane for body area networks," in *IEEE Antennas and Propagation Society International Symposium (APSURSI)* , Memphis, TN, USA , 2014 .

[18] S. Hong, S. H. Kang, Y. Kim and C. W. Jung, "Transparent and Flexible Antenna for Wearable Glasses Applications," *IEEE Transactions on Antennas and Propagation,* vol. 64, no. 7, pp. 2797-2804, 2016.

[19] Y.-Y. Wang, Y.-L. Ban, Z. Nie and C.-Y.-D. Sim, "Dual-Loop Antenna for 4G LTE MIMO Smart Glasses Application," *IEEE Antennas and Wireless Propagation Letters,* vol. 18, no. 9, pp. 1818-1822, 2019.

[20] I. Gani and H. Yoo, "Miniaturized Scalp-Implantable Antenna for Wireless Biotelemetry," in *International Workshop on Antenna Technology (iWAT)*, Seoul, South Korea , 2015.

[21] A. Shamim, "3D Inkjet Printed Flexible and Wearable Antenna Systems," in *2017* , Phuket, Thailand , International Symposium on Antennas and Propagation (ISAP).

[22] H. Xin and M. Liang, "3-D-Printed Microwave and THz Devices Using Polymer Jetting Techniques," *Proceedings of the IEEE ,* vol. 105, no. 4, pp. 737 - 755 , 2017.

[23] B. Sanz-Izquierdo and E. A. Parker, "3-D Printing of Elements in Frequency Selective Arrays," *IEEE Transactions on Antennas and Propagation,* vol. 62, no. 12, pp. 6060-6066, 2014.

[24] C. Garcia, R. Rumpf, H. Tsang and J. Barton, "Effects of extreme surface roughness on 3D printed horn antenna," *Electronics Letters,* vol. 49, no. 12, pp. 734 - 736, 2013.

[25] J. Ren and J. Y. Yin, "3D-Printed Low-Cost Dielectric-Resonator-Based Ultra-Broadband Microwave Absorber Using Carbon-Loaded Acrylonitrile Butadiene Styrene Polymer," *MDPI,* vol. 11, no. 7, pp. 1-13, 2018.

[26] G. McKerricher, D. Titterington and A. Shamim, "A Fully Inkjet-Printed 3-D Honeycomb-Inspired Patch Antenna," *IEEE Antennas and Wireless Propagation Letters,* vol. 15, pp. 544 - 547, 2015.

[27] H. Yi, S.-W. Qu, K.-B. Ng, C. H. Chan and X. Bai, "3-D Printed Millimeter-Wave and Terahertz Lenses with Fixed and Frequency Scanned Beam," *IEEE Transactions on Antennas and Propagation,* vol. 64, no. 2, pp. 442 - 449, 2016.

[28] Z.-X. Xia, K. W. Leung and K. Lu, "3-D-Printed Wideband Multi-Ring Dielectric Resonator Antenna," *IEEE Antennas and Wireless Propagation Letters,* vol. 18, no. 10, pp. 2110-2114, 2019.

[29] B. Zhang, Z. Zhan, Y. Cao, H. Gulan, P. Linn´er, J. Sun, T. Zwick and H. Zirath, "Metallic 3-D Printed Antennas for Millimeter- and Submillimeter Wave Applications," *IEEE Transactions on Terahertz Science and Technology,* vol. 6, no. 4, pp. 592-600, 2016.

[30] R. Xu, S. Gao, B. S. Izquierdo, C. Gu, P. Reynaert, A. Standaert, G. J. Gibbons, I. Dmitry, W. Bösch and M. E. Gadringer, "140 GHz Additive Manufacturing Low-Cost and High-Gain Fabry-Perot Resonator Antenna," in *International Workshop on Antenna Technology (iWAT)*, Bucharest, Romania, Romania , 2020.

[31] S. Y. Jun, B. Sanz-Izquierdo, E. A. Parker, D. Bird and A. McClelland, "Manufacturing Considerations in the 3-D Printing of Fractal Antennas," *IEEE Transactions on Components, Packaging and Manufacturing Technology,* vol. 7, no. 11, pp. 1891 - 1898, 2017.

[32] C. Gu, S. Gao, V. Fusco, G. Gibbons, B. S. Izquierdo, A. Standaert, P. Reynaert, W. Bösch, M. Gadringer, R. Xu and X. Yang, "A D-band 3D-Printed Antenna," *IEEE Transactions on Terahertz Science and Technology(Early Access),* 2020.

[33] R. Xu, S. Gao, B. S. Izquierdo, C. Gu, P. Reynaert, A. Standaert, G. J. Gibbons, W. Bösch, M. E. Gadringer and D. Li, "A Review of Broadband Low-Cost and High-Gain Low-Terahertz Antennas for Wireless Communications Applications," *IEEE Access ,* vol. 8, pp. 57615 - 57629, 2020.

[34] S. Y. Jun, A. Shastri, B. Sanz-Izquierdo, D. Bird and A. McClelland, "Investigation of Antennas Integrated Into Disposable Unmanned Aerial Vehicles," *IEEE Transactions on Vehicular Technology ,* vol. 68 , no. 1, pp. 604 - 612, 2019 .

[35] I. Piekarz, J. Sorocki, M. T. Craton, K. Wincza, S. Gruszczynski and J. Papapolymerou, "Application of Aerosol Jet 3-D Printing With Conductive and Nonconductive Inks for Manufacturing mm-Wave Circuits," *IEEE Transactions on Components, Packaging and Manufacturing Technology,* vol. 9, no. 3, pp. 586 - 595, 2019.

[36] K. N. Paracha, S. K. A. Rahim, P. J. Soh and M. Khalily, "Wearable Antennas: A Review of Materials, Structures, and Innovative Features for Autonomous Communication and Sensing," *IEEE Access,* vol. 7, pp. 56694 - 56712 , 2019.

[37] A. Kiourti, "RFID Antennas for Body-Area Applications: From Wearables to Implants," *IEEE Antennas and Propagation Magazine,* vol. 60, no. 5, pp. 14 - 25 , 2018.

[38] S. Y. Jun, A. Elibiary, B. Sanz-Izquierdo, L. Winchester, D. Bird and A. McCleland, "3-D Printing of Conformal Antennas for Diversity Wrist Worn Application," *IEEE Transaction on Components, Packaging and Manufacturing Techology,* vol. 8, no. 12, pp. 2227-2235, 2018.

[39] M. Rizwan, M. Khan, H. He, J. Virkki, L. Sydänheimo and L. Ukkonen, "Flexible and stretchable 3D printed passive UHF RFID tag," *Electronics Letters,* vol. 53, no. 17, pp. 1054 - 1056, 2017.

[40] W. G. Whittow, "3D printing, inkjet printing and embroidery techniques for wearable antennas," in *10th European Conference on Antennas and Propagation (EuCAP)* , Davos, Switzerland , 2016.

[41] M. Ramadan and R. Dahle, "Characterization of 3-D Printed Flexible Heterogeneous Substrate Designs for Wearable Antennas," *IEEE Transactions on Antennas and Propagation,* vol. 67, no. 5, pp. 2019, 2896 - 2903.

[42] M. Rizwan, M. W. A. Khan, L. Sydänheimo, J. Virkki and L. Ukkonen, "Flexible and Stretchable Brush-Painted Wearable Antenna on a Three-Dimensional (3-D) Printed Substrate," *IEEE Antennas and Wireless Propagation Letters,* vol. 6, pp. 3108 - 3112, 2017.

[43] M. Fawaz, S. Jun, W. Oakey, C. Mao, A. Elibiary, B. Sanz-Izquierdo, D. Bird and A. McClelland, "3D printed patch Antenna for millimeter wave 5G wearable applications," in *12th European Conference on Antennas and Propagation (EuCAP 2018)* , London, UK, 2018.

[44] GSMA, "5G Spectrum GSMA Public Policy Position," GSMA, London, 2020.

[45] M. Pérez-Escribano and E. Márquez-Segura, "Parameters Characterization of Dielectric Materials Samples in Microwave and Millimeter-Wave Bands," IEEE Transactions on Microwave Theory and Techniques, vol. 69, no. 3, pp. 1723 - 1732, 2021.

[46] RS components, "RS PRO Silver Conductive Paint Paint, 20 g Bottle" RS Stock No.: 186-3600 Datasheet [online] https://docs.rs-online.com/cd63/A700000008879603.pdf

[47] Novacentrix®," Metalon® Conductive Inks for Printed Electronics" Metalon® JS-A221AE, datasheet, 2022. Online. Available: Metalon™ Conductive Inks for Printed Electronics (novacentrix.com)

[48] Optomec, *Aerosol Jet® Printed Electronics Overview,* Optomec, white paper [online]. Available: Microsoft Word - aerosol jet printed electronics overview-ntsi Conf.doc (optomec.com)

[49] J. A. Paulsen, M. Renn, K. Christenson and R. Plourde, "Printing conformal electronics on 3D structures with Aerosol Jet technology," in *2012 Future of Instrumentation International Workshop (FIIW) Proceedings* , Gatlinburg, TN, USA , 2012 .

[50] NovaCentrix, "NovaCentrix," NovaCentrix, 13 11 2019. [Online]. Available: https://www.novacentrix.com/. [Accessed 13 11 2019].

[51] Centre for Process Innovation, "CPI," Centre for Process Innovation, 13 11 2019. [Online]. Available: https://www.uk-cpi.com/. [Accessed 13 11 2019].

[52] S. Agarwala, G. L. Goh and W. Y. Yeong, "Optimizing aerosol jet printing process of silver ink for printed electronics," in *IOP Conference Series: Materials Science and Engineering*, Bangkok, Thailand , 2017.

[53] RS components, "RS Pro Straight Panel Mount Bulkhead Fitting SMA End Launcher Connector, jack, Solder Termination" RS Stock No: 526-5779 Datasheet [online] https://docs.rs-online.com/3623/0900766b81585daf.pdf

[54] Southwest Microwave, Inc.," 2.92mm jack (female) end launch connector low profile" DWG. no: 91Y60930 Datasheet [online] https://mpd.southwestmicrowave.com/wp-content/uploads/2018/06/292-04A-6.pdf

[55] D. Sharma, S. K. Dubey and V. N. Ojha, "Wearable Antenna for millimeter wave 5G Communications," in *IEEE Indian Conference on Antennas and Propogation (InCAP)* , Hyderabad, India, 2018 .

[56] X. Tong, C. Liu, Y. Chen, J. Zhu, X. Yang, H. Guo and X. Liu, "A Dual-Mode Multi-Polarization Millimeter Wave Wearable Antenna for WBAN Applications," in *IEEE MTT-S International Microwave Biomedical Conference (IMBioC)* , Nanjing, China , 2019 .

[57] M. Wagih, A. S. Weddell and S. Beeby, "Millimeter-Wave Textile Antenna for On-Body RF Energy Harvesting in Future 5G Networks," School of Electronics and Computer Science, University of Southampton , Southampton, 2019.

CHAPTER 5: FREQUENCY SELECTIVE SURFACES BASED LIQUID SENSOR

5.1 Overview

This chapter presents a novel, simple and easy to fabricate frequency selective surfaces (FSS) based liquid sensors. The sensor concept is based on modifying the capacitance between adjacent FSS elements when liquid materials of different electrical characteristics are inserted between them. The change in capacitance produces a change in the resonant frequency. The FSS design consists of a 9 x 9 array of square loops on 0.31λ x 0.31λ square unit cells with trenches between the loops. The trenches are filled with liquids under test (LUT). The structure operates frequency at 4.6 GHz when empty. The frequency of 4.6 GHz was chosen to provide an optimum FSS size i.e., not too big nor not too small, and thus easy to fabricate. When liquids are inserted in the trenches, it causes the resonance frequency of the FSS to vary in relation to the dielectric constant of the liquid. This is observed by measuring the transmission coefficient (S_{21}). Butan-1-ol, ethanol, methanol, propan-2-ol, and Xylene are used to demonstrate the sensing function. Sensitivity was employed as the design validation parameter. Also, from the tests results, the dielectric properties of the chemicals were derived. Errors of about 5% were observed between the dielectric constant and loss tangent derived from the experiment and measurement procedure and their actual values thus validating the design. The device is inexpensive, compact, and easy to make and scalable for large area operations in liquid detection for microwave sensing applications. The FSS sensor was initially 3D printed using fused filament modelling (FDM) as discussed in Section 5.6. However, problem of reaction of the substrate material, Polylactic Acid (PLA), and the LUTs as well as perviousness to the LUT inserted into the trenches for detection, possibly due to the reactions, were discovered during the testing phase. As an inert 3D printable material could not be found, an RT/Duroid 5880 milled version of the proposed design was fabricated instead.

The rest of this chapter is organized as follows: section 5.2 is the introduction, 5.3 details the geometry of the unit cell with the integrated trenches as well as its characteristic behavior. Section 5.4 details fabrication and measurements of the design while section 5.5 discusses the performance evaluation of the proposed sensor. Section 5.6 discusses the 3D version of the sensor while section, 5.7 discusses the fabrication and measurements of 3D version while 5.8 is the conclusion. The design and simulations were done using CST MWS^{TM} with the results verified by experimental results.

5.2 Introduction

Any material can be characterized by its electrical properties in terms of complex permittivity and permeability. These can determine its electromagnetic response and their potential employment in specific industrial applications. Liquid materials have a wide range of applications, including in the biomedical sector [1] [2]. The methods for sensing and determining the electrical properties of liquids are continuously evolving [3].

Microwave sensors have gained popularity due to their simplicity, inexpensive fabrication process, and ease of use. One widespread technique is the use of a resonating structure for the determination of the complex permittivity of the material. They operate on the principle of measuring the complex permittivity through analysis of the fundamental resonance frequency shift in the transmission/reflection response. At a single or discrete set of frequencies, the resonant technique offers potential for accurate measurements. Waveguide, dielectric, and coaxial cavity resonators have traditionally been employed for materials characterization [4] [5]. The material to be characterized is inserted in the cavity location where the electric field is at its maximum causing cavity perturbation. The introduction of material results in changes in the resonant frequency of the cavity [3] and by exploiting this phenomenon, several sensing devices have been developed. In [6], a planar substrate integrated waveguide cavity resonator has been presented where microfluidic capillaries are used for the insertion of the material. This method is also employed in [7] and [8] with the implementation of a split ring resonator with a microfluidic channel. The split ring and capillary concepts are combined in [9] where a complementary split ring resonator (CSRR) is presented for dielectric characterization of liquids. This is further developed in [10] where an open complementary split-ring resonator is employed with a slot container instead of the microfluidic capillaries. In [11], a dual mode, quarter ring microstrip resonators microfluidic sensor with capillary is presented while [12] presents a sensor that exploits excitation of a resonant mode within a cavity containing a minute sample of a liquid. In [13], an RFID sensor is presented for the identification and evaluation of liquid chemicals based on the shift in the resonant frequency of an applied UHF RFID chipped tag.

Metamaterials are artificially constructed composites that exhibit electromagnetic properties that do not occur naturally [14]. They include electromagnetic bandgap (EBG) structures [15] and FSS [16] which have recently been employed in sensing of liquids. In [17] [18] and [19], metamaterial absorber sensors are proposed where an air gap between a copper plate and backside resonator is used to fill chemicals liquids.

A Casero Fractal element on a planar electromagnetic band gap (EBG) liquid sensing platform [20] has recently been developed. This concept is an advancement of the CPW monopole antenna on a planar EBG presented in [21] and employed in wireless liquid sensing by creating trenches between adjacent cells.

In general, these liquid sensors provide good sensitivity and accuracy, but they also present design and operational complexities and bulkiness while others are delicate and require intricate assembly. Further, their design structures require complicated measurement setups due to their complex designs. Further costs accrue due to additional processes like drilling and cutting, for microfluidic subsystems. Extra parts e.g., capillaries, capsules, and liquid containers are then needed, which further increases the costs. Some of these liquid holding parts are delicate, of micro-dimensions, whose development may require specialized equipment which increases the cost further. Others like EBG-based sensors [20] [21] are multi-part designs, which must be intricately assembled beside their design complexities. A single unit, easy-to-make and use sensor would imply simplicity, lower cost, and ease of assembly.

A low profile, inexpensive, single unit, easy to manufacture and use, square loop FSS based liquid sensor is proposed. The square loop FSS, whose band frequency response depends on its physical dimensions, was employed because it offers a better angular stability, dual polarization, good bandwidth as well as band separation performance [22]. The proposed FSS based sensor can detect and differentiate liquid chemicals of different dielectric properties. From the literature space, no FSS based liquid sensor seems to exist. The nearest equivalent of the proposed sensor are EBG based sensors [20] and [21]. With a maximum measured sensitivity of 8.65%, the proposed sensor offers a better sensitivity than the EBG based [20] which offers a sensitivity of 0.875% while no sensitivity derivation is given in [21]. Further, compared to the two i.e., [20] and [21], the proposed design single-unit nature makes it cheaper to design, fabricate, use as well as eliminates the complexities that come with intricate assembly of multiple units' sensors. The proposed design, however, is a bit wider than the two. Investigations on the sensor's behavior for a reduced arrays size were not done in this instance. The initial objective was the simplicity of the design and alongside that, care was being taken to ensure the FSS array was large enough to adequately model the structure in the design work like they were electrically infinite in size at the microwave frequency. The current prototype is presented as proof of concept and can be further investigated in terms of size. In [13], a sensor capable of detecting different LUTs is presented. The sensor is based on single polarized RFID as opposed to the proposed FSS based design which exhibits a stable dual polarization. Further, it uses a larger amount of LUT, a minimum of 20 ml, compared to the 14 ml required for the proposed design, for the detection process. It also does not give sensitivity measurements.

Frequency selective surfaces (FSS), discussed in Chapter 2, Section 2.5, are electromagnetic filtering structures consisting of arrays of periodic conductors [23] [24] on a supporting dielectric material and are a type of metamaterial [25]. FSS modify the incoming electromagnetic signal in relation to their intrinsic resonant frequency. Their responses are dependent on the geometry, elements' spacing, dielectric material thickness, dielectric properties as well as those of its surroundings [24]. This behaviour can be exploited to develop contact-less sensors. FSS sensors have been designed to monitor structural health [26]-[28], temperature and strain sensing [29], breathing [30], strain [31] and dielectric characterization [32] [33].

In this chapter, evaluation of dielectric properties of analytes (LUT) has been undertaken using a frequency selective surface (FSS) based sensor. The proposed sensor detects liquids falling onto the sensor surface. In the new concept outlined, the sensing function is achieved by altering the capacitance between adjacent FSS elements when materials of different electrical characteristics are inserted in trenches. The change in capacitance produces a change in the frequency resonance, which is detected as a transmission response of the FSS. Trenches were dug in the dielectric around the conductors. The basic principle of operation of the proposed sensor is the excitation of a resonant mode of the FSS with the trenches filled with different liquids under test (LUT). The FSS sensor operates at about 4.6 GHz with a broad range of frequencies in relation to the LUT. To the best of authors' knowledge, this is the first design based on the FSS structure for sensing liquids. The proposed sensor is scalable and can be re-designed to operate in different frequency bands. The motivation of this work is the creation of a wireless sensor for the detection of liquids falling onto the surface. The main application is in the detection of medium to large surfaces that can be adjusted by the array size. The curve fitting approach is employed to estimate the LUT complex permittivity and sensitivity analysis based on the shifted parameters.

5.3 FSS Sensor/Detector Design

This section discusses the design and optimization of the square loop FSS sensor unit cell.

5.3.1 The FSS Sensor Unit Cell Design

Figure 5.1 depicts the geometry of the unit cell element of the FSS sensor design with trenches surrounding the loop conductor. For simplicity, the FSS was simulated as an infinite structure using a unit cell, Figure 5.1(a), with periodic boundaries. A square loop FSS element was used because it offers dual polarization and a good angle of incidence response [34]. A band stop FSS was selected as changes in the sensors could be observed through nulls in the transmission responses. The FSS was designed, simulated, and tested using CST Microwave Studio^{TM}. In the design, the square loops were made of copper. RT/Duroid 5880 of thickness 3.175 mm, dielectric constant, ε_r, 2.2 and loss tangent (tan δ) 0.0004, according to the manufacturer's datasheet [35], was used as the substrate supporting the FSS sensor square loops. The cell has 1 mm wide and 2 mm deep trenches around its edges. Trenches were introduced around the square loop as shown in Figure 5.1(b). The trenches reduce the amount of dielectric material which decreases the permittivity and losses of the FSS in free space. Figure 5.1(c) is a top view of a two-unit cell array.

The unit cell and the square loop dimensions were optimized to operate at 4.6 GHz. The gap *x* between the conductor loop and the edge of the unit cell is 1 mm. The periodicity, *P*, of the square loop array is the sum of *g*, the gap between adjacent loops, and d_2, the length of the conductor. d_1 is the length of the unit cell element. The dimensions are shown in Table 5.1.

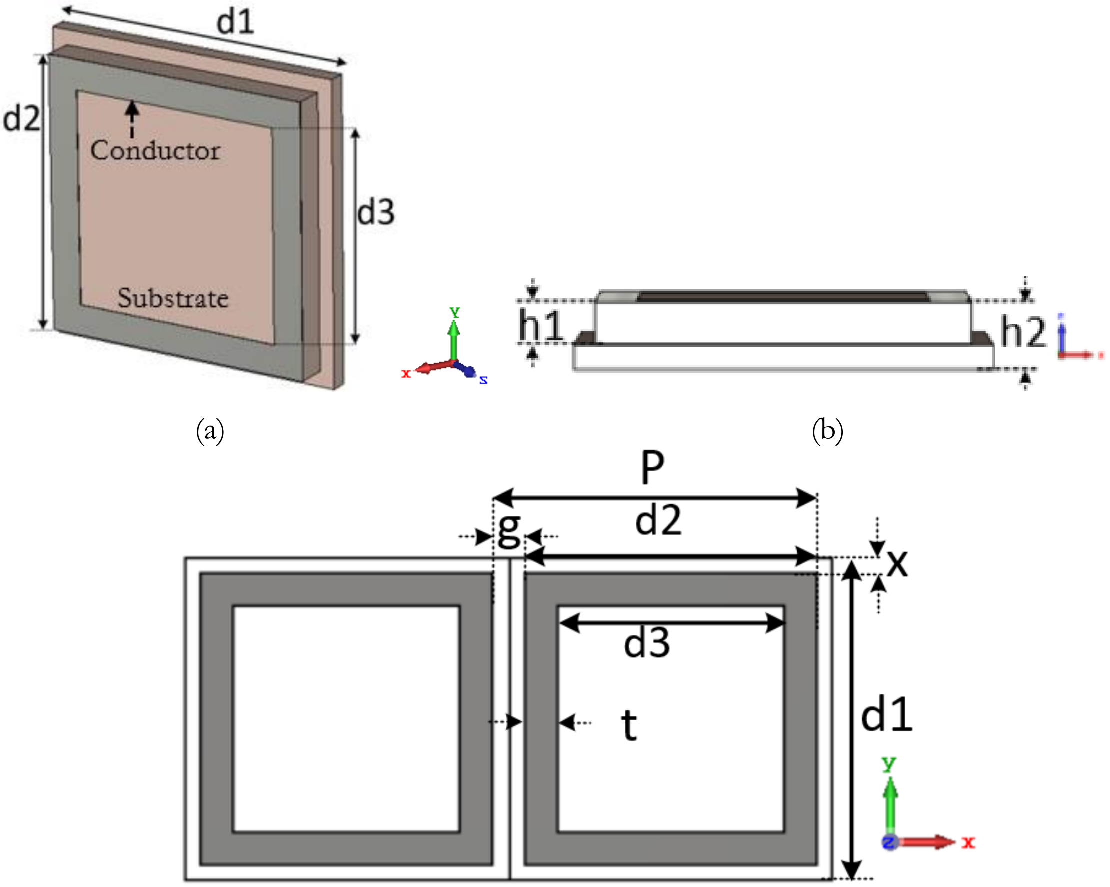

(a) (b)

(c)

Figure 5.1 (a) the perspective view of the FSS cell (b) its cross-sectional view (c) two-unit cell array and dimensions of the FSS

Table 5.1 The dimensions of the unit cell

Parameter	d_1	d_2	d_3	P	g	x	t	h_1	h_2
Value (mm)	20	18	14	20	2	1	2	2	3.175

Figure 5.2 shows the simulated transmission response of the FSS for angle of incidence 0°, TE 45° and TM 45°. TE denotes the E-plane response whereas TM denotes H-plane response. Resonance of the unit cell occurred at normal incidence with a frequency of 4.6 GHz with no appreciable frequency shift at TE 45° and TM 45° i.e., 45° off broadside illumination for TE

and TM polarization. This demonstrates angular stability as well as stable polarization.

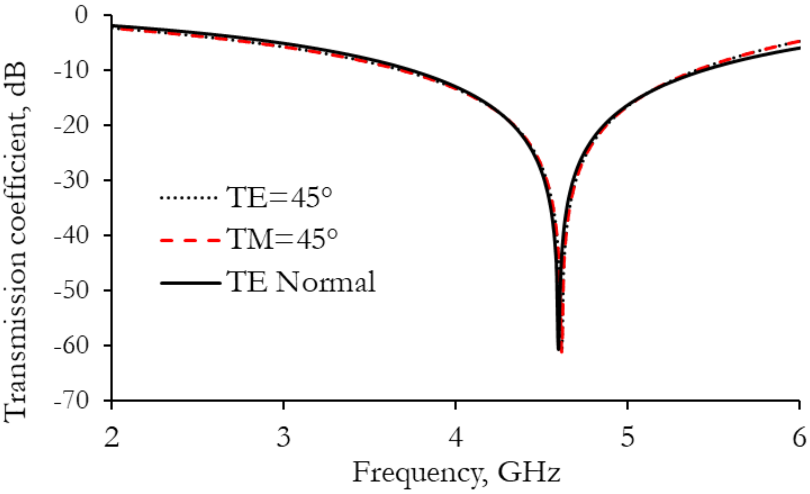

Figure 5.2 Simulated transmission responses of the unit cell

5.3.2 The Equivalent Circuit of Square Loop

The square loop FSS has band rejection frequency response dependent on its physical dimensions [36]. It is a relatively simple shape and ideal to build a prototype for performance assessment or application whose equivalent circuit (EC) has variously been investigated by [37]-[40]. The approximate intrinsic capacitance and inductance of the EC were obtained using the approximation presented in [40], the earliest available EC approximation based on conducting strips. Figure 5.3(a) presents the equivalent circuit (EC) of the square loop band stop filter. The EC model provides a simple and fast method of FSS analysis that is supported by transmission line analogy in which equivalent intrinsic capacitive (C_i) and inductive (L_i) lumped components of the FSS can be calculated. η is the characteristic intrinsic impedance of free space equal to 377**Ω**. As outlined in chapter 2 section 2.5, an FSS square loop acts as a bandstop filter. The proposed FSS array is symmetrical with periodicity P and a gap g between two adjacent conductor loops. It can be represented as lumped elements consisting of capacitance (C_i) and Inductance (L_i). Gap g represents the capacitive elements while the length of the conductor represents the inductive element. Resonance occurs when the perimeter of the loop is approximately one wavelength. The inductance and capacitance values determine the square loop resonance frequency, ω and as in all other filtering circuits is expressed as

$$\omega = \frac{1}{\sqrt{L_i C_i}} \tag{5.1}$$

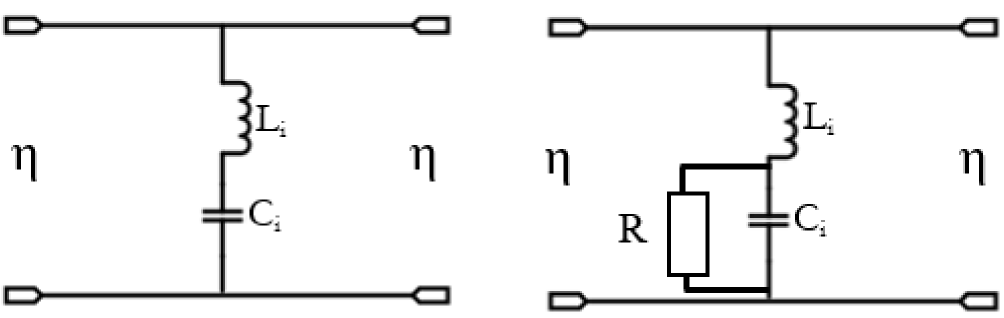

(a) (b)

Figure 5.3 Equivalent circuit models: (a) the square loop FSS (b) the FSS with a lossy liquid in the trenches

The dielectric material affects the reflection or transmission responses. With a finite thickness, the dielectric material effect on the FSS structures can be explained using the equivalent circuit analysis. The designed inductive FSS is a square loop of width (t). Its intrinsic capacitance C_i and inductance, L_i, for TE incident wave can be approximated from path capacitance and strip inductance using equations (5.2) and (5.5) respectively to estimate the L_i and C_i values [40]. For a transverse electrical (TE) incidence wave, the vertical strips of the FSS act as a L_i impedance in the EC, and the horizontal gratings as a C_i impedance [35].

$$\mathrm{Ci} = \frac{2\mathrm{P}}{\eta\pi c}\left\{\mathrm{In}\left(\mathrm{cosec}\left(\frac{\pi \mathrm{g}}{2\mathrm{P}}\right) + \mathrm{G}(\lambda, \mathrm{g}, \mathrm{P})\right\}\right. \tag{5.2}$$

where C_i is the intrinsic capacitance between adjacent loops, determined by periodicity P and the gap g between adjacent loops. $G(\lambda, g, P)$ is a correction term expressed in:

$$G = \left\{\frac{Q_2 cos^4\left(\frac{\pi \mathrm{g}}{2\mathrm{P}}\right)}{1+\mathrm{Q}_2\sin^4\left(\frac{\pi \mathrm{g}}{2\mathrm{P}}\right)} + \frac{1}{16}\left(\frac{\mathrm{P}}{\lambda}\right)^2\left(1 - 3\sin^2\left(\frac{\pi \mathrm{g}}{2\mathrm{P}}\right)\right)^2 \cos^4\left(\frac{\pi \mathrm{g}}{2\mathrm{P}}\right)\right\} \tag{5.3}$$

and the factor Q_2 is as expressed in:

$$\mathrm{Q_n} = \frac{1}{\sqrt{1-\left(\frac{2\mathrm{P}}{\mathrm{n}\lambda}\right)^2}} - 1 \tag{5.4}$$

where the value of n, in this case, is 2. The approximation equations have been obtained using the equivalent static method that employs a static field in the aperture due to the incidence of the two lowest modes [40], hence the value of 2 for n in equation (5.4). To approximate the strip inductance, L_i, the g in the correction term, equation (5.3), is substituted for by t. Li is expressed as:

$$\mathrm{L_i} = \frac{\eta\lambda^2}{32\mathrm{P}\pi\mathrm{c}\left\{\ln\left(\mathrm{cosec}\left(\frac{\pi t}{2P}\right)+G(\lambda,t,P)\right)\right\}} \tag{5.5}$$

where L_i is the strip inductance for conductor loops of periodicity P, width t, speed of light c and free space characteristic impedance η.

From equations (5.2) and (5.5), the theoretical lumped component values for free-standing FSS are: L_i is equal to 3.8114 nH and C_i is equal to 214.26 fF (appendix 5.1). This capacitance needs to be adjusted for the dielectric effect. In a one-sided substrate, the capacitance increases proportionally to the effective relative permittivity [23] and [41] given by

$$\varepsilon_{eff} = \frac{\varepsilon_r + 1}{2} \tag{5.6}$$

Although equation (5.6) is a general equation for the cases when the substrate is sufficiently thick (> λ/5) [36], it can be a good approximation in the case of square loops even in substrates of thicknesses of about 0.05λ [41]. Therefore, from equation (5.6), the resulting capacitance when compensated for the dielectric effect is C_i = 342.9 fF. The resonant frequency for the LC circuit is approximately 4.5 GHz, within the expected 5% error margin [40] of 4.3 GHz, FSS resonance frequency of the simulation of the dielectric loaded FSS i.e., without trenches. In liquid sensing, the dielectric losses of the liquids in the trenches can be high. These losses can be represented as a resistor in parallel with the capacitor as shown in Figure 5.3(b).

5.3.3 Parametric Analysis

A parametric study was conducted to determine the behaviour of the FSS as the trenches' depth (h_1) is incrementally increased from 0.0 mm to 3.0 mm, at 0.5 mm intervals. Figure 5.4 shows the effect of changing trench depth (h_1) on resonant frequency and the corresponding capacitance. From the model, the inductance is constant (L_i = 3.8114 nH) as the parameters it depends on i.e., periodicity P, conductor width t, angle of incidence θ as well as if the incidence is TE or TM are all constant [22]. The FSS frequency at each trench depth h_1 was obtained through simulations. From equation (5.1), C_i for the frequency, f, at each trench depth h_1 was calculated (appendix 5.2). A plot of capacitance, C_i, and frequency, f, versus the trench depth h_1 was plotted, Figure 5.4. From curve fitting technique of the capacitance, C_i, curve, equation (5.7) was obtained. Reducing dielectric material around the conductor decreases the effective permittivity and thus the capacitance, hence increasing the resonant frequency. The capacitance as a function of depth, h_1, was obtained as the polynomial expression:

$$C_i = -3.78h_1^3 + 25.14h_1^2 - 58.10h_1 + 359.76 \text{ fF} \tag{5.7}$$

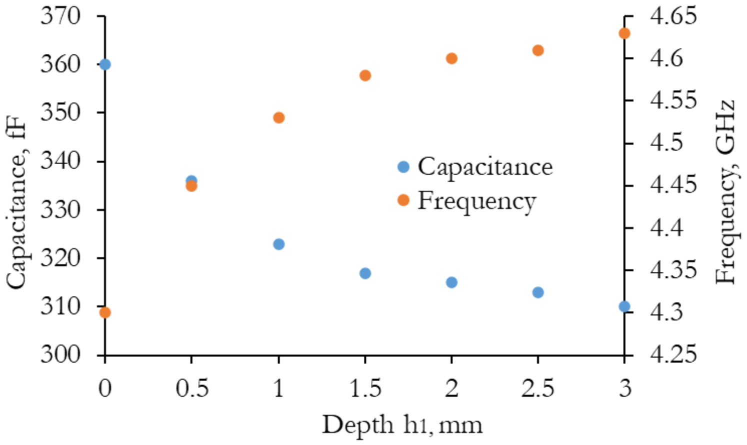

Figure 5.4 A plot of capacitance and frequency vs the trench depth h_1 for the simulated model

To assess the potential behavior of the proposed FSS structure (Figure 5.1) as a liquid sensor, simulations were conducted with the 2 mm wide, and 2 mm deep trenches filled with liquid materials of various dielectric constants, and loss tangents. Figure 5.5 illustrates a section of the FSS structure with trenches filled with liquid. Figure 5.5(a) is the top view while Figure 5.5(b) is the cross-sectional view of the LUT filled trenches.

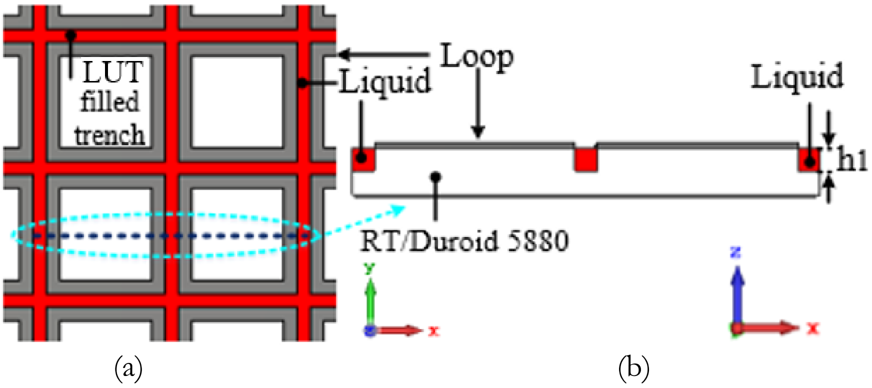

(a) (b)

Figure 5.5 The (a) top view and (b) cross sectional view of a section of the FSS sensor LUT-filled trenches

In the initial study whose results are depicted in Figure 5.6 and Figure 5.7, the dielectric permittivity was varied from 1 to 19, with the loss tangent fixed at 0. The resonant frequency decreased with increase in the dielectric constant, Figure 5.6. From equation (5.1), capacitance C_i due to liquids of varying ε_r values in the trenches were calculated as explained in appendix 5.3. A plot of the capacitance C_i and frequency f versus the ε_r was obtained, Figure 5.7 from which using curve fitting function, equation (5.8) for was obtained from the plot. It shows that C_i increases linearly with ε_r as

$$C_i = 33.31\varepsilon_r + 288.90 \text{ fF} \tag{5.8}$$

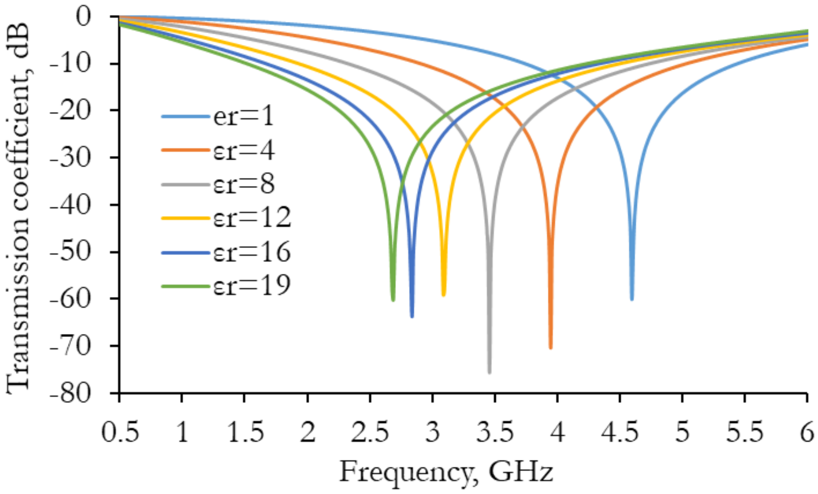

Figure 5.6 Simulated S_{21} of the FSS with liquid of various ε_r in the trenches at h_1= 2 mm

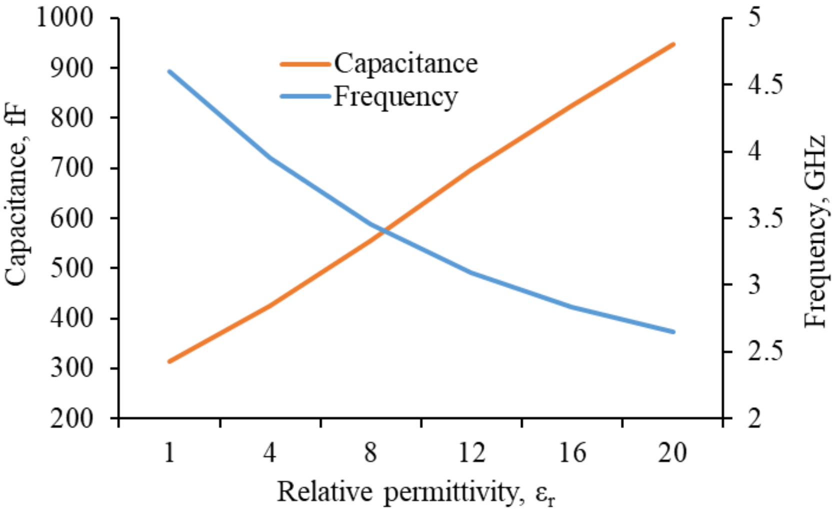

Figure 5.7 Plot of frequency and capacitance as permittivity ε_r of liquid in trench increases

Simulation was also conducted to investigate the effect of changes in loss tangent (tan δ) on the transmission response and resonance frequency and the results are shown in Figure 5.8 and Figure 5.9 respectively. The permittivity of the liquid was kept at 8 while the loss tangent varied between 0 and 0.9.

The depth of the null in the transmission coefficient curve decreases with the increase in loss tangent. A small decrease in resonant frequency is also observed, with a maximum of about 6% shift for a value of tan δ of 0.9.

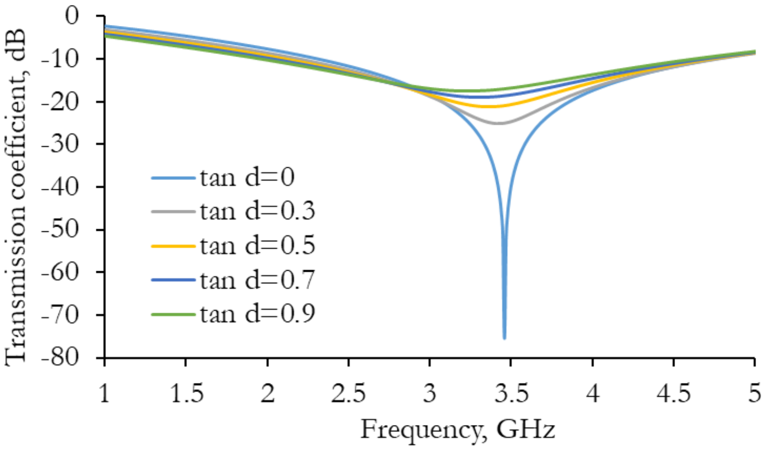

Figure 5.8 Simulated S_{21} versus tan δ of the liquid in the trenches for $\varepsilon_r = 8$

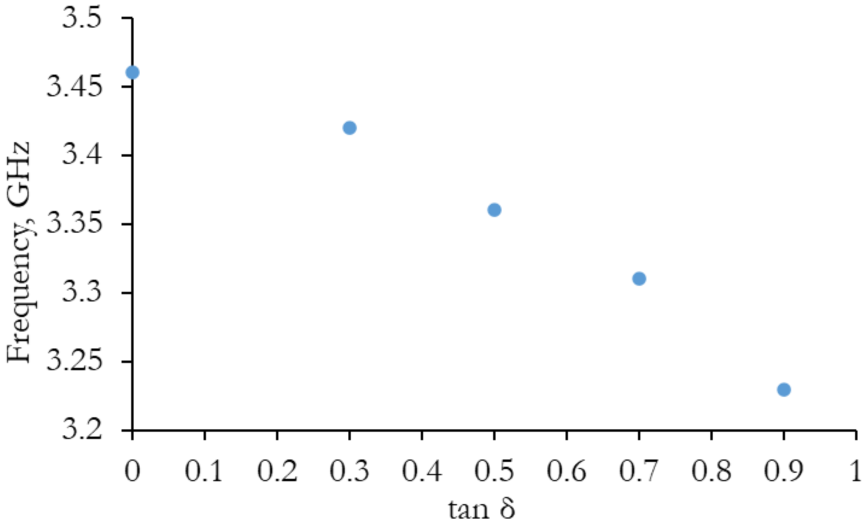

Figure 5.9 Simulated sensitivity of the FSS structure: dependence of the resonant frequency on tan δ.

Further simulations to investigate the behaviour of the proposed sensor for different trench depths, h_1, filled with LUT's of different relative permittivity, ε_r, were done. Simulations were conducted for trench depths 1 mm, 2 mm and 3 mm filled with LUT of low ε_r of 2, medium ε_r of 4 and high ε_r of 20 were done. The results are shown in Figure 5.10. The results show that, for each of the three cases tested, the overall shift in resonance frequency is minimal i.e., the resonance frequency shifts minimally with the trench depth for each of the LUT of the different relative permittivity. The LUT with high relative permittivity however displays a slightly higher variance of the resonance frequency with trench depth h_1 whereas that of the LUT of lower ε_r shows almost no variance.

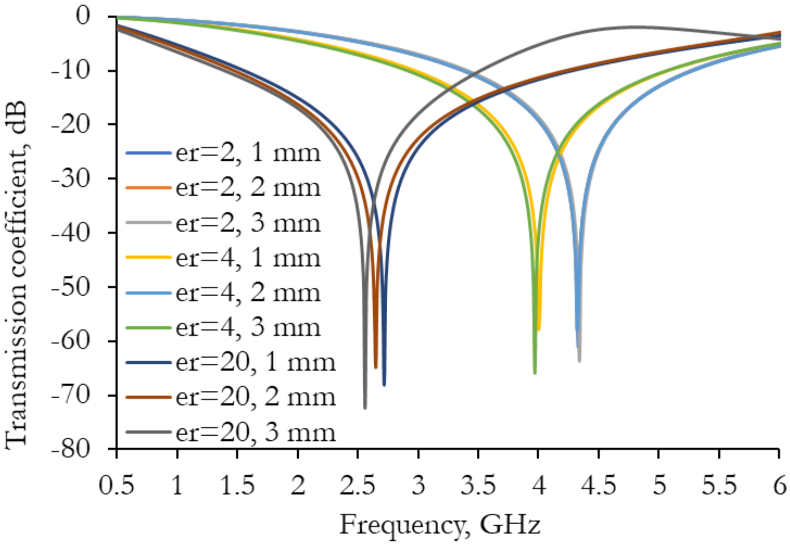

Figure 5.10 Simulated analysis on the effect on S_{21} by the trench depth and relative permittivity

5.3.4 Sensor study for readily available liquids

Five readily available chemical liquids were used to authenticate the sensing/detecting functionality of the proposed design. These were Butan-1-o1, Propan-2-o1, Ethanol, and Methanol whose dielectric properties at 5 GHz and 20°C have been determined and published by National Physical Laboratory (NPL) [43] and Xylene from [44] and are shown in Table 5.2.

Table 5.2 Electrical characteristics of the LUTs [43]

Liquid	**Relative permittivity ε_r**	**Loss tangent (tan δ)**
Butan-1-o1	3.29	0.47
Propan-2-o1	3.8	0.64
Ethanol	5.08	0.96
Methanol	12.42	0.65
Xylene	2.57	0.018

Simulations were conducted with the trenches filled with each of the five liquids (LUTs). The transmission coefficient, S_{21}, of the unit cell elements when the trenches are filled with the different LUTs are shown in Figure 5.11. It shows that the simulated resonance frequency of the FSS with trenches filled with LUT shift towards lower frequencies from the reference resonance frequency i.e., that of the air. This agrees with observations in [45] and [46].

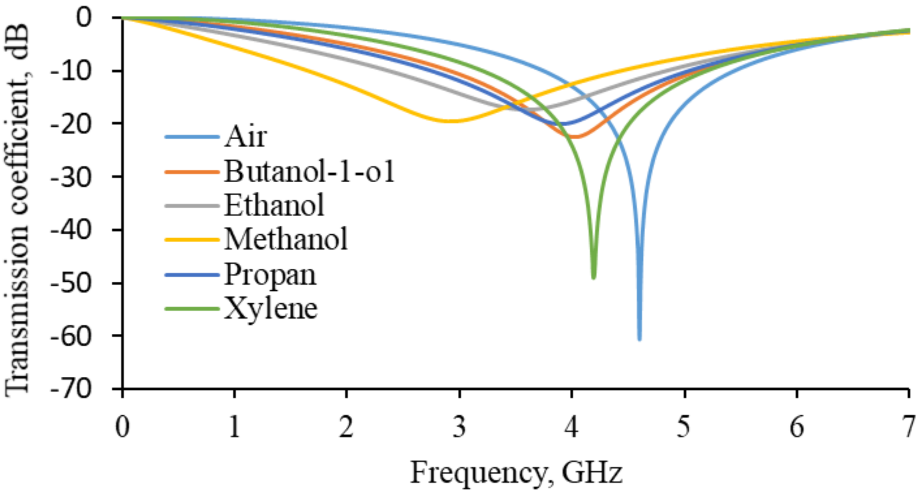

Figure 5.11 Simulated S_{21} of the proposed sensor for the various LUTs in the trenches

5.4 Fabrication and Measurements

As mentioned in Section 5.1, the initial project plan was to design and fabricate a 3D printed liquid sensor. The design was printed inhouse using PLA. The FSS conductive tracks were manually applied using a painter's brush. Manual painting of the conductive tracks minimises the manufacturing costs as no costly equipment are required. However, during the testing, the LUTs were found to react with the substrate causing it to be pervious to the LUT's as well as buckle. It buckled and twisted almost immediately when Xylene was inserted into the trenches. However, with the other LUTs, the buckling did not occur immediately but was discovered to have occurred two days after the initial testing. The perviousness could also have been caused by printing errors such as the print infill being less than 100%. An inert 3D printable material could not be found with which to realise the 3D printed sensor. A milled RT/Duroid 5880 version of the proposed design was fabricated instead as discussed in Subsection 5.4.1. However, the 3D printed sensor was still viable as a disposable single use sensor, and it is discussed in Subsection 5.6.

5.4.1 Fabrication

The FSS unit cell with dimensions as in Figure 5.1 and Table 5.1 was extended to a 9 x 9 array to create a model of the sensor. The model of the sensor is shown in Figure 5.12. It is shown with the trenches filled with an LUT. The liquid filling the trenches is depicted in red colour in the model. To make the sensor robust and able to hold the liquid within it safely, the edge around the model's boundary was made 5 mm wide. The model's dimensions are 192 mm x 192 mm. The prototype was fabricated at Printech Circuit Laboratories using standard printed circuit boards (PCBs) procedures. The FSS loops were etched followed by milling using a high-precision milling machine to create the trenches around the loops.

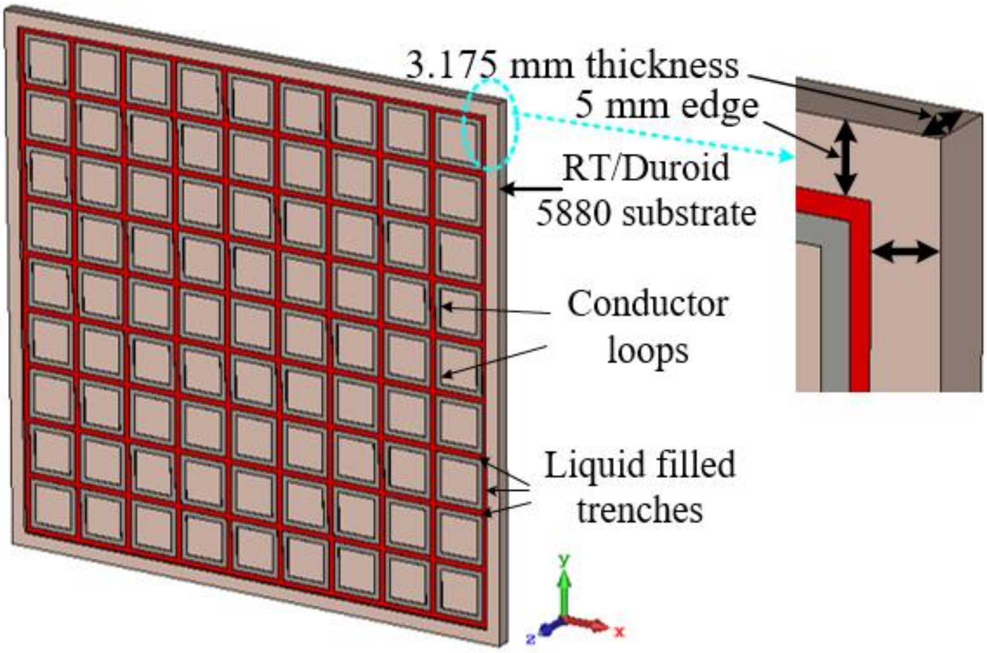

Figure 5.12 The perspective view of the FSS sensor prototype with liquid filled trenches

The fabricated sensor prototype is shown in Figure 5.13. Figure 5.13 (a) is the sensor prototype while Figure 5.13(b) shows a close-up of the milled trenches. Figure 5.13(c) is the LUTs sensing/detection i.e., the measurements set up.

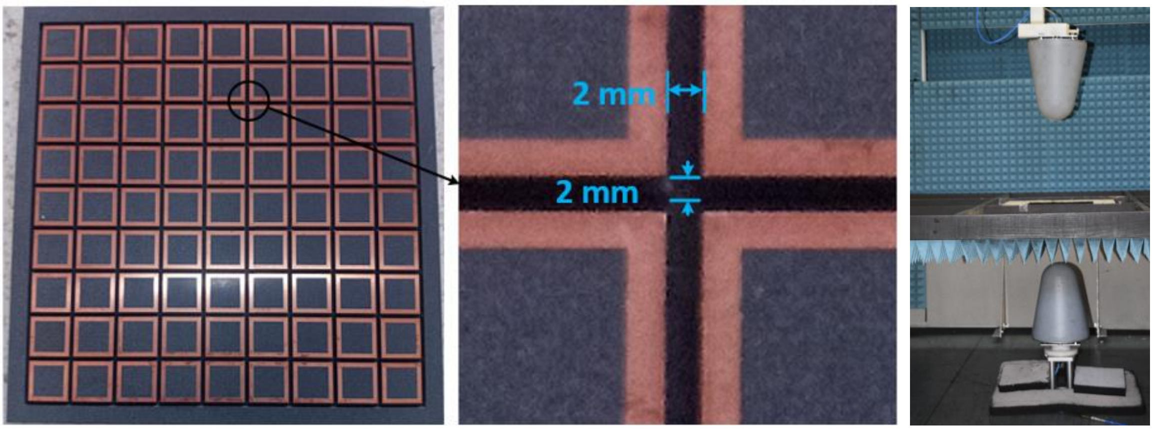

(a) (b) (c)

Figure 5.13 The (a) fabricated FSS sensor (b) trench dimensions (c) measurement set up

5.4.2 Measurements and Results

A Marconi Instruments microwave test set 6204B was used to measure the transmission response of the FSS sensor in a plain wave chamber. The plain wave screen was laid horizontally (Figure 5.13(c)). This is to enable the sensor to hold the LUTs for measurements purposes. The measurements were taken initially with the trenches empty i.e., air filled. The trenches were then filled using a syringe with the correct amount of liquid (14 ml) and the transmission response

(S_{21}) was measured. The S_{21} results are shown in Figure 4.14. The FSS structure was kept level horizontally using a bubble level to ensure that the liquid was uniform throughout the structure. Table 5.3 tabulates both the simulated and measured resonance frequency (f_s) and the frequency shift (Δf) from the reference of the LUT i.e., resonance when trenches are empty.

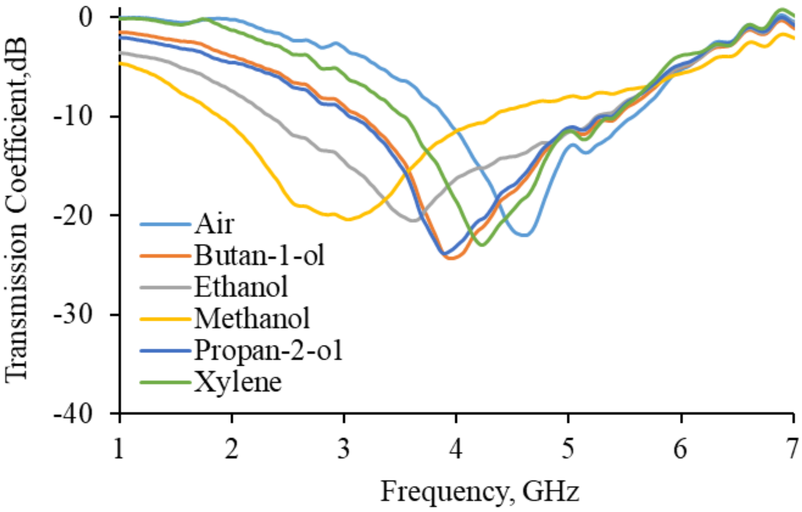

Figure 5.14 The measured S_{21} of the proposed sensor for various LUTs in the trenches

Table 5.3 Measured and simulated resonance frequency and frequency shift of the sensor

LUT	$f_s\ GHz$		$\Delta f\ GHz$	
	Simulated	Measured	Simulated	Measured
Butan-1-o1	4.02	3.92	0.58	0.68
Ethanol	3.59	3.61	1.01	0.99
Methanol	2.92	3.01	1.68	1.59
Propan-2-o1	3.9	3.83	0.7	0.77
Xylene	4.19	4.24	0.41	0.36

The resonance frequency for the measured results shows frequency shift towards lower frequencies from the resonance frequency of air i.e., the reference resonance frequency. This is consistent with the simulated results. The resonance points shift to the lower frequencies when the trench is filled with liquids of high dielectric constant. The differences between simulated and measured results could be due to fabrication errors, potential loss of liquid when inserting into the trenches, quality of the LUT, and potential differences in the permittivity values of LUT from those given in [43].

5.5 The Proposed Sensor Performance Evaluation

5.5.1 Sensitivity analysis

The proposed design sensor prototype performance evaluation was conducted with the integrated fluidic trenches on the FSS filled with the five different liquids of different electrical properties described in subsection 5.2.4. The sensitivity, *S,* as a performance parameter was used to evaluate the sensor performance according to the criterion proposed in [20] and [45]. To estimate the sensitivity, *S,* of the device, the state, and responses of air-filled (empty) trenches was chosen as the reference.

The proposed criterion gives the mathematical expression of the sensitivity, *S*, of the sensor as:

$$\mathrm{S} = \frac{\Delta \mathrm{f}/\mathrm{f_s}}{\Delta \varepsilon} \tag{5.9}$$

Δf is expressed as $(f_o - f_s)$ where f_o and f_s are the resonance frequency of the FSS when filled with air and the LUT respectively. $\Delta\varepsilon$ is $(\varepsilon_s - \varepsilon_o)$ where ε_s and ε_o are dielectric constant of the LUT in the trench and air respectively. Table 5.4 shows the frequency shift and the computed sensitivity (S) of the various LUTs.

Table 5.4 The measured performance analysis of the sensor

LUT	**Resonance Frequency (GHz)**	**Frequency Shift (GHz)**	**Sensitivity (%)**
Air	4.6	-	-
Butanol-1-o1	3.92	0.68	7.58
Ethanol	3.61	0.99	6.72
Methanol	3.01	1.59	4.63
Propan-2-o1	3.83	0.77	7.18
Xylene	4.24	0.36	8.65

5.5.2 Material dielectric characterization

The complex permittivity (ε_r) and loss tangent (tan δ) of the LUT were determined using mathematical models derived using polynomial curve fitting technique, which generates an imperative equation that best fits the given set of data points [2] and [20]. The resonating frequency, f_s, and bandwidth of frequency shifting, Δf, parameters were used to determine the value of the permittivity and loss tangent of LUT, respectively. A Matlab code (appendix 5.4) was developed to compute the coefficient of the polynomial expression of the dataset. The necessary polynomial expressions that best fit the given data set were generated to a 3rd degree for greater accuracy. The resonating frequency (f_s) and frequency shift (Δf)from the reference were used to determine the dielectric constant and loss tangent of the LUT respectively to a good degree of accuracy. The variation of resonating frequency (f_s) and (ε_r) of LUT was formulated using the third-order polynomial expression:

$$\varepsilon_r = -1.68f_s^3 + 24.86f_s^2 - 121.54f_s + 198.72 \tag{5.10}$$

This formulation determines the permittivity of the samples where ε_r is the relative permittivity (dielectric constant) and f_s is the resonance frequency of the FSS with an LUT in the trenches. A similar analysis was conducted to derive the loss tangent (tan δ). The frequency shift, Δf, of the resonance frequency when the FSS trenches is filled with LUT from when it is air-filled were observed and recorded. The relationship between the frequency shift, Δf, and the loss tangent (tan δ) was derived as a 3rd order polynomial best fit of the given dataset and is expressed by

$$tan\,\delta = -2.03\Delta f^3 + 4.31\Delta f^2 - 1.35\Delta f + \ 0.04 \tag{5.11}$$

where tan δ is the calculated loss tangent and Δf is the LUT frequency shift from the reference. Equations (5.10) and (5.11) and Matlab code (Appendix 5.5) that was developed were used to derive the estimated values of the dielectric properties of the LUTs and are shown in Table 5.5. The derived dielectric constant and loss tangent of samples of the LUT were compared to the National Physical Laboratory (NPL) determined and published values [43] and [44] for Xylene, to validate the data. The derived results demonstrate a good agreement with actual published permittivity and loss tangents values of the LUTs. The root means square error between the actual and the derived permittivity and loss tangent were also calculated. The highest error of 1.7% and 5.56% for dielectric constant (ε_r) and loss tangent (tan δ) respectively validate the performance of the device.

These errors are attributable to various factors. These could be geometrical mismatch between the simulated and the fabricated prototypes, possible reaction between the LUTs and the surrounding atmosphere. Other sources of errors could be due to scattering parameters of the microwave sensor being influenced by electric and magnetic properties of its surroundings, which can be reflected in the S_{21} of the resonator. Impurities and LUTs in the trench can have effect on the amplitude as well as the resonance frequency of the sensor [2]. The geometrical errors can be mitigated by using higher precision equipment while the fractional errors due to possible chemical reactions of the samples can be modeled which is beyond scope of this study. The proposed sensor can also be used to estimate dielectric properties of an unknown LUT in the sensor trenches. Using the resonance frequency (f_s) of the FSS when its trenches are filled with the unknow LUT, and the bandwidth of frequency shift (Δf) from the reference (the FSS resonance when trenches are empty), its ε_r and tan δ dielectric properties can be derived to a good degree of accuracy from equations (5.10) and (5.11). Thus, using the proposed sensor, determination of the dielectric constant and loss tangent of unknown liquid substances can be made.

The results of resonance point of Butanol-1-o1 and Propan-2-o1 are almost indistinguishable. This is because of their close dielectric parameters. This implies that the effectiveness of the sensor is dependent on the differences between the dielectric parameters of the LUTs.

Table 5.5 Measurements derived versus published dielectric properties of the LUTs

LUT	**Dielectric constant (ε_r)**			**Loss tangent (tan δ)**		
	Published [43]	**Derived**	**RMS Error (%)**	**Published** [43]	**Derived**	**RMS Error (%)**
Air	1	-	-	-	-	-
Butanol-1-o1	3.29	3.34	1.6	0.47	0.48	2.13
Ethanol	5.08	5.10	0.31	0.96	0.96	0.0
Methanol	12.42	12.42	0.009	0.65	0.65	0.0
Propan-2-o1	3.8	3.74	1.7	0.64	0.63	1.56
Xylene	2.57	2.57	0.19	0.018	0.017	5.56

*Root mean square (RMS) computed as $\frac{\sqrt{(Published-Derived)^2}}{Actual}$

5.6 3D Disposable 3D Printed Liquid Sensor

In this section, the 3D printed version of the sensor is presented. As outlined in Section 5.1 and Section 5.4, problems of reactions between the LUT and the PLA substrates was found with the 3D printed version. However, because it is easy, quick, and inexpensive to fabricate, it is still viable as a disposable single use sensor. Its design and simulation are discussed in Subsection 5.6.1.

5.6.1 The sensor design and simulations

A disposable 3D version of the sensor was fabricated to test the applicability of 3D in the sensor design and is presented in [47]. Polylactide acid (PLA) substrate was used in this version. PLA electrical characteristics are close to those of RT/Duroid 5880. They are, relative permittivity, ε_r of 2.4 and a tan δ of 0.01 [48]. The dimensions of the FFF version of the sensor are the same as in Table 5.1 except for h_2 which was set at 5.2 mm. They are shown in Table 5.6. The thicker bottom allows for a robust bottom of the printed sensor to hold liquids.

Table 5.6 Dimensions of the unit cell

Dimensions	d_1	d_2	d_3	h_1	h_2	P	g	t	x
Value (mm)	20	18	14	2	5.2	20	2	2	1

5.6.2 Simulation results of the 3D version sensor

The designed sensor was re-simulated with the new material, PLA, to test its behavior in terms of transmission coefficient. Figure 5.15 shows the simulated transmission response, S_{21} of the

FSS for TE angle of incidence behaviors at normal and 45° as well as TM 45°. The results indicate that the resonance of the unit cell occurred at normal incidence with a frequency of 4.43 GHz with no appreciable frequency drift at TE 45° and TM 45°. The slight change of resonance frequency from 4.6 GHz to 4.43 GHz could be due to the new substrate material which has a slightly different permittivity and loss tangent as well a bigger bottom thickness.

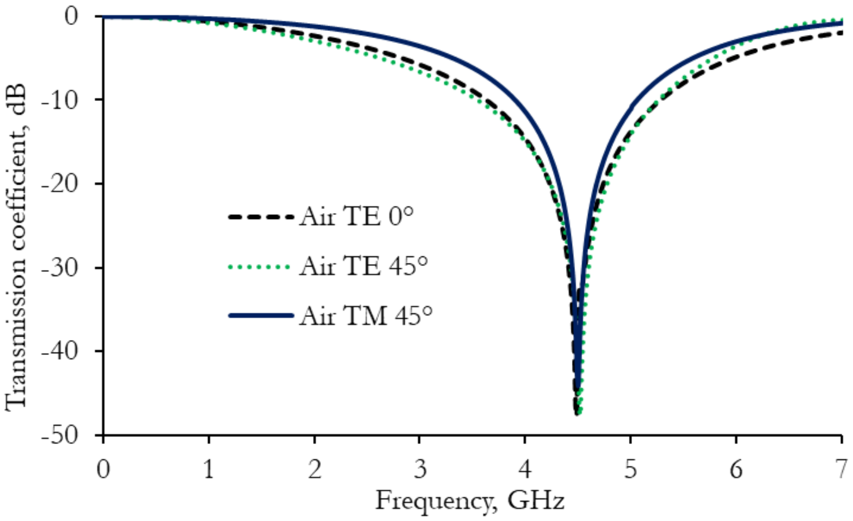

Figure 5.15 Simulated transmission responses of the loop FSS

As in the milled version, the resonance frequency of the unit cell filled with air i.e., free space was considered the sensor's reference.

Simulations were then conducted with the trenches filled with various LUT as depicted in Figure 5.5. The LUTs are the same as in Table 5.2 except Xylene which was found to react with the FSS substrate on contact. The simulation results are presented in Figure 5.16 and Table 5.7. They show that when an LUT fills the trenches, the band stop center frequency shifts to the left. This indicates that the stopband of the FSS can be tuned using the liquid dielectrics. The results shows that the liquids with higher ε_r, produces a bigger frequency shift, Δf, from the reference.

It is also observed that the results due to Butanol-1-o1 and Propan-2-o1 are nearly indistinguishable due to their close dielectric constant values.

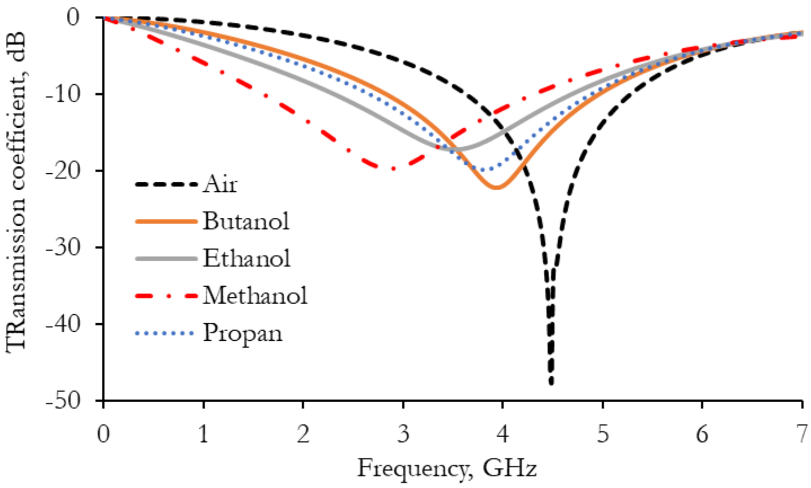

Figure 5.16 The simulated frequency response of the proposed sensor for the various LUTs

Table 5.7 Simulated resonance frequency and shift from reference frequency

	Butanol-1-o1	Ethanol	Methanol	Propan-2-o1
f_s GHz	3.92	3.50	2.87	3.80
Δf GHz	0.51	0.93	1.56	0.63

5.7 Fabrication and Measurement

5.7.1 Fabrication

The sensor fabrication was a two-stage process. The first stage was the printing of polylactide acid (PLA) substrate material. To begin the process, the simulated design unit cell was first extended to a 9 x 9 array to create a model of the proposed sensor. An outer 5 mm wide perimeter edge, 1 mm higher, for liquid containment, was incorporated, making it a 192 mm x 192 mm structure. The cell edges were also raised by 0.175 mm to facilitate application of the silver conductive paint without it flowing onto the surface of the unit cells.

To start the fabrication process, the digital model of the FSS substrate was exported from CST Microwave Studio to an STL file. It was then sent to a Raised 3D printer machine shown in Figure 5.17(a), using CURA software with the print infill density of the print set to 100% which printed the structure as a 26 layers FFF printout. The FFF printed structure substrate material is shown in Figure 5.17(b).

The second stage involved the application of the RS pro Silver Conductive 186-3600 paint [49], Figure 5.17(c), onto the substrate to create the conductive loops. The conductive loops were by-hand painted around the cells using an artist's painting brush. To ensure that this was done in the best way possible, and that the width of the loop's conductor was maintained uniformly, a stencil was printed alongside the substrate and used to apply the paint, Figure 5.17(d). The FFF printed substrate with the by-hand painted square loops is shown in Figure 5.17(e). The silver paint was left for 24 hours to dry. Figure 5.17(f) shows the finished FSS.

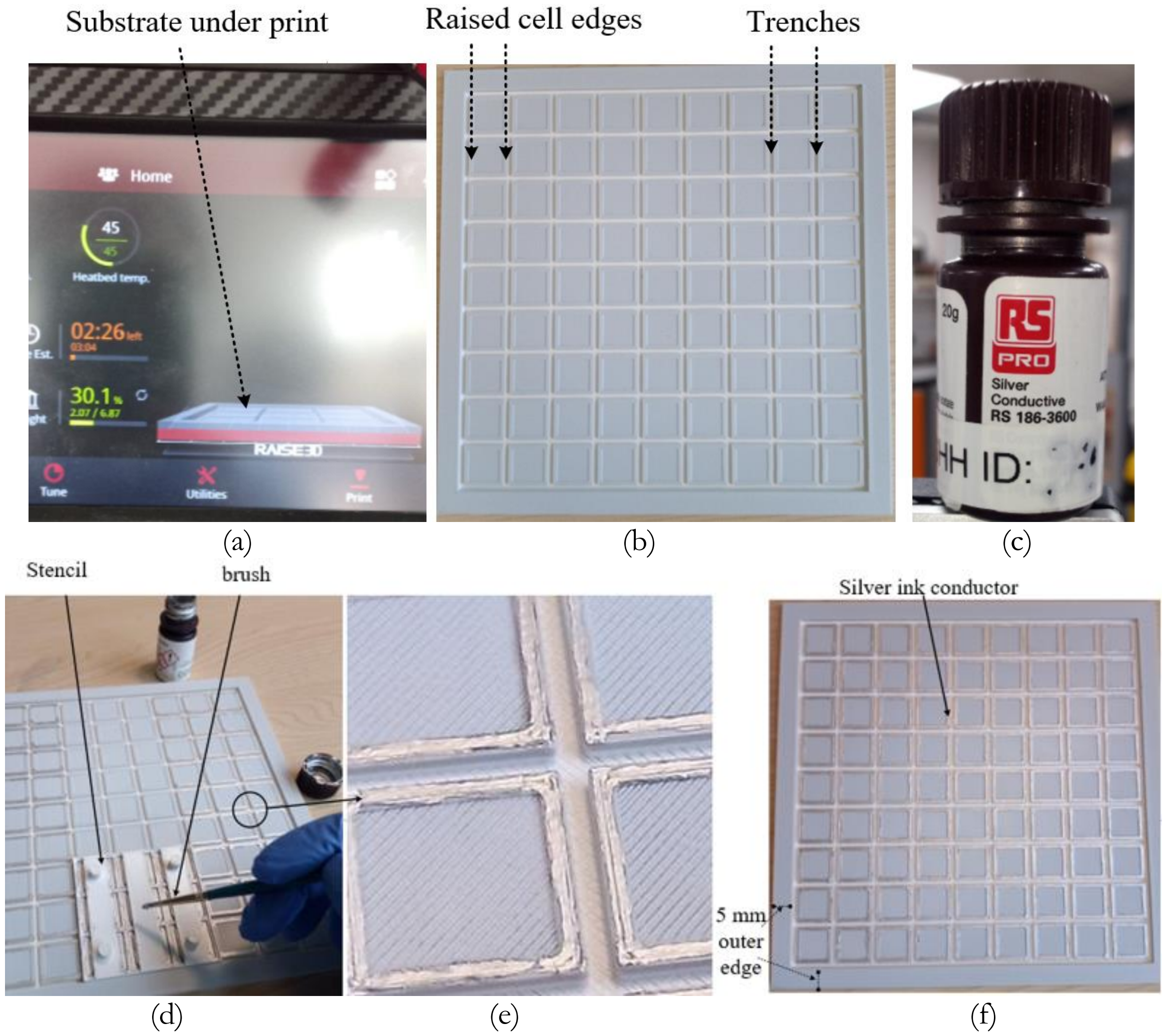

Figure 5.17 The fabrication process of the 3D sensor (a) the printing of the substrate with a Raised 3D printer machine (b) the printed PLA substrate (c) the silver paint the printing of the substrate (d) applying silver loops (e) section of the painted FSS (f) the finished 3D FSS

5.7.2 Measurements and results

Using the Marconi Instruments microwave test set 6204B in a plain wave chamber, the transmission coefficient S_{21} of the FSS was measured with empty trenches. The measurement set up is as in Figure 5.13(c). The trenches were then filled with the liquid chemicals and S_{21} measured to obtain the resonance points for each liquid chemical. The measured frequency resonance of the liquid chemicals deposited in the trenches of the FFF printed FSS sensor were found to be as shown in Figure 5.18. Table 5.8 shows the measured resonance frequency, f_s, and the frequency shift, Δf, from the reference. The results show a trend in frequency shift from the reference frequency i.e., air resonance frequency, consistent with the simulation results. The resonance frequency progressively shifts to lower frequencies as liquid chemicals with higher dielectric constant are deposited in the trenches. A slight deviation was observed in the frequency resonance points in the measured results from the simulated results. A reason for this could be due to errors in the fabrication and measurement processes. Air gaps may exist in the

FFF printed PLA substrate if the printer fails to print 100 percent infill of the substrate. This can potentially affect the relative permittivity of the PLA substrate [50] and [51] and thus the results of any measurements including the frequency resonance point as well as the deviation Δf from the reference.

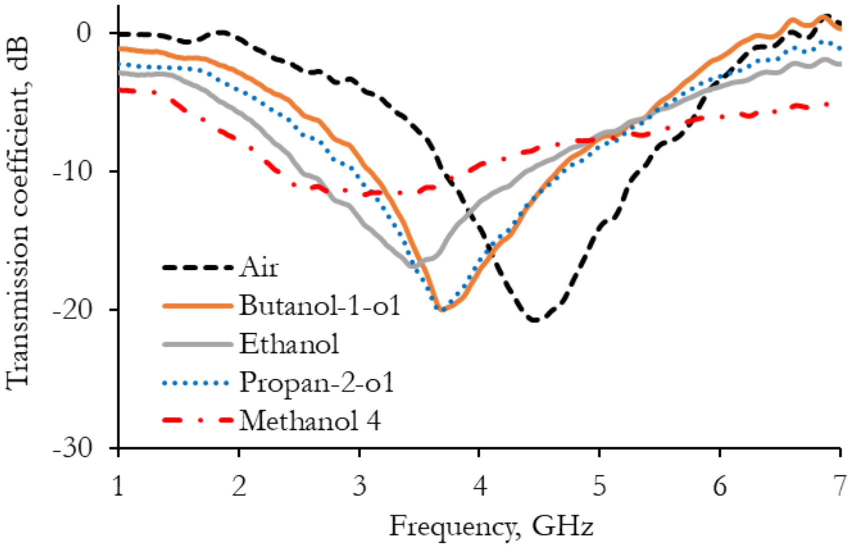

Figure 5.18 The measured frequency response of the proposed sensor for the various LUTs

Table 5.8 Measured resonance frequency and shift from reference frequency

	Butanol-1-o1	Ethanol	Methanol	Propan-2-o1
f_s GHz	3.74	3.49	2.8	3.71
Δf GHz	0.69	0.94	1.89	0.72

5.8 Discussion and Conclusion

A new concept for microwave liquid sensors based on FSS has been demonstrated. The sensor uses trenches between FSS elements to modify the transmission response when liquids with different permittivity are inserted. A mathematical model was developed for the determination of the dielectric constant and loss tangent of the LUT.

The concept for liquid chemical (LUT) identification has been proposed and evaluated based on the shift in the resonant frequency of an the FSS. The evaluated complex relative permittivity, ε_r, and loss tangent, tan δ values were in good agreement with values of the evaluated LUT presented in [43] and [44] for Xylene values at 5 GHz frequency band.

The highest errors in the measured values of the dielectric constant and dielectric loss are within 1.7% for Propan-2-o1 and 5.5% for Xylene respectively. This demonstrates that the proposed microwave sensor is suitable as a low-cost platform for the detection of liquids with good sensitivity and low detection error.

Table 5.9 summarizes the performance analysis of the reported metamaterial EBG detectors closest to the proposed design. It shows that, besides its simplicity, it offers higher sensitivity and thus improved detection performance.

The developed sensor is ideal for instances requiring robust, real-time monitoring at low-cost and low complexity, low-power consumption, and simple fabrication techniques. The independent resonant nature due to each chemical allows the device to be reused for different and various liquids. The contactless nature of the detection process makes it suitable for a safe working environment and is ideal for instances requiring real-time monitoring of liquids falling onto a surface. For instance, it can of use in industrial processes where dangerous chemicals may need to be identified. The size of the FSS sensor can also be scaled up or down.

Table 5.9 The proposed design compared with reported comparable EBG-based sensors

Parameter	[20] (EBG)	[21] (EBG)	This work (FSS)
Resonant Frequency (GHz)	2.45	2.45	4.6
Construction	Complex	Complex	Simple
Maximum Measured Sensitivity	0.875	-	8.65
Minimum frequency shift Δf (GHz)	0.054	-	0.68
No. of units comprising the sensor	three	two	single

Previous work [52] has indicated that even a unit cell can produce a transmission response by adjusting the distance of the antennas used for testing.

Figure 5.19 illustrates a potential setup integrated with a wireless sensor network for detection of dangerous chemical liquids (LUT) in an industrial environment. The sensor is set in such a way that liquids fall onto the FSS structure. To ensure the uniformity of the liquid during the measurements, a bubble level should be used during the installation to prevent erroneous readings. This sensor can potentially also be used in detection of contamination of a known liquid. This design does not purport to be a replacement for what is already in existence for measuring dielectric characteristics. Rather, it is presented as an inexpensive, easy to fabricate alternative for liquid sensing/identification.

This first concept of the sensor has a flat surface which means that some droplets may remain on the surface outside the trenches which may affect measurements. A future version of the design is envisaged where cells could be three-dimensional with a slight slope to allow droplets to be guided towards the trenches.

Note that this is the first concept, and the reading setup is the standard for FSS measurements. However, a more compact arrangement could be developed in the future where the antennas and system only target the specified frequency band of operation. In addition, in an industrial environment, a dedicated space would be desirable.

Even though the main application described here is on liquid sensing, the structure and design have potential applications in reconfigurable FSS using low-loss liquids such as in [53], a radiation beam steering passive antenna using liquid fluidity.

The concept was extended to develop an inexpensive, 3D printed version of the sensor. The 3D version demonstrated the same behavior in resonance when the trenches were filled with liquid chemicals of different electrical properties. The FFF process used for the fabrication of the device has the advantage of reducing material cost, labour, and manufacturing time. Its fabrication process can also be quickly scaled up. The structure of the sensor was however found to twist and buckle after a few uses with the liquid chemical measured. This was due to chemical interaction between the PLA substrate and the solvents employed [54]. This chemical interaction can also cause solvents to pass through the printed structure. This renders it a single-use disposable detecting device. A future version of the design can be made for multiple uses by printing with an inert material that does not react with the chemicals that are to be tested.

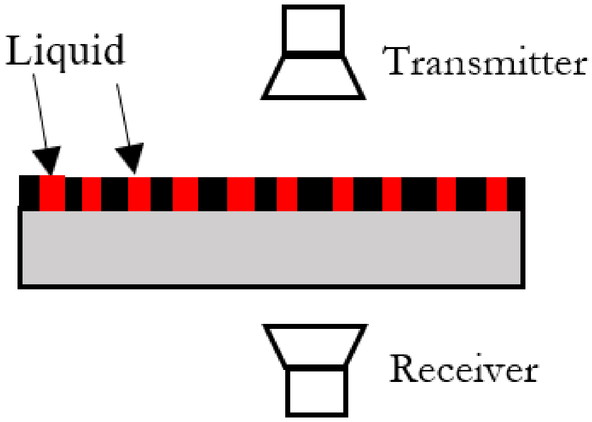

Figure 5.19 Illustrative potential FSS sensor application

Acknowledgement

In this work and the output publications [1] and [47], Peter Njogu did the research, the sensor design and simulation, the laboratory testing, and writing; Benito Sanz-Izquierdo and Prof. Edward Parker gave guidance.

References

[1] A. Ebrahimi, J. Scott and K. Ghorbani, "Microwave reflective biosensor for glucose level detection in aqueous solutions," *Sensors and Actuators A: Physical,* vol. 301, 2020.

[2] A. A. M. Bahar, Z. Zakaria, M. K. M. Arshad, A. A. M. Isa, Y. Dasril and R. A. Alahnomi, "Real Time Microwave Biochemical Sensor Based on Circular SIW Approach for Aqueous Dielectric Detection," S*cientific Reports ,* vol. 9, pp. 1-12, 2019.

[3] L. F. Chen, C. K. Ong, C. P. Neo, V. V. Varadan and V. K. Varadan, Microwave Electronics Measurements and Materials Characterization, Chichester: John Wiley & Sons Ltd, 2004.

[4] B. A. Galwas, J. K. Piotrowski and J. Skulski, "Dielectric Measurements Using a Coaxial Resonator Opened to a Waveguide Below Cut-Off," *IEEE Transactions on Instrumentation and Measurement,* vol. 46, no. 2, pp. 511-514, 1997.

[5] H. Lobato-Morales, A. Corona-Chávez, D. V. B. Murthy and J. L. Olvera-Cervantes, "Complex permittvity measurements using cavity perturbation technique with substrate integrated waveguide cavities," *Review of Scientific Instruments,* vol. 81, pp. 1-4, 2010.

[6] K. Saeed, R. D. Pollard and I. C. Hunter, "Substrate Integrated Waveguide Cavity Resonators for Complex Permittivity Characterization of Materials," *IEEE Transactions on Microwave Theory and Techniques,* vol. 56, no. 10, pp. 2340 - 2347, 2008.

[7] A. A. Abduljabar, D. J. Rowe, A. Porch and D. A. Barrow, "Novel Microwave Microfluidic Sensor Using a Microstrip Split-Ring Resonator," *IEEE Transactions On Microwave Theory And Techniques,* Vols. 62,, no. 3, pp. 679-688, 2014.

[8] D. J. Rowe, S. al-Malki, A. A. Abduljabar, A. Porch, D. A. Barrow and C. J. Allender, "Improved Split-Ring Resonator for Microfluidic Sensing," *IEEE Transactions on Microwave Theory and Techniques,* vol. 62, no. 3, pp. 689 - 699, 2014.

[9] E. L. Chuma, Y. Iano, G. Fontgalland and L. L. B. Roger, "Microwave Sensor for Liquid Dielectric Characterization Based on Metamaterial Complementary Split Ring Resonator," *IEEE Sensors Journal ,* vol. 18, no. 24, pp. 9978 - 9983, 2018.

[10] C.-S. Lee, B. Bai, Q.-R. Song, Z.-Q. Wang and G.-F. Li, "Open Complementary Split-Ring Resonator Sensor for Dropping-Based Liquid Dielectric Characterization," *IEEE Sensors Journal,* vol. 19, no. 24, pp. 11880 - 11890, 2019.

[11] A. A. Abduljabar, N. Clark, J. Lees and A. Porch, "Dual Mode Microwave Microfluidic Sensor for Temperature Variant Liquid Characterization," *IEEE Transactions on Microwave Theory and Techniques,* vol. 65, no. 7, pp. 2572 - 2582, 2017.

[12] A. J. Cole and P. R. Young, "Chipless Liquid Sensing Using a Slotted Cylindrical Resonator," *IEEE Sensors Journal,* vol. 18, no. 1, pp. 149 - 156, 2018.

[13] V. Makarovaite, A. J. R. Hillier, S. J. Holder and J. C. Batchelor, "Passive Wireless UHF RFID Antenna Label for Sensing Dielectric Properties of Aqueous and Organic Liquids," *EEE Sensors Journal,* vol. 19, no. 11, pp. 4299-4307, 2019.

[14] S. S. Bukhari, J. Vardaxoglou and W. Whittow, "A Metasurfaces Review: Definitions and Applications," *Applied Science- MDPI,* vol. 9, pp. 1-14, 2019.

[15] N. Christopoulos, G. Goussetis, A. P. Feresidis and J. C.Vardaxoglou, "Metamaterials With Multiband AMC And EBG Properties," in *2005 European Microwave Conference*, Paris, France, 2005.

[16] F. Bayatpur and K. Sarabandi, "Tuning Performance of Metamaterial-Based Frequency Selective Surfaces," *IEEE Transactions on Antennas and Propagation ,* vol. 57, no. 2, pp. 590 - 592, 2009.

[17] Y. I. Abdulkarim, L. Deng, O. Altıntaş, E. Ünal and M. Karaaslan, "Metamaterial absorber sensor design by incorporating swastika shaped resonator to determination of the liquid chemicals depending on electrical characteristics," *Physica E: Low-dimensional Systems and Nanostructures,* vol. 114, pp. 1-9, 2019.

[18] Y. I. Abdulkarim, L. Deng, H. Luo, S. Huang, M. Karaaslan, O. Altıntas, M. Bakır, F. F. Muhammadsharif, H. N. Awl, C. Sabah and K. S. L. Al-badri, "Design and study of a metamaterial based sensorfor the application of liquid chemicals detection," *Journal of Materials Research and Technology,* vol. 9, no. 5, pp. 10291-10304, 2020.

[19] Y. I. Abdulkarim, L. Deng, M. Karaaslan, O. Altıntas, H. N. Awl, F. F. Muhammadsharif, C. Liao, E. Unal and H. Luo, "Novel Metamaterials-Based Hypersensitized Liquid Sensor Integrating Omega-Shaped Resonator with Microstrip Transmission Line," *Sensors MDPI,* vol. 20, no. 3, pp. 1-18, 2020.

[20] A. Arif, A. Zubair, K. Riaz, M. Q. Mehmood and M. Zubair, "A Novel Cesaro Fractal EBG-Based Sensing Platform for Dielectric Characterization of Liquids," *IEEE Transactions On Antennas And Propagation,* vol. 69, no. 5, pp. 2887-2895, 2021.

[21] S. Y. Jun, B. S. Izquierdo and E. A. Parker, "Liquid Sensor/Detector Using an EBG Structure," *IEEE Transactions on Antennas and Propagation ,* vol. 67, no. 5, pp. 3366 - 3373, 2019.

[22] K. R. Jha, G. Singh and R. Jyoti, "A Simple Synthesis Technique of Single-Square-Loop Frequency Selective Surface," Progress In Electromagnetics Research B, vol. 45, p. 165–185, 2012.

[23] E. A. Parker, "The Gentleman's Guide To Frequency Selective Surfaces," 17 04 1991. [Online]. Available: https://kar.kent.ac.uk/59863/. [Accessed 27 04 2021].

[24] B. A. Munk, Frequency Selective Surfaces Theory and Design, New York: John Wiley & Sons, Inc. , 2000.

[25] J. C. Vardaxoglou, "Metamaterial arrays and applications: FSS, EBG & AMC structures," in *2014 International Workshop on Antenna Technology: Small Antennas, Novel EM Structures and Materials, and Applications (iWAT)*, Sydney, NSW, Australia, 2014.

[26] F. H. W. Mustaffa, S. N. Azemi, M. F. Jamlos, A. A. Al-Hadi and P. J. Soh, "Frequency Selective Surface for Structural Health Monitoring," *IOP Conference Series: Materials Science and Engineering,* vol. 318, pp. 1-9, 2018.

[27] D. Pieper, K. M. Donnell, O. Abdelkarim and M. A. ElGawady, "Embedded FSS sensing for structural health monitoring of bridge columns," in *2016 IEEE International Instrumentation and Measurement Technology Conference Proceedings*, Taipei, Taiwan, 2016.

[28] S.-D. Jang, B.-W. Kang and J. Kim, "Frequency selective surface based passive wireless sensor for structural health monitoring," *Smart Materials and Structures,* vol. 22, pp. 1-7, 2013.

[29] M. Mahmoodi and K. M. Donnell, "Novel FSS-based sensor for concurrent temperature and strain sensing," in *2017 IEEE International Symposium on Antennas and Propagation & USNC/URSI National Radio Science Meeting*, San Diego, CA, USA, 2017.

[30] S. Milici, J. Lorenzo, A. Lázaro, R. Villarino and D. Girbau, "Wireless Breathing Sensor Based on Wearable Modulated Frequency Selective Surface," *IEEE SENSORS JOURNAL,* vol. 17, no. 5, pp. 1285-1292, 2017.

[31] S. Soltani, P. S. Taylor, E. A. Parker and J. C. Batchelor, "Popup Tunable Frequency Selective Surfaces for Strain Sensing," *IEEE Sensors Letters,* vol. 4, no. 4, pp. 2475-1472, 2020.

[32] F. Costa, C. Amabile, A. Monorchio and E. Prati, "Waveguide Dielectric Permittivity Measurement Technique Based on Resonant FSS Filters," *IEEE Microwave and Wireless Components Letters,* vol. 21, no. 5, pp. 273-275, 2011.

[33] M. Mahmoodi and K. M. Donnell, "Performance Metrics for Frequency Selective Surface-Based Sensors," *IEEE Sensor Letters,* vol. 1, no. 6, pp. 1-4, 2017.

[34] A. Shastri, B. Sanz-Izquierdo, E. A. Parker, S. Gao, P. Reynaert, Z. Chen and L. Winchester, "3D Printing of Millimetre Wave and Low-Terahertz Frequency Selective Surfaces Using Aerosol Jet Technology," *IEEE Access ,* vol. 8, pp. 177341 - 177350, 2020.

[35] Rogers Corporation, “RT/duroid® 5870 /5880 High Frequency Laminates” 0939-0311-0.5CC, datasheet*,* Chandler, Arizona: Rogers Corporation, 2021.

[36] D. Ferreira, R. F. S. Caldeirinha, I. Cuiñas and T. R. Fernandes, "Square Loop and Slot Frequency Selective Surfaces Study for Equivalent Circuit Model Optimization," *IEEE Transactions on Antennas And Propagation,* vol. 63, no. 9, pp. 3947-3955, 2015.

[37] R. J. Langley and E. A. Parker, "Equivalent circuit model for arrays of square loops," *Electronics Letters,* vol. 18, no. 7, pp. 294-296, 1982.

[38] C. K. Lee and R. J. Langley, "Equivalent-circuit models for frequency-selective surfaces at oblique angles of incidence," *IEE Proceedings,* vol. 132, no. 6, p. 395 – 399, 1985.

[39] A. E. Yilmaz and M. Kuzuoglu, "Design of the Square Loop Frequency Selective Surfaces with Particle Swarm Optimization via the Equivalent Circuit Model," *Radio Engineering,* vol. 18, no. 2, pp. 95-102, 2009.

[40] N. Marcuvitz, Waveguide Handbook, London: Peter Peregrinus, 1986.

[41] F. Costa, A. Monorchio and G. Manara, "Efficient Analysis of Frequency-Selective Surfaces by a Simple Equivalent-Circuit Model," *IEEE Antennas and Propagation Magazine,* vol. 54, no. 4, pp. 35 - 48, 2012.

[42] P. Callaghan and E. A. Parker, "Element dependency in dielectric tuning of frequency selective surfaces," *Electronics Letters,* vol. 28, no. 1, p. 42 – 44, 1992.

[43] A. P. Gregory and R. N. Clarke, "Tables of the Complex Permittivity of Dielectric Reference Liquids at Frequencies up to 5 GHz," National Physical Laboratory, 2012.

[44] CEM, "Solvent Choice for Microwave Synthesis," 01 06 2021. [Online]. Available: https://cem.com/uk/microwave-chemistry/solvent-choice. [Accessed 01 06 2021].

[45] H. Lobato-Morales, D. V. B. Murthy, A. Corona-Chavez, J. L. Olvera-Cervantes, J. Martinez-Brito and L. G. Guerrero-Ojeda, "Permittivity Measurements at Microwave Frequencies Using Epsilon-Near-Zero (ENZ) Tunnel Structure," *IEEE Transactions On Microwave Theory and Techniques,* vol. 59, no. 7, pp. 1863 - 1868, 2011.

[46] A. C. de C. Lima, E. A. Parker and R. J. Langley, "Tunable frequency selective surface using liquid substrates," *Electronics Letters,* vol. 30, no. 4, pp. 281 - 282, 1994.

[47] P. Njogu, B. Izquierdo, S. Gao and Z. Chen, "Disposable 3D printed Liquid sensor," in *16th European Conference on Antennas and Propagation (EuCAP)*, Madrid, Spain, 2022.

[48] S. Y. Jun, A. Elibiary, B. Sanz-Izquierdo, L. Winchester, D. Bird and A. McCleland, "3-D Printing of Conformal Antennas for Diversity Wrist Worn Applications," *IEEE Transactions on Components, Packaging And Manufacturing Technology,* vol. 8, no. 12, pp. 2227-2235, 2018.

[49] "RS PRO Liquid Conductive Paint," RS, 10 06 2021. [Online]. Available: https://uk.rs-online.com/web/p/adhesives/1863600/. [Accessed 10 06 2021].

[50] P. F. Espin-Lopez, M. Pasian, G. Alaimo, S. Marconi, F. Auricchio, V. Heinänen and J. Järveläinen, "3-D Printed Antenna for Snowpack Monitoring," *IEEE Antennas and Wireless Propagation Letters,* vol. 17, no. 11, pp. 2109 - 2113, 2018.

[51] B. Biernacki, S. Zhang and W. Whittow, "3D printed substrates with graded dielectric properties and their application to patch antennas," in *2016 Loughborough Antennas & Propagation Conference (LAPC)*, Loughborough, UK, 2016.

[52] E. A. Parker, J. -B. Robertson, B. Sanz-Izquierdo and J. C. Batchelor, "Minimal size FSS for long wavelength," *Electronics Letters,* vol. 44, no. 6, p. 394 – 395, 2008.

[53] C. Song, E. L. Bennett, J. Xiao, R. P. Tianyuan Jia, K.-M. Luk and Y. Huang, "Passive Beam-Steering Gravitational Liquid Antennas," *IEEE Transactions on Antennas And Propagation* , vol. 68 , no. 4, pp. 3207-3212, 2020.

[54] K. S. Erokhin, EvgeniyG.Gordeev and V. P.Ananikov, "Revealing interactions of layered polymeric materials at solid-liquid interface for building solvent compatibility charts for 3D printing applications," *Scientific Reports,* vol. 9, pp. 1-14, 2019.

CHAPTER 6: 3D FSS BASED DISPLACEMENT SENSOR

6.1 Overview

This chapter describes a novel displacement sensor using a frequency selective surface (FSS) with a withdrawable complementary substrate. The complementary substrate fits into the FSS and can moves back and forth within it. The new concept sensor is based on modifying the capacitance of the FSS when the substrate complement is gradually withdrawn. This change in capacitance produces a change in resonant frequency. The FSS consists of an array of square loop elements in a square lattice. A 3D convoluted version of the FSS sensor improves the angle of incident behavior and increases the physical displacement range. The complementary substrate of the 3D FSS sensor were 3D printed while the metal layers were painted using silver conductive paint. Transmission response, S_{21}, was employed as the validation parameter. The sensor operates in a frequency range between 2.0 GHz and 2.8 GHz. Simulated and measured results were consistent. The device is compact, inexpensive, and easy to make and operate. The envisaged application is the wireless detection of structural movement which can be critical in civil structures such as bridges, buildings or in post-earthquake assessment of such structures for damage. Presented as proof of concept in this work is the wireless displacement sensor, a concept that that can enabled by the advent of low-cost vector network analyser (VNA) that can be realized using off the shelf components [1][2].

Alongside the structural displacement sensing application, an inexpensively fabricated wireless security/signal quality application integrated into an indoor wall is also proposed. The filtering properties of FSS loop structures renders them ideal for prevention of wireless signal quality loss as well as signal eavesdropping by unauthorized entities. Inexpensive screen printing of FSS on a plasterboard block that reduces the drop in wireless signals strength within indoor settings thus was investigated. The proposed low-cost square loops FSS array solution operates at a frequency of 2 GHz, covering some of the existing mobile phone frequency bands. The array structure was screen-printed on a plasterboard using a stencil. Simulated transmission responses compared well with measurements.

The rest of this chapter is organized as follows: section 6.2 is the introduction, Section 6.3 details the initial sensor concept, Section 6.4 describes the 3D convoluted sensor concept, Section 6.5 details the fabrication, measurements, and the surface profile analysis of the design. Section 6.6 discusses the screen-printed FSS plasterboard for wireless indoor application while Section 6.7 discusses the conclusion. The design and simulations in this chapter were done using CST MWS^{TM} with the results verified by experimental results.

6.2 Introduction

Displacement measurements technologies that exploit remote monitoring wirelessly can deliver real time data about the health of structures in a non-destructive way. Further, if the sensor in such a wireless system is passive, no energy is required which drives the cost down boosting the design's environmental credentials. A summary of previous wireless sensors is given in [3]. Displacement of a structure such as building or bridge can occur because of a sudden impact e.g., an earthquake or it can develop slowly over a period. A way of detecting such displacement is proposed in this work. Measuring such displacement can provide information on the level of damage to a structure and such information as whether a building should be evacuated or not to save life. The proposed detector is envisioned for functions such as structural health monitoring as well as assessment after an earthquake has occurred.

Frequency selective surfaces (FSS) are periodic arrays of conductive elements on dielectric materials that exhibit specific transmissive or reflective frequency responses when the electromagnetic energy impinges. Their frequency response depends on the spacing between the periodic elements, the geometry of the elements, the dielectric substrate properties, and thickness as well as the local environment [4] and [5]. FSS essentially behaves as a spatial filter to certain frequencies of impinging electromagnetic radiation.

The filtering properties of FSS enable exploitation of the electromagnetic responses i.e., reflection and transmission properties, resonance frequency, and Q-factor which depends on the unit cell geometry and the dielectric material characteristics. Alterations of parameters such as layering of the dielectric structure [6] or composition [7] affect the response of the FSS.

These FSS filtering properties enable the application of FSS in advanced antenna systems and technology such as offset reflector antennas [8] [9], absorbers [10], radomes [11], and Butler matrix [12], RF shielding [13] [14], beam switching and beam steering [15]-[17].

Recent research activities extend to the use of FSS and meta-materials for sensing applications. These include applications such as strain sensing [18] [19] and remote sensing [20]. Others include chemical liquid sensing [21] [22], thin film sensing [23], CO_2 monitoring [24], structural health monitoring of bridge columns [25], biochemical [26] and corrosion sensing [27].

Recently, interest has developed in the use of FSS and meta-materials for displacement applications. EBG based displacement sensors have been presented in [28] and [29].

FSS based displacement sensors have been presented in the literature space. A structural health monitoring FSS based sensor is presented in [30]. This sensor involves a cross FSS which would tear or deform to indicate a structural health problem. A wireless two-dimensional lateral displacement sensor using bilayer graphene based FSS is presented in [31]. It constitutes conductors sliding over each other. [32] presents a displacement sensor for remote structural monitoring that uses an antenna coupling in the near field with two split ring metamaterials that gradually move to and from each other by the displacement to be detected. Of the FSS based displacement sensors in the literature space, [30] can only detect cracks on structures. [31] though a displacement sensor is developed using expensive to manufacture graphene material [32] which would render its development expensive. Metamaterial based displacement sensor presented in [33] is potentially capable of the function envisioned in the proposed design. However, subtractive manufacturing method has been employed in its fabrication. Subtractive manufacturing methods are expensive, material wasteful as well as energy and time inefficient as discussed in Sections 1.1 and 2.1. Use of an AM method, fused filament fabrication (FFF) lowers cost, quickens prototyping and fabrication process as well as reduce the amount material used, further reducing the cost. Using the dual polarity, angular stable square loops FSS enhances the accuracy of the sensor. The FSS loops were meandered or convoluted in the z-axis direction. This reduces the size of the unit cell without affecting the angular stability [34].

FSS exists in different shapes [35] and [36]. They are usually planar (2D) but can also come in 3D form [37] [38]. It has been found that some 3D elements offer improved wave angle of incidence stability thereby improving the field of view [39]-[43]. The usual question regarding 3D structures is whether there is any applicational advantage over the 2D structures.

In this work, an FSS-based displacement sensor is proposed. This is made possible by the emergence of low cost VNAs as alluded to in Section 6.1.

A low material wasteful, quick to prototype and inexpensive to fabricated FFF developed FSS-based displacement design is proposed. The design has two main components, a 3D FSS, and a retractable complementary substrate part. The proposed displacement sensing platform includes a transmitter and receiver external to the prototype for illuminating and receiving signals from the FSS. Its illustrative operational set up is shown in Figure 6.1.

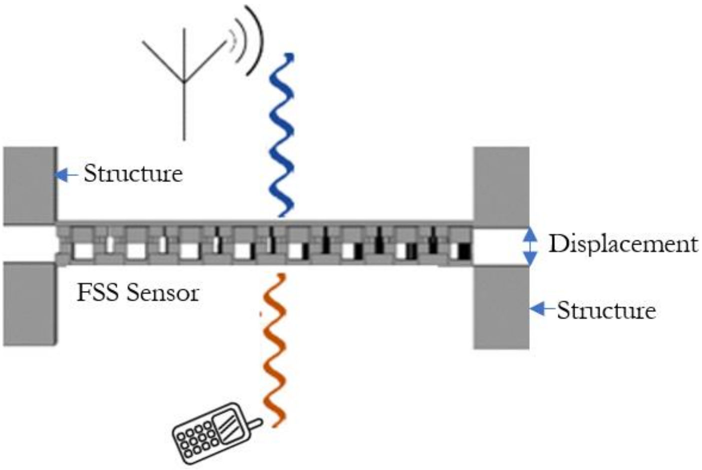

Figure 6.1 Potential conceptual set up of the displacement sensor

The two parts are such that the complement part slides back and forth along the z-plane of the 3D FSS and are made of the same substrate material. Inexpensive manual application of the conductive tracks by hand using an artist's brush was employed to reduce the cost of the fabrication. A 3D FSS design is adopted here to improve the angle of incidence property of the sensor as well as to increase the displacement range. The sensing occurs as the capacitance is altered as the complement substrate retracts thus altering the resonance frequency of the FSS, seen by measuring its transmission response. The FSS sensor operates at about 2.0 GHz with a broad range of frequencies in relation to the displacement distance of the complement dielectric. The proposed sensor is adaptable and can be adjusted in size by increasing or decreasing the number of cells. The dielectric layers of the FSS were fabricated using fused filament fabrication (FFF), a method that enables the creation of intricate 3D objects [44]. The proposed prototype offers another method of detecting structural displacement. It does not purport to replace the already existing methods, but to augment them.

6.3 The Sensor Concept

6.3.1 Initial FSS Displacement Sensor Concept

It is well known that FSS structures are sensitive to their surrounding materials as well as substrate characteristics. This has been exploited in the development of the displacement sensor proposed in this chapter. A square loop [5] FSS element offers dual polarization and good angle of incidence behavior [22] and was employed in the development of the displacement sensor prototype. A circular loop FSS could also have been used. Both the square-loop and circular-loop FSS filters perform comparably when fabricated to high accuracy [45]. However, when fabrications tolerances are allowed, the results of circular-loop FSS filter have more consistency, predictability, and accuracy. Effort was made to ensure that the fabrication was as accurate as possible and therefore it can be assumed a circular loop FSS would have produced the same results. However, only design and fabrication of the circular FSS can attest to that which was not done in this instance.

The FSS have was designed such that a complementary substrate fits and locks into it. The design is depicted in Figure 6.2. The square loop of length 21.7 mm is set on a 26 mm square unit cell. The square loop conductive material is RS pro Silver Conductive 186-3600 paint [46], whose conductivity has been calculated in Subsection 4.3.1. The substrate of FSS unit cell is a hollow square ring whose geometry is shown in Figure 6.2(a). This is to allow the complement substrate shown in Figure 6.2(b) to fit into it. The corners of the unit cell are slightly extended for ease of handling. A substrate made of the same material as the substrate of the FSS and whose structure is complementary to the FSS was made to fit into the FSS. The two parts perfectly fit into each other to form a solid structure as shown in Figure 6.2(c). Figure 6.2(d) illustrates a withdrawn state of the complement from the FSS while Figure 6.2(e) illustrates two cell arrays of the design. A Polylactic acid (PLA) material of relative permittivity, ε_r, of 2.4 and loss tangent (tan δ) of 0.01 [47] was used as the substrate. The thickness of the substrate of the FSS was 3 mm. The rest of the dimensions are given in Table 6.1. The sensor was designed and simulated using Floquet port analysis in CST Microwave Studio^{TM}.

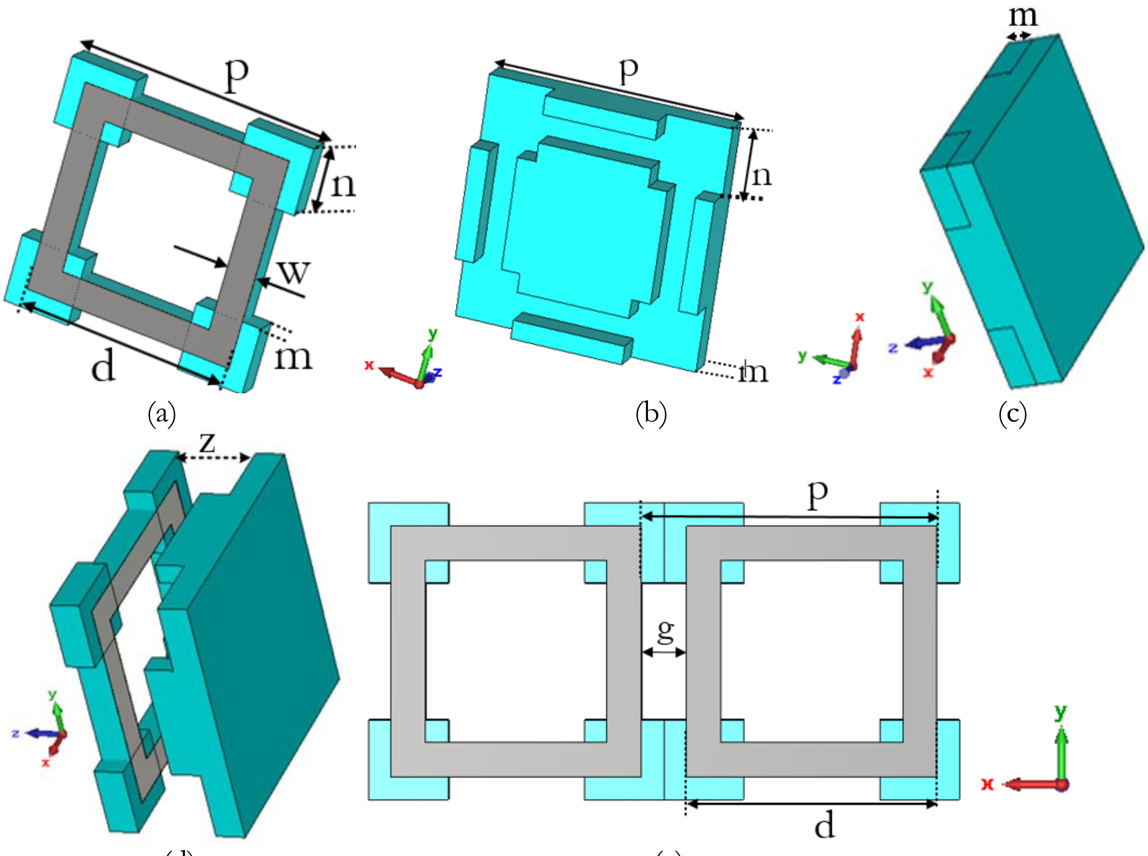

(a) (b) (c)

(d) (e)

Figure 6.2 The sensor concept: (a) the FSS (b) complement substrate (c) FSS, and complement (d) complement substrate withdrawn (e) two-unit cells array

Table 6.1 Dimension of the initial concept FSS

Dimension	p	w	m	n	d	g
Value (mm)	26	2	3	7	21.7	4.4

The transmission response of the FSS sensor is shown in Figure 6.3. The FSS without the complement resonated at 4.4 GHz with a frequency shift of 5% at TE 45°, and 1.8% at TM 45° wave incidence. With the complement, the FSS resonated at 3.5 GHz with a frequency shift of 2.9% at TE 45°, and 2.0% at TM 45°.

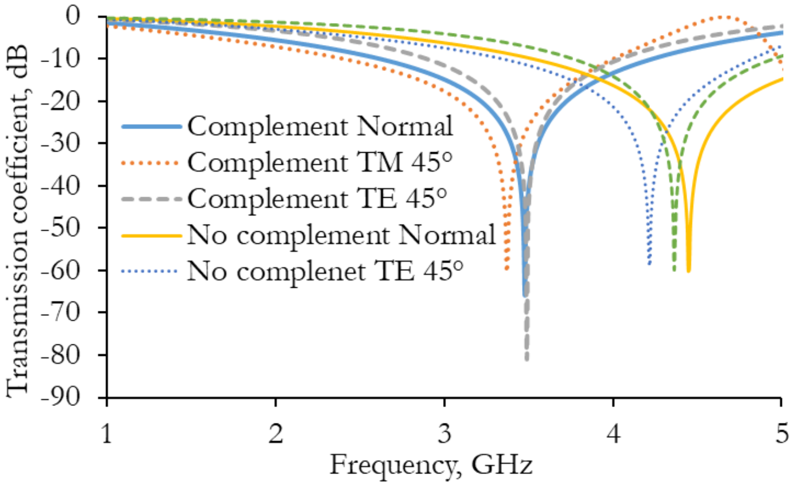

Figure 6.3 Simulated ttransmission coefficient, S_{21} of the FSS displacement sensor with and without complement of the simulated prototype

Further study of the resonant frequency of the FSS sensor for the complementary substrate displacement distance, z (Figure 6.2(d)), along the z-plane, was conducted. The result is shown in Figure 6.4. The substrate complement was withdrawn in the z-plane direction at intervals Δz of 2 mm, ranging from 0 mm (Figure 6.2(d)) to 10 mm. The sensor's response is linear up to a displacement of 4 mm. It then flattens as the complementary substrate withdraws completely from the FSS. This shows that this initial concept sensor is sensitive to displacement. However, it has a low displacement range limiting its applicability. An alternative approach to the design of the sensor was thus investigated to mitigate against the low sensitivity of the current design. The alternative approach involved convoluting the FSS in the z-plane direction as discussed in Section 6.4. But before that, the sensor's operating principle is discussed in Subsection 6.3.2.

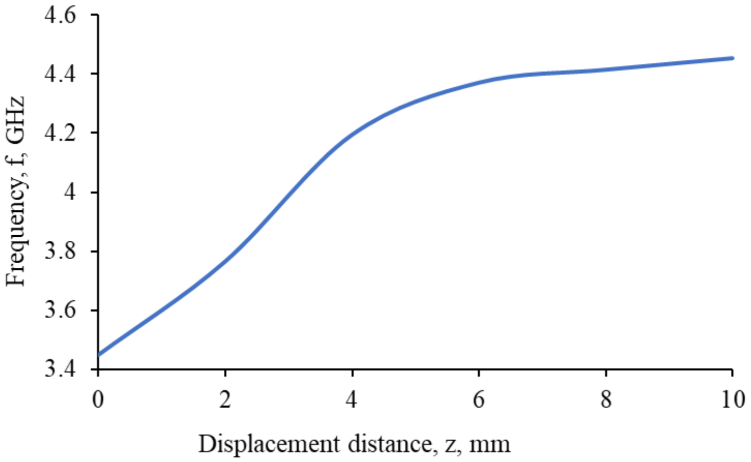

Figure 6.4 Simulated resonance frequency, f, versus substrate complement displacement distance, z for the 2D FSS as the complementary substrate completely withdraws from FSS.

6.3.2 The Operation principle

A typical bandstop FSS can be modeled as an equivalent circuit theory [48] and [49]. Adjacent square loops with a gap between them interact capacitively while the metallic conductor strip is equivalent to an inductor, creating a series LC resonance circuit, as shown in Figure 6.5.

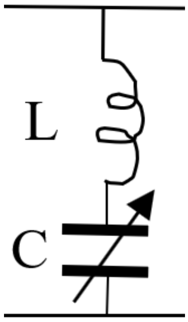

Figure 6.5 Equivalent circuit of the FSS sensor

The resonance frequency of this circuit is expressed as:

$$f = \frac{1}{2\pi\sqrt{LC}} \tag{6.1}$$

where L is the inductance created by the conductors of the square loops while C is the capacitance between adjacent loops. The capacitance is dependent on the dielectric permittivity of the substrate. In the case of parallel plate capacitors, the capacitance can be calculated as:

$$C = \frac{\varepsilon_r \varepsilon_o A}{d} \tag{6.2}$$

where A and d are the plate area and the distance separating the plates respectively. The operating principle of the sensor is based on the idea of varying the capacitance of the LC circuit when the dielectric complement moves in and out of the FSS structure, as illustrated in Figure 6.6. In the initial state, Figure 6.6(a), the FSS is symmetrically embedded into the dielectric substrate of permittivity is ε_r. In this case, the effective permittivity can be approximated to ε_r as the substrate is moderately thick and square loops are used [50].

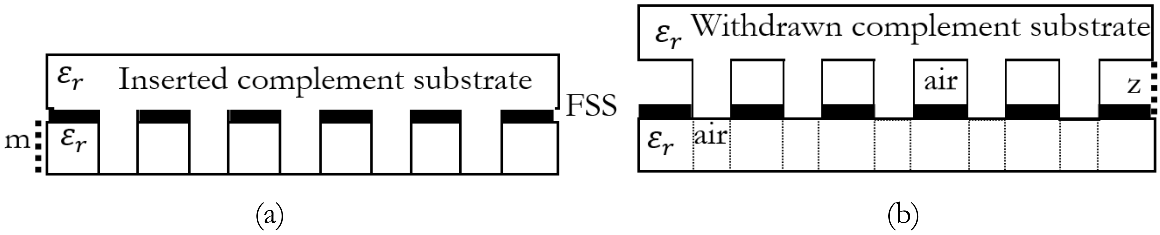

Figure 6.6 Operation principle of the FSS sensor at (a) FSS-complement fully locked, z is zero (b) complement withdrawn to FSS height, z is 3 mm

When the dielectric complement is moved out of the FSS, the effective permittivity of the structure decreases, which decreases the inter-element capacitance of the FSS. The effective permittivity for the state when the substrate is as shown in Figure 6.6(b) could be approximated to a substrate which is partly dielectric and partly air, thus the effective permittivity, ε_{eff}, is:

$$\varepsilon_{eff} = \frac{\varepsilon_r + 1}{2} \tag{6.3}$$

The gradual change of ε_{eff} between these two states i.e., Figure 6.6(a) and Figure 6.6(b)) is expected to be linear with a sketch curve type as in Figure 6.7 and can thus be expressed as:

$$\varepsilon_{eff} = \varepsilon_r + \frac{(1-\varepsilon_r)}{2m} z \tag{6.4}$$

where z is the displacement along the z-axis and *m* is the height of the FSS.

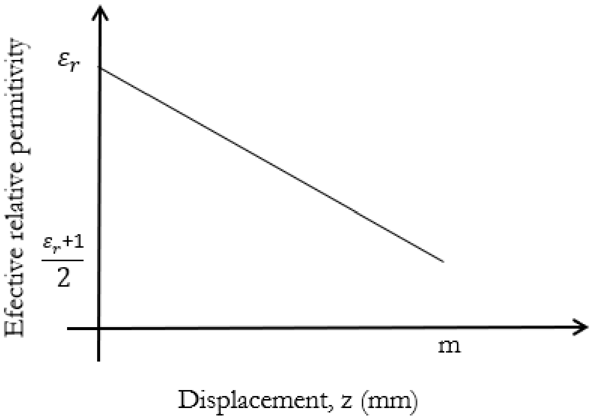

Figure 6.7 A sketch of expected linear change of effective relative permittivity with displacement z

Equation (6.4) is only valid for the linear part of the sensor which is intermediate to Figure 6.6(a) and Figure 6.6(b). In the case of the initial sensor (Figure 6.2), this is for z between 0 and 4 mm (Figure 6.4).

A more accurate equation for the change in effective permittivity, ε_{eff}, for the structure in Figure 6.2 can be obtained using the ratios between the resonant frequency, f_z at any withdrawal distance z, and the resonance frequency, f_0, for z = 0, and the ratio of ε_{eff} at any withdrawal distance z, and ε_r (ε_{eff} at z = 0), which can be obtained from equations (6.1) and (6.2), considering that *L*, *d*, *A* are constant. Using these ratios, ε_{eff} for any frequency can be calculated as:

$$\varepsilon_{eff} = \left(\frac{1}{\left(\left(\frac{fz}{f_0}\right)^2\right)}\right)\varepsilon_r \tag{6.5}$$

Applying equation (6.5) to the values for the frequencies in Figure 6.3, the value of ε_{eff} as a function of z can be obtained as shown in Figure 6.8.

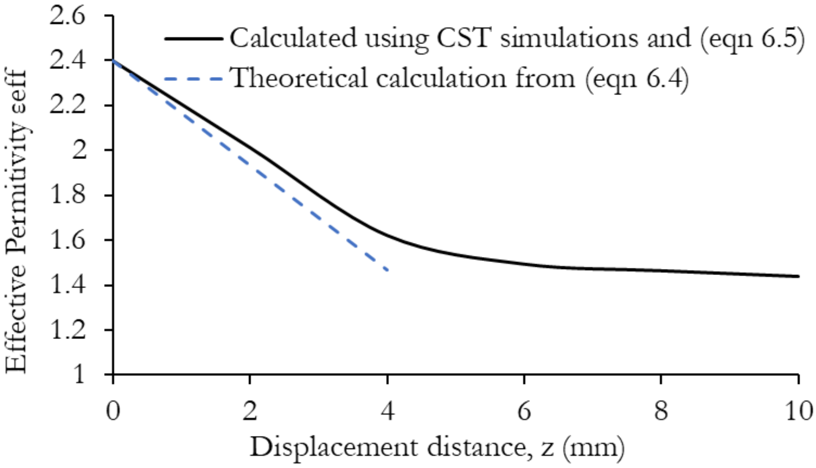

Figure 6.8 Effective permittivity for displacement distance, z.

The equation for the effective permittivity for the linear part (0 < z < 4) of the graph is:

$$\varepsilon_{eff} = 2.4 - 0.1947z \tag{6.6}$$

Equation (6.6) is consistent with equations (6.3) and (6.4). For example, at 4 mm, ε_{eff} the half-loaded FSS from equation (6.3) is just 5% higher than that using equation (6.6). The difference could be due to the non-uniformity of the dielectric material extracted during displacement and errors in the initial assumption that the substrate might be sufficiently thick to be considered fully loaded with dielectric [48].

6.4 3D Convoluted FSS Displacement Sensor

6.4.1 3D Convoluted Design

To improve the sensor's angular response and increase the displacement range, the initial square loop (Figure 6.2) was convoluted in the z axis, resulting in the 3D square loop in Figure 6.9(a) which has a periodicity of 26 mm. The substrate complement for this FSS is shown in Figure 6.9(b). Figure 6.9(c) shows when the two parts fit into each other, and Figure 6.9(d) when the complement is slid out. Figure 6.9(e) shows the top view of two FSS cells array without the complement. The sensor was optimized to operate at a starting frequency of about 2.16 GHz when the complementary substrate is fully locked with the FSS. The final dimensions are given in Table 6.2. In Figure 6.9(d), z is the displacement distance of the complement substrate from the FSS, and h is the height of the FSS. The transmission coefficients of the FSS at normal incidence, TE 45° and TM 45° angles of wave incidence is shown in Figure 6.10 for simulations of the FSS with and without the substrate complement substrate inserted. The FSS without the complement resonated at 2.8 GHz with a frequency shift of 1.2% at TE 45°, and 0.7% at TM 45° from TE normal. When FSS is coupled together with the complement resonance occurred at 2.16 GHz with a frequency shift of 0.5% at TE 45° and 0.15% at TM 45° from TE normal.

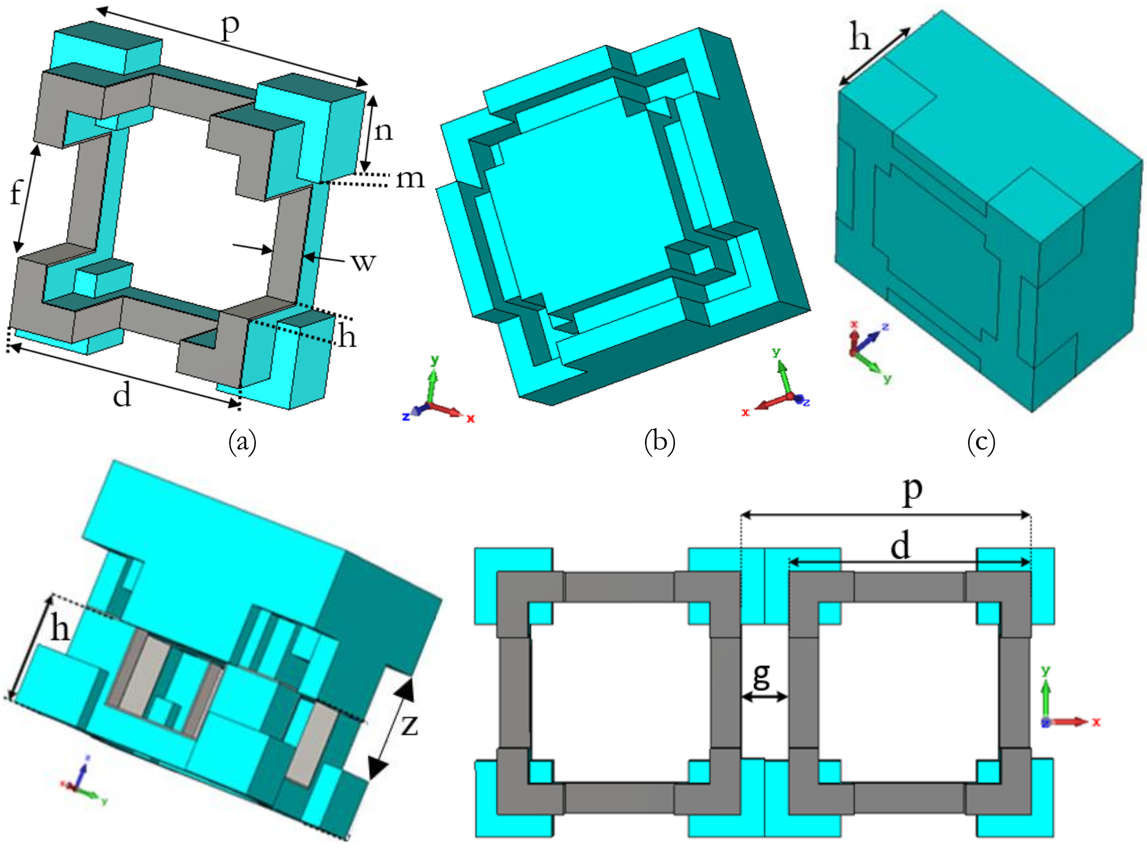

(a) (b) (c)

(d) (e)

Figure 6.9 The convoluted sensor: (a) convoluted FSS (b) complement dielectric layer (c) FSS-complement join (d) complement slid out (e) two unit cells array

Table 6.2 Dimensions of the 3D convoluted FSS

Dimension	p	n	d	f	w	d	h	g
Value (mm)	26	6.85	4.7	10	2.6	21.7	11	4.4

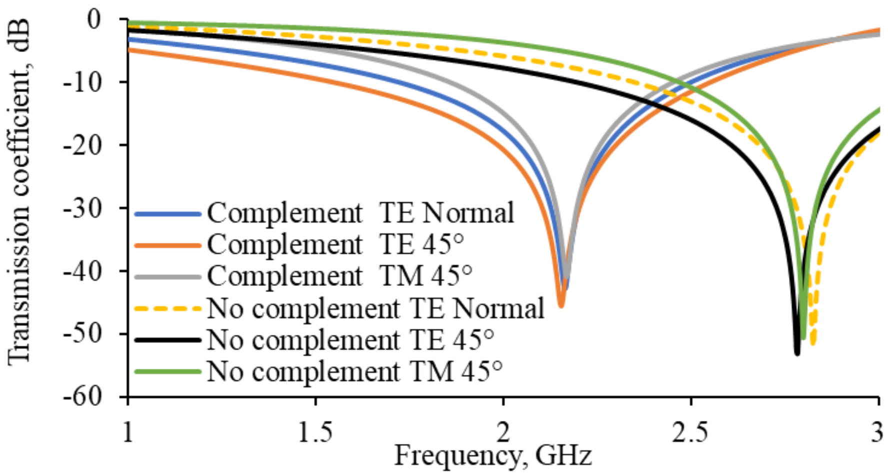

Figure 6.10 Simulated 3D sensor simulated S_{21} with and without the complement substrate

6.4.2 Parametric Analysis of the Sensor

A study of displacement sensing for the convoluted FSS sensor was carried out by gradually withdrawing the complementary substrate by distance, z, (Figure 6.9(d)). Figure 6.11 shows the effect of complementary substrate displacement on the resonant frequency, and the equivalent effective permittivity calculated using equation (6.5). The response is mainly linear up to about 10 mm i.e., when the complement is still inside the FSS. It then starts flattening at about 12 mm at which point the complement substrate is completely outside the FSS.

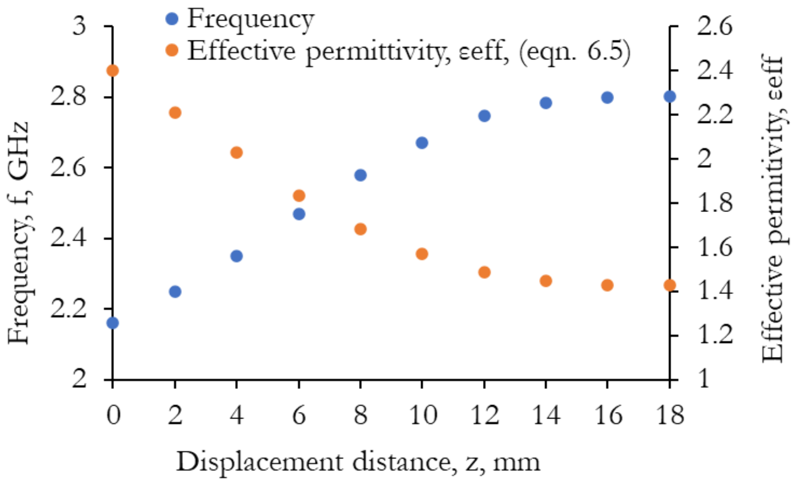

Figure 6.11 Simulated effect of displacement z on resonance frequency, and the equivalent effective permittivity for the 3D convoluted FSS sensor.

The transmission coefficients for various z values for the linear part of the sensor ($0 \leq z \leq 10$ mm) is shown in Figure 6.12. As the displacement distance, z, of the substrate complement changes from 0 mm to 10 mm, the resonance frequency increases 2.16 GHz to 2.67 GHz.

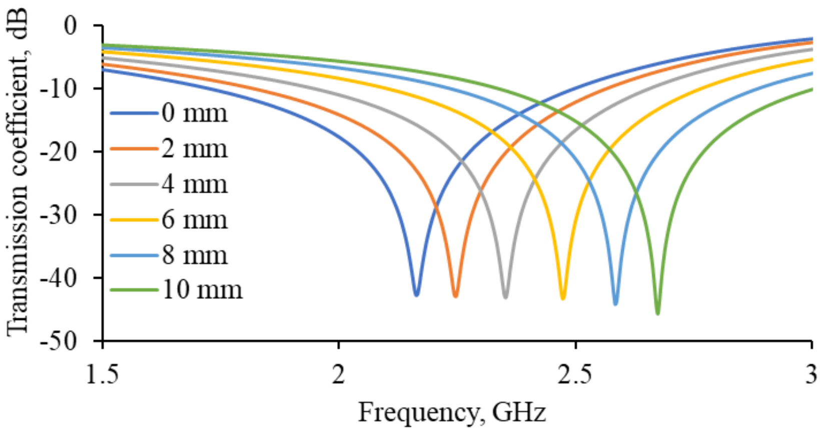

Figure 6.12 Simulated S_{21} results for complement withdrawn distance

The effect of displacement, z on resonant frequency is as shown in Figure 6.13 and Table 6.3. The resonance frequency response follows the linear function:

$$f = 0.052z + 2.1481 \tag{6.7}$$

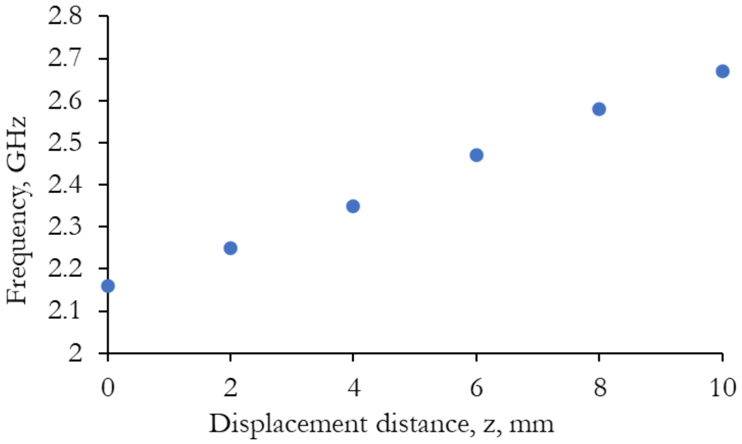

Figure 6.13 Simulated resonance frequency, *f*, versus complement substrate withdrawal *z* for the 3D convoluted sensor

Table 6.3 Sensitivity of the simulated 3D convoluted sensor

Displacement distance, z (mm)	0	2	4	6	8	10
Simulated frequency (GHz)	2.16	2.24	2.35	2.47	2.58	2.67

The sensitivity *(S)* of the sensor [29] and [30], is the slope of the linear equation of Figure 6.12, as given by:

$$S = \frac{\Delta f_z}{\Delta z} \tag{6.8}$$

where Δf_z represents the resonant frequency shift from the reference i.e., initial state resonance frequency in the z-plane direction. It can be expressed as $\Delta f_z = f_{z\_h} - f_{z\_l}$ wheref_{z_h} and f_{z_l}

are the corresponding higher and lower resonance frequencies in the frequency range. The resulting sensitivity, S, is 0.052 GHz/mm, which is consistent with equation (6.7).

6.5 Fabrication and Measurements and Profile Analysis

This subsection describes the sensor fabrication, measurements, and profile analysis.

6.5.1 Fabrication

To fabricate the sensor, the design with dimensions in Figure 6.9 and Table 6.3 was extended to an 8 x 8 array as shown in Figure 6.14. Figure 6.14(a) and Figure 6.14(b) are convoluted FSS and complementary substrate respectively. The dimension of the sensor was 207 mm x 207 mm. Spacers, shown in Figure 6.14(c) for positioning the complement substrate to the correct height during measurements as illustrated in Figure 6.14(d) were also designed. The fabrication process consisted of two stages. The first stage was the printing of both the FSS-bearing substrate and the complement substrate using polylactic acid (PLA) thermoplastic filament in a 3D printer. Stage two involved manual painting of the conductive loops on the printed FSS substrate.

To begin the fabrication process, the CST models of both the convoluted FSS and complement substrate were exported to .stl file. The .stl files were converted to a format compatible with 3D printing and sent to a Raised 3D printer machine. The initial prints of the FSS and the complement substrate from the simulation could not fit into each other. This was attributed to the flowing of the hot PLA during printing. Several iterations were therefore done in during both the FSS and the complement substrate simulations were optimized until they fitted into each other. The optimization involved extraction of small portions of both from every direction. This would be followed by reprinting of the samples until the printed FSS and complement substrate easily slid in and out of each other. A 0.1 mm thick portion was extracted from all directions of both to achieve the dimensions that enabled the two parts to fit into each other.

The second stage involved the application of the RS pro Silver Conductive 186-3600 paint [46], onto the FSS substrate to create the conductive loops. The conductive loops were manually hand-painted around the cell's edges on the substrate of the FSS using an artist's painting brush. To mimic the displacement of the substrate, complement from the FSS, Polystyrene foam spacers were employed. The spacers were fabricated using polystyrene foam blocks which were cut using a Denford Router 2600 CNC cutting machine. Polystyrene foam was used because it has relative permittivity closest to air and thus would have minimal effect on the measurements.

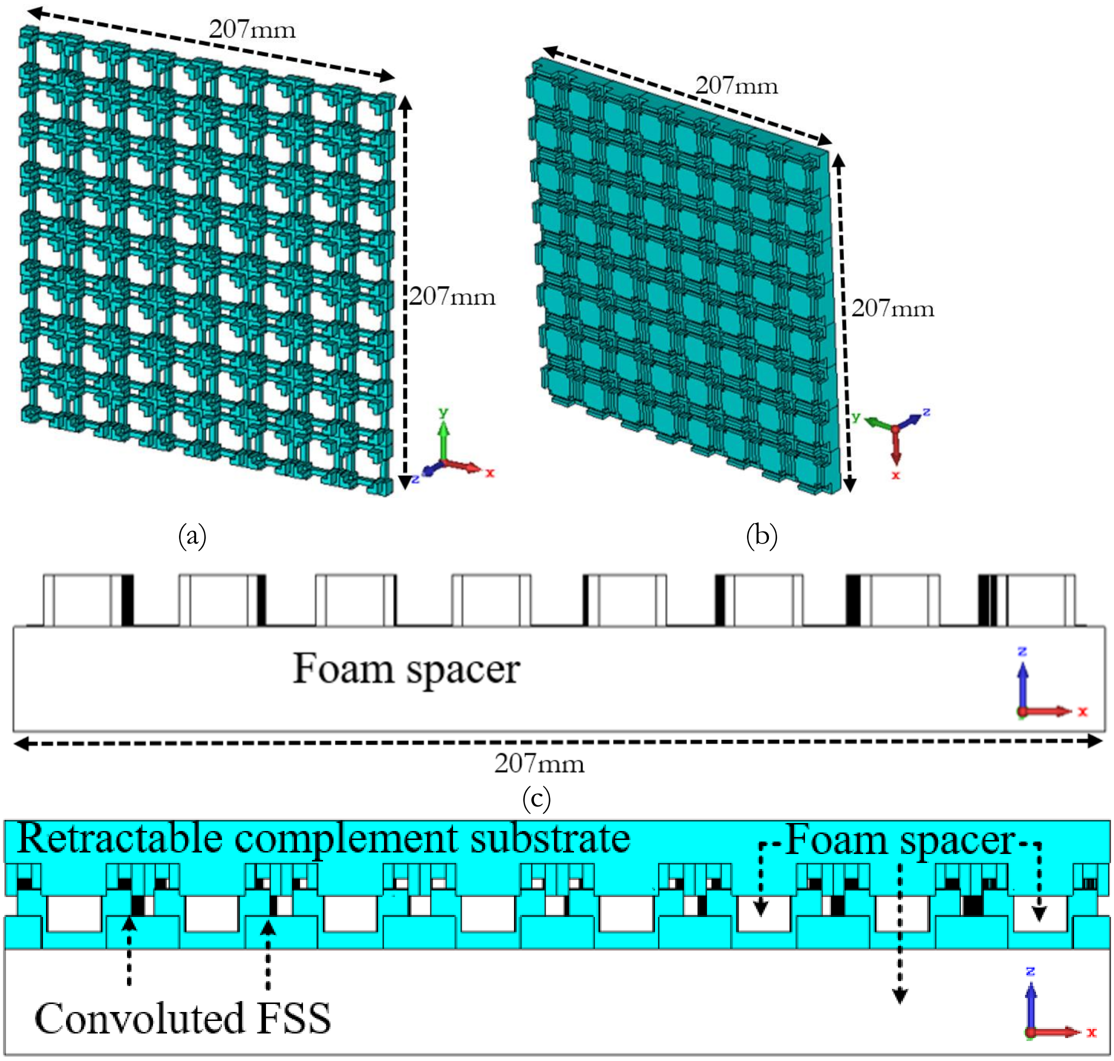

(a) (b)

(c)

(d)

Figure 6.14 FSS sensor and spacer models (a) FSS array, (b) complement substrate, (c) foam spacer model, (d) mounting mechanism of the FSS sensor with spacer.

The fabricated sensor and spacer are shown in Figure 6.15. The FFF printed FSS structure substrate material is shown in Figure 6.15(a) while Figure 6.15(b) shows the printed retractable complement substrate. Figure 6.15(c) demonstrates how the two parts lock together under normal circumstances. Figure 6.15(d) shows the RS pro Silver Conductive 186-3600 paint that was used while Figure 6.15(e) shows the painting process. The painted square loops are shown in Figure 6.15(f). The applied silver paint was left for 24 hours to dry though according to the data sheet [44], 30 minutes are required. Figure 6.15(g) shows a sample of the foam spacers. Figure 6.15(h) is a side view demonstrating how the substrate complement was positioned at the correct height using a foam spacer during measurements.

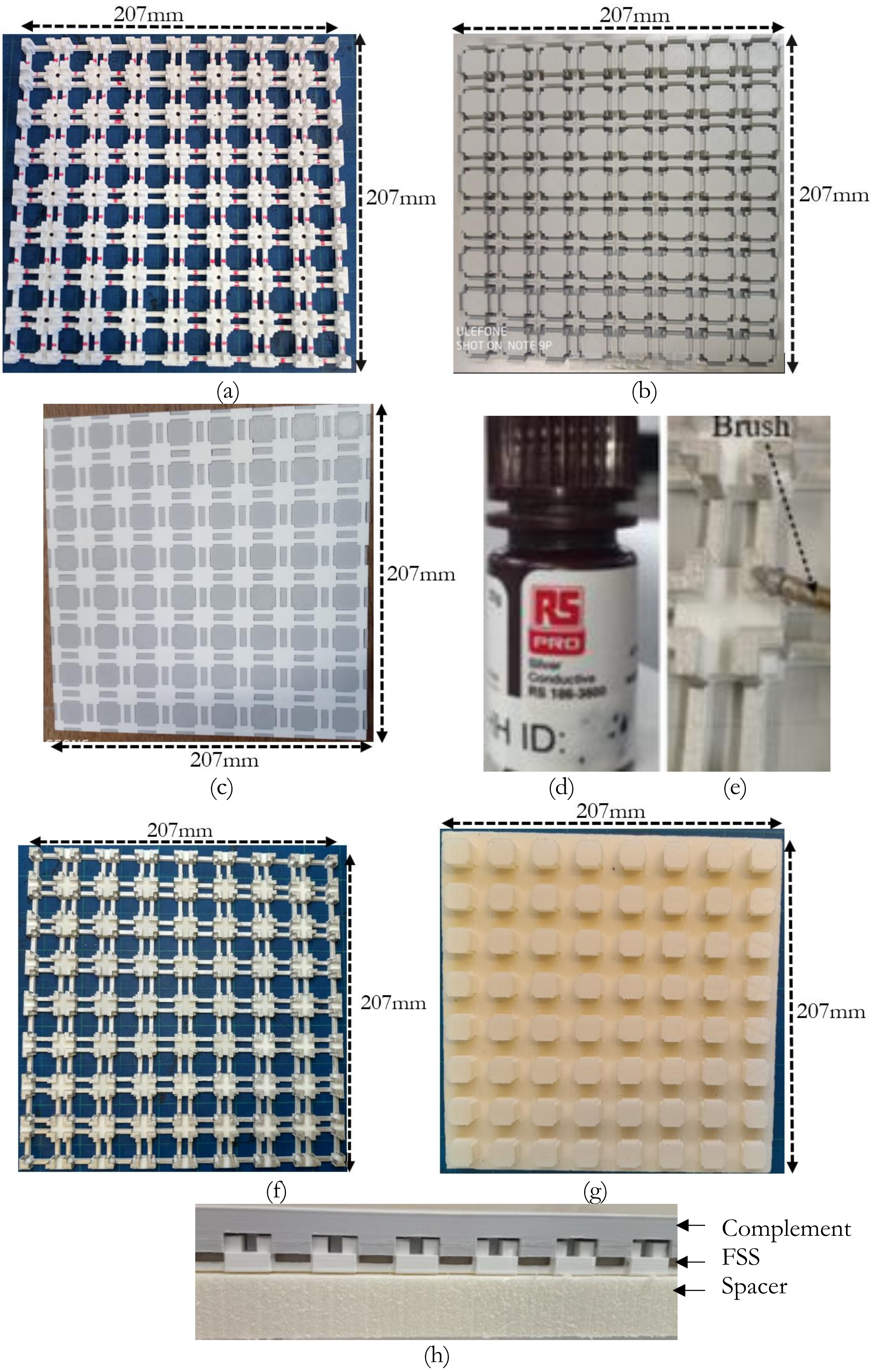

(a) (b) (c) (d) (e) (f) (g) (h)

Figure 6.15 The (a) printed FSS substrate, (b) substrate complement (c) FSS and complement locked together (d) RS pro Silver Conductive 186-3600 paint (e) brush painting the FSS (f) painted FSS (g) foam spacer (h) side view of spacer positioning the complement

Figure 6.16 are close-ups showing more details of the fabricated pieces. Figure 6.16(a); the FSS conductive tracks after painting, Figure 6.16(b), the complement substrate, Figure 6.16(c); the joined FSS and complement, Figure 6.16(d) and the spacer sample, Figure 6.16(e).

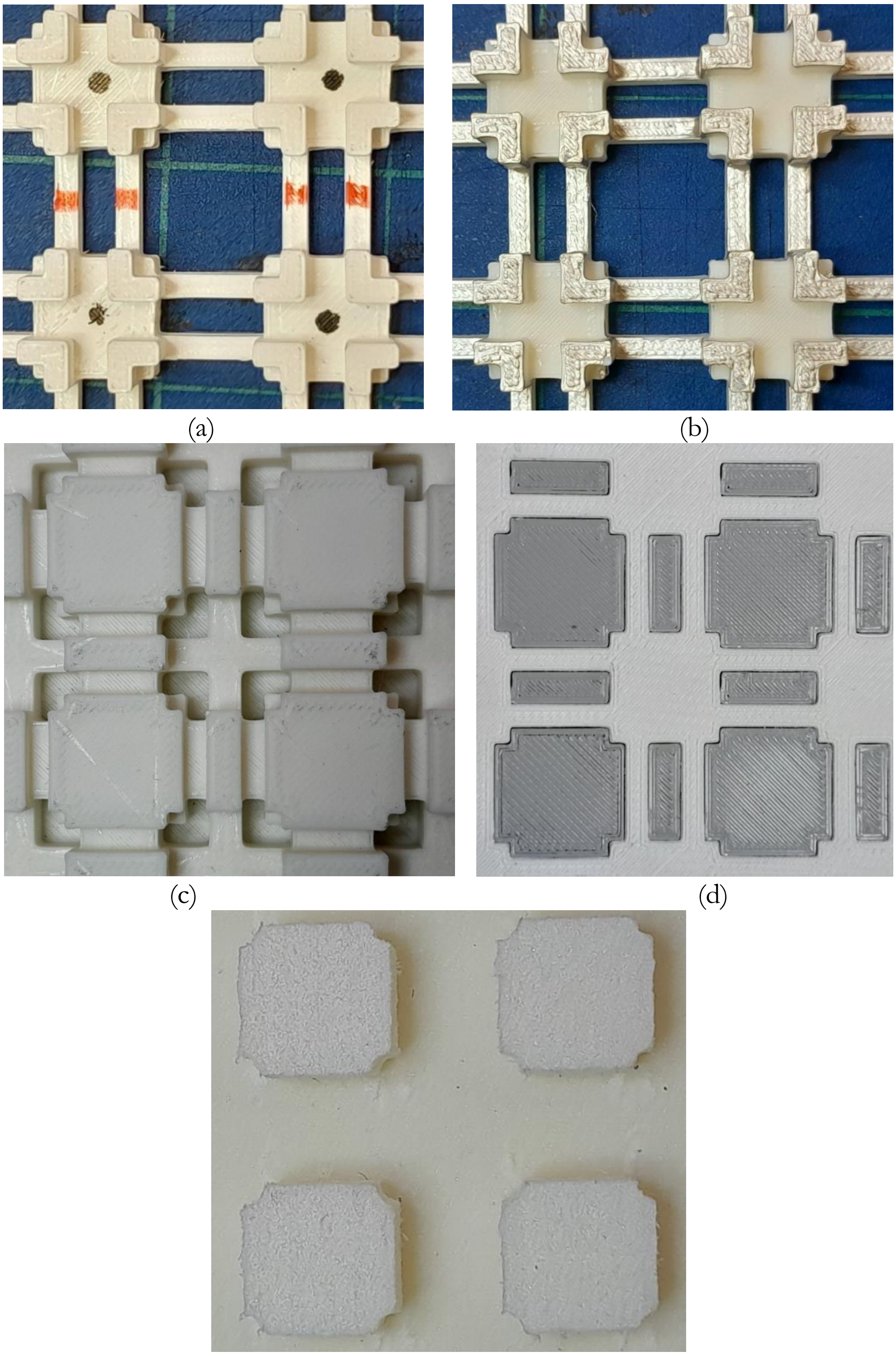

(a) (b)

(c) (d)

(e)

Figure 6.16 Close ups of the (a) FSS substrate (b) FSS conductive tracks (c) complement (d) joined FSS and complement (e) the spacer

6.5.2 Measurements and Results

The FSS sensor was placed in the plane wave chamber and transmission coefficient measurements, S_{21} were conducted as shown in Figure 6.17. Figure 6.17(a) shows the plain wave chamber measurement set up while Figure 6.17(b) shows the sensor position during the testing. The equipment used for the measurement was the Marconi Instruments microwave test set 6204B. The initial measurements were conducted on the FSS without complement (Figure 6.15(f)) and then with the complement substrate fully locked together (Figure 6.15 (c)).

(a) (b)

Figure 6.17 The (a) plain wave chamber measurement set up (b) sensor on chamber screen

Figure 6.18 shows the FSS sensor's angle of incidence behavior with and without the substrate complement. The FSS without the complement resonated at 2.7 GHz with a frequency shift of 0.37% at TE 45, and 0.74% at TM 45°. The FSS coupled to the complement resonates at 2.16 GHz with a 0.4% frequency shift at TE 45°, and 0.9% at TM 45°. Measurements are consistent with simulations (Figure 6.10). The variation of the resonance frequency between the simulated and measured fabrication errors. Fabrication errors can be caused by the printed substrate infill not being 100% and thus having air trapped air within the structure. This can cause potential deviation in the relative permittivity of the printed structure [51]-[53]. The manual application of the conductive FSS tracks could have potentially created a non-uniformity of the conductor both in its height and breath. Measurement errors could also occur due to potential non calibration of the measuring equipment as well as human error.

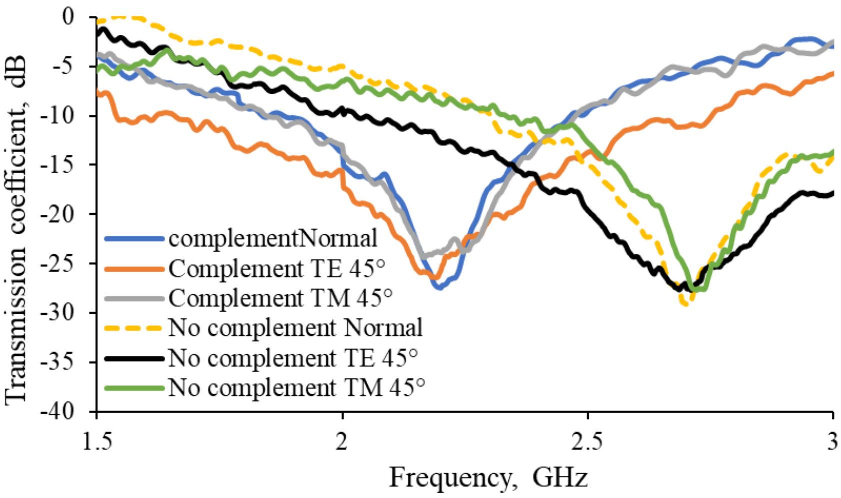

Figure 6.18 Measured S_{21} for TE normal, TE 45°and TM 45° angles of incidence of the FSS with and without the complement substrate.

Further measurements were carried out for displacement distance, z, from 0 mm to 10 mm at normal incidence, and are presented in Figure 6.19 and Table 6.4. A set of 5 foam spacers were used for the experiments. The results show that the resonance frequency progressively shifted to high frequencies with increase in withdrawal distance of the complement substrate.

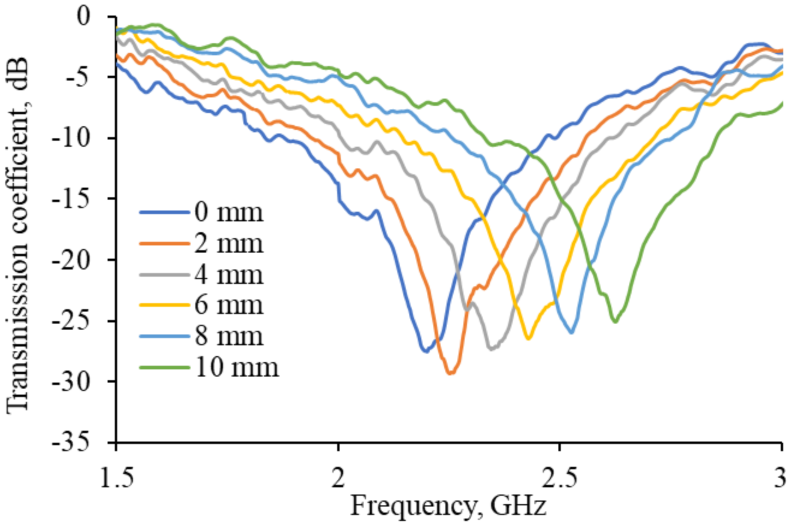

Figure 6.19 The measured S_{21} for TE normal as the complement substrate is withdrawn

Table 6.4 Sensitivity of the fabricated sensor

Displacement distance, z, mm	0	2	4	6	8	10
Measured frequency, GHz	2.16	2.24	2.35	2.47	2.58	2.67
Simulated frequency, GHz	2.17	2.25	2.37	2.48	2.57	2.66

Figure 6.20 shows the measured response of the sensor and its comparison with simulated response. The behavior of the fabricated sensor is consistent with simulated on with minimal deviation observed. This could be due to fabrication and measurements inaccuracies.

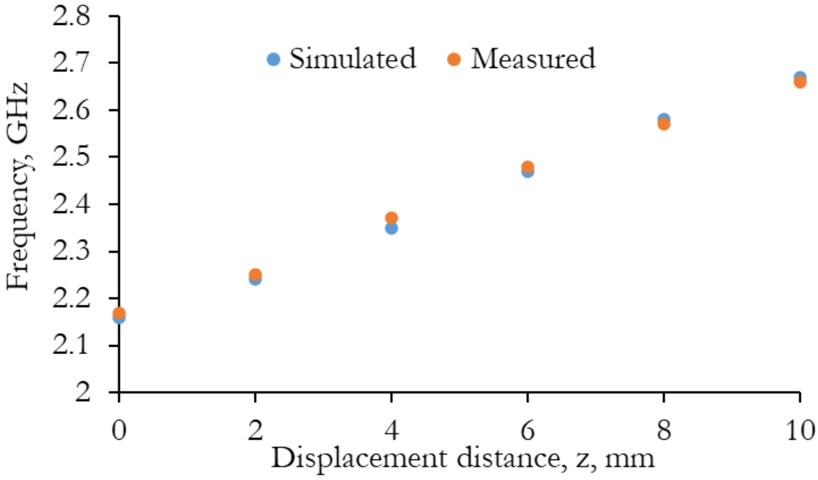

Figure 6.20 Curve of resonance frequency, f, versus substrate complement withdrawal distance z of the fabricated sensor

6.5.3 Surface profile analysis of the silver print of the sensor

A Keyence microscope VHX-7000 was used to observe the silver ink conductive surface. Its image is shown in Figure 6.21 at a x40 magnification.

Figure 6.21 Magnified silver nanoparticle conductive surface

Figure 6.22 show the nanoparticle silver ink conductive surface profile of Figure 6.21, observed, and measured at a magnification of x5000 using the Keyence microscope VHX-7000.

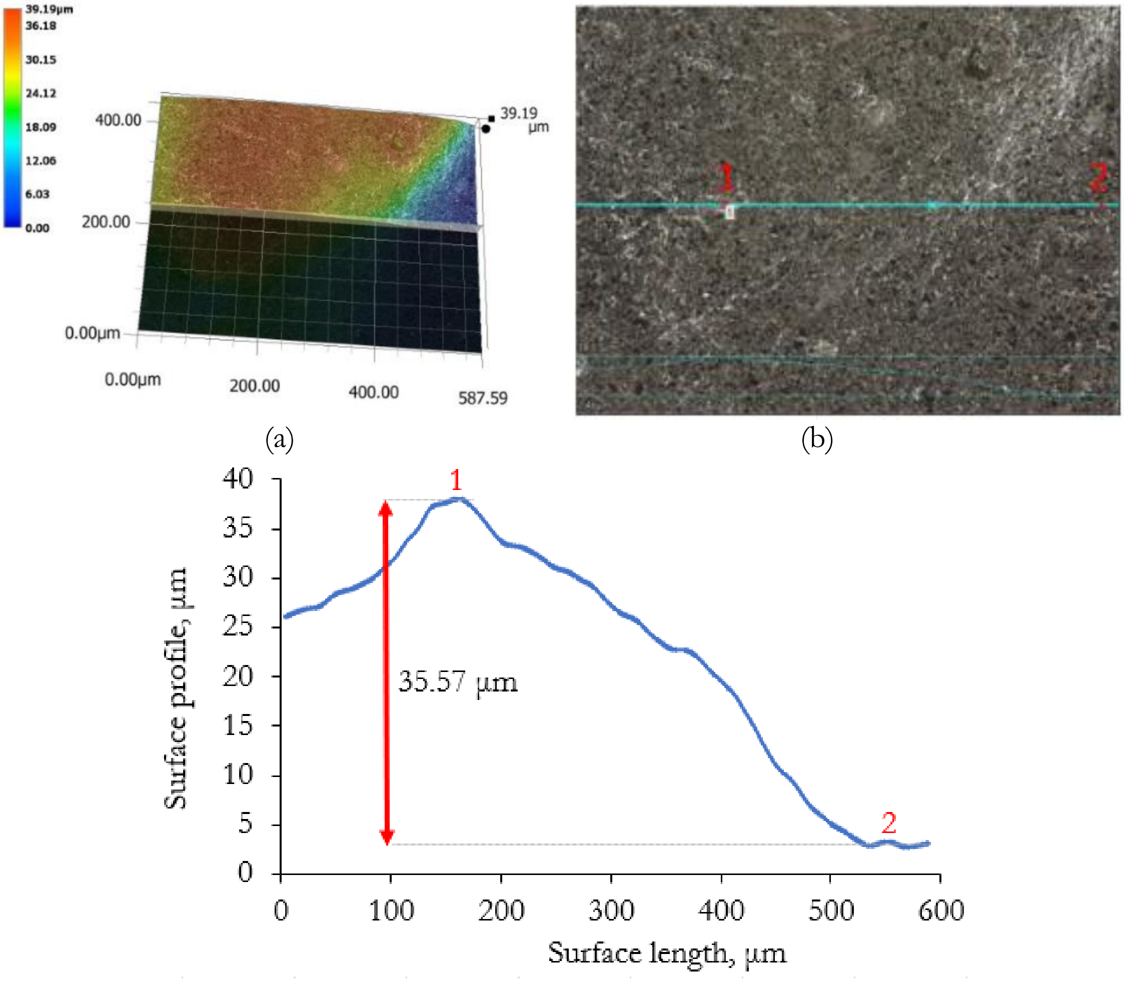

(a) (b)

(c)

Figure 6.22 Evaluation of the conductor surface (a) conductor surface profile (b) measurement point (c) the height profile between point

The profile measurements were taken at two points on the conductive track. The profile showed a differential of 35.57µm between two points on the conductor surface. This differential could be due to the uneven dielectric layer produced by the FDM process [54]. This implies that though the application is viable, the fabrication process produces an uneven surface.

The sensing of civil structures displacement has been discussed up to this point. Keeping with the theme of application of wireless applications in building structures, building material with embedded RF characteristics for enhancement of indoor signal is proposed in Section 6.6.

6.6 Screen-printed FSS Plasterboard for Wireless Indoor Application

Inexpensive method of reduction of wireless signals loss in indoor settings is a desirable for reasons such as cost reduction, better communication, security enhancements, etc. A method that involves screen printing of a frequency selective surfaces (FSS), on the inside walls of a room or building within which the signal needs to be contained is described in this section. The proposed low-cost FSS solution operates at 2 GHz that covers some of the existing mobile phone frequency bands. As already mentioned, an array of FSS square loop elements used in this application acts as a band-stop filter. An illustrative depiction of a 5G network FSS integrated into the walls of a room is shown in Figure 6.23. Incorporation of the FSS into building materials coupled with the employment of cheaper AM fabrication method answers for environment sustainability. The array structure was screen-printed on a plasterboard, such as would be used for the construction of an indoor wall of a room or building. Screen printing allows the direct printing of FSS on the surfaces of plasterboards with the details necessary for various microwave and mm-wave applications and provide the necessary conductivity for filtering. The intended application is the production of plasterboard FSS as a building material with embedded RF properties i.e., an FSS embedded plasterboards for the control of wireless propagation.

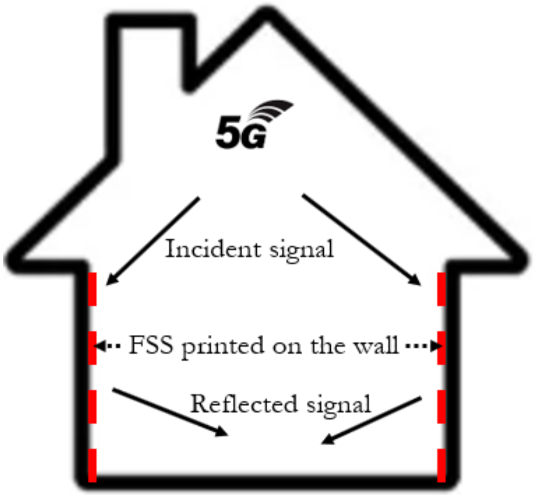

Figure 6.23 Implementation of a 5G reflector FSS as a reflector in a typical house [57]

An array of square loop elements is arranged in a lattice on the plasterboard to provide a stop band filtering response. Screen printing the FSS directly onto the plasterboard substrate means no other substrate material or fixtures are required thus reducing the cost.

6.6.1 Wireless signal security in indoor environment

In indoor environments, the loss of strength of a signal is caused mainly by its reflection and/or transmissions through building materials. Building architecture, electrical characteristics, as well as signal's angle of incidence and wall periodicity are some of the factors that may determine the signal penetration loss. Bandstop FSS designs have been used to filter out specific frequencies and thus reducing the interference indoors [55]-[60] as well as outdoors [61]-[64] when mounted on walls or windows depending on the applicational need. This is especially in applications where RF signals need to be confined to a specific area for wireless security and/or signal strength improvements which can help with interference management. There are other instances where the signals require amplifications to augment wireless coverage or system stability. Further, signal quality within a building normally drops due to absorption by the building materials used in the construction. To counter the problem of wireless security and signal quality within a building, reflective screens that reflects the signal away from the absorbing material can be employed such as the inkjet-printed paper poster FSS [56]. Full 3D printed wall mountable FSS is presented in [58] while in [59], an interwoven loops for electromagnetic architecture of buildings for potential applications for control of electromagnetic propagation in building is presented. In [60], a basic electromagnetic signal isolation and passive amplification using FSS structure on a FR4 substrate is presented. A hexagonal elements FSS bandpass filter on a non-magnetic glass that enhances efficiency in RF management in indoor-outdoor communication is proposed in [63] while [64] proposes a screen printed FSS on a thin polyethylene terephthalate (PET) bonded on the glass windowpane as an RF signal shielded secure environment for transmission through office widows. A lightweight 3D printed FSS structure that can potentially be incorporated in the walls of a building to control electromagnetic wave propagation within it is proposed in [65] and [66]. In [67], a band signal isolating FSS device on copper foil which can potentially offer improvement of mobile communications and efficiency of radio spectrum use within buildings is proposed. Self-adhesive aluminum foil square loops on a cardboard paper band-stop frequency-selective wall has been proposed in [68] which is shown to improve the signal to noise ratio of indoor communication network. The above methods though effective has inherent drawbacks. These includes fragility e.g., when paper is used [59] and [64], cost due to the materials required as well as the method of manufacture and equipment required [58]-[63] and [65]-[68]. [62] presents an application whose substrate material, glass, is fragile and the method used requires expensive equipment.

An inexpensive solution is proposed that uses the plasterboard that forms the building walls as the substrate using screen-printing fabrication method [55]. FSS square loops are printed on the plasterboard. All frequencies are passed through except the frequency of interest, in this case 2 GHz which is reflected within the room/building by the band-stop FSS filter. This method of fabrication is inexpensive, uses no energy and requires minimal training for the personnel doing the printing and the room's wall is the substrate on which the FSS is printed.

6.6.2 The FSS Unit Cell Design and Simulation

This subsection discusses the design and simulation of the unit cell of the solution.

6.6.2.1 The FSS Cell Simulation

A unit cell square loop of 34 x 34 mm with a track width of 5 mm on a plasterboard substrate of 36 mm x 36 mm x 15 mm dimensions with a relative permittivity, ε_r of 2.75 and tan δ of 0.0075 [69]. Square loop FSS resonates when the boundary of the loop is approximately a wavelength of the resonance frequency. Dycotech material silver electronic ink DM-SIP-3060S was used. According to its manufacturer datasheet [70], it is a low temperature curable screen printable conductive silver paste that is commonly used for membranes, thin film PVs and general printed electronics applications. It has a viscosity of 5-15 Pa.s, density of 2.25 g/ml, solids content 61-66%, sheet resistance of <10 mΩ/sq/mil (140°C cure temperature) and volume resistivity <28 μΩ.cm (140° C cure temperature).

The conductivity of the silver ink was computed so that it could be used in the simulation.

$$\rho s = \frac{\rho}{t}\ [\Omega/\mathrm{sq}] \tag{6.9}$$

where ρs is the sheet resistance, ρ is the resistivity and t is the print thickness. Therefore,

$$\rho = \rho s \times t \tag{6.10}$$

According to the datasheet, typical print thickness is 6-8 μm. Therefore,

$$\rho = 0.01\Omega/sq \times 6 \times 10^{-3} m = 6 \times 10^{-5}\ \Omega m \tag{6.11}$$

Thus, conductivity of the Dycotech silver paste is:

$$\sigma = \frac{1}{\rho} = \frac{1}{6\times10^{-5}\ \Omega m} = 1.67 \times 10^{5}\ S/m \tag{6.12}$$

The geometry of the unit cell is shown in Figure 6.24. Figure 6.24(a) is the perspective view and Figure 6.24(b) the top view of the design. Table 6.5 represents the cells dimensions.

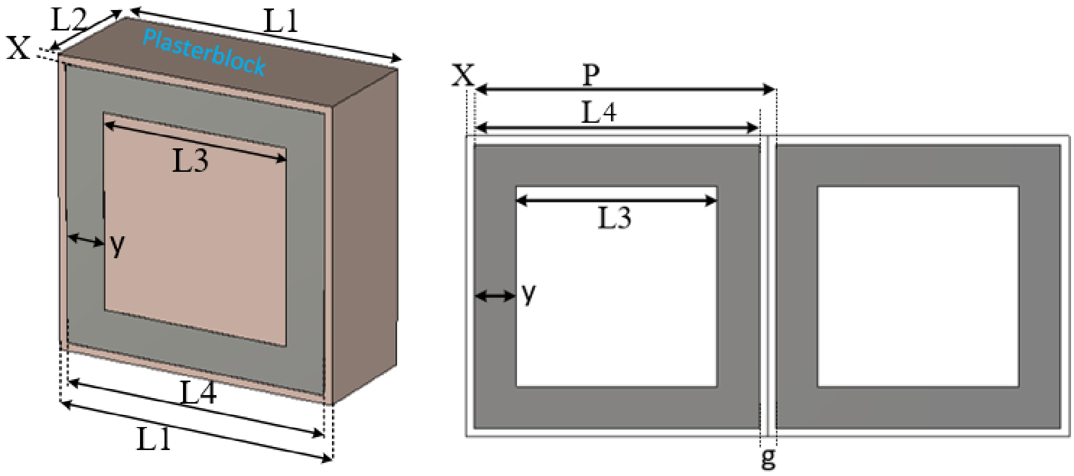

(a) (b)

Figure 6.24 Unit cell geometry with (a) perspective view with plasterboard and (b) front view

Table 6.5 Dimensions of the unit cell

Dimensions	L_1	L_2	L_3	L_4	x	y	g	P
(Values in mm)	36	15	24	34	1	5	2	36

The square loop was optimized to operate at a frequency of 2.0 GHz. The dimensions can be seen in Table I. L_1 represent the length of the unit cell. The track width is 5 mm. Gap x between the conductor loop and the edge of the cell is 1 mm while the gap g between two adjacent square loops is 2 mm. The periodicity, P, of the square loop array is the sum of g, the separation between conductor loops, and the length L_4 of the square loop and is equal to 36 mm.

6.6.2.2 The Simulation results

The designed filter was simulated using CST Microwave Studio™ to test its behavior in terms of transmission coefficient. According to the manufacturer's datasheet [70], typical print thickness after drying is 6-8 μm. Figure 6.25 shows the simulated transmission response of the FSS for the normal response along with that of TE and TM angle of incidence of 45°. TE denotes the E-plane response whereas TM denotes H-plane response. The results indicate that the resonance of the unit cell occurred at normal incidence with a frequency of 2.0 GHz with no considerable frequency drift at TE 45° and TM 45°.

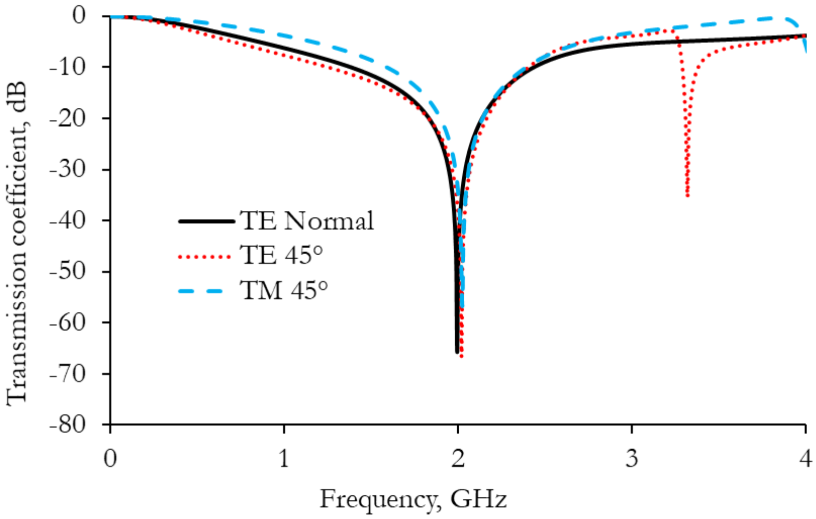

Figure 6.25 S_{21} response of the plasterboard FSS

6.6.3 Fabrication and Measurements

This subsection discusses the fabrication and measurement of the screen-printed FSS on plasterboard.

6.6.3.1 Screen printing

Screen printing was employed in the fabrication of the FSS screen. Screen printing is a technique in which a mesh is used to transfer the ink onto predetermined area of a substrate while other areas of the substrate are made impermeable to the ink by a blocking stencil. A squeegee is moved across the screen to fill the open mesh apertures with ink. A reverse stroke then causes the screen to touch the substrate momentarily along a line of contact. This causes the ink to dampen the substrate and be pulled out of the mesh apertures as the screen springs back after the squeegee has passed [71]. This process of using a mesh-based stencil can be used to apply ink onto substrates such as posters, Kapton and as proposed through this work, plasterboard. The first stage of the fabrication process was to develop a mesh stencil. The unit cell of CST model was extended to 7x5 array and then exported as a drawing exchange format (DXF) from which the mesh stencil was made at [72]. Figure 6.26(a) shows the extended 7x5 array model, Figure 6.26(b) is the stencil. Dycotec material conductive silver electronic paste, Figure 6.26(c), was used to print the FSS. The silver paste was put on the stencil screen. The stencil screen was on a plasterboard substrate of 15 mm thickness. A squeegee was then used to run and spread the paste on the screen as in Figure 6.26(d).

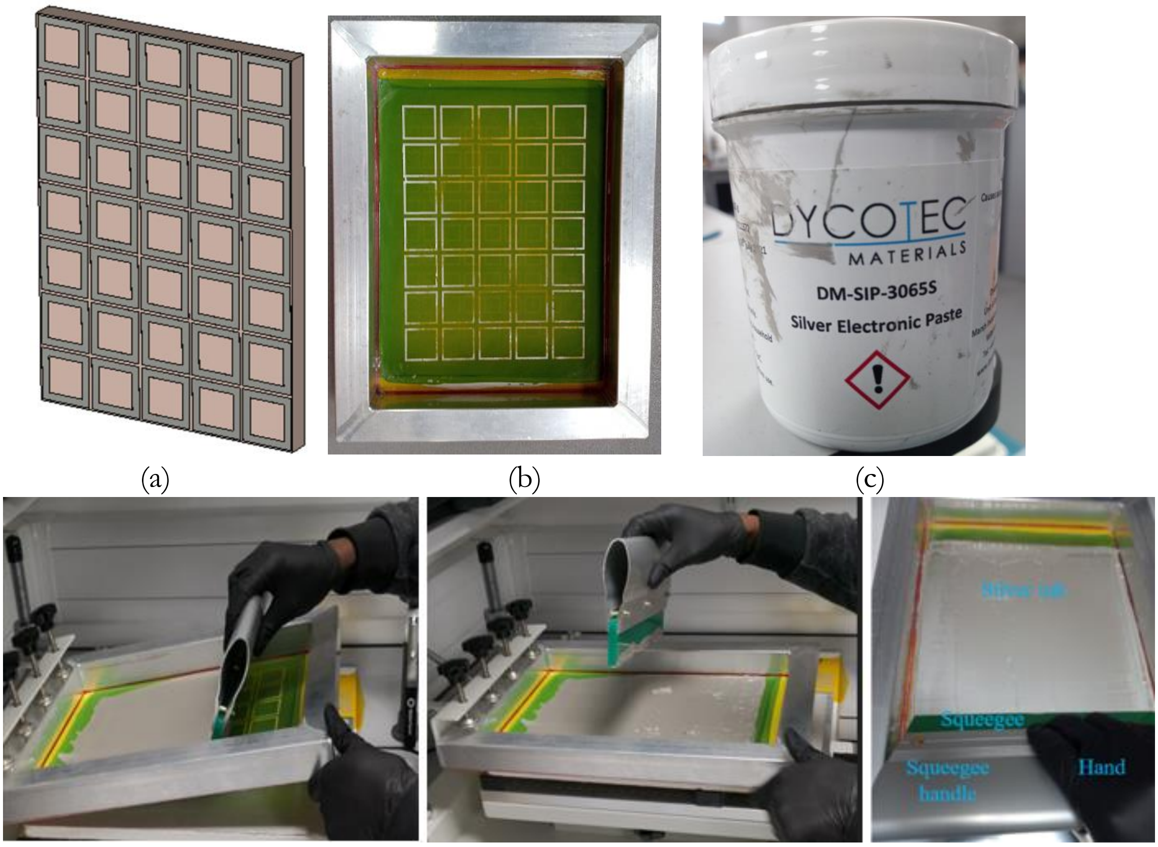

(a) (b) (c)

(d)

Figure 6.26 The (a) extended 7x5 array model (b) the stencil (c) DM-SIP-3065S silver paste and (d) Screen printing process

The FSS bearing plasterboard was then cured in a Gallenhamp hotbox oven shown in Figure 6.27(a), for 20 minutes at a temperature of 140°C, as per the manufacturer's datasheet [69] instructions. Figure 6.27(b) shows the cured FSS, Figure 6.27(c) shows the print profile of the track while Figure 6.27(d) is a close-up view of the track at 10x magnification by Keyence microscope VHX-7000.

6.6.3.2 Measurements and results

A Marconi instruments® microwave test set 6204B was used to measure the transmission response of the FSS in a plane-wave chamber. Figure 6.28 depicts the measurement setup. Figure 6.28(a) shows the FSS on plasterboard on the screen of the plain wave chamber, while Figure 6.28(b) shows the chamber set up for the measurements which shows the transmitter and the receiver antennas denoted by Tx and Rx respectively mounted at one meter from each other. The measurements were done for normal, TE 45˚ and TM 45˚ responses respectively and the results are presented in Figure 6.29. The normal angle of incidence response, or TE 0° resonated at a marginally higher 2.08 GHz. The TE 45˚ resonated at the same frequency whereas TM 45° resonated at exactly 2 GHz.

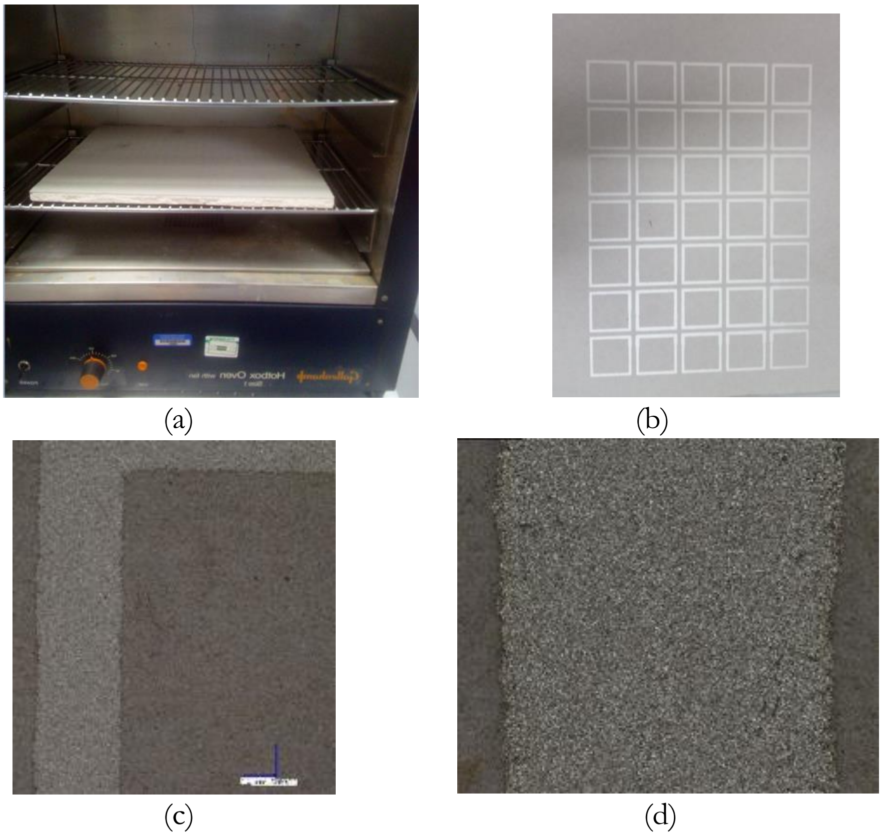
(a) (b)
(c) (d)

Figure 6.27 Final FSS (a) curing in the Gallenkamp hotbox oven (b) the printed FSS on a plasterboard, (c) print profile of the track and (d) a close-up view of the track at 10x zoom

(a) (b)

Figure 6.28 The FSS on the plain wave screen (b) chamber the measurements set up

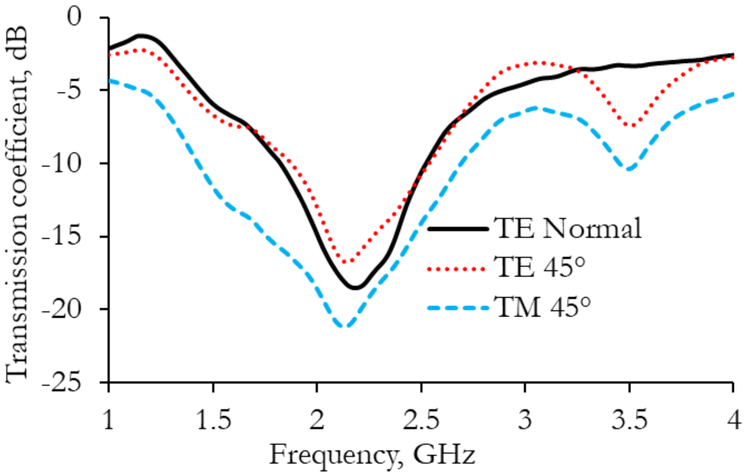

Figure 6.29 Measured S_{21} Results

6.7 Discussion and Conclusion

A novel FSS based displacement wireless sensor based on a retractable complement substrate has been demonstrated. It can be useful in situations like after an earthquake for post-earthquake damage assessment of civil structures. The sensor uses a substrate complement to modify the transmission response of an FSS as the complement is withdrawn in the z-axis. The range of the sensor can be extended using 3D convoluted techniques described, resulting in a new 3D convoluted FSS sensor. Extending the sensor in 3D also improves its angle of incidence behavior and increases the range the sensor can measure. The FSS structures developed are based on a modified square loop FSS element and are inherently dual polarized. In terms of sensor operation, the withdrawable dielectric substrate has the effect of changing the effective permittivity and therefore capacitance of the FSS array. The FSS sensor provides a good displacement sensing of up to 0.1λ which can be extended. The range of the FSS could be potentially increased by extending the FSS in the z plane.

The FSS sensor was fabricated using 3D printing techniques and painting of the conductive tracks of the square loop FSS was done manually. Table 6.6 summarizes the performance of other reported metamaterial sensors compared to the proposed design.

Table 6.6 Comparison of the proposed design with the reported FSS based sensing designs

Parameters	References		
	[31]	[33]	This work
Frequency (GHz)	10	0.4	2.0
Sensitivity (GHz/mm)	0.326	0.008	0.052
Geometry	2D	2D	3D
Dynamic range (mm)	5	7	10
Sensor type	FSS	Metamaterial	FSS
Polarization	Single	Single	Dual
Complementary structures	No	No	Yes
Displacement direction	Horizontal	Horizontal	Vertical

The proposed sensor also differs conceptually and geometrically to those in the table. [31] is based on the concept of two sliding conductors horizontally, while [33] focuses on the separation of conducting metamaterials in the horizontal plane and the detection through coupling to antenna in the near field. Besides its simplicity, the proposed FSS sensor offers good sensitivity, dual polarization, and a higher dynamic range. The range of the sensor can be extended further by increasing the length of the conductor of the square loop element in the z-plane (Figure 6.8). The sensitivity could be increased further by using a complement substrate with higher dielectric constant.

The proposed sensor is ideal for instances requiring real-time monitoring of structural changes such as movement or cracks due to deformation due to earthquakes or natural movement. It could also be ideal for detection of likely structural damage after an earthquake.

The proposed displacement sensor technique can be integrated into a structure as illustrated in Figure 6.30. The movement of the structure from an initial state, Figure 6.30(a) to a displaced state, Figure 6.30(b) leads to a change in the state of the FSS and thus change in the resonance frequency. The initial state of the structure is the FSS, and the substrate complement locked together (Figure 6.30(a)). The FSS is protected by the dielectric layer, which is ideal for external applications. In the event of structural movement, the change is picked up through the change in S_{21} of sensor attached to the structure. As a proof-of-concept, the experimental results suggests that the proposed prototype holds promises to be a future prospective structural movement or displacement detector/sensor both locally and remotely.

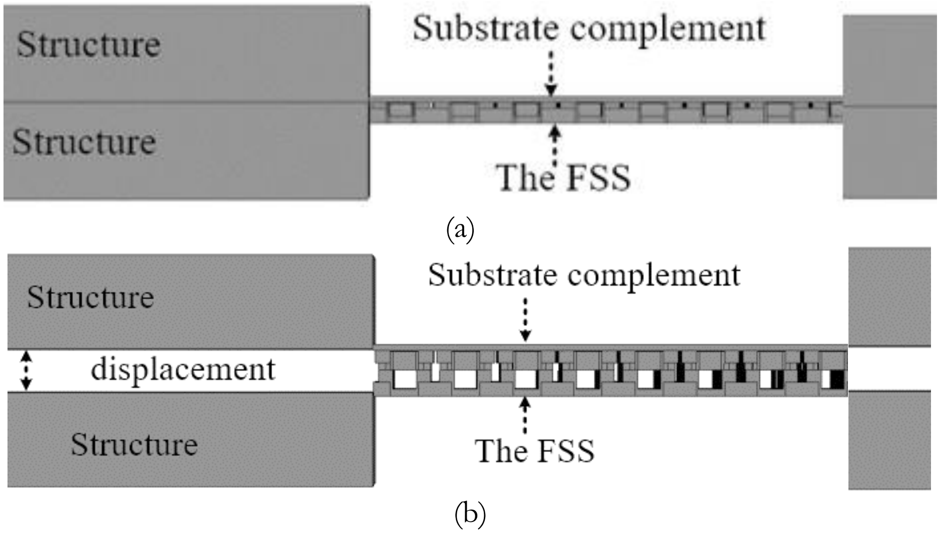

(a)

(b)

Figure 6.30 Illustrative potential conceptual arrangement of the structural displacement sensor (a) before displacement, and (b) after displacement

The FFF process used in the fabrication of the device offers reduction in material cost, labour as well as manufacturing time. The fabrication process can also be scaled up.

A 3D printed FSS operating at 2 GHz on a plasterboard has also been demonstrated. The inexpensive FSS design was screen printed using silver paste on a plasterboard used in walls. The rapid printing made this printing method a suitable alternative for ready to use FSS filtering building materials. The measured transmission response demonstrated consistency with the simulated transmission response at the frequency of operation at around 2 GHz which caters for some of the existing mobile communication bands. The FSS plasterboard can be used to control propagation in buildings either by filtering unwanted signals or guiding signals to areas where coverage is weak. The performance of the proposed design can be further enhanced by printing multiple layers of the FSS structure on top of one another. Furthermore, by adding active components, this FSS can also be developed as a smart reconfigurable FSS.

Acknowledgement

In this work, Peter Njogu did the research, sensor design and simulation, fabrication, laboratory testing and writing; Benito Sanz-Izquierdo and Prof. Edward gave guidance. In the conference paper [55], Peter Njogu did the research, simulations, fabrications, measurements as well as wrote the paper. Adam Smith participated in the measurements, Anshuman Shastri did pre-submission review while Dr. Benito Sanz-Izquierdo gave guidance.

References

[1] A. Depold, S. Erhardt, R. Weigel and d. F. Lurz, "A 10 kHz to 6 GHz Low-Cost Vector Network Analyzer," Advances in Radio Science, vol. 19, pp. 17–22, 2021.

[2] J. Verhaevert and P. V. Torre, "A low-cost vector network analyzer: Design and realization," in Loughborough Antennas & Propagation Conference (LAPC 2017), Loughborough, 2017.

[3] A. Deivasigamani, A. Daliri, C. H. Wang and S. John, "A Review of Passive Wireless Sensors for Structural Health Monitoring," *Modern Applied Science,* vol. 7, no. 2 , pp. 57-76, 2013.

[4] B. A. Munk, Frequency Selective Surfaces: Theory and Design, Chichester: John Wiley & Sons, Inc., 2000.

[5] E. A. Parker, "The Gentleman's Guide to Frequency Selective Surfaces," in *17th Q.M.W. Antenna Symposium*, London, April 1991.

[6] D. F. Pieper and K. M. Donnell, "Application of frequency selective surfaces for inspection of layered structures," in *IEEE International Instrumentation and Measurement Technology Conference (I2MTC) Proceedings*, Pisa, Italy, 2015.

[7] P. Callaghan, E. A. Parker and R. J. Langley, "Influence of supporting dielectric layers on the transmission properties of frequency selective surfaces," *IEE Proceedings-H,* vol. 138, no. 5, pp. 448 – 454, 1991.

[8] A. Chatterjee and S. K. Parui, "Performance Enhancement of a Dual-Band Monopole Antenna by Using Frequency Selective Surface Based Corner Reflector," *IEEE Transactions on Antennas And Propagation,* vol. 64, no. 6, pp. 2165- 2171, 2016.

[9] L. E. Comtesse, R. J. Langley, E. A. Parker and J. C. Vardaxoglou, "Frequency Selective Surfaces in Dual and Triple Band Offset Reflector Antennas," in *17th European Microwave Conference*, Rome, Italy, 1987.

[10] S. Chakravarty, R. Mittra and N. Williams, "Application of a microgenetic algorithm (MGA) to the design of broadband microwave absorbers using multiple frequency selective surface screens buried in dielectrics," *IEEE Transactions on Antennas and Propagation,* vol. 50, no. 3, pp. 284 - 296, 2002.

[11] F. Costa and A. Monorchio, "A Frequency Selective Radome With Wideband Absorbing Properties," *IEEE Transactions on Antennas and Propagation,* vol. 60, no. 6, pp. 2740 - 2747, 2012.

[12] C.-C. Chang, R.-H. Lee and T.-Y. Shih, "Design of a Beam Switching/Steering Butler Matrix for Phased Array System," *IEEE Transactions on Antennas and Propagation ,* vol. 58, no. 2, pp. 367 - 374, 2010.

[13] A. A. Dewani, S. G. O'Keefe, D. V. Thiel and A. Galehdar, "Window RF Shielding Film Using Printed FSS," *IEEE Transactions on Antennas and Propagation,* vol. 66, no. 2, pp. 790 - 796, 2018.

[14] E. A. Parker, C. Antonopoulos and N. E. Simpson, "Microwave Band FSS in Optically Transparent Conducting Layers: Performance of Ringelement Arrays," *Microwave and Optical Technology Letters,* vol. 16, no. 2, pp. 61-63, 1998.

[15] L. Zhang, Q. Wu and T. A. Denidni, "Electronically Radiation Pattern Steerable Antennas Using Active Frequency Selective Surfaces," *IEEE Transactions on Antennas and Propagation,* vol. 61, no. 12, pp. 6000 - 6007, 2013.

[16] B. Liang, B. Sanz-Izquierdo, E. A. Parker and J. C. Batchelor, "Cylindrical Slot FSS Configuration for Beam-Switching Applications," *IEEE Transactions on Antennas and Propagation,* vol. 63, no. 1, pp. 166 - 173, 2015.

[17] C. Gu, B. S. Izquierdo, S. Gao, J. C. Batchelor, E. A. Parker, F. Qin, G. Wei, J. Li and J. Xu, "Dual-Band Electronically Beam-Switched Antenna Using Slot Active Frequency Selective Surface," *IEEE Transactions on Antennas and Propagation,* vol. 65, no. 3, pp. 1393 - 1398, 2017.

[18] S. Soltani, P. S. Taylor, E. A. Parker and J. C. Batchelor, "Popup Tunable Frequency Selective Surfaces for Strain Sensing," *IEEE Sensors Letters,* vol. 4, no. 4, 2020.

[19] R. Melik, E. Unal, N. K. Perkgoz, C. Puttlitz and H. V. Demir, "Metamaterial-based wireless strain sensors," *Applied Physics Letters,* vol. 95, pp. 1-3, 2009.

[20] B. G. Xia, D. H. Zhang, J. Meng, J. Huang, C. F. Yao and J. S. Zhang, "Terahertz FSS for space borne passive remote sensing application," *Electronics Letters ,* vol. 49, no. 22, pp. 1398–1399, 2013.

[21] S. Y. Jun, B. S. Izquierdo and E. A. Parker, "Liquid Sensor/Detector Using an EBG Structure," *IEEE Transactions on Antennas and Propagation,* vol. 67, no. 5, pp. 3366 - 3373, 2019.

[22] A. Arif, A. Zubair, K. Riaz, M. Q. Mehmood and M. Zubair, "A Novel Cesaro Fractal EBG-Based Sensing Platform for Dielectric Characterization of Liquids," *IEEE Transactions on Antennas and Propagation,* vol. 69, no. 5, pp. 2887 - 2895, 2021.

[23] Al-Naiba, I. A, Ibraheem, C. Jansen and M. Koch, "Thin-film sensing with planar asymmetric metamaterial resonators," *Appl. Phys. Lett.,* vol. 93, no. 8, pp. 1-3, 2008.

[24] D. Hasan and C. Lee, "Hybrid Metamaterial Absorber Platform for Sensing of CO2 Gas at Mid-IR," *Advanced Science,* vol. 5, no. 5, pp. 1-13, 2018.

[25] D. Pieper, K. M. Donnell, O. Abdelkarim and M. A. ElGawady, "Embedded FSS sensing for structural health monitoring of bridge columns," in *2016 IEEE International Instrumentation and Measurement Technology Conference Proceedings*, Taipei, Taiwan, 2016.

[26] C. Debus and P. H. Bolivar, "Frequency selective surfaces for high sensitivity terahertz sensing," *Appl. Phys. Lett.,* vol. 91, no. 18, pp. 1-3, 2007.

[27] A. M. J. Marindra and G. Y. Tian, "Chipless RFID sensor for corrosion characterization based on frequency selective surface and feature fusion," *Smart Materials and Structures,* vol. 29, pp. 1-10, 2020.

[28] M. Joodaki and M. Rezaee, "Coplanar Waveguide (CPW) Loaded With an Electromagnetic Bandgap (EBG) Structure: Modeling and Application to Displacement Sensor," *IEEE Sensors Journal,* vol. 16, no. 9, pp. 3034 - 3040, 2016.

[29] J. Basseri and M. Joodaki, "An Angular Displacement Sensor With a Curved Two-Metal-Layer CPW Loaded by an EBG Structure," *IEEE Sensors Journal,* vol. 18, no. 6, pp. 2335 - 2341, 2018.

[30] S.-D. Jang, B.-W. Kang and J. Kim, "Frequency selective surface based passive wireless sensor for structural health monitoring," *Smart Materials and Structures,* vol. 22, no. 2, pp. 1-8, 2013.

[31] J.-J. Zhang, B. Wu, Y.-T. Zhao, L. Song, H.-R. Zu, R.-G. Song and D.-P. He, "Two-Dimensional Highly Sensitive Wireless Displacement Sensor With Bilayer Graphene-Based Frequency Selective Surface," *IEEE Sensors Journal,* vol. 21, no. 21, pp. 23889-23897, 2021.

[32] Q. Abbas, P. A. Shinde, M. A. Abdelkareem, A. H. Alami, M. Mirzaeian, A. Yadav and A. G. Olabi, "Graphene Synthesis Techniques and Environmental Applications," *MPDI Materials,* vol. 15, pp. 1-49, 2022.

[33] B. Ozbey, E. Unal, H. Ertugrul, O. Kurc, C. M. Puttlitz, V. B. Erturk, A. Altintas and H. V. Demir, "Wireless Displacement Sensing Enabled by Metamaterial Probes for Remote Structural Health Monitoring," *Sensors,* vol. 14, no. 1, pp. 1691-1704, 2014.

[34] M. Nauman, R. Saleem, A. K. Rashid and M. F. Shafique, "A Miniaturized Flexible Frequency Selective Surface for X-Band Applications," *IEEE Transactions on Electromagnetic Compatibility,* vol. 58, no. 2, pp. 419 - 428, 2016.

[35] R. S. Anwar, L. Mao and H. Ning, "Frequency Selective Surfaces: A Review," *MPDI Applied Sciences,* vol. 8, no. 9, pp. 1-47, 2018.

[36] T. Liu and S.-S. Kim, "Ultrawide Bandwidth Electromagnetic Wave Absorbers Using a High-capacitive Folded Spiral Frequency Selective Surface in a Multilayer Structure," *Scientific Reports,* vol. 9, pp. 1-11, 2019.

[37] S. N. Azemi and W. S. T. Rowe, "Development and analysis of 3D Frequency Selective Surfaces," in *Asia-Pacific Microwave Conference 2011*, Melbourne, VIC, Australia, 2011.

[38] S. N. Azemi, K. Ghorbani and W. S. T. Rowe, "3D Frequency Selective Surfaces," *Progress In Electromagnetics Research C,* vol. 29, pp. 191–203, 2012.

[39] J. H. Barton, C. R. Garcia, E. A. Berry, R. Salas and R. C. Rumpf, "3-D Printed All-Dielectric Frequency Selective Surface With Large Bandwidth and Field of View," *IEEE Transactions on Antennas and Propagation,* vol. 63, no. 3, pp. 1032 - 1039, 2015.

[40] B. Sanz-Izquierdo and E. A. Parker, "3-D Printing of Elements in Frequency Selective Arrays," *IEEE Transactions On Antennas and Propagation,* vol. 62, no. 12, pp. 6060-6066, 2014.

[41] I. Lee and I. Hong, "3D frequency selective surface for stable angle of incidence," *Electronics Letters,* vol. 50, no. 6, pp. 423–424, 2014.

[42] J. H. Barton, C. R. Garcia, E. A. Berry, R. G. May, D. T. Gray and R. C. Rumpf, "All-Dielectric Frequency Selective Surface for High Power Microwaves," *IEEE Transactions on Antennas and Propagation,* vol. 62, no. 7, pp. 3652 - 3656, 2014.

[43] D. Z. Zhu, M. D. Gregory, P. L. Werner and D. H. Werner, "Fabrication and Characterization of Multiband Polarization Independent 3-D-Printed Frequency Selective Structures With UltraWide Fields of View," *IEEE Transactions on Antennas and Propagation,* vol. 66, no. 11, pp. 6096 - 6105, 2018.

[44] Tractus3D, "FDM 3D printing – Fused Deposition," Tractus 3D, 01 10 2021. [Online]. Available: https://tractus3d.com/knowledge/learn-3d-printing/fdm-3d-printing/. [Accessed 01 10 2021].

[45] W. Mohyuddin, D. H. Kim, H. C. Choi and K. W. Kim, "Comparative Study of Square and Circular Loop Frequency Selective Surfaces for Millimeter-Wave Imaging Diagnostics Systems," *Sensors (Basel),* vol. 18, no. 9, pp. 1-13, 2018.

[46] "RS PRO Liquid Conductive Paint," RS, 10 06 2021. [Online]. Available: https://uk.rs-online.com/web/p/adhesives/1863600/. [Accessed 10 06 2021].

[47] S. Y. Jun, A. Elibiary, B. Sanz-Izquierdo, L. Winchester, D. Bird and A. McCleland, "3-D Printing of Conformal Antennas for Diversity Wrist Worn Applications," *IEEE Transactions On Components, Packaging and Manufacturing Technology,* vol. 8, no. 12, pp. 2227-2235, 2018.

[48] I. Anderson, "On the Theory of Self-Resonant Grids," *The Bell System Technical Journal,* vol. 54, no. 10, pp. 1725 - 1731, 1975.

[49] N. Marcuvitz, Waveguide Handbook, Exeter: Short Run Press, 1986.

[50] P. Callaghan and E. A. Parker, "Element dependency in dielectric tuning of frequency selective surfaces," *Electronics Letters,* vol. 28, no. 1, pp. 42 – 44, 1992.

[51] S. Moscato, R. Bahr, T. Le, M. Pasian, M. Bozzi, L. Perregrini and M. M. Tentzeris, "Infill-Dependent 3-D-Printed Material Based on NinjaFlex Filament for Antenna Applications," *IEEE Antennas and Wireless Propagation Letters,* vol. 15, pp. 1506 - 1509, 2016.

[52] A. Goulas, S. Zhang, D. A. Cadman, J. Järveläinen, V. Mylläri, W. G. Whittow, J. (. C. Vardaxoglou and D. S. Engstrøm, "The Impact of 3D Printing Process Parameters on the Dielectric Properties of High Permittivity Composites," *MPDI Designs,* vol. 3, no. 4, pp. 1-10, 2019.

[53] J. Huang, S. J. Chen, Z. Xue, W. Withayachumnankul and C. Fumeaux, "Impact of Infill Pattern on 3D Printed Dielectric Resonator Antennas," in *2018 IEEE Asia-Pacific Conference on Antennas and Propagation (APCAP)*, Auckland, New Zealand, 2018.

[54] M. S. Alsoufi and A. E. Elsayed, "Surface Roughness Quality and Dimensional Accuracy—A Comprehensive Analysis of 100% Infill Printed Parts Fabricated by a Personal/Desktop Cost-Effective FDM 3D Printer," *Material Science and Application,* vol. 9, no. 1, pp. 11- 40, 2018.

[55] P. Njogu, A. Shastri, A. Smith, S. Gao and B. Sanz-Izquierdo, "Screen-Printed FSS Plasterboard for Wireless Indoor Applications," in 2022 *Microwave Mediterranean Symposium (MMS)*, Pizzo Calabro, Italy, 2022.

[56] G. Kiani, A. Weily and K. Esselle, "A Novel Absorb/Transmit FSS for Secure Indoor Wireless Networks With Reduced Multipath Fading," IEEE *Microwave and Wireless Components Letters*, vol. 16, no. 6, pp. 378 - 380, 2006.

[57] A. Shastri, P. Njogu, B. Sanz-Izquierdo, S. Gao and Z. Chen, "Low-cost Inkjet Printed Paper Poster FSS for 5G Applications," in 15th European Conference on Antennas and Propagation (EuCAP), Dusseldorf, Germany, 2021.

[58] A. Shastri, B. Sanz-Izquierdo, A. Elibiary and E. A. Parker, "Manufacturing, Developments, and Constraints in Full 3-D Printing of Frequency-Selective Surface Using Low-Cost Open-Source Printer," in *IEEE Transactions on Components, Packaging and Manufacturing Technology*, vol. 11, no. 12, pp. 2193-2200, Dec. 2021.

[59] B. Sanz-Izquierdo, E. Parker, J. Robertson, J. C. Batchelor, M. J. Neve and A. Williamson, "Interwoven loops for electromagnetic architecture of buildings," in 2010 IEEE Antennas and Propagation Society International Symposium, Toronto, ON, Canada, 2010.

[60] M. Raspopoulos and Stavros Stavrou, "Frequency Selective Buildings Through Frequency Selective Surfaces," *IEEE Transactions on Antennas and Propagation*, vol. 59 , no. 8, pp. 2998-3005, 2011.

[61] E. A. Parker, C. Antonopoulos and N. E. Simpson, "Microwave Band FSS in Optically Transparent Conducting Layers:Performance of Ringelement Arrays," *Microwave and Optical Technology Letter*, vol. 16, no. 2, pp. 61-63, 1997.

[62] A. Shastri, K. Putta, E. A. Parker, S. Gao, L. Winchester and A. McClelland, "Evaluation of Aerosol Jet Printing of Frequency Selective Surface on Glass for Building and RF Applications," in 2020 14th European Conference on Antennas and Propagation (EuCAP), Copenhagen, Denmark, 2020.

[63] M. Gustafsson, A. Karlsson, A. Rebelo and B. Widenberg, "Design of frequency selective windows for improved indoor outdoor communication," *IEEE Transactions on Antennas and Propagation*, vol. 54, no. 6, pp. 1897 - 1900, 2006.

[64] A. A. Dewani, S. G. O'Keefe, D. V. Thiel and A. Galehdar, "Window RF Shielding Film Using Printed FSS," *IEEE Transactions on Antennas and Propagation*, vol. 66, no. 2, pp. 790 - 796, 2018.

[65] B. Sanz-Izquierdo and E. A. Parker, "3-D Printing of Elements in Frequency Selective Arrays," *IEEE Transactions On Antennas and Propagation*, vol. 62, no. 12, pp. 6060-6066, 2014.

[66] M. Philippakis, C. Martel, D. Kemp, R. Allan, M. Clift, S. Massey, S. Appleton, W. Damerell, C. Burton and E. A. Parker, "Application of FSS Structures to Selectively Control the Propagation of signals into andout of buildings," Ofcom , Surrey, 2004.

[67] E. Parker, J.-B. Robertson, B. Sanz-Izquierdo and J. Batchelor, "Minimal size FSS for long wavelength operation," *Electronics Letters*, vol. 44, no. 6, p. 394 – 395, 2008.

[68] G. H.-h. Sung, K. W. Sowerby, M. J. Neve and A. G. Williamson, "A Frequency-Selective Wall for Interference Reduction in Wireless Indoor Environments," *IEEE Antennas and Propagation Magazine*, vol. 48, no. 5, pp. 29 - 37, 2006.

[69] S. S. Zhekov, O. Franek and G. F. Pedersen, "Dielectric Properties of Common Building Materials for Ultrawideband Propagation Studies," *IEEE Antennas & propagation magazine*, vol. 62, no. 1, pp. 72-81, 2020.

[70] "Dycotech materials," datasheet, DM-SIP-3060S, 30 01 2022. [Online]. Available: https://www.dycotecmaterials.com/product/dm-sip-3060s/. [Accessed 20 01 2022].

[71] C. Bondy, A. Pardiwala and M. Morgan, "Screen Printing Standard Operating Procedure," Rochester Institute of Technology, Rochester, USA , undated.

[72] "Handprinted," Handprinted, 21 01 20222. [Online]. Available: https://handprinted.co.uk/. [Accessed 31 01 2022].

CHAPTER 7: CONCLUSION AND FUTURE WORK

7.1 Summary and Conclusion

This chapter summarises the outcomes and contributions of the technical topics covered in this thesis and concludes with suggestions for future work. The work begins with a review of the AM processes and an overview of Additive manufacturing (AM) applications for antenna and electromagnetic devices. AM has been demonstrated to be a better alternative fabrication solution to the traditional methods because it is faster, more accurate, reliable as well as relatively cheaper material wise due to its additive nature as opposed to subtractive, from the antenna and electromagnetic devices fabrication standpoint. It has emerged as an important product prototyping method as well as an alternative method for direct manufacture of customized and complex designs. It improves design fabrication/manufacturing by allowing design flexibility as well as rapid prototyping, manufacturing, and testing using various types of dielectric materials of differing relative permittivity. The use of two types of AM techniques, DW and FFF has been extended in this work to the printing of antennas and dielectric substrates structures for frequency selective sensors, exploiting the process's quick machine time, low cost and flexibility compared to the subtractive methods.

In this thesis, different types of electromagnetic devices fabricated on various substrates using different AM techniques have been reported. The AM techniques employed are DW to print the antennas and Fused Filament Fabrication (FFF) to print the required substrate for FSS based sensors. Inkjet printing was employed to print the antennas on a paper substrate and aerosol jet printing on a fake fingernail made of Acrylonitrile butadiene styrene (ABS). A study of the surface profile of the printed surface was done using white light interferometry (profilometer) and Talysurf CCI. FFF was employed in the printing of the substrate for the sensor applications, followed by by-hand application of silver loaded conductive paint to create the applications conductive track using a painter's brush.

From each of the four pieces of work, an application has been presented that can potentially be integral to development of future wireless applications.

The four topics covered are: Evaluation of planar inkjet-printed antennas on a low-cost origami flapping robot, 3D Printed Fingernail Antennas for 5G, A Liquid Sensor based on Frequency Selective Surfaces and An FSS based displacement sensor. Detailed simulations and measurements of the fabrications were carried out to check for consistencies.

In Chapter 3, a compact dual-band monopole antenna consisting of a triangular shape with a horizontal slot on top of a semi-elliptic on a photo paper substrate integrated onto a flapping origami robot was proposed. The antenna fits on the available space on the traditional origami structure and can operate at the required bands. Two optimal solutions were achieved: one on the spine and the other on tail and/or neck. A diversity system involving the tail and neck antennas was also realized. This potentially increases coverage in a communication system. The monopole antennas were fabricated on standard photo paper substrate using a commercially available, low-cost, inkjet printer with cartridges filled with nanoparticle silver conductive ink. A chemical sintering-based silver nanoparticle conductive ink cartridge was used to print the antennas using an inexpensive and ordinary home inkjet printer and photo paper. This makes fabrication of the antenna inexpensive and fast. The successful outcome promises the potential of integration of antennas with flexible electronic systems using inkjet printing technology.

Chapter 4 has discussed the application of 3D printing in the development of wearable antennas for on fingernail for potential 5G application. Aerosol Jet printing and flush curing has been successfully employed to deposit layers of silver ink on the curved nails. Two antennas were developed using the aerosol jet technique. One at microwave and the other at millimetre wave. The technique has produced the high resolution required for the printed antennas as well as smooth and thin metallic layers. An additional copper layer was added to the millimetre wave antenna through a copper plating. The fabricated antennas provided good performance in terms of impedance match and bandwidth. Radiation patterns was as expected for patch antenna with a main lobe out of the fingernail and low radiation towards the finger and body. The antenna designs can potentially be deployed in IoT solutions for 5G technology. The proposed nail antenna is light, cheap, easy to install, part of beauty accessory, which occupies a small surface area and is easy to wear. The requirement of different equipment at different stages presents a case for a production chain process. This could enable scaling up to a mass production industrial process. This application having been confirmed to effectively operating in a laboratory environment, future work can focus in employing this system in an industrial environment.

In Chapter 5, a new concept for microwave liquid sensor based on Frequency Selective Surfaces was discussed. The sensing behaviour was achieved by introducing trenches between FSS elements to modify the transmission response when liquids with different permittivity were inserted. The developed sensor can be used as a part of wireless sensing network can be ideal for instances requiring robust and real-time. It has been demonstrated that additive manufacturing technologies can be employed in the developed of the FSS based sensor. Inexpensive PLA material has been found suitable for this purpose. The conductive tracks were applied on the 3D FSS structure using hand painting by a painter’s brush.

In chapter 6, a novel convoluted square loop FSS based displacement wireless sensor based on a retractable inserted dielectric substrate was developed. The reconfigurable behaviour of the sensor was achieved by a retracting substrate complement. The complement was made of the same material as the FSS substrate. The sensor can be integrated with a wireless sensing network. Inexpensive PLA material has been found suitable for this purpose. Fused filament fabrication (FFF) additive process is employed to fabricate both the FSS substrate for the FSS and the complement. The printing of the conductive tracks for the FSS was achieved through hand painting of conductive silver paint using a painter's brush. The sensor is ideal for instances requiring real-time monitoring of a structural changes e.g., sinking, or lateral displacement.

7.2 Future work

The potential of AM for the fabrication of electromagnetic propagation structures has been demonstrated in this report. In all methods employed, i.e., inkjet printing, aerosol jet printing and by-hand application technique, the conductive ink was deposited on the dielectric materials to form the conductive parts of the electromagnetic propagation devices. Future works on each of the pieces of work can be achieved along the following lines.

Inkjet-printing technique capability for printing of antenna on an origami folded photo paper substrate can be extended to integrate 3D printed actuators for moving the wings as envisioned in [1] and possibly the electronics required to control them. Further, the paper origami antenna application can be incorporated in other foldable electronics for possible soft robotics, soft robots, smart biorobots where compactness, flexibility and versatility of the electronic circuits would be required [2] or in the development of further lightweight and low-cost deployable origami concept-based antennas [3].

The proposed fingernail antenna designs proposed are potentially deployable in IoT ecosystem in 5G technology environment such as sensing, data collection/exchange, tracking and wireless communication. It can also be used in medical applications. The antennas can be as worn beauty accessory as it is light, easy to install and wear and is also inexpensive. For future work, with multiple fingers on a human hand, the work can be extended to make antenna arrays and diversity systems feasible for signal reception improvement.

The FSS based liquid sensor concept can be extended for multiband dielectric characterization of liquids for the proposed approach in future. Further, the proposed sensor was found to be accurate, easy, and inexpensive to fabricate, have a good detection response and can be integrated with other electronic components in microwave and RF engineering environment. The results can contribute more widely to intrinsic chemical liquids information and can potentially be extended for various applications. Specifically, the LUT parameters of the resonant frequency set in this study can allow users to transfer this valuable information by means of a remote sensing technique. Further work could include investigating the behaviour of the design if the array size of the sensor were reduced. Further, the concept can also potentially be adapted in reconfigurable FSS using low loss liquids in radiation beam steering using liquid fluidity as in [4].

The experimental results of the displacement sensor shows that the FSS based sensor offer good prospects as a local or remote structural health monitor in situations such as during an earthquake or for post-earthquake structural damage sensor. The proposed concept can further be developed as an application in reconfigurable FSS and metasurfaces using an electromechanical process to displace the complement substrate from the FSS. The displacement sensing is achieved wirelessly implying its application can be achieved remotely. Future could include looking into designing a custom sensor with dielectric substrate selected such that it optimises the measurement range for good accuracy and precision.

References

[1] G. Grau, E. J. Frazier and V. Subramanian, "Printed unmanned aerial vehicles using paper-based electroactive polymer actuators and organic ion gel transistors," *Microsystems & Nanoengineering,* vol. 2, pp. 1-8, 2016.

[2] F. B. Kadumudi, J. Trifol, M. Jahanshahi, T.-G. Zsurzsan, M. Mehrali, E. Zeqiraj, H. Shaki, M. Alehosseini, C. Gundlach, Q. Li, M. Dong, M. Akbari, A. Knott, K. Almdal and A. Dolats, "Flexible and Green Electronics Manufactured by Origami Folding of Nanosilicate-Reinforced Cellulose Paper," *ACS Appl. Mater. Interfaces ,* vol. 12, pp. 48027−48039, 2020.

[3] S. I. H. Shah, S. Bashir, M. Ashfaq, A. Altaf and H. Rmili, "Lightweight and Low-Cost Deployable Origami Antennas—A Review," *IEEE Access,* vol. 9, pp. 86429 - 86448, 2021.

[4] C. Song, E. L. Bennett, J. Xiao, R. P. Tianyuan Jia, K.-M. Luk and Y. Huang, "Passive Beam-Steering Gravitational Liquid Antennas," IEEE Transactions on Antennas And Propagation , vol. 68 , no. 4, pp. 3207-3212, 2020.

Appendices

Appendix 3.1

ver. 1.0.2

Bring the fun of circuit design to everyone!

Datasheet: AGIC-AN01 Silver Nano Ink
AGIC-CP01A4 Special Coated Paper

AgIC Silver Nano Ink is conductive ink that lets you print electric circuits with printers for home use. Youcan design and print any pattern of electric circuits in the same way as you print ordinary documents.

There are a wide variety of applications: from making prototypes of electric products to creatingsomething new, letting your imagination expand.

We recommend using this ink with AGIC-CP01A4 Special Coated Paper so that the ink's conductivitycan be fully exerted.

Product name	**AGIC-AN01 Silver Nano Ink**
Composition	-Silver (15% wt) -Water -Ethylene glycol -Ethanol
Conductivity (*)	0.2 [Ω/sq]
Viscosity	2 - 3 [mPa•s]
Surface tension	30 - 35 [mN/m]
Flash point (**)	Non-flammable
Specific weight	1.2
Length of time before drying (*)	3 [sec]

(*) when printed on the exclusive paper (AGIC-CO01A4) with DCP J740N

(**) Although the ink itself is not flammable, high current or high voltage might result in burning the printed paper.

Product name	**AGIC-CP01A4 Special Coated Paper**
Thickness	177±12 [μm]
Weight	11.1[g] (one sheet of A4 size)

Conductivity emerges only when you print patterns on the front (shiny) side of the paper.

Manufacturer information

Manufacturer	AgIC Inc.
Office	Meiwa-hongo bldg., 4-1-3, Hongo, Bunkyo-kTokyo 1130033 JAPAN
Contact	hello@agic.cc

Please visit http://agic.cc for more information.

Appendix 5.1

```
%Author: Peter Njogu
%Matlab code that computes the capacitance and inductance of the free
%standing FSS as per equation 5.5 in chapter 5

clear all; clc; close all;
Q=0.0506; %Q is Q factor (equation 5.4) in the correction term G
%(equation 5.3)

Z=377;
C=3*10^8; %speed of light
F=5.3*10^9; % Minus substrate
% F=4.29*10^9; % with substrate
labda=C/F; %wavelength
P=20*10^-3; % FSS period
t=2*10^-3; % thickness of the FSS tracks
g=2*10^-3; % gap between the FSS cells

S1=sin((pi*g)/(2*P)); % equation term
% S2=S1^4; %sin^4
S2=sin((pi*g)/(2*P)).^4;
% S3=S1^2; %
S3=sin((pi*g)/(2*P)).^2;
C1=cos((pi*g)/(2*P));
% C2=C1^4;
C2=cos((pi*g)/(2*P)).^4;
A=((1-(3*S3))^2);% equation term
D=(((1/16)*(t/labda))^2);% equation term
E=(A*D*C2);
F=((2*P)/(Z*pi*C));
G=log(csc((pi*t)/(2*P)));
H=((Q*C2)/(1+Q*S2));
Ci=F*[(G+H+D)]
I=(Z*labda^2)/(32*P*pi*C);
Li=I*[(G+H+D)]
```

Code output

```
Ci =

  2.1426e-13

Li =

  3.8114e-09
```

Appendix 5.2

$Capacitance = \frac{1}{4\pi L_1 f^2}$, where L_1 is equal to 3.8114 nH obtained from equation (5.5), f is the frequency of the FSS at each trench depth h_1 and from L1 and f, capacitance was obtained. Using the scatter function of the Excel spreadsheet application, Figure 5.4 was obtained and from the trendline function, equation (5) was obtained for the capacitance.

Depth h_1	Capacitance	Frequency
0	360	4.3
0.5	336	4.45
1	323	4.53
1.5	317	4.58
2	315	4.6
2.5	313	4.61
3	310	4.63

$$C_i = -3.7778h_1^3 + 25.143h_1^2 - 58.103h_1 + 359.76 \text{ fF} \quad (5.7)$$

Appendix 5.3

With capacitance, $C = \frac{1}{4\pi L_1 f^2}$, where L_1 is inductance and equal to 3.8114 nH, obtained from equation (5.5), f is the frequency of the FSS at each value of ε_r according to simulations, the capacitance was obtained. Using the scatter function of the Excel spreadsheet application, Figure 5.7 was obtained and from the trendline function, equation (5.8) was obtained for the capacitance.

er	Frequency	Capacitance
1	4.6	314.3985392
4	3.95	426.3850723
8	3.46	555.7045917
12	3.09	696.7536044
16	2.84	824.8206073
20	2.65	947.3368587

$$C_{er} = 33.312\varepsilon_r + 288.8956 \text{ fF} \quad (5.8)$$

Appendix 5.4

```
%MATLAB code that derives the coeeficients of the relative permitivity (Er)
%and loss tangent (tan delta)
 clear all; close all; clc
 % Array of the resonant frequency of the FSS with LTU in the trenches
Resonance_Freq = [3.01 3.61 3.83 3.92 4.24];
% Array of the Er of the LTU in the trenches
Di=[12.42 5.08 3.8 3.29 2.57];
 %This line gives the Er polynomial coeffient
pcoeff3_Er=polyfit(Resonance_Freq, Di, 3)

% Array of the frequency shift from the reference
Freq_Shift=[1.59 0.99 0.77 0.68 0.36];
% Array loss tangent (Tand)of the LTU in the trenches
Tand=[0.65 0.96 0.64 0.47 0.018];
%This line gives the Tan delta polynomial coeffient
pcoeff3_Tand =polyfit(Freq_Shift, Tand, 3)
```

Code output (Coefficients of the polynomial expression)

```
pcoeff3_Er =
  -1.6763,   24.8613, -121.5387,  198.7187
pcoeff3_Tand =
  -2.0252 ,   4.3111,   -1.3509,   0.0395
```

Appendix 5.5

```
%Author: Peter Njogu
%MATLAB code that calculates the permittivity and tan delta (dielectric properties of the
LUTs based on equations (5.10) and (5.11). These equations were derived from appendix 5.4)

clear all; close all; clc

fr_Methanol = 3.01; % Resonance frequency of Methanol
fr_Ethanol = 3.61; % Resonance frequency of Ethanol
fr_Butanol = 3.92; % Resonance frequency of Butanol
fr_Propan = 3.83; % Resonance of frequency Propan
fr_Xylene = 4.24; % Resonance of frequency Xylene
fs_Methanol = 1.59; % Frequency shift of Methanol
fs_Ethanol = 0.99; % Frequency shift of Ethanol
fs_Butanol = 0.68; % Frequency shift of Butanol
```

```
fs_Propan = 0.77; % Frequency shift of Propan
fs_Xylene = 0.36; % Frequency shift of Xylene

%Calculation of permittivity and tan delta of Butanol-o1-o1
Er_Butanol= -1.6763*fr_Butanol^3 + 24.8613*fr_Butanol^2 -121.5387*fr_Butanol
+198.7187
tand_Butanol=-2.02252*fs_Butanol^3 + 4.3111*fs_Butanol^2 -1.3509*fs_Butanol +0.0395

%Calculation of permittivity and tan delta of Ethanol
Er_Ethanol= -1.6763*fr_Ethanol^3 + 24.8613*fr_Ethanol^2 -121.5387*fr_Ethanol
+198.7187
tand_Ethanol=-2.02252*fs_Ethanol^3 + 4.3111*fs_Ethanol^2 -1.3509*fs_Ethanol +0.0395

%Calculation of permittivity and tan delta of Methanol
Er_Methanol= -1.6763*fr_Methanol^3 + 24.8613*fr_Methanol^2 -121.5387*fr_Methanol
+198.7187
tand_Methanol=-2.02252*fs_Methanol^3 + 4.3111*fs_Methanol^2 -1.3509*fs_Methanol
+0.0395

%Calculation of permittivity and tan delta of Propan-2-o1
Er_Propan= -1.6763*fr_Propan^3 + 24.8613*fr_Propan^2 -121.5387*fr_Propan +198.7187
tand_Propan=-2.02252*fs_Propan^3 + 4.3111*fs_Propan^2 -1.3509*fs_Propan +0.0395

%Calculation of permittivity and tan delta of Xylene
Er_Xylene= -1.6763*fr_Xylene^3 + 24.8613*fr_Xylene^2 -121.5387*fr_Xylene +198.7187
tand_Xylene=-2.02252*fs_Xylene^3 + 4.3111*fs_Xylene^2 -1.3509*fs_Xylene +0.0395
```

Code output

```
ɛr_Butanol-1-o1 = 3.3416

tan δ_Butanol-1-o1 = 0.4784

 ɛr_Ethanol = 5.0959

tan δ_Ethanol = 0.9650

ɛr_Methanol = 12.4189

tan δ_Methanol = 0.6606

ɛr_Propan-2-o1 = 3.7357

tan δ_Propan-2-o1 = 0.6320

 ɛr_Xylene = 2.5651

tan δ_Xylene = 0.0175
```